UNIVERSITY OF SOUTHAMPTON

FACULTY OF NATURAL AND ENVIRONMENTAL SCIENCES

School of Ocean and Earth Science

Iron isotopes in seawater: method development and results from the Atlantic Ocean

by

Jessica Katharina Klar

Thesis for the degree of Doctor of Philosophy

September 2014

UNIVERSITY OF SOUTHAMPTON

ABSTRACT

FACULTY OF NATURAL AND ENVIRONMENTAL SCIENCES

Ocean and Earth Science

Doctor of Philosophy

IRON ISOTOPES IN SEAWATER: METHOD DEVELOPMENT AND RESULTS FROM THE ATLANTIC OCEAN

by Jessica Katharina Klar

The analysis of the iron (Fe) isotopic composition of seawater can provide unique information about Fe sources to seawater, and Fe cycling within the oceans, which are important for understanding global climate because of the links between the marine carbon and iron cycles. The low dissolved Fe (dFe) concentrations found in seawater mean that analyses of the iron isotopic composition of seawater is an analytical challenge. This thesis describes the development methods for accurate and precise analysis of Fe isotopes in seawater with concentrations as low as ~0.4 nM Fe, and the results of iron isotope analysis of seawater samples from within the oxygen minimum zone (OMZ) of the tropical Atlantic Ocean, and the dissolved phase of hydrothermal plumes in the Southern Ocean.

Briefly, Fe is preconcentrated from seawater using NTA resin and is then purified by anion exchange chromatography. Iron isotope ratios are determined by high resolution multi-collector inductively coupled plasma mass spectrometry (MC-ICPMS, Thermo Fisher Neptune) and mass bias effects are corrected using a double-spike technique. The Fe isotope spike consists of 47 % of ^{57}Fe, 53 % of ^{58}Fe, and a small amount (< 0.5 %) of ^{54}Fe, which allows precise measurement of a wide range of sample to spike mixing ratios. Isotope ratios are expressed in delta notation (δ^{56}Fe), relative to ^{54}Fe and relative to IRMM-14. The precision of the MC-ICPMS measurements is δ^{56}Fe ~ 0.06 ‰ (2 SD), based on replicate analyses of two different iron isotope standards.

The iron isotopic composition of dissolved Fe ($\delta^{56}Fe_{dFe}$) was measured in seawater samples collected along an E-W transect along ~12 °N in the tropical Atlantic Ocean (GEOTRACES section GA06), extending from the Senegalese shelf towards the open ocean in order to assess the behaviour of dFe in the OMZ. Bottom waters within the OMZ have elevated dFe concentrations and low δ^{56}Fe signatures, as low as ~ -0.3 ‰, which suggests that dFe is principally derived from sediment pore waters that have undergone dissimilatory iron reduction. Towards the open ocean, $\delta^{56}Fe_{dFe}$ values within the OMZ increase, due to formation of iron ligands and/or mixing with adjacent water masses. Dissolved aluminium concentrations in surface waters at the open ocean stations are very high (up to 27 nM), indicating significant supply from atmospheric dust, and the surface waters have high δ^{56}Fe values (up to +0.5 ‰), much higher than bulk silicate Earth, indicating that Fe isotopes are fractionated during dust dissolution.

Analyses of the Fe isotopic composition of dFe in hydrothermal plumes from 3 sites in the East Scotia Sea reveal that during the early stages of mixing between hydrothermal fluids and seawater, Fe isotopes are significantly fractionated from the vent fluid; the $\delta^{56}Fe_{dFe}$ value in the plume is as low as -1.2 ‰, compared to vent fluid values of -0.64 to +0.28 ‰. As the plume continues to mix with seawater, $\delta^{56}Fe_{dFe}$ values increase, converging to values of between -0.6 to -0.3 ‰. This strongly suggests that dFe is stabilised by the formation of colloidal Fe-(oxy)hydroxides and Fe-L in the distal parts of the plume. This stabilised dFe is likely to be transported long distances away from its source, contributing to the deep ocean dFe budget.

List of Contents

List of tables

List of figures

DECLARATION OF AUTHORSHIP

I, **Jessica Katharina Klar**, declare that this thesis entitled **Iron isotopes in seawater: method development and results from the Atlantic Ocean** and the work presented in it are my own and has been generated by me as the result of my own original research.

I confirm that:

1. This work was done wholly or mainly while in candidature for a research degree at this University;
2. Where any part of this thesis has previously been submitted for a degree or any other qualification at this University or any other institution, this has been clearly stated;
3. Where I have consulted the published work of others, this is always clearly attributed;
4. Where I have quoted from the work of others, the source is always given. With the exception of such quotations, this thesis is entirely my own work;
5. I have acknowledged all main sources of help;
6. Where the thesis is based on work done by myself jointly with others, I have made clear exactly what was done by others and what I have contributed myself;
7. None of this work has been published before submission.

Signed: .....

Date: .....

Acknowledgements

In first place I would like to thank my supervisors Rachael James, Eric Achterberg, Doug Connelly and Martha Gledhill for giving me the opportunity to take on this exciting PhD project and for their guidance and patience over the past 4 years. It is a privilege to have been part of the Marine Geochemistry Group at NOC. Ian Parkinson is especially thanked for his involvement in this project for providing the modelling results for the isotope spiking. And a big thank you to my panel chair, Rachel Mills, who always showed encouragement for my project.

I am deeply thankful to François Lacan, Seth John, Tim Conway, Silke Severmann and Olivier Rouxel for providing me with expert advice at any point I needed support for the method development. There have been a lot of emails full of questions and without your guidance this project would have taken even longer than 4 years… the geochemistry community is truly supportive and great to be part of. I also express my gratitude to Christian Schlosser, Will Homoky, Jeff Hawkes, Anna Lichtschlag for many lab and science discussions and advice given throughout the years.

I am also thankful that my project consisted in the exciting undertaking of seawater sample collection in the Atlantic Ocean on board research vessels Discovery and James Cook. I am grateful to have taken part on two UK GEOTRACES cruises, and to the people that made this possible were Eric Achterberg and Gideon Henderson. Sampling at sea is hard work and tiring due to the long hours filtering seawater every day. But we had the best trace metal team ever (!). A big thank you to Eric and Christian Schlosser who participated in running the flow injection analyser 24 hours and to the rest of the trace metal team (Maeve Lohan, Angie Milne, Maxi Castrillejo, Felix Morales and Rosie Chance) for combined sample collection efforts.

A special thanks to Dakota Gibbs and Aly Lough for joining me on the iron isotopes journey in the clean lab. Dakota has proven to be a talented trace metal chemist and prepared most of the hydrothermal samples for isotopic analysis. Having Dakota and Aly in the lab has definitely made the long hours in the clean lab more fun and interesting

Without the help from Andy Milton and Matt Cooper with training, method set-up and sample analysis I would have been lost in finding out how to use these instruments. The instrument handling skills I have learned are probably of the most valuable in my career.

I have been received with great hospitality during my visit to LEGOS in Toulouse. I am grateful to Francois Lacan for making me feel part of his team for 10 days and to Marie Labatut and Ciril Abadie for all their support and advice. Ever since my visit to Toulouse I am hoping for a future opportunity to work at LEGOS.

It has been great to be part of the PhD community, in which I have met interesting people from all over the world and created strong bonds with many of them. I am especially happy to have shared office with three of the most amazing female scientists Cathy Cole, Sarah Wright, Caroline Graves and Morelia Urlaub. Office cake and discussions have always cheered me up.

The friends I have made in Southampton have gained a special place in my heart: Justine, Ally, Debbie, Anna, Libby and Jess (plus other halves), you have made me feel truly at home and made me discover the best side of this country during our various adventures. Exceptional friends that have also given me support in that past 4 years are Lavinia, Sophia, Katsia, Helen, Ben, Ethan, Gonzalo, Anna L. and Konstantina. A big thank you, Sharon and Rachel Gatrell, for looking after Chamaco during the writing up period; you have taken a heavy work load off me. Many loving thoughts go especially to my family: mum, Naty, Michael and Tony have inspired me and supported me to fulfil my dreams.

Definitions and Abbreviations

AABW	Antarctic Bottom Water
AAIW	Antarctic Intermediate Water
AC	Adventure Caldera
ACC	Antarctic Circumpolar Current
Al	Aluminium
BC	Brazil Current
Chl-a	Chlorophyll-a
Cl^-	Chloride
Cr	Chromium
CTD	Conductivity Temperature Density
CVFZ	Cape Verde Frontal Zone
dAl	Dissolved Al
dFe	Dissolved Fe
DIP	Dissolved inorganic phosphate
DIR	Dissimilatory iron reduction
dMn	Dissolved Mn
DS	Double spike
ESR	East Scotia Ridge
ESS	East Scotia Sea
Fe	Iron
Fe-L	Fe-ligand
FeS	Fe sulphide
GD	Guinea Dome
H_2O_2	Hydrogen peroxide
H_2S	Hydrogen sulphide
HCl	Hydrochloric acid
HDPE	High density polyethylene

HNLC	High-nutrient, low-chlorophyll
HNO_3	Nitric acid
ICP-MS	Inductively coupled plasma mass spectrometer
ITCZ	Intertropical convergence zone
KC	Kemp Caldera
LCDW	Lower Circumpolar Deep Water
LDPE	Low density polyethylene
LOD	Limit of detection
LSS	Light scattering sensor
MADCOW	Model of Aluminium for Dust Calculation in Oceanic Waters
MC-ICP-MS	Multi-collector ICP-MS
Mg	Magnesium
Mn	Manganese
MQ	Milli-Q water (18.2 MΩ)
NACW	North Atlantic Central Water
NADW	North Atlantic Deep Water
NEC	North Equatorial Current
NECC	North Equatorial Countercurrent
NEUC	North Equatorial Undercurrent
Ni	Nickel
nNECC	northern North Equatorial Countercurrent
NOC	National Oceanography Centre
NTA	Nitriloacetic acid
O_2	Oxygen
OMZ	Oxygen minimum zone
OTE	Ocean Test Equipment
P	Phosphorus
PF	Polar Front
SACCF	Southern Antarctic Circumpolar Current Front

SACW	South Atlantic Central Waters
SAF	Subantarctic Front
SBACC	Southern Boundary of the Antarctic Circumpolar Current
SD	Standard deviation
SO_4^{2-}	Sulphate
SW	Seawater
TD	Thermally distilled
tFe	Total Fe
UCDW	Upper Circumpolar Deep Water
VF	Vent fluid
WDW	Warm Deep Water
WSDW	Weddell Sea Deep Water
$\delta^{56}Fe$	Delta notation of isotope ratios
$\delta^{56}Fe_{dFe}$	$\delta^{56}Fe$ of dFe

Chapter 1: Introduction

1.1 Iron isotope biogeochemistry in the oceans

Certain trace metals, including iron (Fe), are essential nutrients for the growth of oceanic phytoplankton as they are required in the functioning of fundamental enzymes (Geider and LaRoche, 1994; Falkowski *et al.*, 1998; Morel and Price, 2003). However, the availability of Fe in the modern ocean is limited over vast regions, wherever the rate of removal of Fe mainly (which has low solubility; (Liu and Millero, 2002) exceeds the supply of Fe from external sources to the ocean. Marine photosynthesis, which takes place in the surface layer of the ocean (or euphotic zone), is responsible for uptake of a significant portion of atmospheric carbon dioxide (CO_2), but Fe availability (co)-limits primary production in ca. half of the world's ocean (Martin and Fitzwater, 1988; Martin *et al.*, 1990; Boyd and Ellwood, 2010). Although primary production is mainly limited by light and macro-nutrients, large parts of the global ocean have relatively high concentrations of major nutrients (nitrate, phosphate and silicate) in surface seawater but very low levels of chlorophyll due to limitation of phytoplankton growth as a result of low Fe. These areas have huge potential for CO_2 drawdown and are referred to as High Nutrient Low Chlorophyll (HNLC) regions (Martin and Fitzwater, 1988; Martin *et al.*, 1990). Other areas of the ocean, such as the high latitude North Atlantic Ocean, may be seasonally Fe limited (Nielsdottir *et al.*, 2009). As the Fe cycle is closely linked to the global carbon cycle, research into the sources and biogeochemical cycling of Fe is important for climate simulations, both in the past and in the future.

Iron is delivered to the ocean from multiple sources, but their individual fluxes vary spatially and temporarily. Fe is directly delivered to the surface layer by (natural and anthropogenically sourced) atmospheric dust deposition (Jickells and Spokes, 2001; Baker *et al.*, 2003). However, atmospheric dust is heterogeneously distributed over the globe, with very high dust deposition in the North Atlantic Ocean but very low inputs closer to the poles (Jickells *et al.*, 2005). Iron is also supplied to the ocean by continental runoff (via rivers) and

sediment dissolution at the seafloor. Iron from these sources has the greatest impact on coastal regions, but it is now known that a significant part of Fe delivered to the coastal regions can be exported offshore into the open ocean (Laës *et al.*, 2003; Siedlecki *et al.*, 2012). In addition, the upwelling, entrainment or mixing of deeper waters (especially during the winter season), that are enriched in nutrients and micronutrients, are important sources of Fe to the surface ocean on a global scale (Watson, 2001). Another source of Fe to the deep ocean is hydrothermal venting along mid ocean ridges (MOR). Fluxes of hydrothermal Fe are thought to be relatively constant over time, and occur all over the globe (Elderfield and Schultz, 1996; Tagliabue *et al.*, 2010).

The distribution of Fe in ocean waters is also controlled by internal biological and chemical processes. The speciation of Fe in seawater is regulated by redox conditions, inorganic speciation and inorganic and organic ligand complexation and size fractionation (Ussher *et al.*, 2004). Iron speciation regulates its bioavailability to phytoplankton. In oxic seawater, Fe is mostly found in its oxidised Fe(III) form. Fe(III) is very insoluble at seawater pH (~ 8), forming (oxy)hydroxides, that tend to aggregate (Liu and Millero, 2002). Some of these aggregates are stable in seawater (especially those in the colloidal fraction, < 0.4 µm) but most will eventually sink towards the seafloor. The complexation of Fe(III) with organic ligands plays an important role in maintaining Fe in solution in seawater and making it bioavailable to phytoplankton. Over 99 % of Fe in the dissolved phase (< 0.2 µm fraction) is bound to organic ligands (Gledhill and Buck, 2012). Iron in the < 0.02 µm fraction is considered to be truly soluble. Other forms of Fe include labile Fe (the fraction that is complexed with an added electro-active ligand), colloidal Fe (0.02 to 0.4 µm) and particulate Fe (> 0.2 or 0.4 µm) (Schlosser and Croot, 2008). However, a wide range of different chemical forms of Fe may be found in each of those size fractions.

While analysis of Fe concentrations in seawater are valuable for assessing the potential for Fe limitation, they provide little information on the sources of Fe, or the internal processes that affect the distribution of Fe. To do this, analysis of Fe isotopes are required (Zhu *et al.*, 2000; Beard *et al.*, 2003b). However, while measurement of the Fe isotopic composition of the principal sources of Fe to

the ocean can be done with relative ease, as the concentrations of Fe are relatively high, the determination of Fe isotopes in seawater is much more challenging. This is because Fe concentrations in seawater are commonly found in the picomolar range. Recent advances in analytical techniques and improvements in measurement precision with the advent of multi-collector inductively coupled plasma mass spectrometry (MC-ICPMS) technology have led to the acquisition of reliable seawater Fe isotope data in recent years (Lacan *et al.*, 2008; John and Adkins, 2010; Lacan *et al.*, 2010; Radic *et al.*, 2011; John and Adkins, 2012; Conway and John, 2014). An ocean transect across the North Atlantic Ocean showing high resolution $\delta^{56}Fe_{dFe}$ in seawater confirms the utility of Fe isotopes to identify sources and processes and estimate their contribution to the dFe (dissolved Fe) inventory (Conway and John, 2014). Here $\delta^{56}Fe_{dFe}$ data was used to predict the aerosol, reductive and non-reductive sediment dissolution and hydrothermal inputs into the ocean, as well as to identify internal cycling processes, such as biological uptake. This is the first study presenting this kind of magnitude in Fe isotope data in open ocean seawater, which gives insight into the complexity of the Fe cycle, proving to be a new tool to estimate flux data, as well as confirming the need to better understand Fe isotope fractionation in seawater. Ultimately, the attainment of Fe isotope data in different oceanic regions will provide a better understanding of Fe cycling pathways. The assumptions made in Conway and John (2014) to estimate Fe fluxes need to be further investigated. This thesis attempts to bring better understanding of the Fe cycle in the oceans.

1.1.1 Iron isotope fundamentals

Iron is a transition metal and has a relative atomic mass of 55.847 amu. It has four stable isotopes ^{54}Fe, ^{56}Fe, ^{57}Fe and ^{58}Fe, with respective natural atomic abundances of 5.82, 91.66, 2.19 and 0.33 %, under Earth surface conditions (Turner *et al.*, 2001). There are also two short-lived Fe isotopes, ^{55}Fe and ^{59}Fe and one long-lived Fe isotope, ^{60}Fe. It is not possible to obtain the absolute or 'true' Fe isotope ratio by external normalisation, so Fe ratios are reported in delta notation relative to a reference material. In this thesis, Fe isotopic

compositions are given as the ratio of ^{56}Fe to ^{54}Fe, normalised to the $^{56}Fe/^{54}Fe$ ratio of the Fe isotope standard IRMM-14, and expressed as $\delta^{56}Fe$ as follows:

$$\delta^{56}Fe = 1000 \cdot \left[\frac{\left(^{56}Fe/^{54}Fe\right)_{sample}}{\left(^{56}Fe/^{54}Fe\right)_{IRMM-14}} - 1 \right] \qquad \text{Equation 1-1}$$

The abundances of Fe isotopes in IRMM-14, expressed in %, are 5.845 ± 0.023 for ^{54}Fe, 91.754 ± 0.024 for ^{56}Fe, 2.1192 ± 0.0065 for ^{57}Fe and 0.2818 ± 0.0027 for ^{58}Fe (Taylor *et al.*, 1992). The $\delta^{56}Fe$ value of IRMM-14 is -0.09 ± 0.05 ‰ relative to the igneous rock baseline (Beard et al., 2003a), which is also widely used as a reference value. All $\delta^{56}Fe$ values given in this thesis are reported relative to IRMM-14.

Differences in the Fe isotopic composition of natural materials are the result of (i) mass-dependent processes, whereby isotope ratios are determined by mass difference, and (ii) mass-independent processes. Iron exhibits $\delta^{56}Fe$ variations of ~ 5 ‰ in natural materials (Anbar, 2004). Iron in the human body exhibits the largest natural fractionations so far observed, with $\delta^{56}Fe$ variations of ~ 5.5 ‰ (Walczyk and von Blanckenburg, 2002). The natural variation of $\delta^{56}Fe$ so far observed in the ocean is ~ 4.1 ‰ (Lacan *et al.*, 2008; Radic *et al.*, 2011; John and Adkins, 2012; John *et al.*, 2012; Conway and John, 2014).

1.2 Iron isotope fractionation processes in the ocean

Isotope fractionation between the reactants and products of a reaction may be governed by equilibrium or kinetic processes, or a combination of both. If the reactants and products are in chemical equilibrium, the driving forces for isotopic exchange are due to small free energy differences (Beard *et al*., 2003a). An example of this is shown below, electron transfer:

$^{54}Fe^{2+} + {}^{56}Fe^{3+} \leftrightarrow {}^{54}Fe^{3+} + {}^{56}Fe^{2+}$

Kinetic isotope fractionation occurs in systems that are far from chemical equilibrium, where reaction rates may be quite fast. Examples include precipitation, which is usually a unidirectional reaction. The magnitude and sign of kinetic isotope fractionation is strongly dependent on initial conditions and the

pathway of the reaction, and may be significantly different from the equilibrium value (Beard *et al*., 2003a). Generally, during kinetic isotope fractionation the lighter isotopes are transferred more rapidly to the products of the reaction than the heavy isotopes. Nonetheless, there may be no isotopic fractionation if reaction rates are extremely fast (Balci *et al*., 2006).

In this section I discuss the main processes likely to cause Fe isotopic fractionation of the dissolved Fe pool in seawater. A simple summary of these processes and reactions is given in Table 1-1.

Table 1-1: Summary showing the variation of δ^{56}Fe in the products relative to the reactants for different processes and/or reactions likely to cause Fe isotopic fractionation of dFe in seawater. References are given in the text.

Process	Variation in δ^{56}Fe (products – reactants)
Fe(III) → Fe(II)	negative
Fe(III) → Fe(III)-L	positive or negative
Biological Fe(III) mineral → $Fe(II)_{aq}$	negative
Biological $Fe(II)_{aq}$ → $Fe(III)_{ppt}$	negative
dFe → Fe-phytoplankton	positive or negative
dFe → Fe-scavenged	negative
dFe → Fe-aggregates	negative

1.2.1 Fractionation between Fe(II) and Fe(III)

The chemical speciation and solubility of Fe largely control Fe availability to phytoplankton in the photic layer of the ocean. Generally, iron solubility is very low at seawater pH and oxygen concentrations. Iron can be found in seawater in two oxidation states, +2 (ferrous) and +3 (ferric). Fe(II) is soluble at pH values below 8, but in the modern oxygen rich oceans Fe is mostly found in its +3 oxidation state (Ussher *et al.*, 2004). At seawater pH (~8), $Fe(III)_{aq}$ becomes hydrolysed, forming Fe(III)-(oxy)hydroxides, which tend to aggregate, eventually forming large particles that sink to the seafloor (e.g., Liu and Millero, 1999). The presence of Fe(II) in seawater depends on the temperature, oxygen concentrations, pH and salinity (Millero *et al.*, 1987):

$$t_{1/2} = \frac{\ln(2)}{k_1}$$ Equation 1-2

$$k_1 = K \cdot [OH^-]^2 \cdot [O_2] \qquad \text{Equation 1-3}$$

$$logK = 21.56 - \frac{1545}{T} - 3.92 \cdot I^{1/2} + 1.52 \cdot I \qquad \text{Equation 1-4}$$

where $t_{1/2}$ is the Fe(II) oxidation half-life (min), k_1 is the pseudo-first-order rate constant (min^{-1}), K is the overall rate constant ($(kg\ H_2O)^3\ mol^{-3}\ min^{-1}$), $[OH^-]$ is the concentration of hydroxide ions (M), $[O_2]$ is the concentration of O_2 (M), T is the temperature (ºK) and I is the ionic strength (which is 0.723 for salinity = 35). It is thought that Fe(II) is more bioavailable to phytoplankton than Fe(III) (Baker and Croot, 2010). Fe(II) may be produced by photoreduction (caused by UV irradiation) of colloidal and ferric species and by reductive dissociation in the presence of phytoplankton (Ussher *et al.*, 2004).

The biogeochemical cycle of Fe in the ocean includes a large number of processes involving redox reactions, which may result in changes in Fe isotope signatures. Experimental observations have shown that equilibrium fractionation during reduction of Fe(III) to Fe(II) results in the $\delta^{56}Fe$ value of $Fe(III)_{aq}$ (aq = aqueous) being up to 3.0 ‰ greater than it is in the $Fe(II)_{aq}$ produced (Johnson *et al.*, 2002; Beard *et al.*, 2003a; Welch *et al.*, 2003; Balci *et al.*, 2006). These findings are in agreement with thermodynamic calculations (Anbar *et al.*, 2005).

Kinetic fractionation of Fe isotopes between $Fe(III)_{aq}$ and Fe(III)oxyhydroxides during precipitation, leads to enrichment of heavy isotopes in the remaining $Fe(III)_{aq}$ fraction (Balci *et al.*, 2006). However, if precipitation rates are very high, no isotopic fractionation is observed (Johnson *et al.*, 2002; Balci *et al.*, 2006),

1.2.2 Biological fractionation

In natural environments, redox reactions may be mediated by microbial organisms. It has been observed that anaerobic microbial reduction of Fe(III) in ferrihydrite (Fe(III)-oxide) and hematite (Fe_2O_3) produces $Fe(II)_{aq}$ with a $\delta^{56}Fe$ value up to1.3 ‰ lower than the remaining mineral substrate (Beard *et al.*, 1999; Beard *et al.*, 2003a). However, no significant fractionation has been found between either $Fe(II)_{aq}$ or $Fe(III)_{aq}$ and magnetite produced intracellularly by two different strains of bacteria (Mandernack *et al.*, 1999). Isotope fractionation has

also been observed during the oxidation of $Fe(II)_{aq}$ by anaerobic photoautotrophic bacteria; the $Fe(III)_{ppt}$ (ppt = precipitate) produced was 1.5 ‰ lower than the $\delta^{56}Fe$ value of the remaining $Fe(II)_{aq}$ (Croal *et al.*, 2004).

It has been argued that any isotope fractionation directly related to relatively slow microbial oxidation of Fe(II) or reduction of Fe(III) is likely to be overprinted by the effects of relatively rapid isotopic equilibrium between the $Fe(II)_{aq}$ and $Fe(III)_{aq}$ pools (Balci *et al.*, 2006). It is suggested that the rapid isotopic equilibrium between $Fe(II)_{aq}$ and $Fe(III)_{aq}$ due to electron transfer dominates any isotopic effects associated with microbial Fe(II) oxidation or Fe(III) precipitation. It is also suggested that biological fractionation signals are altered by the formation of $Fe(III)_{ppt}$ or by the formation of organic ligand complexation with Fe (Croal *et al.*, 2004).

The uptake of Fe by marine phytoplankton in the surface layer of the ocean may also fractionate Fe isotopes. Plankton collected in the plume waters from the Amazon in the open ocean have an average $\delta^{56}Fe$ value of -0.24 ‰ compared to -0.17 ‰ in the dissolved fraction (Bergquist and Boyle, 2006). However, the authors concluded that the $\delta^{56}Fe$ value of the plankton most likely reflects that of the Fe attached to the surface of the plankton rather than the intracellular Fe. The removal of light Fe by phytoplankton has been observed in the chlorophyll maximum of the equatorial Pacific Ocean (Radic *et al.*, 2011). On the other hand, Conway and John (2014) have observed the removal of heavy Fe from the dissolved phase, associated with biological activity in several seawater profiles in the North Atlantic Ocean. The Fe fractionation associated with biological uptake therefore needs to be better constrained.

1.2.3 Organic ligand formation

The availability of Fe to phytoplankton is strongly enhanced in the presence of strong Fe-binding organic ligands, to the extent that > 99% of dissolved Fe is strongly coordinated to organic ligands (Gledhill and van den Berg, 1994; van den Berg, 1995; Witter *et al.*, 2000). Two iron binding ligand classes have been characterised in seawater, the strong Fe-binding L1, commonly found in the upper ocean, and the weak Fe-binding L2, found throughout the water column

(Boyd and Ellwood, 2010). Siderophores are very important L1 organic ligands, produced by bacteria and fungi, forming very strong complexes with Fe(III) (Rue and Bruland, 1995; van den Berg, 1995). Siderophore-Fe bonding is strong enough to mediate mineral dissolution of Fe (Cheah *et al.*, 2003).

Isotope fractionation between organically bound Fe(III) and inorganic Fe(III) species may be important in controlling the Fe isotope composition in seawater (e.g., Dideriksen *et al.*, 2008; Morgan *et al.*, 2010). While redox reactions usually have the strongest effect on Fe isotope compositions, organic ligands have a secondary effect. Strong Fe complexes may stabilise iron delivered to the oceans in the Fe(II) form (e.g. hydrothermal vents, reducing sediments), that according to thermodynamic calculations would otherwise be unstable and likely to precipitate from seawater.

Kinetic isotope fractionation has been observed during the dissolution of hornblende promoted by the siderophore desferrioxamine B (DFOB), leading to a dFe pool that is 0.6 ‰ lighter than the Fe in the mineral (Brantley *et al.*, 2004). On the other hand, the equilibrium isotope fractionation between inorganic $Fe(III)_{aq}$ and Fe-DFOB complexes results in a 0.6 ‰ difference between the two forms of Fe, with the Fe-DFOB form being isotopically heavier (Dideriksen *et al.*, 2008; Morgan *et al.*, 2010). In support of this, the dFe fraction of the organic-rich river waters is isotopically heavier than the recorded in organic-poor rivers (Bergquist and Boyle, 2006; Escoube *et al.*, 2009). In addition, it is suggested that other organic ligands that have similar stability but do not feature a rigid ligand structure, may compensate by coordinating more covalently to the central Fe, possibly resulting in even greater Fe isotope fractionation between organic Fe and inorganic Fe. If Fe is bonded more strongly, or more stiffly, in the products of a reaction, relative to the reactants, then the products are likely to preferentially incorporate heavier Fe isotopes (Schauble *et al.*, 2001). This is supported by recent observations of river and lake waters, where the low molecular weight organic-rich fraction (< 10 kDa) is 1.0 to 2.7 ‰ heavier in δ^{56}Fe than Fe-rich colloids (< 0.22 µm) (Ilina *et al.*, 2013). This strongly suggests that strong bonds with organic ligands favour the heavier Fe isotopes. Complex ligand-Fe dentation may have an altogether different isotope

fractionation effect. Future research is needed to investigate isotope fractionation associated with Fe-L formation with different ligand types.

1.2.4 Other processes

Iron is very particle reactive. The adsorption of dFe onto particle surfaces is a process known as scavenging and occurs throughout the water column. A first attempt to estimate Fe isotope fractionation associated with particle scavenging showed that fractionation was relatively small, with scavenged Fe being 0.3 to 0.18 ‰ lighter than the $\delta^{56}Fe_{dFe}$ (Radic *et al.*, 2011). Iron is also removed from the dissolved phase by particle aggregation (such as the aggregation of colloidal (oxy)hydroxides) and sinking. It is argued that this process may also lead to small isotopic fractionation, the aggregated Fe being 0.05 ± 0.07 ‰ lighter than $\delta^{56}Fe_{dFe}$ (Radic *et al*., 2011).

The remineralisation of sinking biogenic particles is the major process affecting concentrations of dFe below the surface mixed layer and leads to increased dFe concentrations with depth (Boyd and Ellwood, 2010). The isotopic signal associated with this process will depend on the isotopic signal of the Fe taken up by phytoplankton in the surface waters. The isotopic signature of remineralised iron may be either isotopically lighter (Radic *et al*., 2012) or isotopically heavier (Conway and John, 2014), than the adjacent water masses.

1.3 Iron sources to the ocean and their isotopic signatures

In this section I discuss the isotopic signatures of the different sources of Fe to seawater (Table 1-2). However, it is important to note that these signatures are likely to be altered within the oceans due to the operation of the biotic and abiotic processes explored above.

Table 1-2: Fluxes and isotopic composition of iron sources to the world's oceans

Fe source to the ocean	Range of δ^{56}Fe (‰)	Flux estimate (Tg Fe y^{-1})
Atmospheric total[a]	0.04 to 0.08	16
Atmospheric dissolved[b]	0.13	0.32
Fluvial particulate[c]	-0.90 to 0.31	625 to 962
Fluvial dissolved[d]	-1.16 to 0.51	1.50
Continental margins[e]	-3.5 to -0.6	0.12 to 2.23
Hydrothermal vents[f]	-0.69 to -0.12	0.05
Ice dissolved[g]	-1.51 to 0.94	0.001 to 0.003

a: isotope data from: Beard *et al.* (2003b); de Jong *et al.* (2007); Waeles *et al.* (2007); flux data from: Jickells *et al.* (2005), assuming average Fe content in dust of 3.5 %

b: isotope data from: Waeles *et al.* (2007); flux data from: Jickells *et al.* (2005), assuming average dust dissolution in seawater of 2 %

c: isotope data from: Beard *et al.* (2003b); Bergquist and Boyle (2006); Ingri *et al.* (2006); de Jong *et al.* (2007); Escoube *et al.* (2009); flux data from: Poulton and Raiswell (2002)

d: isotope data: Bergquist and Boyle (2006); de Jong *et al.* (2007); Escoube *et al.* (2009); flux estimate: Poulton and Raiswell (2002)

e: isotope data from: Bergquist and Boyle (2006); Severmann *et al.* (2006); Rouxel *et al.* (2008b); Homoky *et al.* (2009); Severmann *et al.* (2010); flux of dFe to euphotic zone from: Elrod *et al.* (2004); Siedlecki *et al.* (2012)

f: total and dissolved Fe isotope data from: Sharma *et al.* (2001); Beard *et al.* (2003b); Severmann *et al.* (2004); Rouxel *et al.* (2008a); Bennett *et al.* (2009); flux of dFe delivered to the global ocean from: Tagliabue *et al.* (2010)

g: isotope data: de Jong *et al.* (2007); flux estimate: Raiswell *et al.* (2008)

1.3.1 Atmospheric dust deposition

Wind-blown dust particles originating from dry land masses (especially extensive deserts) can be transported in the atmosphere over long distances and delivered to the surface ocean (Jickells *et al.*, 2005). This is one of the most important supply mechanisms of Fe directly to the marine photic layer, where primary production takes place. Crustal material has variable amounts of Fe, with an average composition of 3.5 % by weight (Jickells and Spokes, 2001). The global flux of dFe delivered to the ocean through aerosol dust deposition is ~ 30 x 10^{10} mol yr^{-1} (wet and dry deposition), assuming 2 % Fe solubility in seawater (Jickells and Spokes, 2001; Jickells *et al.*, 2005).

However, Fe input from atmospheric dust is both spatially and temporarily variable. High amounts of dust are deposited over the ocean close to extensive deserts and arid regions, such as the Saharan desert on the North African continent. On the other hand dust deposition is very low at high latitudes, especially the Polar Regions. Dust production is dependent on the climatic conditions (such as rainfall, wind and temperature) and the properties of the land surface (surface roughness, topography and vegetation cover), which determine the amount of wind-erodible land (Jickells *et al.*, 2005). The transport and lifetime of aerosols depends on particle size, wind speed and atmospheric structure. During atmospheric dust transport, photoreduction of Fe(III) to Fe(II) and aerosol cloud processing under acidic conditions, increase the Fe solubility of dust ultimately delivered to the oceans (Jickells and Spoke, 2002). Thereafter, deposition of atmospheric dust into the oceans mainly depends on wind speed and precipitation. Dissolved Fe supply fluxes to the ocean from dust deposition cannot directly be assessed using the aerosol optical thickness from satellite imaging (Schlosser *et al*., 2013). The release of dFe from dust to the surface of the subtropical Atlantic Ocean is mainly a function of rain precipitation rate and sea surface salinity, indicating that wet deposition of dust plays a key role. This may be due to the increased acidity in rain, the presence of organic ligands and photoreduction within rain droplets.

The Fe isotopic composition of aerosol dust is similar to that of bulk silicate Earth, averaging at +0.10 ± 0.11 ‰ (2 SD, n = 82) (Beard *et al.*, 2003b; Fantle and DePaolo, 2004; de Jong *et al.*, 2007; Waeles *et al.*, 2007; Mead *et al.*, 2013). A time series of two different size fractions of aerosols collected at Bermuda showed that the Fe isotopic composition of the coarse fraction (> 2.5 µm) does not change seasonally (+0.10 ± 0.11 ‰, 2 SD, n = 55) and is dominantly of crustal origin. However, the isotopic composition of the fine fraction (< 2.5 µm) changed seasonally, indicating the presence of a non-crustal source with $\delta^{56}Fe$ < -0.5 ‰, which has been attributed to biomass burning (Mead *et al.*, 2013). The isotopic composition of the fraction of Fe that is dissolved from dust particles has been determined during dissolution experiments using ammonium acetate extracts and is +0.13 ± 0.18 (1 SD, n =

9) (Waeles *et al.*, 2007), which suggests that fractionation of Fe during dissolution is minimal. However, recent observations in the surface ocean in the North Atlantic, to which aerosol dust is estimated to be the dominant supply mechanism of Fe (71 to 87 %) (Conway and John, 2014), shows that $\delta^{56}Fe_{dFe}$ values range from +0.3 to +0.7 ‰ across the entire ocean section. This relatively higher $\delta^{56}Fe_{dFe}$ is attributed to Fe fractionation during aerosol dissolution (e.g., mediated by organic ligands).

Dissolved aluminium (dAl) concentrations in the surface mixed layer are commonly used as a tracer of atmospheric dust deposition (Measures and Brown, 1996; Measures and Vink, 2000). Aluminium is the third most abundant element on the Earth's crust, ~ 8.1 % by weight (Taylor, 1964). After aerosol dust deposition, it is estimated that between 1.5 and 3.0 % of Al is dissolved in seawater, resulting in trace (nanomolar) concentrations of dAl. Aluminium has a short residence time in the surface seawater of 2 to 6 years (Orians and Bruland, 1986; Kramer *et al.*, 2004). As dAl is only removed from seawater by scavenging processes and by minor incorporation into siliceous frustules of living diatoms ($Al:Si_{frustules}$ ~ 1:400; Gehlen *et al.*, 2002), this makes it a nearly conservative tracer of dust. The Model of Aluminium for Dust Calculation in Oceanic Waters (MADCOW) may be used to estimate the supply of dust to the surface mixed layer (Measures and Brown, 1996). By knowing the average elemental composition of dust and the amount of dissolution, the supply of dust-derived dFe can be calculated.

1.3.2 Rivers and continental runoff

Rivers are an important source to the ocean, supplying 625 to 962 Tg yr^{-1} of total Fe (Poulton and Raiswell, 2002). Even though 70 to 95 % of the riverine dFe is removed through salt induced flocculation of Fe-humic-colloids during estuarine mixing (Chester, 2000), it has been estimated that rivers supply 1.5 Tg yr^{-1} of dFe to the oceans (Poulton and Raiswell, 2002). A large variety of processes control the composition of rivers and these processes may vary spatially and temporarily. The river water composition is dependent on the type of weathering regime (which includes chemical and physical processes) and the

catchment lithology. The chemical composition of the river water is also dependent on biological and chemical processes, occurring in soils and in the river, ligand complexation processes and redox conditions. Hence, the isotopic composition of the different Fe pools transported in river systems is also dependent on the relative importance of these processes.

δ^{56}Fe values of dissolved Fe in rivers range from -1.2 to +0.6 ‰ (Bergquist and Boyle, 2006; Ingri *et al.*, 2006; de Jong *et al.*, 2007; Escoube *et al.*, 2009; Rouxel and Auro, 2010). It is hypothesised that Fe is not fractionated during weathering, mineral dissolution processes and continental runoff, as the δ^{56}Fe value of total Fe in rivers is similar to the crustal average (Escoube *et al.*, 2009). The dominant binding environment in the river system may have a key impact on the isotopic composition of riverine dFe. The formation of secondary clays and Fe-oxides may leave the dissolved pool (organically complexed and colloidal) enriched in heavy isotopes (Escoube *et al.*, 2009). It has been suggested that humic acids (that may provide a stronger binding environment than Fe-hydroxides or clay particles) are preferentially complexed to isotopically light Fe and Fe-hydroxides (likely formed from groundwater sourced Fe(II)) are formed of heavier Fe isotopes (Ingri *et al.*, 2006). In addition, the presence of strongly coordinating ligands may preferentially bind to heavy Fe(III) (Dideriksen *et al.*, 2008). It has been observed that there is no preferential removal of Fe isotopes by colloidal Fe relative to labile Fe (Escoube *et al.*, 2009). As yet, there is no evidence that estuarine mixing changes the isotopic composition of the dFe fraction (Escoube *et al.*, 2009; Rouxel and Auro, 2010). The particulate fraction of river waters is isotopically lighter than the dissolved phase (Bergquist and Boyle, 2006; Escoube *et al.*, 2009). In contrast to the dissolved pool, the isotopic composition of the particulate Fe delivered by rivers is modified during estuarine mixing (Escoube *et al.*, 2009); however the processes behind this fractionation are not clear.

1.3.3 Benthic iron fluxes

Large amounts of particulate Fe are supplied to coastal regions through continental weathering transported via continental runoff and river systems

(Raiswell *et al.*, 2006). This terrestrial Fe is deposited on the seafloor together with sinking biogenic matter originating from the marine photic zone. The Fe and the organic matter go through repetitive oxidation-reduction steps within the benthos, before a fraction of dissolved Fe is re-injected into the bottom water. Relative oxidation-reduction conditions vary as a function of the rates of organic matter mineralisation and advective supply of oxygenated bottom water. In general terms, according to the redox conditions, continental margins can be divided into two groups, anoxic reducing and oxic non-reducing (Homoky *et al.*, 2013).

During dissimilatory iron reduction (DIR) within anoxic sediments, the oxidation of carbon, which is supplied to the sediments from sinking biogenic matter, and the reduction of Fe, are mediated by bacteria. The oxidation of carbon in the upper sediment layer generates a pool of dissolved Fe(II) that may be transported into bottom waters by diffusion or bioturbation (or bioirrigation). The dissolved and fine particulate Fe may be transported to the surface ocean via fluid advection and diffusion and/or during upwelling events (Aller 1998, 2004; Chase *et al*., 2005). The relatively high concentrations of biovavailable Fe in waters overlying the continental shelf lead to high levels of primary productivity, producing high amounts of sinking organic matter (Chase *et al*., 2005; Lohan and Bruland, 2008; Severmann *et al*., 2010). The supply of dFe from continental margin sediment and its redissolution is an important delivery vector of Fe to the global ocean (Elrod *et al.*, 2008; Severmann *et al.*, 2010). The continental dFe flux is estimated to be 4.7×10^{10} mol yr^{-1}, but it is temporarily (influenced by the seasonality of river supply rates) and spatially highly variable (Elrod *et al.*, 2004). It has recently been estimated that 10 to 50 % of sediment derived Fe from eastern boundary upwelling systems is exported offshore, which is equivalent to ten times the estimated supply of dFe through atmospheric transport (Siedlecki *et al.*, 2012).

The Fe isotopic composition of pore-waters within reducing sediments ranges from -3.9 to -0.6 ‰ (Severmann *et al.*, 2006; Rouxel *et al.*, 2008b; Homoky *et al.*, 2009; Severmann *et al.*, 2010), with minimum δ^{56}Fe values observed beneath the sediment-seawater interface, coinciding with the oxidised sediment

layer (Severmann *et al.*, 2006; Homoky *et al.*, 2009). Chamber experiments confirm that dFe with low $\delta^{56}Fe$ values is transported from sediments into bottom waters, and the importance of bio-irrigation (Severmann *et al.*, 2010). The source of Fe rich fluids can be well below the sediment-water interface in areas where bio-irrigation contributes to sediment-water solute exchange (Aller, 2001). Minimum $\delta^{56}Fe$ values down to -4.0 ‰ have been observed in pore-waters of a subterranean estuary (Rouxel *et al.*, 2008b). Groundwater discharge of Fe(II) into rivers, estuaries and coastal waters is therefore expected to carry a negative $\delta^{56}Fe$ signature (Rouxel *et al.*, 2008b; Rouxel and Auro, 2010).

The light Fe isotopic composition of the dFe pool in pore-waters is the result of Fe reduction and partial removal of heavy isotopes into precipitating Fe(III)-oxyhydroxide compounds (Bullen *et al.*, 2001; Rouxel *et al.*, 2008b). The isotopic composition becomes heavier in contact with oxygen rich bottom water as a result of Fe(II) re-oxidation. It is likely that significant amounts of dFe delivered by sediments are re-precipitated within close proximity of the benthic boundary layer (Severmann *et al.*, 2010). The isotopic composition of dFe ultimately delivered to the ocean may be furthermore modified during transport (e.g., Fe-L formation).

Further, it has recently been observed that the light isotopic composition of benthic derived Fe persists in the water column (John *et al.*, 2012, Conway and John, 2014). Suboxic bottom waters off the coast of California displayed $\delta^{56}Fe_{dFe}$ values as low as -3.45 ‰ and $\delta^{56}Fe_{dFe}$ values of -1 ‰ persisted in the water column up to > 400 m above the seafloor (John *et al.*, 2012). In addition, $\delta^{56}Fe_{dFe}$ values as low as -0.5 ‰ off the Mauritanian coast were attributed to Fe released from anoxic sediments (Conway and John, 2014). This distinct light Fe isotopic signature was observed to persist within the water column and the OMZ up to ~ 1000 km from the coast. However, there are no $\delta^{56}Fe_{dFe}$ data for waters shallower than 3000 m water depth (i.e., on the continental shelf), that are needed to trace the source of this isotopic signal.

By contrast, non-reducing sediments supply Fe to overlying seawater at much lower rates (0.11 to 0.23 µmol Fe m^{-2} d^{-1}). The $\delta^{56}Fe$ of the Fe supplied from

these sediments (+0.22 ± 0.18 ‰) is much closer to the crustal value, possibly reflecting dissolution of sulphide, oxide and silicate minerals and a very low contribution of Fe supplied by reductive dissolution from anoxic sediments at deeper depths (Homoky *et al.*, 2013). The $\delta^{56}Fe_{dFe}$ value (+0.37 ‰) of equatorial Pacific seawater originating from the continental margin of New Guinea has also been attributed to input of Fe from non-reductive dissolution of sediments (Radic *et al.*, 2011). It has been suggested that the sedimentary signal of Fe sourced from non-reducing sediments (attributed to non-reductive dissolution of sediments and/or resuspension of sedimentary colloidal Fe) persists in the water column up to ~ 1000 m off the coast of northwest America (Conway and John, 2014), estimating to represent 10 to 19 % of dFe delivered to the eastern North Atlantic. This is significantly higher than the estimated dFe contribution from reductive sedimentary dissolution on the African margin (1 to 4 %) to the same section in the western North Atlantic Ocean.

1.3.4 Hydrothermal vents

Hydrothermal activity is usually associated with oceanic spreading centres along mid ocean ridges, but may also occur at submarine volcanoes. Metals (especially Fe and Mn) are leached from the host rock during hydrothermal circulation of water through the ocean crust at temperatures that can exceed 450 °C (German and Von Damm, 2003). High temperature hydrothermal fluids are expelled at the seafloor and form plumes as they rise through the water column and mix with the surrounding seawater. As the plume reaches waters of similar density, it becomes neutrally buoyant and spreads laterally. As the low pH, reducing, high-temperature hydrothermal fluids mix with the cold and oxygen rich seawater, Fe sulphide (FeS) and Fe-oxyhydroxide minerals rapidly precipitate. However, it is now clear that a proportion of the hydrothermal Fe may be stabilised and transported into the deep ocean. The lack of observations makes it difficult to estimate the global dFe flux to the ocean supplied by hydrothermal systems, and different hydrothermal systems have very variable Fe concentrations. However, some estimates indicate that

hydrothermal Fe could support up to ~ 10 to 30 % of global primary productivity (Boyle and Jenkins, 2008; Tagliabue *et al.*, 2010).

A series of reactions and processes lead to Fe isotope fractionation in hydrothermal systems. Precipitation of Fe sulphide is a kinetic isotope fractionation process, leading to enrichment of the lighter Fe isotopes in FeS (Rouxel *et al.*, 2008a; Bennett *et al.*, 2009). It is thought that the precipitation of FeS occurs within the earliest stages of mixing between hydrothermal fluids and seawater, in close proximity to the chimney. In addition, partial oxidation of Fe(II) to Fe(III), followed by the formation of Fe(III)-oxyhydroxides leads to an Fe(III) fraction enriched in heavy isotopes (Welch *et al.*, 2003; Balci *et al.*, 2006). The ferrihydrite (hydrous ferric oxide or HFO) that forms is enriched in the heavier Fe isotopes, and the HFO fraction may be up to 3.2 ‰ heavier than the remaining Fe(II) (Bullen *et al.*, 2001; Wu *et al.*, 2011). The binding of Fe with organic ligands may lead to a dissolved fraction enriched in heavy (Dideriksen *et al.*, 2008) or in light (Brantley *et al.*, 2004) Fe isotopes.

Hydrothermal fluids have δ^{56}Fe values ranging from -0.64 to +0.28 ‰ (Sharma *et al.*, 2001; Beard *et al.*, 2003b; Severmann *et al.*, 2004; Rouxel *et al.*, 2008a; Bennett *et al.*, 2009). The Fe isotopic composition of high-temperature hydrothermal fluids is consistently lower than the δ^{56}Fe of mid ocean ridge basalts (+0.12 ‰) (Beard *et al.*, 2003a). The processes that fractionate Fe isotopes in hydrothermal fluids relative to the host rock are not well understood, but the relative proportion of hydrothermal Fe that precipitates as sulphides, versus the proportion that precipitates as oxides appears to regulate the Fe isotopic composition of the fluid as it mixes with seawater. Vent fluids from ultramafic-hosted hydrothermal systems have very low levels of H_2S, leading to the domination of Fe-oxyhydroxide formation during seawater mixing. At the Rainbow site on the Mid-Atlantic Ridge the isotopic composition of the particulate Fe fraction of the endmember fluid (-0.23 ‰), the non-buoyant plume (-0.18 ‰) and the underlying sediments (-0.19 ‰) is very similar, suggesting that the isotopic composition of the endmember fluids is preserved in the stabilised dFe fraction transported into the deep ocean (Severmann *et al.*, 2004).

Nevertheless, ultramafic-hosted hydrothermal systems are not as common as basalt-hosted systems, where sulphide concentrations are relatively high. The endmember FeS fraction in the buoyant plume is 0.6 ‰ lighter than the original vent fluid (Bennett *et al.*, 2009). However, Fe isotope fractionation only appears to occur during rapid precipitation of FeS, suggesting that fractionation is kinetically controlled. In contrast, when this process occurs slowly (e.g., in low temperature systems) the δ^{56}Fe value of FeS is similar to that of the hydrothermal fluid (Rouxel *et al.*, 2008a), indicating either that the system is in equilibrium and/or that there are multiple stages of mineralisation.

It has been suggested that the stabilised fraction of dFe delivered to the ocean through hydrothermal venting may have a δ^{56}Fe value that is heavier than the bulk silicate Earth (Bennett *et al.*, 2009). To date, however, the Fe isotopic composition of the dissolved fraction of hydrothermal plumes has not been determined. Iron may be stabilised in the dissolved fraction through the formation of Fe-L complexes, colloidal Fe-oxyhydroxide particles and nano-particulate FeS. Analyses of the Fe isotopic composition of seawater across a transect in the North Atlantic Ocean, reveals that the $\delta^{56}Fe_{dFe}$ values of seawater from close to the TAG hydrothermal site on the Mid-Atlantic Ridge is much lower than adjacent seawater (~ +0.6 ‰), at -1.35 ‰ (Conway and John, 2014). These authors suggest that this is due to the input of hydrothermal Fe, with a lighter δ^{56}Fe value than measured in the high temperature hydrothermal fluids (~ -0.4 ‰, Severmann *et al*., 2004). The influence of the hydrothermal source appears to extend ~ 2 km above the seafloor and ~ 1 km to the west. However, hydrothermal Fe only contributed 1.7 to 6.3 % to the Fe budget in this North Atlantic section.

1.3.5 Other sources (ice melt, volcanic ash)

Iron may also be seasonally delivered to the ocean from melting sea-ice and drifting icebergs close to the poles. The polar ice sheets may trap atmospheric dust over a long period of time before they break up into icebergs. The $\delta^{56}Fe_{dFe}$ observed in Antarctic sea ice is -1.5 to +1.0 ‰ (de Jong et al., 2007).

The eruption of continental volcanoes and the deposition of volcanic ash into the surface ocean is an additional source of Fe (Duggen *et al.*, 2010; Achterberg *et al.*, 2013). However, these events are intermittent and scarce and therefore their impacts are difficult to quantify. In the high latitude North Atlantic Ocean, dFe concentrations in surface waters increased during the deposition of volcanic ash delivered from the explosive eruption of the Icelandic Eyjafjallajökull volcano (Achterberg *et al*., 2010), which resulted in enhanced draw down of nutrients. As yet there are no Fe isotope data for volcanic ash, but it may be expected to exhibit the isotopic composition of igneous rocks, +0.09 ‰ (Beard *et al.*, 2003a).

1.4 Iron removal processes from seawater and residence times

Dissolved Fe is removed from seawater through the processes described below. Due to the insolubility of Fe in seawater, when it is not stabilised in the form of Fe-L, it rapidly precipitates as oxi-hydroxides, most of which aggregates and sinks towards the seafloor, (e.g., Ussher *et al.*, 2004). Iron stabilised in the dissolved fraction (through Fe-L or colloidal oxi-hydroxides) that is present in the surface ocean is rapidly removed through biological uptake (e.g., Boyd and Ellwood, 2010). Part of the organic matter produced in the photic zone then settles towards the seafloor. Because Fe is highly particle reactive, unstabilised Fe is also removed from the dissolved fraction of seawater through the adsoption onto sinking particles (formed of particulate organic matter and oxi-hydroxide aggregates). This scavenging of Fe is the main removal process of Fe from the oceans (e.g., Ussher *et al.*, 2004; Boyd and Ellwood, 2010).

Due to its reactivity, Fe has a short residence time in seawater. Surface waters can have residence times as short as 10 days to 4 months in regions of relatively high atmospheric dust deposition (de Baar and de Jong, 2001), but can also be < 2 to 5 years in regions of lower dust inputs and with presumably more efficient biological recycling of iron (Jickells, 1999; Sarthou *et al.*, 2003; Bergquist *et al.*, 2007; Ussher *et al.*, 2013). The residence time of Fe in deep waters was reported to be 15 to 41 years (0.76 to 1 nmol L^{-1} Fe) (de Baar and

de Jong, 2001), and as short as 5 years (Moore and Braucher, 2008; Klunder *et al.*, 2012) in deep waters with a strong scavenging regime. This is low compared to deep water circulation, which is in the order of about 1000 years.

1.5 Thesis outline

The main aims of this thesis are (i) to develop a technique for accurate and precise measurement of $\delta^{56}Fe_{dFe}$ in seawater samples, and (ii) to apply these techniques to improve understanding of the sources and internal cycling of Fe in the marine system. Chapter 2 details the methodologies established at the NOC for the analysis of Fe isotopes in seawater samples at low concentrations, using a double spike high-resolution multi-collector inductively coupled plasma mass spectrometry (HR-MC-ICPMS) technique. Chapter 3 presents Fe isotope data for dFe in the (sub)tropical North Atlantic Ocean in waters within and adjacent to an oxygen minimum zone. Chapter 4 explores the evolution of $\delta^{56}Fe_{dFe}$ values as hydrothermal fluids mix with seawater in hydrothermal plumes in the newly discovered vent sites in the Southern Ocean. Finally, chapter 5 summarises the key findings and suggests future work required to further understanding of the marine Fe cycle.

Chapter 2: Development of methodology for the accurate and precise measurement of iron isotopes in seawater

2.1 Introduction

Certain trace metals, including iron (Fe), are essential micronutrients for the growth of oceanic phytoplankton as they are required for the functioning of fundamental enzymes and as electron transporters in photosystems (Geider and LaRoche, 1994; Falkowski *et al.*, 1998; Morel and Price, 2003). However, the availability of Fe in the modern ocean is frequently limited in many ocean regions due to the low supply rates and the very low solubility of the dominant Fe(III) ion under oxygenated conditions (Liu and Millero, 2002; Ussher *et al.*, 2004). Given that marine photosynthesis is responsible for ~40 % of total productivity on Earth (Martin and Fitzwater, 1988; Falkowski *et al.*, 1998), and that Fe controls primary production in half of the world's oceans (especially high-nutrient low-chlorophyll regions, and nitrogen fixation limited regions) (Boyd and Ellwood, 2010), then a better understanding of the biogeochemical cycling of Fe is a crucial component of global models used for making accurate predictions as to the effects of future climate scenarios.

Iron is delivered to the ocean from a number of different sources (Table 1-1), but the strengths of these sources vary both temporally and also from region to region. For example, atmospheric input of naturally and anthropogenically sourced Fe to the surface ocean is very high in the North Atlantic (because of close proximity to Saharan mineral dust source regions), but very low closer to the poles (Jickells and Spokes, 2001; Baker *et al.*, 2003; Jickells *et al.*, 2005; Mahowald *et al.*, 2005; Baker *et al.*, 2010). Rivers are another source of Fe; it is generally thought that uptake of fluvial Fe by coastal phytoplankton and flocculation processes in estuaries make this a negligible source to open ocean surface waters (Chester, 2000), although recent observations (Laës *et al.*, 2003) indicate that off-shore transport of Fe-enriched water from the continental margins, including fluvial as well as sedimentary Fe, may be important. In

addition, modelling by Siedlecki *et al.* (2012) suggests that the transport of sediment-derived dissolved Fe (dFe) to the open ocean could be ten times larger than the atmospheric input. New dFe (not recycled) can also be injected into the deep ocean from hydrothermal vents (Elderfield and Schultz, 1996; Boyle and Jenkins, 2008; Tagliabue *et al.*, 2010) and it is estimated that the hydrothermal input could support ~10 % of global primary production (Boyle and Jenkins, 2008). The upwelling, entrainment or mixing of deeper waters enriched in nutrients and micrconutrients are important supply mechanisms to the surface ocean on a global scale (Watson, 2001).

A promising tool to trace these different Fe sources to the ocean is the measurement of their isotopic composition (Zhu *et al.*, 2000; Beard *et al.*, 2003b; Severmann *et al.*, 2006) (Table 1-1). The δ^{56}Fe value of atmospheric dust appears to be close to the average crustal value of 0.07 ± 0.02 ‰ (Beard *et al.*, 2003b; Poitrasson, 2006; de Jong *et al.*, 2007; Waeles *et al.*, 2007), and the isotopic composition of the soluble fraction seems to be similar (+0.13 ‰; Waeles *et al.,* 2007). Hydrothermal fluids are characterised by lower δ^{56}Fe values (-0.69 to +0.28 ‰; Sharma *et al.*, 2001; Beard *et al.*, 2003b; Severmann *et al.*, 2004; Rouxel *et al.*, 2008a; Bennett *et al.*, 2009) and very high Fe concentrations (up to several mM), compared to sub-nano-molar levels in open ocean seawater (Douville *et al.*, 2002; Gallant and Von Damm, 2006). However, most of this Fe is removed to insoluble sulphide and oxide phases as soon as the hydrothermal fluids mix with seawater, so the quantity delivered to the deep ocean is small (Field and Sherrell, 2000; Statham *et al.*, 2005). Nevertheless, iron and δ^{56}Fe anomalies, due to venting of hydrothermal fluids, may be traced many kilometres from their source (Conway and John, 2014). Reducing pore fluids expelled from continental margins have low δ^{56}Fe values (approx. -3.5 to -1.8 ‰) (Severmann *et al.*, 2006; Homoky *et al.*, 2009; Severmann *et al.*, 2010), and these low δ^{56}Fe signals may persist in the overlying water column (John *et al.*, 2012). On the other hand, oxic dissolution of seafloor sediments appears to produce a trace of higher δ^{56}Fe values (+0.22 to +0.37 ‰; Radic *et al.*, 2011; Homoky *et al.*, 2013). The isotopic composition of dissolved Fe delivered by rivers is somewhat variable, with δ^{56}Fe showing a range of between -1.2 and +0.51 ‰, while the fluvial particulate pool shows a δ^{56}Fe range of -0.9 to +0.4

‰ (Bergquist and Boyle, 2006; Ingri *et al.*, 2006; de Jong *et al.*, 2007; Escoube *et al.*, 2009). Further research is needed to characterise the fluvial processes that lead to isotopic fractionation between the dissolved and particulate Fe pools, where differences have been observed in different river systems (de Jong *et al.*, 2007; Escoube *et al.*, 2009).

It is likely that the isotopic composition of these Fe sources is altered after delivery to the ocean, because Fe participates in a range of biotic (biological uptake, bacterial remineralisation, bacterial dissimilatory Fe reduction, organic complexation, etc.) and abiotic processes (dissolution, precipitation, sorption, redox reactions, photoreduction etc.), which affect δ^{56}Fe (Beard *et al.*, 1999; Anbar *et al.*, 2000; Bullen *et al.*, 2001). Although these processes may hinder the tracing of Fe sources in the ocean, they potentially provide powerful new information about the internal Fe cycle in the ocean.

The determination of Fe isotopes in oceanic waters is not straightforward, because seawater Fe concentrations are commonly in the picomolar range, and at least ~20 ng of Fe are required for precise isotope analysis (Weyer and Schwieters, 2003; Schoenberg and von Blanckenburg, 2005; Lacan *et al.*, 2010). This means that Fe must be separated from the sample matrix with a high recovery, avoiding contamination to achieve low blanks, and even then, large volumes of seawater are required for each analysis. Over the past few years, a handful of laboratories have started to develop techniques for the analysis of Fe isotopes in seawater (Lacan *et al.*, 2008; John and Adkins, 2010; Lacan *et al.*, 2010; Rouxel and Auro, 2010; Radic *et al.*, 2011; Conway *et al.*, 2013), mainly using multi-collector inductively coupled plasma mass spectrometry (MC-ICPMS), which allows precise measurement of isotope ratios. This technique is relatively fast (compared to analysis by thermal ionisation mass spectrometry), but care must be taken to properly correct for instrumental mass bias and potential isobaric interferences (e.g. ^{54}Cr on ^{54}Fe, ^{58}Ni on ^{58}Fe). Approaches taken include sample-standard bracketing (Zhu *et al.*, 2002; Poitrasson *et al.*, 2004), doping with an element of similar mass (e.g., Cu; Sharma *et al.*, 2001), or isotope spiking (e.g., Dideriksen *et al.*, 2006; Lacan *et al.*, 2010). The latter is increasingly the method of choice, not

only because it requires only one analysis of the sample in one measurement cycle, but also because it can correct for any fractionation that occurs during the preconcentration and separation procedures, and it provides precise measurements of the Fe concentration. In addition, the spike can be used to drastically reduce the relative contribution of isobaric interferences.

Thus far, there are relatively few measurements of the iron isotope composition of seawater (Lacan *et al.*, 2008; John and Adkins, 2010; Lacan *et al.*, 2010; Rouxel and Auro, 2010; Radic *et al.*, 2011; John and Adkins, 2012; John *et al.*, 2012; Conway and John, 2014). The acquisition of more Fe isotope data, from different oceanic regions, is crucial for more detailed studies on Fe fluxes, as well as our understanding of Fe cycling within the oceans. This information is required for models of oceanic productivity, which is affected by changing environmental conditions (Parekh *et al.*, 2005). Here, we report techniques for the accurate and precise measurement of iron isotopes in seawater using a novel isotope spiking technique, which we have developed at the National Oceanography Centre (NOC).

2.2 Materials and methods

All analytical chemistry was carried out in a class 100 clean laboratory. Seawater samples and acids were handled in laminar flow cabinets to minimize contamination. All samples and equipment were kept sealed in clean bags when outside of the laminar flow cabinet. All acids were thermally distilled (TD) in Teflon stills, and diluted using 18.2 MΩ Milli-Q (MQ) water. All labware that came into contact with the samples or acids was cleaned using a three step procedure: (1) 2.5 % Decon, (2) 50 % HCl, and (3) 50 % HNO_3. High density polyethylene (HDPE) and low density polyethylene (LDPE) labware was cleaned for one week in each solution, whereas Teflon ware was cleaned for two weeks in each solution. Savillex Teflon vials used for evaporation were cleaned with the three step cleaning procedure, followed by a bath in hot 50 % HNO_3, followed by hot 3 M TD-HCl (both steps at least 24 hours). The hot bath cleaning steps were repeated between uses of Teflon vials. Polypropylene vials used for elemental analysis were cleaned in Decon followed by 20 % HCl.

Analysis of concentrations of Fe and other elements for blanks and yields was done by inductively coupled plasma mass spectrometry (ICP-MS) (Thermo Scientific Element 2XR or Thermo Scientific X-Series II) at the University of Southampton. Concentrations were calculated by external calibration using a certified Fe standard (Inorganic Ventures). Instrumental drift was corrected using an external drift monitor which was measured every ~10^{th} sample throughout the analysis sequence. The drift monitor was usually a 18 nM Fe solution sampled from the same vial during that sequence. The limit of detection (LOD) was 0.11 nM Fe on the Element, and 1.3 nM Fe on the X-Series, where the LOD is defined as three times the standard deviation of the blank (the solution of 0.3 M HNO_3 used to dilute the samples).

2.2.1 Seawater sampling

The seawater samples used to validate our analytical protocols were collected along the 40° South Atlantic transect during cruise JC068 (UK GEOTRACES section GA10, Dec 2011 – Jan 2012). This oceanic region receives low dust input and surface seawater typically has very low Fe concentrations. Seawater was collected from a trace metal clean surface sampling system, the towed torpedo fish, and filtered in-line through 0.2 µm AcroPak Supor polyethersulfone membrane filter capsules (Pall) into 10 L LDPE carboy containers. The carboys were bagged and well-sealed, then shipped back to the NOC. Methods have also been validated by replicate analyses of seawater samples from the tropical Atlantic Ocean (cruise D361, 2011, GEOTRACES transect GA06) and the East Southern Ocean (cruise JC055, 2011).

2.2.2 Iron preconcentration procedure

Iron was extracted from seawater with nitriloacetic acid (NTA) Superflow resin (Qiagen), using (i) a column method based on (Lacan *et al.*, 2010) and (ii) a batch method based on John and Adkins (2010). NTA resin binds strongly to Fe(III) at pH above 1.7, with recoveries of up to 100 % (Lohan *et al.*, 2005). The ability to preconcentrate Fe onto NTA resin at pH < 1.8, below which organic ligands bound to Fe dissociate, makes this resin more attractive compared to other resins that require higher pH for Fe preconcentration.

The NTA resin needs thorough cleaning before use, using weak (<1.5 M) HNO_3 or HCl to avoid damaging/oxidising the resin. Moreover, it is thought that Fe can diffuse from within the resin beads into solution over time, even after cleaning, so the cleanliness of the resin must be carefully monitored (Lee *et al.*, 2011). Thus, the resin was first rinsed repeatedly in MQ water to wash off the ethanol in which the resin is supplied. It was then cleaned several times by suspending in 1.5 M HCl and shaking on a shaking table over night to help mobilize adsorbed ions, decanting and repeating the procedure with fresh 1.5 M HCl. The resin was then transferred into a Solid Phase Extraction (SPE) column and several bed volumes of 1.5 M HCl were passed through. Finally, the resin was rinsed with MQ water and stored in a Teflon bottle suspended in MQ water. The blank contribution of newly cleaned resin and resin stored for longer periods was checked before each use.

At least 24 h before starting the preconcentration procedure, the pH of the acidified seawater sample is adjusted to be between 1.7 and 1.8. Samples that were acidified to a pH > 2 were allowed to stand for one week after adjusting the pH to between 1.7 and 1.8 to allow for dissociation of Fe-ligand complexes and desorption of Fe from the bottle walls. A known amount of our calibrated isotope spike (of known isotopic composition) is added to the acidified seawater sample at least 12 hours before preconcentration so that the sample and spike can equilibrate. Because the sample to spike ratio needs to be ~1:1, the Fe concentration of the sample needs to be determined beforehand.

2.2.2.1 Preconcentration using the NTA batch method

This method was developed for sample volumes of <1 L. Thirty minutes before the start of the preconcentration procedure, 10 µM of hydrogen peroxide (Romil, Super Purity Reagent) is added to the sample to oxidize any Fe(II). 650 µL of clean and blank checked NTA resin is then added to the sample, and left on a shaker table outside the clean lab for 2 h well sealed and triple bagged. The seawater / resin mixture is then filtered through a 1 µm polycarbonate Nucleopore filter housed in an all-Teflon (Savillex) filtration system (47 mm diameter). The seawater is collected in a clean bottle, and the original sample bottle is rinsed with filtered seawater three times, to make sure that all of the

NTA resin is transferred to the filter. The resin in the filter holder is then rinsed with 3 x 20 mL of MQ water to wash off any adhering salts, before being transferred to a handmade polypropylene “Pasteur column” (conical shaped with a 5 mm diameter frit) using 4 x 3 mL aliquots of MQ water. The Fe is then eluted from the resin with 4 mL (1 x 2 mL + 2 x 1 mL) of 1.5 M HCl, which is collected in a Teflon (Savillex) vial. The Fe fraction is then evaporated to dryness on a hotplate at 110° C and redissolved in 6 M HCl for anion exchange chromatography.

2.2.2.2 Preconcentration using NTA column method

This method was developed for sample volumes of up to 4 L in volume. At least 30 min before start of the procedure 10 µM hydrogen peroxide is added to the sample. The NTA column (homemade with FEP tubings and frits; 9.6 mm internal diameter, 10 mm length, Lacan *et al.,* 2010) is loaded with approximately 1 mL of wet NTA resin beads. After assembly the column is cleaned with 150 mL of 1.5 M HCl and then rinsed with MQ water until the pH is neutral for storage. The blank from each new column was checked before they were used for samples. Between uses and before loading a sample the column is rinsed with 75 mL 1.5 M HCl followed by MQ rinse until the pH is neutral. The seawater sample is then passed over the column by gravity flow (approximately 10 mL/min). Afterwards, the column is rinsed with 80 mL of MQ water to rinse off any salts, and the Fe fraction is eluted with 10 mL of 1.5 M HCl. The column is rinsed with MQ until a neutral pH is obtained before storage. The Fe fraction is evaporated on a hotplate at 100 °C and redissolved in 6 M HCl for anion exchange chromatography.

2.2.3 Iron purification procedure

After the initial extraction from seawater using NTA resin, the Fe fraction is further purified by anion exchange chromatography (Strelow, 1980), using BioRad AG1-X8 resin. While NTA resin may bind to many cations, Fe can be efficiently separated from these cations by conversion to $FeCl_4^-$ in high molarity HCl that is retained on the anion exchange resin. $FeCl_4^-$ dissociates in low molarity HCl, and Fe can then be eluted from the resin. To this end, a large

batch of AG1-X8 resin was pre-cleaned as follows. The resin is combined with 6 M HCl in a pre-cleaned Teflon bottle, shaken on a shaker table over night, left to settle and the solution decanted. The bottle is then filled with new 6 M HCl, and the same procedure is repeated twice. The bottle is then filled with 1 M HCl, shaken on a shaker table over night, left to settle and the solution decanted. This procedure is again repeated twice, then the cleaned resin is stored in 0.01 M HCl. Approximately 500 µL of the cleaned resin is loaded in a homemade polyethylene column (height ~ 40 mm; internal diameter ~ 4 mm, ~ 5 mL reservoir), and the resin is washed in consecutive fractions of ~ 5 mL of 0.1 M HF, 6 M HCl, and 7 M HNO_3. All of these acids contain 0.001 % H_2O_2. This cleaning cycle is repeated five times between uses of the columns, except for the HF step, which is only carried out occasionally. Before using the columns, they are additionally cleaned by adding 3 x 500 µL 1 M HCl. The columns are then conditioned with 2 x 500 µL 6 M HCl (with 0.001 % H_2O_2) before loading the sample in 500 µL 6 M HCl (with 0.001 % H_2O_2). Most of the matrix elements are eluted with 3 mL (3 x 1 mL) of 6 M HCl (with 0.001 % H_2O_2). The Fe fraction is then eluted with 3.5 mL (1 x 1.5 + 2 x 1 mL) of 1 M HCl (with 0.001 % H_2O_2). The columns are cleaned as described above prior to storage in 0.01 M HCl. The Fe eluted in the 1 M HCl fraction is evaporated on a hotplate at 100° C and later reconstituted in 0.3 M HNO_3 for isotopic analysis.

2.2.4 Isotopic analysis

2.2.4.1 Instrumental set up

Fe isotope measurements are performed on a multi-collector inductively coupled plasma mass spectrometer (MC-ICPMS) (Thermo Scientific Neptune) at the National Oceanography Centre in Southampton. The sample is introduced to the plasma via a desolvating inlet system, either a CETAC Aridus II or an ESI Apex-Q without a membrane to increase sensitivity (Dauphas *et al.*, 2009), using a 75 µL/min Teflon nebuliser. An “X”-type skimmer cone is used to increase ion transmission. We started by using cones made out of Ni, but finally decided to use Al cones to minimise interference risks. The instrument is operated in high-resolution mode using a narrow (25 µm) slit, to resolve

polyatomic interferences (mainly argon oxides) on masses 54, 56 and 57. In addition to the four Fe isotopes (^{54}Fe, ^{56}Fe, ^{57}Fe, ^{58}Fe), ^{53}Cr and ^{60}Ni are also measured (Table 2-1), so that any isobaric interference of ^{54}Cr on ^{54}Fe and ^{58}Ni on ^{58}Fe can be corrected. Note that the correction procedure assumes that the instrumental mass bias is the same for Fe, Cr and Ni and that ^{54}Cr/^{53}Cr and ^{58}Ni/^{60}Ni ratios are equal to the natural average (Dauphas *et al.*, 2009). 10^{12} Ω resistors are used to measure the small signals of ^{53}Cr on detector L3 and ^{60}Ni on detector H3 with more accuracy, whereas 10^{11} Ω resistors are used on the rest of the collectors. Use of the 10^{12} Ω resistors results in a 10 fold increase in amplifier gain (relative to the 10^{11} Ω resistor) with only a √10 increase in Johnson noise (electronic noise on the detectors). In practise this offers a two to three fold improvement in signal/noise. The benefit (low noise, improved precision) is most apparent with small beams, < 100 mV. 10^{12} Ω resistors can only be used to detect signals of < 5 V compared to 50 V for the 10^{11} Ω resistors.

Table 2-1: Cup configuration for isotopic analysis of Fe by MC-ICPMS. Also shown are the natural abundances of the different Fe isotopes, as well as those of its isobaric interferences.

Collector configuration		L3	L1	C	H1	H2	H3
Nominal mass		53	54	56	57	58	60
Isotope abundance (%)	Cr	9.501	2.365				
	Fe		5.845	91.754	2.119	0.282	
	Ni					68.0769	26.2231

The instrument is tuned for optimum performance. Firstly, the sample introduction system is tuned and then the source lenses. Mass resolution is optimized using the zoom optics. The mass resolution needs to be > 8000, with a plateau > 200 ppm, before measurements can begin. The measuring mass is selected to be 2/5^{ths} along the signal plateau. The relative positions of the cups are also checked, to make sure there are no interferences at the measuring point, either in the Fe solutions or in the blank.

Each analysis of a sample or standard consists of 50 replicate measurements of 4.2 s, and the instrumental blank (determined by analysis of the 2.5 % HNO_3 solution used to prepare the samples and standards) is determined before and after each sample/standard analysis by 20 replicate measurements of 4.2 s. The sample uptake time is 80 s, and the wash time is set to 60 s before analysis of each sample or standard (as the preceding sample is a blank) and 300 s before a blank (to ensure washout of Fe from the preceding sample or standard; 900 s if using the Aridus). The beam intensity of the average of the two bracketing blanks is subtracted from each sample or standard. The isotopic composition of the samples and standards is corrected for mass bias by iteratively deconvolving the spike + sample mixture, and at the same time Cr and Ni interferences are corrected based on the intensity of the ^{53}Cr and ^{60}Ni beams (Albarède and Beard, 2004a; Albarède and Beard, 2004b). See Appendix B for a detailed description of this procedure, which was created by Dr. Ian Parkinson (University of Bristol).

After purification the sample is evaporated and redissolved in 0.3 M HNO_3 for isotopic analysis. A 1 L batch of 0.3 M HNO_3 is prepared to dissolve all samples and standards and the same solution is used for instrumental blanks, bracketing samples and standards throughout the analysis sequence. Standards are also prepared in sufficiently big batches for each isotope analysis sequence.

The isotopic composition of each sample is expressed in delta notation relative to the average IRMM-014 standard value on that day. Whenever possible samples are analysed in duplicate. The isotopic composition of two external standards are closely monitored during each session for quality control; an in-house hematite (HEM) standard and Eidgenössische Technische Hochschule Zürich (ETH) hematite standard, prepared by Franck Poitrasson, that has a well documented Fe isotope composition (Poitrasson and Freydier, 2005; Lacan *et al.*, 2010).

The concentration of Fe in the sample can be calculated using the isotope dilution technique, as long as the weights of the sample and the spike are known.

2.2.4.2 Iron isotope spike

In order to determine the optimal composition of the iron isotope spike, a series of mathematical model simulations using a combination of all or some of the four Fe isotopes and different spike/sample mixing ratios, have been conducted. These model simulations were carried out by Dr. Ian Parkinson (University of Bristol). The model is similar to that described in Rudge *et al.* (2009) and full details of the model are given in Appendix A.

Having determined the optimal composition of the isotope spike (see Discussion), the spike was prepared by mixing the appropriate amounts of enriched ^{54}Fe, ^{57}Fe and ^{58}Fe isotopic spikes (prepared from Fe oxides supplied by Cambridge Isotope Laboratories). The exact composition of the mixed spike was determined by inverse deconvolution of a mixed spike - certified Fe isotope reference material IRMM-014 solution (the data deconvolution excel macro spread-sheet was constructed by Dr. Ian Parkinson (University of Bristol), see Appendix B for more details). To this end, we firstly made 10 replicate measurements of a 200 ppb solution of IRMM-014, followed by 20 replicate measurements of a mixed (1:1) 200 ppb IRMM-014 + spike solution, followed by 10 replicate measurements of a 200 ppb spike solution. The instrumental blank (2.5 % HNO_3) was measured before and after each sample analysis, and subtracted. As the isotopic composition of IRMM-014 is well documented, the inverse deconvolution of the IRMM-014/spike mixture can be used to determine the true composition of the spike. The Fe concentration of the spike solution was determined precisely by inverse isotope dilution of a spike - certified iron standard (Inorganic Ventures) of known concentration and low relative standard error (± 0.3 %).

2.3 Results and discussion

2.3.1 Chemical separation of iron from seawater

2.3.1.1 Method blanks

The blank of the total preconcentration procedure was determined on one litre of acidified MQ water and is 1.5 ± 0.5 ng Fe (n=11) for the batch method and 2.0 ± 0.7 ng Fe (n=10) for the column method. These values are slightly higher than the expected value based on the blanks measured for each individual part of the procedures: (i) The blank contribution from the "Pasteur column" is 0.09 ± 0.06 ng Fe (n=3). (ii) The blank contribution from 650 µL of NTA resin is 0.17 ± 0.10 ng Fe (n=9); this includes the blank contribution from the "Pasteur column". (iii) The NTA column blank is 0.36 ± 0.13 ng Fe (n=10). (iv) The elution acid (1.5 M HCl) has a blank of 0.17 ± 0.03 ng Fe (n=8) for 4 mL and 0.3 ± 0.2 ng Fe (n=2) for 10 mL. (v) The H_2O_2 blank is 9.3 ± 0.7 pg Fe (n=3) per litre of sample. Based on the addition of the individual components the total preconcentration blank should therefore be of the order of 0.26 to 0.67 ng Fe. This indicates that handling makes a major contribution to the blank. Although the column blank is consistently higher than the batch blank, they are both in the same range.

The anion exchange procedure blank was determined to be 0.26 ± 0.10 ng Fe (n=19). Acids contribute 0.044 ± 0.016 ng Fe (n = 2) to this blank.

The overall procedure blank (preconcentration blank + purification blanks) is therefore 1.7 ± 0.5 ng Fe (n=11) when using the batch preconcentration and 2.3 ± 0.7 ng Fe (n=10) when using the column preconcentration. The isotopic composition of the blank is unknown, but it is assumed that it has the composition of the crustal average (+0.09 ± 0.10 ‰; Beard *et al.*, 2003b). We have assessed how increasing the difference between the isotopic composition of the blank and the sample affect the measured isotopic composition of the sample, as a function of the proportion of Fe derived from the blank (Figure 2-1). Ideally the blank should account for less than 5 % of the total amount of sample derived Fe (assuming that the difference in their isotopic composition is

unlikely to be > 1 ‰) to remain within the external analytical error. This means that at least 46 ng of Fe are required for each sample analysis.

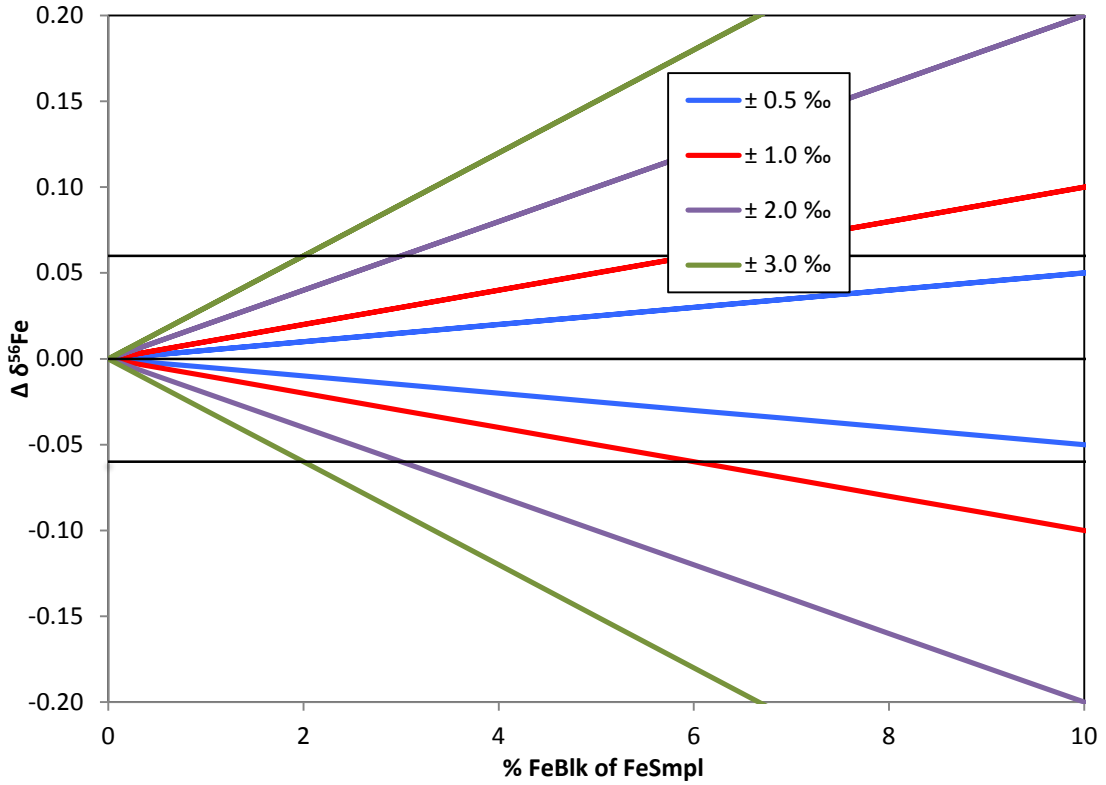

Figure 2-1: Effect of increasing blank contribution on the δ^{56}Fe value of the sample. As the isotopic composition of the blank is unknown, the effect of changing the difference between the isotopic composition of the blank and the sample is also shown. Black lines indicate δ^{56}Fe value of the blank is the same as the sample, and the external precision (± 0.06 ‰, 2 SD) of the isotopic analyses.

2.3.1.2 Yields

The yield of the Fe from each procedure (NTA batch and column; and purifications) is calculated, using both isotope dilution and standard techniques. The entire procedure (preconcentration + purification) recovers 95 ± 8 % of the Fe (n=15).

As Cr and Ni produce isobaric interferences on some of the Fe isotopes, we also assessed the affinity of these elements for the NTA resin. Assuming that the 40° South Atlantic Ocean surface waters have a concentration of ~4 nM Ni (Dr. Christian Schlosser, personal communication) and ~ 2 nM Cr (Corami *et*

al., 2005), then ~0.3 % of the Ni and ~0.2 % of the Cr is eluted together with Fe. This estimate is made on the basis of Cr and Ni doping experiments taken through the NTA procedure.

We also screened each sample for the presence of other elements eluted at the same time as Fe during the preconcentration step. Small quantities (< 0.1 % of the total) of the major elements in seawater were eluted with the Fe. In an effort to reduce the concentration of these elements, we tried increasing the volume of MQ water used to rinse the resin from 20 to 70 mL. This did not make a significant difference for most elements, but concentrations of Na were reduced by a factor of 4. Thus, our procedure utilises a wash step of 80 mL of MQ water. Small quantities of Cu and Zn are also eluted with Fe. Although the concentrations of these elements have not been precisely quantified, they were less than 1 ppb per extraction. The presence of Ga, Sb and U was also detected.

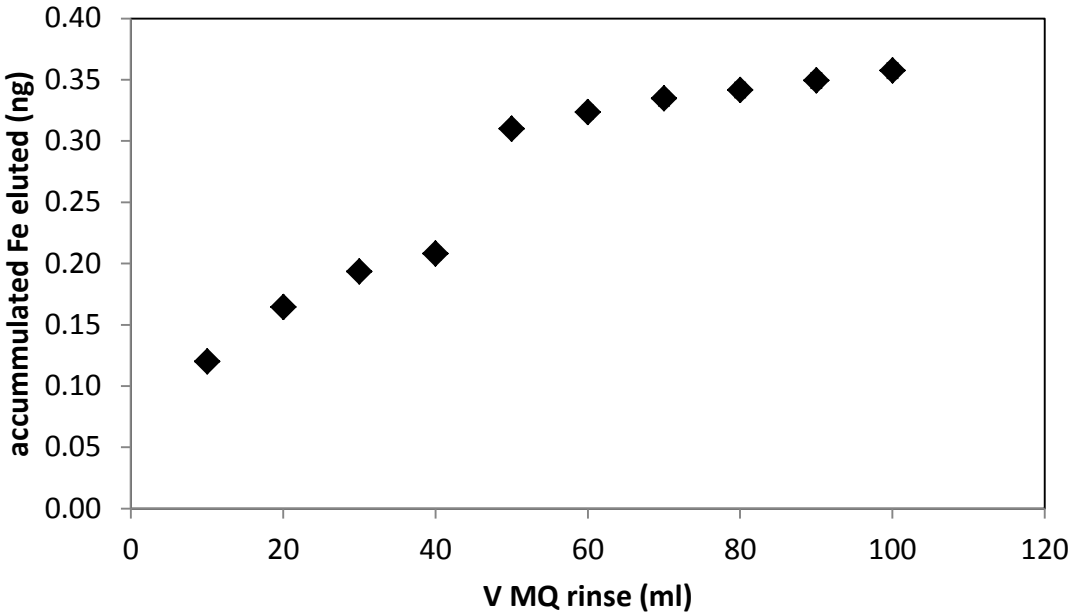

Figure 2-2: Loss of iron during washing of the NTA resin with MQ. The quantity of iron loaded onto the resin is ~100 ng Fe.

In their study, John and Adkins (2010) used acidified MQ water with H_2O_2 to wash the NTA resin, in order to maintain resin binding conditions (i.e. the same as the sample). In order to ascertain whether this is necessary, we tested whether Fe is lost during subsequent wash steps that consisted of MQ water only. Only small amounts of Fe were observed in the wash solution (a total of 0.4 % of the Fe loaded on the NTA resin) of NTA loaded with ~100 ng of Fe, indicating that loss of Fe during this step is insignificant (Figure 2-2).

Elution profiles of Fe, Cr and Ni from the anion exchange column are shown in Figure 2-3a. The anion exchange resin effectively separates Fe from Cr and Ni; small amounts of Fe are eluted with Cr and Ni, but this is < 5 % of the total amount of Fe (Figure 2-3b). Importantly, all seawater salts (Na, Mg etc.) are effectively stripped from the sample within the first 2 mL of the 6 M HCl wash step. The Fe fraction (recovered in 1 M HCl) was also screened for the presence of other elements. Only small amounts of uranium are eluted along with the Fe; this is not likely to compromise the analysis of Fe.

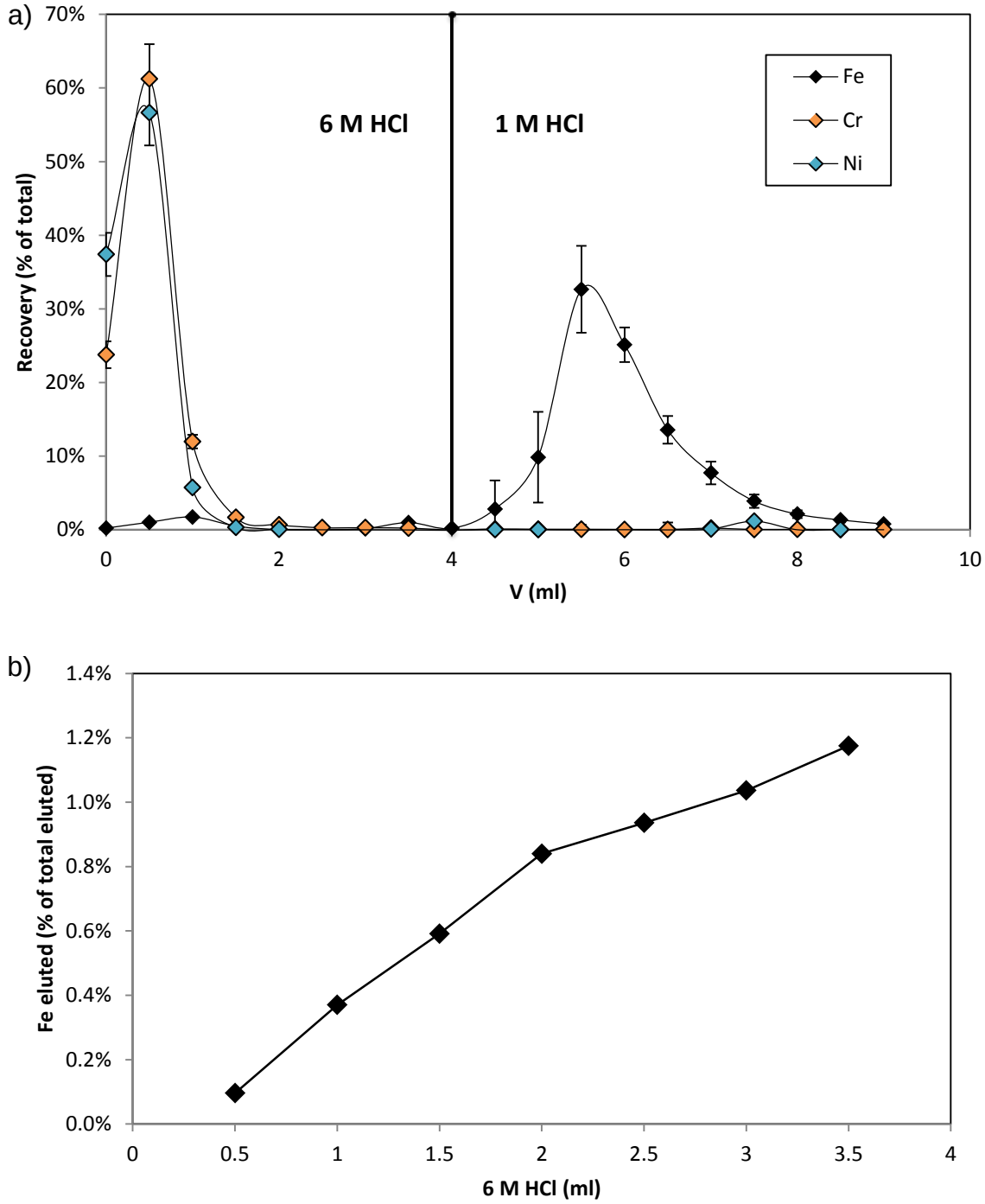

Figure 2-3: a) Elution profiles of Fe, Cr and Ni during anion exchange chromatography. Error bars for Fe represent the standard deviation of the mean of three replicate elutions. Error bars for Cr and Ni represent the standard deviation of one analysis. b) Accumulative elution of Fe from the anion exchange resin during the 6 M HCl rinse step.

2.3.2 Sensitivity and mass resolution

Using the high resolution slit, a mass resolution of ~9000 or higher was typically achieved, allowing Fe to be effectively resolved from argon oxides and nitrides (Figure 2-4). The Aridus II is used without any N_2 make-up gas, as this leads to a loss of peak shape. Highest sensitivity was achieved using the Aridus II sample introduction system (~0.07 V of ^{56}Fe per ppb); the sensitivity achieved using the Apex-Q sample introduction system was ~0.05 V of ^{56}Fe per ppb.

In order to assess the reproducibility of the Fe isotope measurements, replicate analyses of two external standards (ETH and in-house Haematite) were made over the course of each analytical session. Replicate analyses of the ETH standard over a period of over one year produced an average δ^{56}Fe value of 0.51 ± 0.06 ‰ (2 SD, measured at 200 ppb, n = 131), which compares well to the values reported in Lacan *et al.* (2010) (0.52 ± 0.08 ‰, 2 SD, n = 81) and Poitrasson and Freydier (2005) (0.52 ± 0.12 ‰, 2 SD, n = 55). The in-house Haematite standard produced an average δ^{56}Fe of 0.25 ± 0.06 ‰ (measured at 200 ppb, n = 139). The effect of sample size on the precision of the δ^{56}Fe measurements was assessed by repeat analyses (n = 4) of the external standards with Fe concentrations ranging from 25 ppb to 150 ppb. The standard deviation of the replicate measurements does not change significantly for Fe concentrations in this range (Figure 2-5). As less than 400 µL of sample is required for each analysis, this means that as little as 10 ng of Fe is required for one analysis.

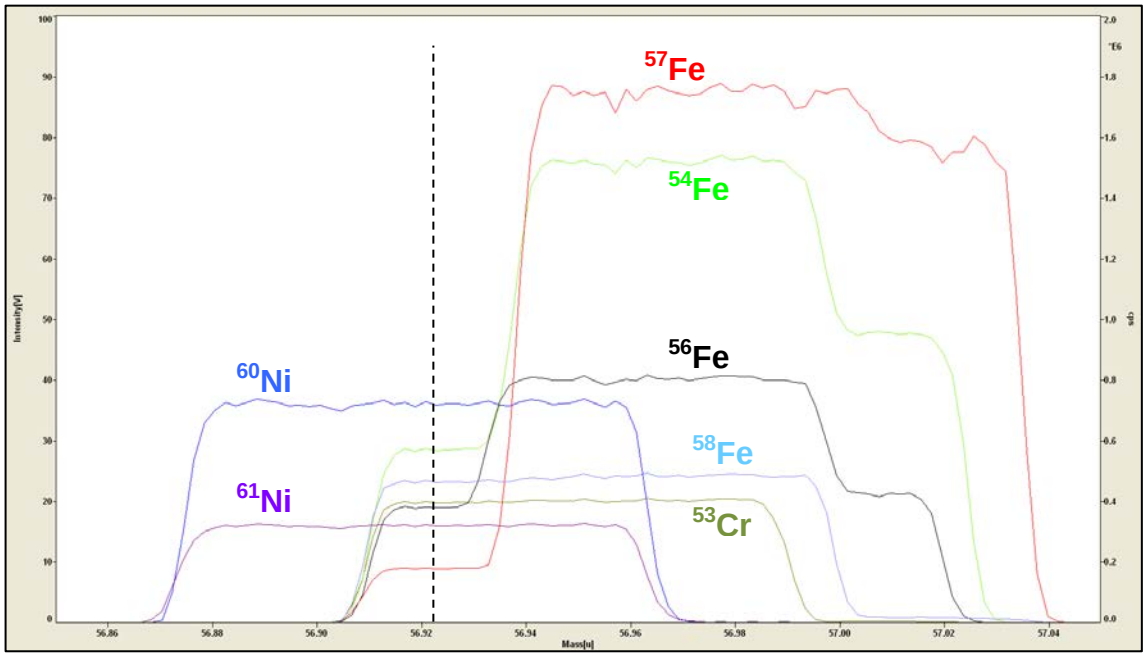

Figure 2-4: Peak alignment of the measured isotopes: ^{53}Cr, ^{54}Fe, ^{56}Fe, ^{57}Fe, ^{58}Fe, ^{60}Ni, ^{61}Ni; and position of the measured mass (black dotted line), which is chosen to be 2/5^{ths} from the peak shoulder. The mass resolution is calculated as follows; $m/\Delta m = \frac{m_c}{m_{95}-m_5}$, where m_C is the centre mass and m_5 and m_{95} are 5 % and 95 % of the peak height measured on the shoulder of the same peak.

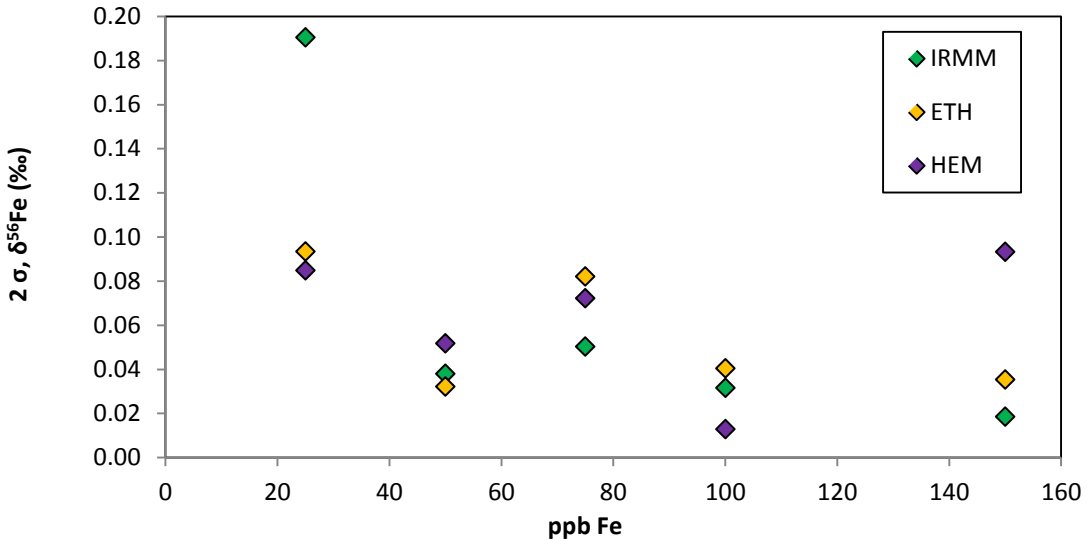

Figure 2-5: Reproducibility (reported as 2 times the standard deviation of the mean) of δ^{56}Fe values as a function of Fe concentration. The ETH and in-house (HEM) hematite standards were analysed 4 times, and the IRMM-014 standard was analysed 5 times.

At first glance, the reproducibility of the isotope measurements performed using the Apex-Q (0.06 ‰, n = 73, 2 SD) is slightly better than it is using the Aridus II (0.07 ‰, n = 52, 2 SD). Tuning conditions are found to be more stable using the Apex-Q and therefore this desolvator was preferred. Lacan *et al.* (2010) found that the instrumental mass bias is much more stable with the Apex-Q compared to the Aridus II. They also report higher sensitivity with the Apex-Q, but this was not observed in our case. The Aridus II requires a longer wash out time of 15 minutes compared to the Apex (7 minutes), likely due to the membrane present in the Aridus II.

2.3.3 Method Validation

To validate our methodology, several samples of acidified Milli-Q and seawater (SW) with pico-molar trace metal concentration (from cruise JC068) were doped with iron isotope standards, taken through the preconcentration and purification procedures and their Fe isotopic composition was measured. Both the NTA column and NTA batch preconcentration protocols were tested. Two of the Milli-Q doping experiments (one for ETH and one for IRMM-014) were only taken through the preconcentration step, as this has the highest procedure blank. In all of the experiments, the measured δ^{56}Fe value was within error of the standard value, which indicates that any isotopic fractionation that occurs during the chemical processing procedures can be dealt with by the double spike (Table 2-2 and Figure 2-6).

Table 2-2: Consensus and measured δ^{56}Fe values for the Fe isotope standards used in the validation experiments. Validation experiments were carried out in Milli-Q (MQ) and in seawater (SW). The quantity of Fe used in each experiment is displayed in column 2. n indicates the number of isotopic analyses. 2 SD (‰) indicates the reproducibility of replicate analyses of the Fe isotope standards over the course of that analytical session.

Fe Isotope Standard	ng Fe	SD	Solution	Procedure	δ^{56}Fe (‰)	2 SD (‰)	n
	Consensus Standard value				**0.52**	**0.06**	**191**
ETH	123	1.2	1 L MQ	NTA column + Purification	0.54	0.10	1
	111	3	1 L MQ	NTA column	0.53	0.10	2
	560	16	1 L SW	NTA batch + Purification	0.52	0.09	3*
	562	16	1 L SW	NTA column + Purification	0.49	0.09	4*
	Consensus Standard value				**0.25**	**0.06**	**174**
HEM	550	16	1 L SW	NTA batch + Purification	0.22	0.09	3*
	561	16	1 L SW	NTA column + Purification	0.30	0.09	3*
	Consensus Standard value				**0.00**	**0.07**	**313**
IRMM-014	104	3	1 L MQ	NTA column	0.09	0.10	1
	1618	15	1 L SW	NTA batch + Purification	-0.04	0.09	6*

* indicates replicates of isotopic analyses on different MC-ICPMS sessions

In addition, we have also participated in an intercalibration exercise with F. Lacan (LEGOS, Toulouse, France). This involved blind analysis of two low-Fe seawater samples. The seawater samples were collected from Station 14 during Cruise R/V Kilo Moana 06252006 and Fe isotope results obtained at LEGOS are published in Radic *et al.* (2011). Sample ‘Blind A’ corresponds to Go-flo 2 at 849 m depth and ‘Blind B’ corresponds to Go-flo 6 at 198 m depth. Fe concentrations are sub nano-molar, which is characteristic of open ocean seawater (Table 2-3).

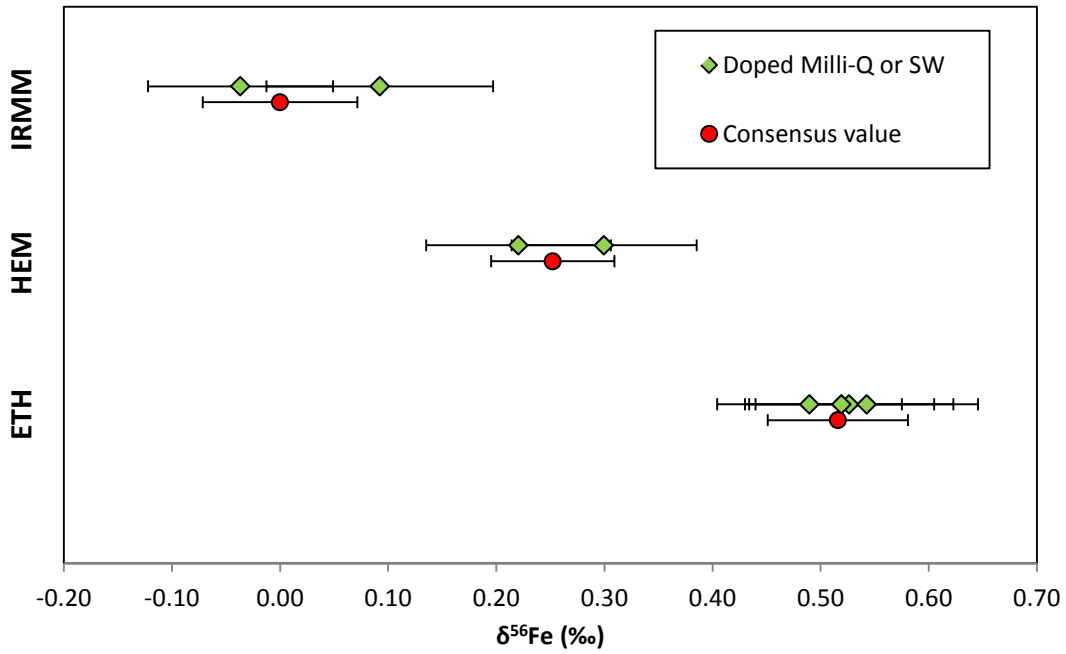

Figure 2-6: δ^{56}Fe values of seawater and MQ doped with various Fe isotope standards and taken through the preconcentration and purification procedures. Error bars indicate 2 times the standard deviation of the mean δ^{56}Fe values obtained by replicate analyses of an iron isotope standard over the course of the analytical session.

The samples were received in well-sealed and bagged carboys from Francois Lacan. The volume of 'Blind A' was 3.5 L and it had a pH of 1.81; the volume of 'Blind B' was 4.2 L and it had a pH of 1.82. The pH was adjusted with ultra-clean HCl to 1.77 before adding an appropriate amount of the double spike. The NTA column procedure was used for the preconcentration step in both cases. Results are displayed in Table 2-3 and Figure 2-7.The results for Blind test B agree within analytical error but are just outside agreement for Blind test A (Figure 2-7). The two samples were analysed at different times, and the performance of the instrument during the analysis of Blind test A was unusually poor. Therefore, the Blind test A sample was only analysed once, in order to keep some of the solution for further analysis at a later date.

Table 2-3: Results of the intercomparison exercise between NOCS and LEGOS. The number of replicates indicates the number of repeat isotopic analyses (split after chemical handling) by the Neptune for NOCS, but indicates analytical replicates (split before chemical handling) for LEGOS.

		δ^{56}Fe (‰)	2 SD (‰)	n	dFe (nM)	SD (nM)
Blind A	NOC	0.06	0.10	1	0.72	0.02
	LEGOS	0.22	0.05	2	0.59	
Blind B	NOC	0.34	0.06	2	0.63	0.02
	LEGOS	0.40	0.06	2	0.53	

In addition the dFe concentration values obtained by both labs are not in agreement. The concentrations obtained by us are higher in both cases (~ 20 %). This may be due to a higher blank in our lab, contamination of the sample during storage or transport or the need to re-calibrate either of the double spike solutions (LEGOS and/or NOC). Hence this discrepancy needs to be further investigated.

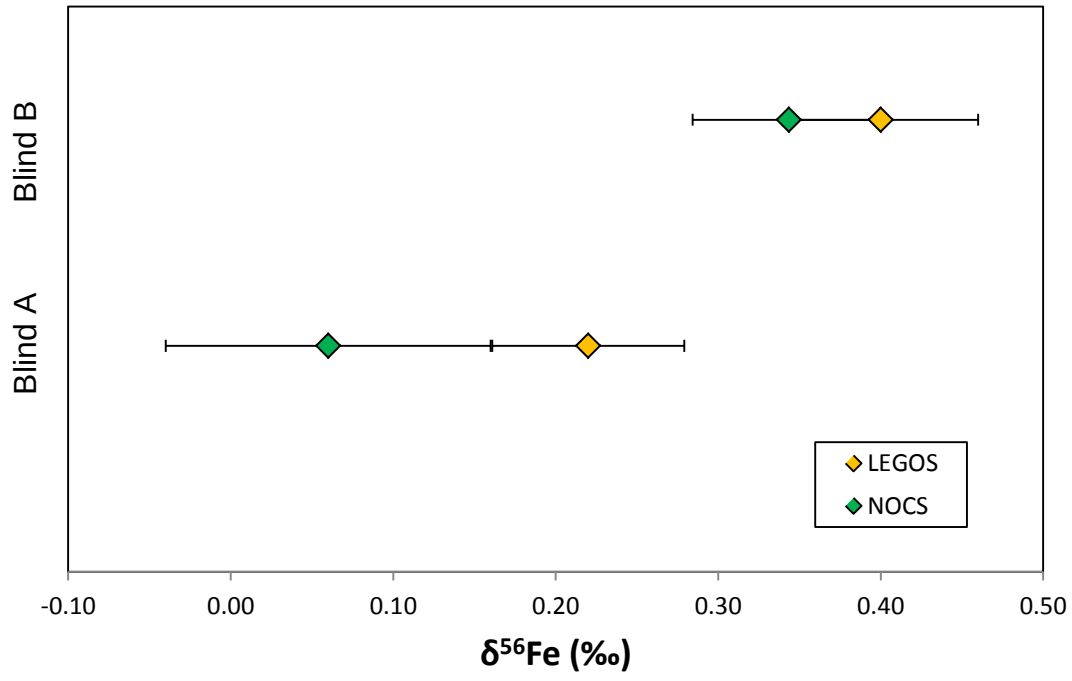

Figure 2-7: Results of Fe isotope analyses of two open ocean samples by NOCS and LEGOS. Error bars represent reproducibility (2 SD) of replicate analyses of Fe isotope standards analysed during the same analytical session.

To further assess the reproducibility of our Fe isotope measurements, three seawater samples that range in concentration from 1.82 to 19.51 nM Fe, were analysed twice. The samples were split before chemical processing, treated as separate samples and analysed on the MC-ICPMS on different sessions. Samples 08_13 and 06_16 originate from GEOTRACES transect GA06 (Cruise D361, 2011) in the tropical Atlantic Ocean. Sample 483_2 was collected from within a hydrothermal plume during Cruise JC055 (2011) to the East Scotia Sea in the Southern Ocean.

Table 2-4: Results of replicate δ^{56}Fe analyses of three seawater samples. 2 SD indicates the standard deviation of replicate analyses of an Fe isotope standard analysed during the same analytical session; n indicates number of replicate analyses on the MC-ICPMS; and nM Fe indicates the Fe concentration of the sample calculated by isotope dilution, for which the SD is the reproducibility of one measurement.

Cruise	ID	Latitude	Longitude	Depth (m)	δ^{56}Fe (‰)	2 SD (‰)	n	nM Fe	SD (nM)
D361	08_13	12.610	-17.716	1002	-0.27	0.04	2	2.93	0.08
					-0.21	0.05	2	2.94	0.09
D361	06_16	12.590	-17.917	750	0.12	0.08	1	2.17	0.02
					0.10	0.10	1	1.99	0.02
JC055	438_2	-59.695	-28.351	1066	-0.26	0.05	1	21.8	0.9
					-0.18	0.10	1	21.2	0.6

3 x 1 L samples were collected in acid cleaned HDPE bottles for samples 08_13 and 06_16. All samples were preconcentrated using the column NTA method except for one of the 08_13 and one of the 483_2 samples, which used the NTA batch method. Replicate analyses agree within the analytical error (2 SD, Table 2-4, Figure 2-8).

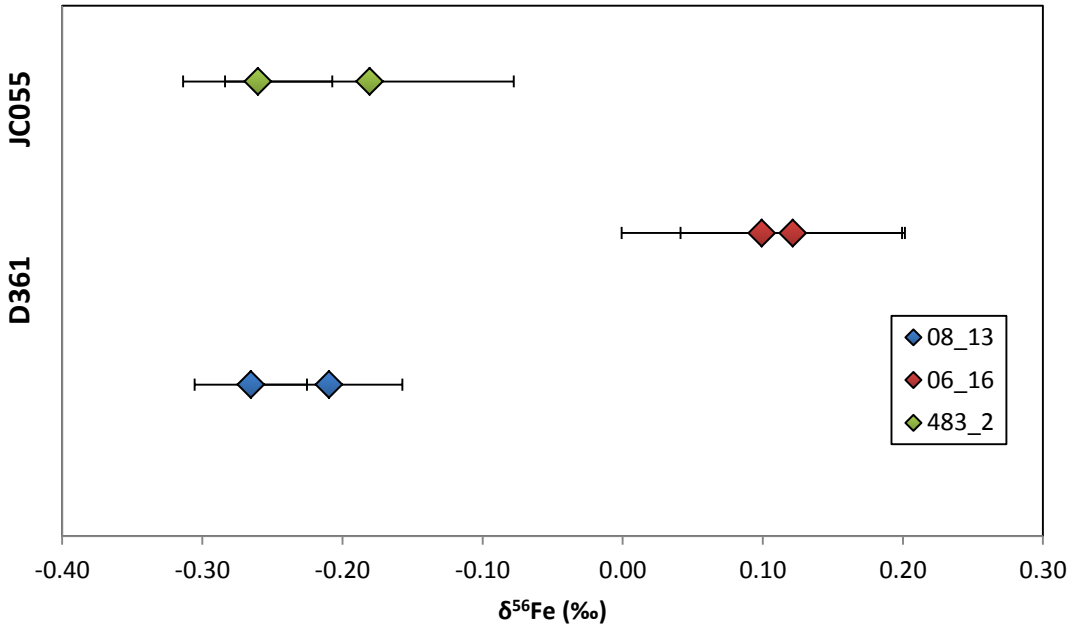

Figure 2-8: Replicate analyses of seawater samples from Cruises D361 (samples 08_13 and 06_16) and JC055 (483_2). Error bars indicate the standard deviation (2 SD) of repeat analyses of an Fe isotope standard during the same analytical session.

2.3.4 Optimum composition of the isotope spike

The model outputs presented in this section are courtesy of Dr. Ian Parkinson (University of Bristol). Figure 2-9a shows that the most precise δ^{56}Fe values are obtained using a double spike made from ^{57}Fe-^{58}Fe; the precision that can be obtained using a ^{54}Fe-^{58}Fe double spike is slightly poorer, and that obtained using a ^{54}Fe-^{57}Fe mixture is poorer still. These results are in agreement with Rudge *et al.* (2009), and although these authors noted that a ^{56}Fe-^{58}Fe gives the best precision, the ^{57}Fe-^{58}Fe spike gives good precision over a far wider range of spike/sample ratios, making this the preferred combination. Figure 2-9b explores the effects of instrumental electronic background on the precision of the isotope measurements. Our calculations reveal that the ^{54}Fe-^{57}Fe spike is particularly sensitive to the electronic background, because for 10 V of total Fe, the ^{58}Fe beam is very small (~30 mV) and therefore extremely sensitive to any background changes. The other two spike combinations are much less sensitive to the electronic background because they both contain ^{58}Fe. By contrast, there

is usually several hundred mV of ^{54}Fe in most sample-spike mixtures, because ^{54}Fe is the most abundant of the minor Fe isotopes.

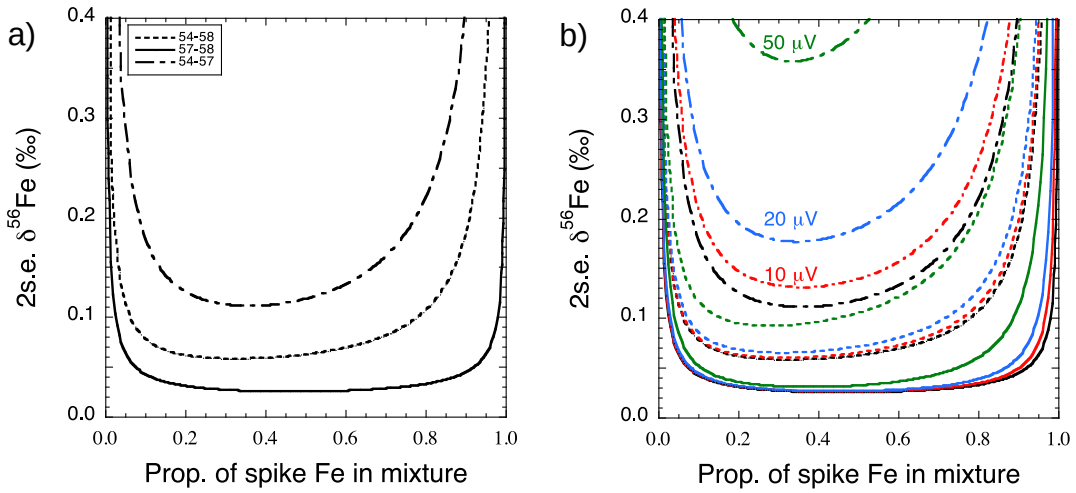

Figure 2-9: a) Model output of the likely precision of δ^{56}Fe values for three different double spike mixtures. In this case, the electronic background is zero. b) Model output of the likely precision of δ^{56}Fe values for three different double spike mixtures, with variable electronic background.

We have also assessed the precision of δ^{56}Fe values obtained using different triple spike combinations (^{54}Fe, ^{57}Fe and ^{58}Fe). Figure 2-10a illustrates the effect of adding variable amounts of ^{54}Fe to the triple spike mixture. The key result is that the addition of ^{54}Fe degrades the precision of the δ^{56}Fe values, such that addition of 5 % of ^{54}Fe produces precisions that are only slightly better than the ^{54}Fe-^{58}Fe double spike. However, Figure 2-10b illustrates that the addition of a small amount of ^{54}Fe (in this case 3 %) produces a spike that is less sensitive to background effects across a wide range of spike/sample ratios. This is because the addition of even small quantities of ^{54}Fe decreases the background sensitivity. Nevertheless, the best precisions are still obtained for a ^{57}Fe-^{58}Fe double-spike.

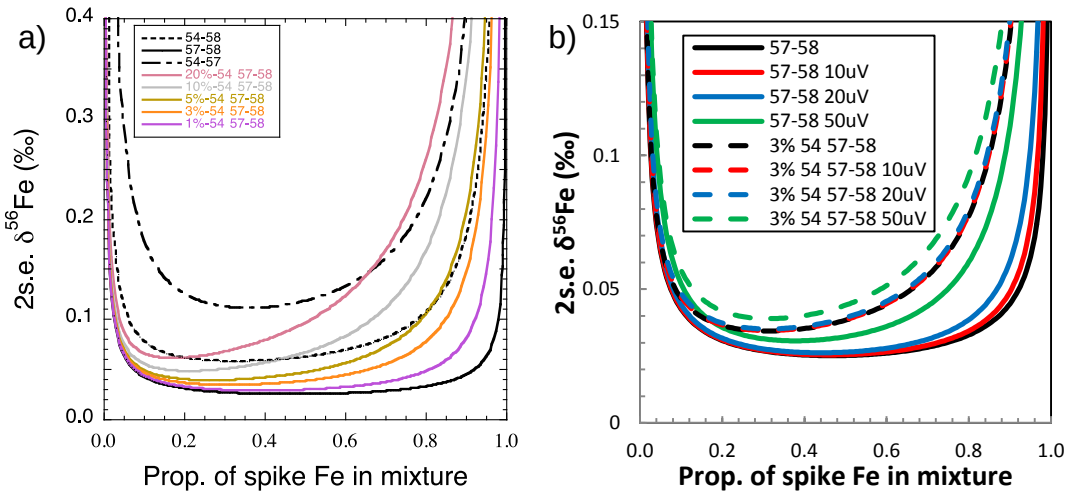

Figure 2-10: a) Model outputs of the likely precision of δ^{56}Fe values for different double spike combinations, and a ^{54}Fe-^{57}Fe-^{58}Fe triple spike with varying amounts of ^{54}Fe. b) Effect of varying electronic background on the likely precision of δ^{56}Fe values for a ^{57}Fe-^{58}Fe double spike and a ^{54}Fe-^{57}Fe-^{58}Fe triple spike with 3 % ^{54}Fe.

It is important to note that the ^{57}Fe-^{58}Fe double spike contains extremely low amounts of ^{54}Fe. A total Fe beam of 10 V would contain only 0.47 mV of ^{54}Fe, which is extremely difficult to measure precisely. Even 1 % of ^{54}Fe in the triple spike would produce ~ 90 mV of ^{54}Fe, which would be easier to measure. For the ^{57}Fe-^{58}Fe double-spike, accurate determinations of the ^{57}Fe/^{54}Fe and ^{58}Fe/^{54}Fe ratio are critical, although systematic shifts in both ratios seem to have a less detrimental effect than if one ratio is inaccurate.

A thorough assessment of the model simulations suggests that the optimal spike composition for Fe isotopes analysis is a double spike that consists of ~47% ^{57}Fe and ~53 % ^{58}Fe with the addition of less than 0.5 % ^{54}Fe for easier measurement of this isotope. For this spike composition the ideal sample to spike ratios has a relatively wide window (9:1 to 1:4), with the optimum at 1:1.

The effects of Cr and Ni interferences on the precision of δ^{56}Fe values are explored in Figure 2-11. In order to correct for Cr and Ni interferences, it is necessary to assume that they have 'natural' Cr and Ni isotope compositions. However, this is unlikely to be the case, as Cr and Ni will be fractionated during column chemistry. In order to test how fractionation would theoretically affect the precision of δ^{56}Fe values, an optimally spiked sample - ^{57}Fe-^{58}Fe double spike mixture was 'contaminated' with variable quantities of Cr and Ni, with

variable isotopic composition, and deconvolved. Figure 2-11 shows that the precision of the δ^{56}Fe measurements is much more sensitive to Ni interferences because ^{58}Ni is the most abundant Ni isotope (~68 %). By contrast, ^{54}Cr makes up only ~2.4 % of the total Cr. Note however that the effects of Ni contamination will be mitigated to some extent by the use of a spike containing ^{58}Fe. As the isotopic composition of Cr and Ni moves away from the natural value, the precision of δ^{56}Fe values falls. Thus, good separation of Cr and Ni from Fe is important because large uncertainties are induced by not knowing the isotopic composition of Cr and Ni in the final solution.

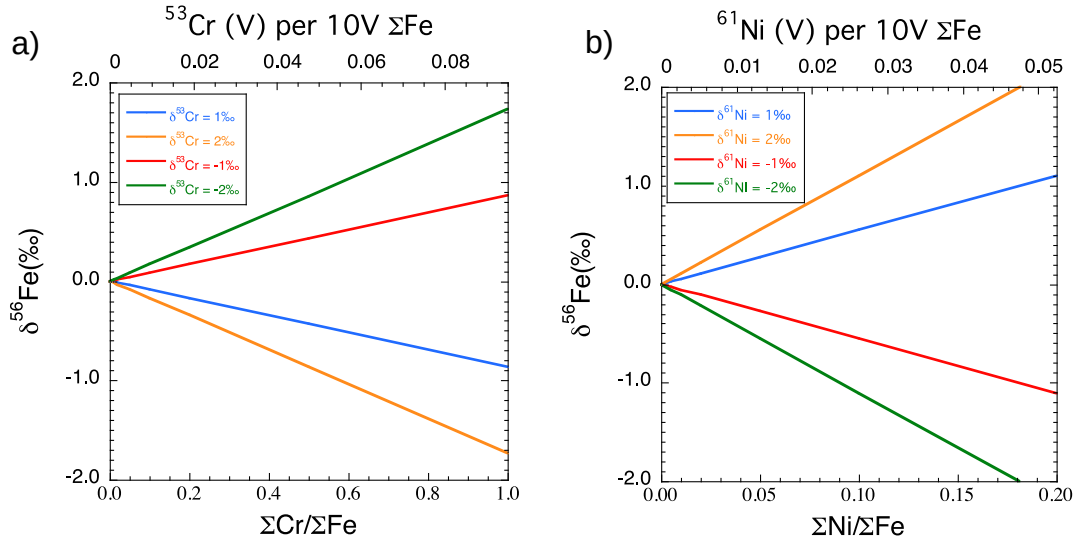

Figure 2-11: Effect of addition of a) Cr and b) Ni on the precision of δ^{56}Fe values. The horizontal axes show the proportion of total Cr or Ni relative to the total amount of Fe in the sample (∑Cr or Ni/∑Fe) at the bottom and also the signal (V) of ^{53}Cr or ^{61}Ni per 10 V of total Fe signal (∑Fe) in the sample at the top. The vertical axis displays the deviation of the δ^{56}Fe value as a result of the Cr or Ni interference, where 0.0 ‰ refers to the unchanged composition. Coloured lines show the effect of various non-natural isotope compositions.

The real composition of our double spike solution, obtained from inverse deconvolution of the IRMM-014/spike mixture, is displayed in Table 2-5. Although no ^{56}Fe spike was added to the double spike solution, the ^{54}Fe, ^{57}Fe and ^{58}Fe spikes are not pure, and contain small quantities of ^{56}Fe. Importantly,

there is virtually no Cr or Ni in the spike (less than 0.004 % of Cr and less than 0.0002 % of Ni).

Table 2-5: Isotopic composition of our double spike, obtained by inverse deconvolution of the IRMM-014/spike mixture.

	^{54}Fe	^{56}Fe	^{57}Fe	^{58}Fe
Proportion in spike (%)	0.49031	0.70145	45.732	53.077
2 SD	0.00004	0.00007	0.005	0.008

2.3.5 Isotope dilution for Fe concentrations

Isotope dilution (ID) was used to determine the Fe concentration of samples during isotopic measurements. The relative standard deviation (RSD) of a single measurement is 2 % (RSD, n = 37), which is higher than the precision of the Fe standard (Inorganic Ventures) used to calibrate the Fe concentration in the isotope spike (RSD = 0.3 %). The external reproducibility was determined by measuring two replicates of three randomly picked seawater samples, carried out at the same time as their $\delta^{56}Fe$ replicates were determined (see section 2.3.3). The samples were split before chemical separation of Fe. The RSD of each replicate analysis was 1, 2 and 6 % (Table 2-6).

As discussed in section 2.3.3 there is a discrepancy between the dFe concentrations obtained by us and LEGOS of two intercalibration samples, with our values being ~ 20 % higher (Table 2-3).

Table 2-6: Results of dFe concentration measurements using isotope dilution (ID) and flow-injection-analysis (FIA) for three samples. The average and external SD and RSD of each replicate is displayed. SD is the standard deviation of the single measurement or of the average of each replicate; RSD is the relative standard deviation.

Sample ID	**FIA dFe (nM)**	**SD (nM)**	**ID dFe (nM)**	**SD**	**RSD (%)**
D361, 08_13	2.90	0.18	2.90	0.09	3
D361, 08_13b			2.94	0.09	3
average			**2.92**	**0.03**	**1**
D361, 06_16	1.82	0.05	2.17	0.02	1
D361, 06_16b			1.99	0.02	1
average			**2.08**	**0.12**	**6**
JC55, 438-2			21.82	0.89	4
JC55, 438-2b			21.19	0.61	3
average			**21.51**	**0.44**	**2**

The accuracy and precision of dFe concentration values obtained from flow injection analysis (FIA) and ID were also compared. These concentration data were obtained from samples collected during cruise D361. FIA measurements were carried out on board during D361 by Dr. Christian Schlosser (GEOMAR) and have a RSD of 4 to 11 % for replicate analyses (Schlosser *et al.*, 2014). Dissolved Fe concentrations obtained with both methods are compared in Figure 2-12a and are in good agreement (< 15 % discrepancy) for dFe > 2 nM. However, the discrepancy increases at lower dFe concentrations. Overall, the correlation between both measurements has a slope of 1.1 and an R^2 of 0.95. A detailed comparison and discussion between dFe concentrations obtained by FIA and ID can be found in Chapter 3.

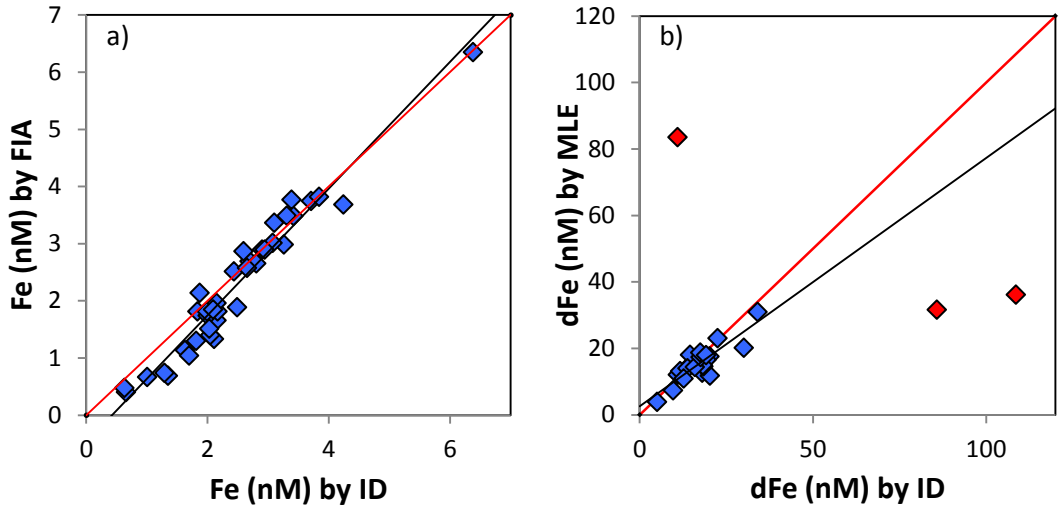

Figure 2-12: Cross-plots showing the comparison between dFe concentration values obtained by ID and (a) FIA (slope = 1.1, R^2 = 0.95) and (b) MLE (slope = 0.7, R^2 = 0.75). Outliers are not included in the trend lines and are shown in red. Trend lines are shown in black and the optimal slope (= 1.0) is shown in red.

Iron concentrations obtained by ID were also compared to Fe concentrations obtained by a mixed ligand extraction (MLE) method (Hawkes, 2013). Dissolved Fe concentrations were measured by Jeff Hawkes in hydrothermal plume seawater samples collected during JC055 using the MLE method at NOC. For quality control, NASS-5 certified seawater (3.7 ± 0.62 nM Fe) was also analysed using the MLE method, obtaining 3.74 ± 0.62 nM Fe (n = 7). The RSD of the MLE method is ~ 18%. The correlation between MLE and ID concentration values is displayed in Figure 2-12b. The correlation between MLE dFe and ID dFe (slope = 0.7, R^2 = 0.75) is poorer than the correlation between ID dFe and FIA dFe. Samples for Fe isotopic analyses and for MLE concentration measurements were collected in different bottles. Therefore the "bottle blanks" may be different. The observed differences in the Fe concentrations may also be due to the differences in the methodology.

In summary, Fe concentrations obtained by ID have a higher precision, but more replicate concentration measurements using ID are required to obtain a representative average external RSD. In addition, the measurement of dFe by ID of seawater concentration intercalibration samples, such as SAFe or

GEOTRACES, for which multiple international labs determined Fe concentrations, would provide the best quality control of our concentration data.

2.4 Summary

We have developed a technique for the accurate and precise analysis of Fe isotopes in seawater. Fe is first separated from the seawater matrix by preconcentration using NTA resin followed by purification on an anion exchange column (AG1-X8 resin). This methodology has high Fe recovery, and effectively separates Fe from the seawater matrix and isobaric elements (Cr and Ni).

The Fe blank associated with the separation procedure is of the order of 1.7 ± 0.5 to 2.3 ± 0.7 ng. This value is of the same order of magnitude as blank values reported by other groups (i.e., 1.06 ± 0.6 ng Fe (2 SD, n = 6), Lacan *et al.,* 2010; 1.1 ± 1.2 ng Fe (2 SD, n = 9), John and Adkins, 2010; 0.28 ± 0.10 ng Fe, Conway *et al.,* 2013). Given that the amount of Fe in the blank must be ideally less than 5 % of the amount of Fe in the sample in order to minimise the external error of the isotope analyses, this means that a minimum of 46 ng of Fe is required for isotopic analysis of a sample. This enables us to measure Fe isotopes in 1 L of seawater that has an iron concentration as low as 0.8 nM. Larger sample volumes are required if the Fe concentration is lower.

A protocol for the measurement of iron isotopes by MC-ICPMS has also been established. Depending on the sample introduction system used, the sensitivity ranges from 0.05 to 0.07 V of ^{56}Fe per ppb, and effective separation of Fe (and Cr) from argon oxide and nitride interferences is achieved by analysis at high resolution (m/Δm~9000). Replicate analysis of two iron isotope standards, using a double spike technique to correct for mass fractionation effects, indicates that the reproducibility of the δ^{56}Fe values is 0.06 to 0.07 ‰, 2 SD. This compares well to external reproducibilities reported by others, i.e., 0.08 ‰, 2 SD (Lacan *et al.,* 2010); 0.2 to 0.05 ‰, 2 SD (John *et al.,* 2010); and 0.02 ‰, 2 SD (Conway *et al.*, 2013).

Instrumental mass bias is corrected using a double isotope spike. Model simulations indicate that the optimal spike composition is 47 % ^{57}Fe, 53 % ^{58}Fe

and <0.5 % ^{54}Fe. The relative proportions of each individual isotope in the spike have been determined to a high level of precision (< 0.021 %). The seawater samples are doped with the spike before the Fe is separated from the seawater matrix, to account for any isotopic fractionation that may occur during this procedure. Isotope ratios are calculated by deconvolving the sample/spike mixture and are expressed in delta notation relative to the average IRMM-014 value measured on that day. The use of the double spike also provides a precise measurement of the concentration of Fe in the seawater sample by isotope dilution, with an external reproducibility of up to 6 % (RSD).

These analytical methodologies have been verified by (i) analysis of Fe isotope standards in a seawater matrix, (ii) intercomparison with the LEGOS Laboratory (François Lacan), and (iii) multiple analyses of seawater samples with a range of Fe concentrations. δ^{56}Fe measurements of seawater doped with our in-house Fe standard, the ETH standard, and IRMM-014 are all within error of the consensus values. Our analyses of two low Fe seawater samples provided by LEGOS are within error of their δ^{56}Fe measurements, and the external reproducibility of the δ^{56}Fe analyses of the seawater samples is comparable to the external reproducibility of the in-house and ETH hematite standards.

Chapter 3: Iron isotopic composition of seawater within the oxygen minimum zone in the tropical Atlantic Ocean

3.1 Introduction

Vast areas of the ocean have the potential for high levels of primary production but phytoplankton growth is limited by the availability of iron, an essential micronutrient for phytoplankton, including nitrogen fixers (Martin and Fitzwater, 1988; Martin *et al.*, 1994). This coupling between the oceanic iron (Fe) and carbon cycles has made research in the marine biogeochemistry of Fe a priority in recent decades. The complexity of Fe behaviour in seawater poses a challenge for its incorporation into global climate models used to predict future climate scenarios (Boyd and Ellwood, 2010).

As a result of its low solubility, Fe is found in the pico- to nano-molar range in the open ocean. Fe availability in seawater is limited by its solubility, which decreases with increasing temperature, decreases with decreasing salinity and decreases with increasing pH (Liu and Millero, 2002). Fe has two redox states, Fe(III) and Fe(II). The ferrous form (Fe(II)) is very soluble; however, this form is unstable in oxygenated seawater. Fe(II) is rapidly oxidised to the ferric form Fe(III), which rapidly forms inorganic complexes of (oxy)hydroxides (e.g., $Fe(OH)^{2+}$, $Fe(OH)_2^{+}$, $Fe(OH)_3$) at the pH of normal seawater (Ussher *et al*., 2004). These Fe-(oxy)hydroxides are highly particle reactive. Aggregation and scavenging by particles, which subsequently sink below the depth of the thermocline, play a key role in regulating concentrations of dissolved iron (dFe) in surface waters (Johnson *et al.*, 1997), in addition to biological uptake. However, a proportion of Fe(III) remains in solution, stabilised by complexation to organic ligands (Fe-L). Over 99 % of Fe in the dissolved phase is in the form of Fe-L (Gledhill and Buck, 2012).

Oxygen minimum zones (OMZs) are found in subsurface waters at depths of between ~100 and ~700 m depth in eastern boundary ocean regions with sluggish circulation, such as the eastern tropical Atlantic and eastern tropical Pacific Oceans, as well as the northern tropical Indian Ocean (Stramma *et al*., 2005). These OMZs develop as a result of the upwelling of nutrient enriched water masses, and subsequent high levels of biological productivity in surface waters followed by the sinking of biogenic particles, which cause high levels of respiration and oxygen depletion in sub-surface waters. Anthropogenic climate change has resulted in the expansion and intensification of the OMZs in the world's oceans (Stramma *et al.*, 2008; Brandt *et al.*, 2010). This may have important effects on the biogeochemical cycling of many redox-sensitive elements, including iron, carbon and nitrogen, as well as ecosystem functioning (Chan *et al.*, 2008; Keeling *et al.*, 2010). OMZs are characterised by relatively high dFe concentrations, but the supply, removal and stabilisation processes are not yet clear. Dissolved Fe concentrations of 1 to 1.5 nM have been observed within the (sub)tropical North Atlantic Ocean OMZ away from the shelf (Measures *et al.*, 2008; Rijkenberg *et al.*, 2012; Fitzsimmons *et al.*, 2013; Conway and John, 2014). These elevated dFe concentrations may be the result of remineralisation of Fe from high amounts of sinking organic matter from the surface (Rijkenberg *et al*., 2012; Fitzsimmons *et al*. 2013), combined with the transportation of high dFe – low oxygen waters from the African continental shelf (Conway and John, 2014).

Dissimilatory iron reduction (DIR) is a bacterial process that occurs in anoxic sediments leading to the release of Fe(II) into sediment pore waters (Crosby *et al.*, 2007). Fe(II) diffuses upwards towards the seafloor. As the Fe(II) comes into contact with oxygenated water, it rapidly oxidises to Fe(III), which precipitates as Fe-oxyhydroxide unless stabilised through Fe-L formation (Ussher *et al.*, 2004). If the overlying seawater is oxygen depleted (such as in OMZs), then relatively large amounts of dFe in the form of Fe(II) may be transported away from the sediment source. As Fe(II) is immediately oxidised to Fe(III) in seawaters with O_2 concentrations > 1 µmol/kg, rapid stabilisation of Fe through the formation of Fe-L must play an important role in transporting dFe away from

the sedimentary source (Millero *et al.*, 1987; Ussher *et al.*, 2004). Fe produced by DIR is characterised by very light Fe isotope compositions, with $\delta^{56}Fe$ values as low as -4.88 ‰ ($\delta^{56}Fe_{porewaters}$ = -3.5 to +0.4; Bergquist and Boyle, 2006; Severmann *et al.*, 2006; Homoky *et al.*, 2009; Severmann *et al.*, 2010). This light isotopic signature of sediment derived Fe may persist in the overlying water column. $\delta^{56}Fe$ values of < -1 ‰ have been reported in seawater on the Peru shelf (Chever *et al.*, submitted), and a light isotopic signature (as low as ~ -0.5 ‰) has been detected up to > 1000 km offshore within an OMZ on the eastern Atlantic shelf (Conway and John, 2014). However, $\delta^{56}Fe$ values in shelf and slope waters (< 3000 m water depth), that are necessary to trace the Fe supplied from the benthic source, are missing in the Conway and John (2014) study.

Not all continental margins are dominated by DIR. A large proportion of the global margins (located in non-OMZ waters) are controlled by non-reductive dissolution of Fe from marine sediments, but the flux is generally considered to be low, and $\delta^{56}Fe$ values (+0.22 to +0.37 ‰) are similar to the crustal value (Radic *et al.*, 2011; Homoky *et al.*, 2013). The extent of benthic redox recycling seems to be reflected in the range of $\delta^{56}Fe$ values of sediment derived Fe. Values are lowest where inputs of reactive carbon and Fe are high. Oxidative weathering of Fe (producing higher $\delta^{56}Fe$ values, close to 0 ‰) becomes more important in low organic carbon, deep-water settings with slow sediment accumulation rates and deeper O_2 penetration depths.

Dissolved Fe released from sediments on continental margins has a $\delta^{56}Fe$ signature that is distinct to atmospheric dust (+0.09 ‰; Beard *et al.*, 2003; de Jong *et al.*, 2007; Waeles *et al.*, 2007; Mead *et al.*, 2013), which is a key source of Fe to the surface waters in the global ocean. The isotopic signature of the Fe fraction that is dissolved in seawater from dust, determined through leaching experiments of aerosols in an ammonium acetate buffer, is predicted to have a very similar signature as the crustal value (~ +0.13 ‰; Waeles *et al*., 2007). However, recent observations in surface seawater suggest that the atmospheric signature is very distinct, with $\delta^{56}Fe$ values from +0.6 to +0.8 ‰ (Conway and

John, 2014), which may be the result of Fe isotope fractionation due to ligand mediated dissolution of aerosols.

Another tracer of atmospheric dust deposition to the surface ocean is dissolved aluminium (dAl) in surface seawater, as it is a nearly conservative tracer (Measures and Brown, 1996; Measures and Vink, 2000). The main removal mechanism of dAl from the surface layer of the ocean is by scavenging processes (Moran and Moore, 1992). Al has no function within biological cells, however, small amounts of Al are incorporated into the siliceous frustules of living diatoms in the photic layer (the Al:Si ratio of the frustules is ~ 1:400; (Gehlen *et al.*, 2002). An estimate of the supply of dFe from dust can be calculated by using the Model of Aluminium for Dust Calculation in Oceanic Waters (MADCOW) (Measures and Brown, 1996), which uses the average Al and Fe compositions of the Earth's crust of, respectively, 8.2 and 5.6 % by weight (Taylor, 1964), and the proportion of dust dissolution in seawater (1.5 to 5 %) (Prospero *et al.*, 1981; Maring and Duce, 1987; Lim and Jickells, 1990; Chester *et al.*, 1993).

Upon delivery of Fe to the ocean, Fe isotope signatures may be altered by internal cycling processes, whenever chemical reactions occur. Partial redox reactions between Fe(II) and Fe(III) result in an isotopically heavy oxidised fraction and a light reduced fraction (with an equilibrium isotope fractionation of up to 2.8 ‰; Welch *et al.*, 2003). The formation of Fe-L is preferentially with heavier Fe isotopes (Dideriksen *et al.*, 2008; Morgan *et al.*, 2010). Fe isotope fractionation during biological activity in oceanic surface waters is still poorly constrained. One study observed preferential uptake of light Fe isotopes from seawater, leaving the remaining dissolved Fe pool isotopically heavy (Radic *et al.*, 2011). On the other hand, the removal of isotopically heavy Fe isotopes associated with biological uptake (inferred from fluorescence maximums and dFe minimums) have been reported (Conway and John, 2014). Hence, remineralisation of the sinking biogenic particles formed in the photic layer may release isotopically light, or heavy Fe at subsurface depths. Scavenging of Fe onto sinking particles and particle aggregation are the main removal processes

of Fe from the dissolved pool, together with biological uptake. Isotopic fractionation associated with scavenging and aggregation processes is thought to be relatively small (scavenged Fe being 0.30 ‰ lower than dFe and Fe in particle aggregates being 0.5 ‰ lower than dFe; Radic *et al*., 2011).

This chapter reports the variation in the dissolved Fe isotopic signature of seawater for 5 sampling stations within the OMZ offshore Senegal in the (sub)tropical North Atlantic ocean. In addition, dAl has been measured to help constrain the fluxes of dFe from atmospheric dust deposition to the surface ocean of the (sub)tropical North Atlantic. The stations are located on an E-W transect along ~12º N, from the African shelf out in to the open ocean, at water depths of between 51 and 5022 m. This work forms part of the UK contribution to the international GEOTRACES project (www.ukgeotraces.com), whose main aim is to "identify processes and quantify fluxes that control the distribution of key trace elements and isotopes in the ocean, and to establish the sensitivity of these distributions to changing environmental conditions". The results of this study are used to identify the sources of dFe in the OMZ, and to assess internal processes, such as Fe-L formation, biological uptake, remineralisation and scavenging.

3.2 Study area

Samples for this study were collected from the oligotrophic (sub)tropical North Atlantic Ocean, south of Cape Verde Islands, east of the Mid Atlantic Ridge and overlying the Gambia abyssal plain (Figure 3-1). In this area old low oxygen, high nutrient waters are upwelled along the coast. Surface waters are depleted in bioavailable nitrogen, which leads to the proliferation of nitrogen fixers or diazotrophs, dominated by the cyanobacteria Trichodesmium spp (Moore *et al*., 2009). The absolute requirement of Fe for nitrogenase (the enzyme responsible for N_2 fixation) makes these organisms dependent on Fe availability (Falkowski, 1997; Richier *et al.*, 2012; Schlosser *et al.*, 2013). The (sub)tropical North Atlantic surface waters are characterised by high dFe, because this region receives large amounts of dust from the Sahara and Sahel deserts via aeolian

transport (Jickells *et al.*, 2005). Because concentrations of dFe are relatively high in surface waters, diazotrophic activity is significant, resulting in low concentrations of dissolved inorganic phosphate (DIP) (Moore *et al.*, 2009; Schlosser *et al.*, 2013). By contrast, the (sub)tropical South Atlantic Ocean has low dFe and high DIP, and low diazotrophic activity.

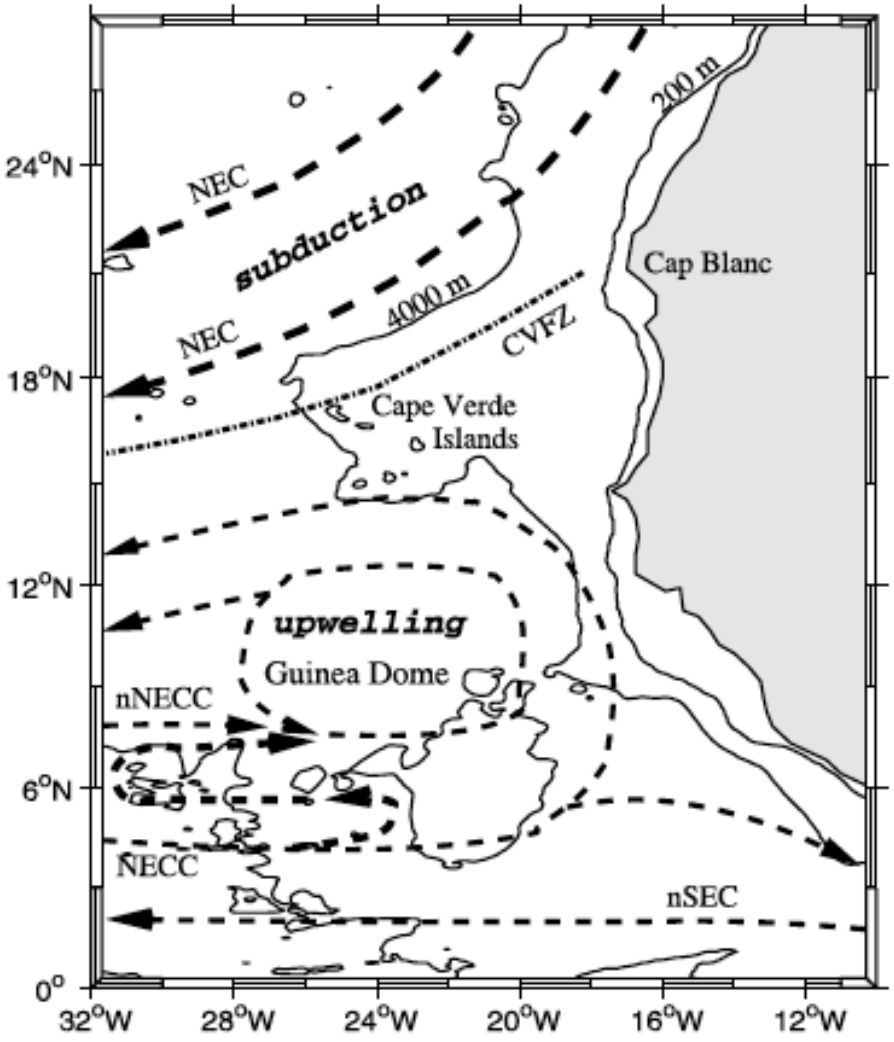

Figure 3-1: Map showing the general surface circulation in the eastern (sub)tropical Atlantic Ocean. Figure taken from Stramma *et al*. (2005). North Equatorial Counter Current (NECC); northern North Equatorial Counter Current (nNECC); Guinea Dome; North Equatorial Current (NEC); Cape Verde Frontal Zone (CVFZ).

The Atlantic intertropical convergence zone (ITCZ) is a band of low-pressure systems located a few degrees north of the equator, stretching from the east-American to the west-African coast, that forms due to rapidly rising humid air,

which leads to heavy precipitation (Chiang *et al.*, 2002). The ITCZ seasonally migrates a few degrees north and south (between ~6º N in February and ~15º N in August; Molinari *et al.*, 1986), but it is located in the northern hemisphere throughout most of the year. The heavy rainfall leads to reduced sea surface salinity (Schlosser *et al*., 2013). The ITCZ plays a major role in delivering atmospheric dust derived Fe to the surface ocean, as precipitation scavenges aerosols of air suspended dust. Wet deposition, in addition to dry deposition, is important for delivering bioavailable Fe to the surface ocean. Further, the ITCZ restricts southward transport of the desert dust-rich air masses (Schlosser *et al*., 2013).

The surface and thermocline circulation (up to 200 m depth) in the tropical North Atlantic Ocean is vigorous (Figure 3-1). North of the Equator, (5 – 6° N) the North Equatorial Undercurrent (NEUC) and the North Equatorial Countercurrent (NECC) flow eastward, originating from the northward flowing Brazil Current (BC). Further north (8 – 10° N), the northern North Equatorial Countercurrent (nNECC) also flows eastwards. Further north again, the North Equatorial Current (NEC) (which originates from the southward flowing Canary Current) flows west-southwest-wards, forming the southern boundary of the North Atlantic subtropical gyre. South of the Cape Verde Islands cyclonic circulation is found around the Guinea Dome (GD), associated with the NEC, the NECC, the nNECC and the NEUC. The GD is a permanent, quasi-stationary feature forming a large-scale near-surface flow field (Stramma *et al*., 2005). The eastwards flowing surface currents meet the westwards flowing surface currents at 12 – 14° N. Below the thermocline the flow is generally weaker. More comprehensive details of the surface current systems can be found in Bourles *et al.* (1999), Zhou *et al.* (2000) and Stramma *et al.* (2005). The coastal current (African Coastal Current) is southward in the winter season (compared to northward in summer, Mauritania Current), caused by the southward wind field present off the North African coast south of 20º N (Stramma and Schott, 1999). This leads to upwelling during the winter and spring, which is supressed during the summer and fall (Mittelstaedt, 1983). The Guinea Dome and its related

circulation are weakened during the winter, even though they exist throughout the year (Siedler *et al.*, 1992).

The flow field in the upper 800 m of the northeastern subtropical Atlantic is controlled by the wind driven subtropical gyre (Stramma *et al.*, 2005). The seasonal variability of sea surface currents is linked to the variability in wind fields caused by the seasonal migration of the ITCZ (Stramma and Schott, 1999). Offshore Ekman transport is driven by equatorward winds caused by forcing at the eastern Atlantic part of the ITCZ. Upwelling replaces the water moved offshore by Ekman transport (Stramma *et al*., 2005).

Low-oxygen South Atlantic Central Waters (SACW) are found from about 100 to 500 m depth between the isopycnals σ_θ = 25.8 and 27.1 kg/m^3, salinities between 35.1 and 35.4 and temperatures above 8ºC. SACW is formed of Indian Ocean Central Water, which is transferred to the Atlantic Ocean by the Benguela Current (Stramma *et al.*, 2005). SACW meets and mixes with NACW along the Cape Verde Frontal Zone (CVFZ), located at about 20º N off Africa and at about 16ºN in the central tropical Atlantic with a southwestward orientation. Both water masses have similar densities and therefore it is difficult to differentiate between the two after mixing. The CVFZ acts as a barrier between the low oxygen SACW and the well-oxygenated NACW, leading SACW northwards and NACW southward.

Northward flowing AAIW is found from 600 to 900 m depth and is identified by its relatively low salinity and enhanced nutrient concentrations. During the northward flow from the Southern Ocean a gradual increase in salinity and density and decrease in oxygen is observed. The oxygen concentrations in this water mass are strongly influenced by low-oxygen waters in the eastern tropical Atlantic (Stramma *et al*., 2005). Between 1000 m and the seafloor southward spreading North Atlantic Deep Water (NADW) is present. This water mass originates in the North Atlantic Ocean and has a relatively higher salinity compared to the Antarctic water masses. Above the seafloor Antarctic Bottom Water (AABW) can be found, although the Mid-Atlantic Ridge deviates most of

the northward flow of this water mass towards the western part of the mid Atlantic ridge.

The OMZ in the tropical North Atlantic Ocean is hypoxic, with oxygen concentrations from < 60 to 120 µmol/kg, whereas oxygen concentrations within the OMZ in the eastern tropical Pacific Ocean are much lower (suboxic), at < 10 µmol/kg (Stramma *et al*., 2008). The OMZ in the tropical North Atlantic Ocean is located at the 27.1 kg/m^3 isopycnal between Central Waters and AAIW (Fitzsimons *et al*., 2013). Oxygen concentrations within the tropical Atlantic OMZ are declining at a higher rate compared to other OMZs (Stramma *et al.*, 2008). The OMZ in the tropical Atlantic Ocean is located at depths between 200 and 800 m, and consists of low oxygen upwelled waters, flowing westward from the African coast. The OMZ is contained by ventilation from the bottom by AAIW; in the north and south by the eastward flowing zonal jets; and in the west by subtropical gyre waters.

3.3 Materials and Methods

3.3.1 Cleaning procedure

Seawater samples were collected in one litre high density polyethylene (HDPE) bottles (Nalgene), which were acid cleaned following a 3 step procedure. Firstly, the bottles were filled and submerged for at least 3 days in 2 % Decon. After a thorough rinse in reverse osmosis (RO) water, the bottles were filled and submerged in a 50 % HCl bath for one week. The bottles were then rinsed with Milli-Q water and transferred into a 50 % nitric acid bath for another week. Finally, the bottles were thoroughly rinsed with MQ water, double bagged and stored in clean boxes for transportation to the ship.

4 L LDPE cubitainers (Cole Parmer), used to recombine the 1 L samples, were cleaned following the same 3 step cleaning procedure, but with an additional step that consisted of filling each one with 0.03 M thermally distilled HCl for a week before rinsing and storing.

3.3.2 Sample collection

Samples were collected during research RRS *Discovery* cruise D361 between 7th February and 19th March, 2011. The aims of this cruise were to assess the supplies of Fe and P to nitrogen fixers in the tropical Atlantic Ocean and to determine their uptake rates (www.ukgeotraces.com/UK_Research/tropical_atlantic). Water samples were collected along an east-west transect along ~12 ºN, starting from the African shelf and ending in the open ocean, through the core of the OMZ (Figure 3-2).

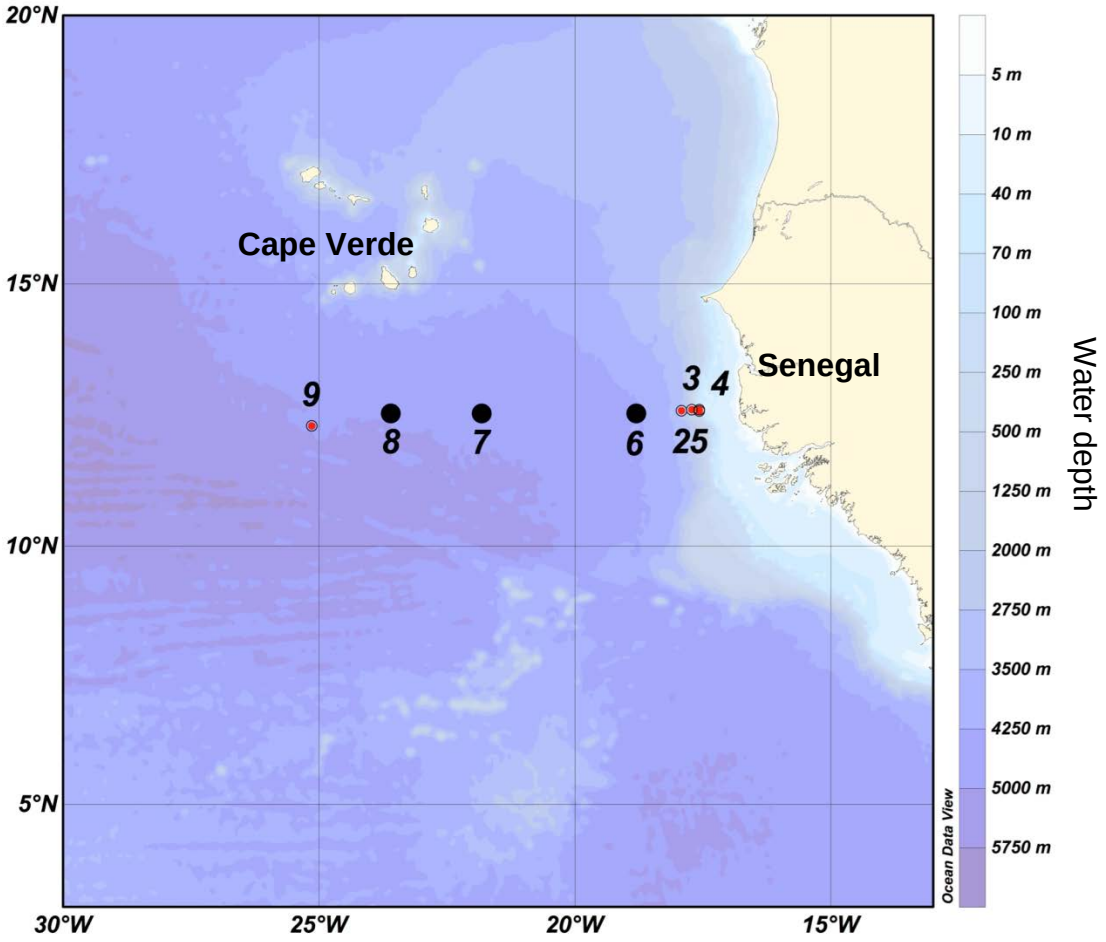

Figure 3-2: Map showing positions of sampling stations in the tropical Atlantic Ocean. Stations sampled for Fe isotope analysis are shown by the red dots.

Samples for this study were collected from five stations, ranging from 51 to 5022 m depth, using the trace metal clean conductivity-temperature-pressure (CTD) rosette system. The trace metal clean CTD rosette had 24 10 L OTE

(Ocean Test Equipment, Inc.) bottles (with external springs, modified for trace metal work) mounted onto a titanium frame, and the rosette was deployed on a non-conducting Kevlar wire fitted with a Seabird auto-fire unit that enables the OTE bottles to be triggered at pre-programmed depths. Sampling depths were selected according to salinity, temperature, oxygen and transmission profiles, measured immediately beforehand using the standard stainless steel CTD system. Immediately after recovery of the CTD rosette, the OTE bottles were transferred into a trace metal clean container for sub-sampling.

Samples for this study were filtered through 0.2 µm Supor Acropak filter capsules (Pall Corp.), that were pre-rinsed with ~5 L surface seawater from the trace metal clean 'towfish", or through acid cleaned 0.45 µm polyethersulfone filters (Supor, Pall Gelman), depending on the water budget. The filters were rinsed with several 100 mL of sample, followed by three rinses of the HDPE sample bottle before filling up. 3 x 1 L samples were collected in the acid cleaned HDPE bottles. Filtration was carried out under oxygen-free N_2 gas with a low overpressure of 10-50 kPa.

At least 24 hours after sampling, samples were acidified to pH ~2 with concentrated HCl (Romil, Ultra Purity Acid, UpA), double bagged and stored for shipping back to the National Oceanography Centre (NOC) for analysis.

3.3.3 Analysis of dissolved iron Isotopes and iron concentrations

Samples were processed according to the procedure detailed in Chapter 2. Briefly, Fe was preconcentrated using nitriloacetic acid (NTA) Superflow resin (Qiagen) and purified by anion exchange chromatography using AG1-x8 resin. Two preconcentration protocols were used, a batch method, modified from John and Adkins (2010) and a column method, based on Lacan *et al.* (2010). The average yield from both methods was 95 ± 8 % Fe (n=15) and the procedure blank was 1.7 ± 0.5 ng Fe (n=11) for the batch method and 2.3 ± 0.7 ng Fe (n=10) for the column method. Sample volumes ranged from 1 to 3 L and sample sizes varied from 103 to 351 ng Fe. When a sample volume of > 1 L was needed, the 3 L sample, that was initially collected in individual 1 L bottles,

was combined in a 4 L LDPE cubitainer. Dissolved Fe concentrations were determined on board by Dr. Christian Schlosser (GEOMAR) using a chemiluminescence flow-injection-analysis (FIA) method adapted from Obata *et al.* (1993). Dissolved Fe concentrations were also determined using isotope dilution during isotopic analysis.

Isotopic measurements were carried out on a multi-collector inductively coupled plasma mass spectrometer (MC-ICP-MS) (Thermo Fisher Neptune) at the NOCS. Instrumental mass bias was corrected for by using a ^{57}Fe-^{58}Fe double spike and $^{56}Fe/^{54}Fe$ ratios are expressed as $\delta^{56}Fe$ relative to the average $^{56}Fe/^{54}Fe$ value for the iron isotope reference material IRMM-014 determined during the analytical session. The external precision and accuracy was assessed by multiple analyses of two iron isotope standards. The average external precision of the technique is ± 0.07 ‰ (2 SD).

3.3.4 Auxiliary data

The salinity (conductivity), temperature, depth (pressure) and oxygen were measured for each water column profile using a Seabird CTD sensor mounted on the rosette frame. Discrete samples of seawater for oxygen and salinity analysis were taken from each OTE bottle to cross-calibrate the sensors and to identify miss-fired bottles. Additionally, Chlorophyll a measurements were taken during the standard CTD casts and during the underway tow fish. Fluorescence was determined using a fluorometer fitted on the rosette frame.

Dissolved aluminium (dAl) concentrations were determined on board by flow injection analysis using a lumogallion-Al fluorescence technique originally developed by Resing and Measures (1994) and modified according to Brown and Bruland (2008).

Concentrations of seawater nitrate, nitrite, silicate, ammonium and phosphate were determined by Malcolm Woodward (Plymouth Marine Laboratory) on board during the cruise, using a 5 channel segmented flow auto-analyser system (Bran and Luebbe AAIII) (Woodward and Rees, 2001).

3.4 Results

3.4.1 Hydrography

Water masses can be identified from potential temperature, salinity and density measurements. Figure 3-3 shows a potential temperature-salinity (TS) plot of all CTD casts performed along the ~12º N transect. To give a better understanding of the water mass distribution, salinity sections are also provided in Figure 3-4 and in Figure 3-5, for all sampling stations along this transect. At this latitude, the NECC and the GD are found in the surface layer (Stramma *et al.*, 2005; Stramma *et al.*, 2008). As the cruise took place in the boreal spring, the ITCZ was located at its southernmost boundary, at ~1º N (Schlosser *et al.*, 2013). Subsurface waters up to 500 m depth display a nearly linear TS relationship between the 25 and 27 kg/m^3 isopycnals. At Station 9 the subsurface waters are relatively saline compared to the stations near the coast. This water is mainly SACW (Stramma *et al.*, 2005). Below, northward flowing AAIW is observed, with its core at 900 m (identified by a salinity minimum). Southward flowing NADW is present between about 1100 to 3000 m depth, distinguished by its relatively high salinity. The bottom layer of the water column is formed of northward flowing AABW, which has relatively low salinity.

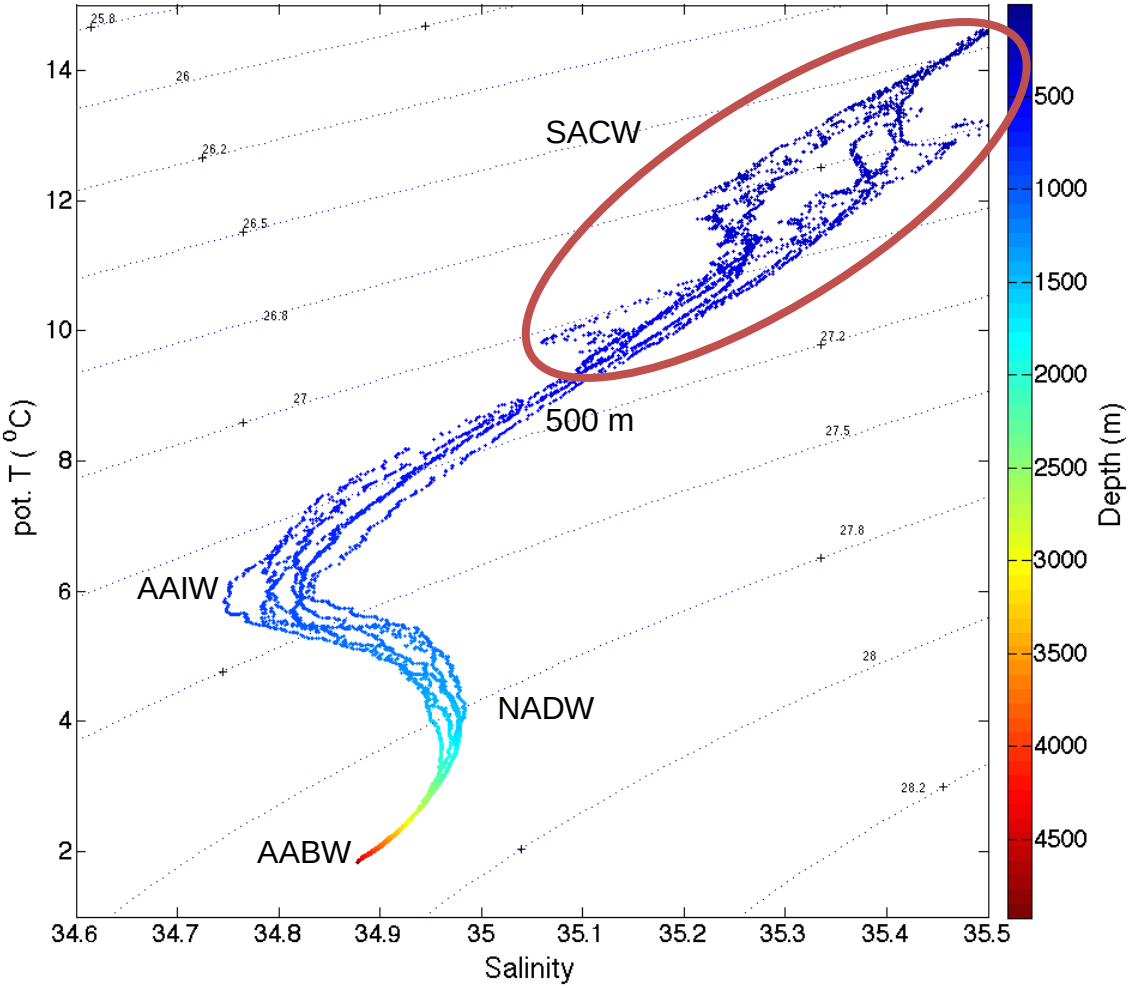

Figure 3-3: Temperature-salinity plot along ~12° N, showing density contours and water depths in a colour scale. The 500 m depth is annotated. Water masses are South Atlantic Central Water (SACW), circled in red, Antarctic Intermediate Water (AAIW), North Atlantic Deep Water (NADW), and Antarctic Bottom Water (AABW).

Oxygen concentrations are displayed in Figure 3-4 and in Figure 3-5. In the top 100 m of the water column, oxygen concentrations are up to 250 µmol/kg, and then they rapidly decline to ~100 µmol/kg at ~100 m. The OMZ is located between 100 and 800 m depth along the sampling transect, and is defined by oxygen concentrations of < 100 µmol/kg. Oxygen concentrations reach a minimum of 41 µmol/kg at ~450 m depth along the transect. The surface layer, NADW and AABW are well oxygenated (> 170 µmol/kg). A 100 m deep layer with ~150 µmol/kg O_2 is located at 1000 m depth. From 1500 m depth to the seafloor O_2 concentrations are ~250 µmol/kg.

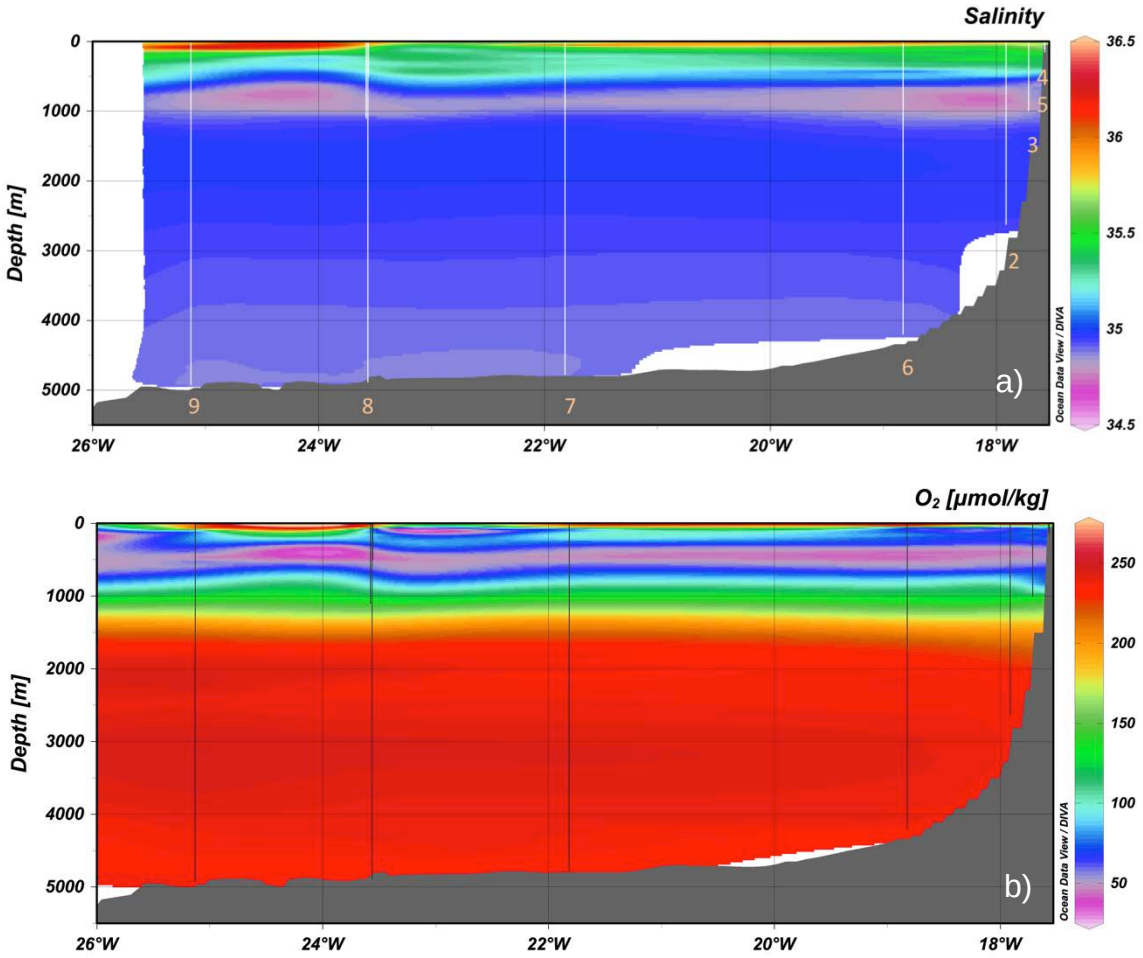

Figure 3-4: Cross sections of a) salinity and b) oxygen. Salinity and oxygen plots are integrated between the full depth profiles from the CTD sensors for stations 2 to 9 (shown by the vertical white or black lines).

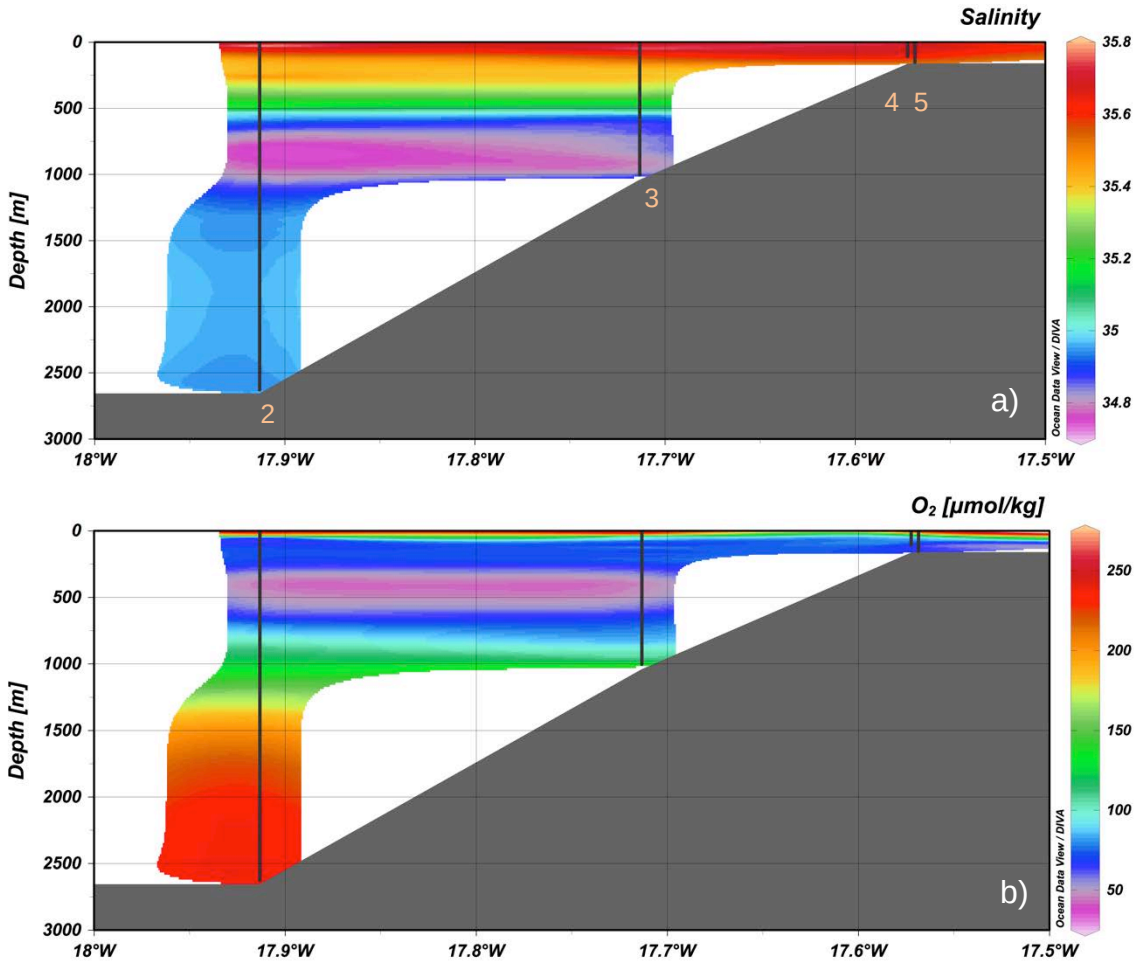

Figure 3-5: Cross sections of a) salinity and b) oxygen, for stations close to the coast (stations 2 – 5).

3.4.2 Distributions of dFe, dAl and nutrients

Nutrient distributions (courtesy of Malcolm Woodward, Plymouth Marine Laboratory) are displayed in Figure 3-6 and in Figure 3-7. Nitrate and phosphate have similar distributions throughout the water column with elevated values within the OMZ. Up to 37 µM nitrate and 2.37 µM phosphate are observed close to the bottom of the OMZ at ~ 750 m. Below 1500 m depth, nitrate concentrations are ~ 20 µM and phosphate concentrations are ~ 1.6 µM. Phosphate concentrations are slightly higher close to the seafloor close to the continental slope, compared to the western side of the section. Silicon distributions are different from phosphate and nitrate, with concentrations

gradually increasing with depth, from ~ 2 µM at the sea surface to ~ 55 µM at 4000 m depth. AAIW, at ~ 900 m depth, is characterised by relatively high dissolved silicon concentrations (~26 µM).

The distribution of dFe (courtesy of Dr. Christian Schlosser, GEOMAR, Figure 3-6 and Figure 3-7) is similar to the distributions of nitrate and phosphate along the section. However, dFe displays a surface maximum, which is not observed for nitrate and phosphate. Relatively high dFe concentrations of up to 4 to 6 nM are observed at the coastal stations. Relatively high dFe concentrations are also observed within the OMZ, but concentrations in the core of the OMZ decrease from the coast (2.2 nM) towards the open ocean (1.4 nM). Deep waters (1500 to 5000 m) have higher dFe concentrations on the eastern side of the transect (1.4 to 1.5 nM), compared to the open ocean waters (0.6 to 0.9 nM). Surface dFe concentrations range from 0.2 nM in open ocean waters to 1.5 nM in waters over the continental slope.

The distribution of dAl along the transect (Figure 3-4 c) is more similar to the distribution of dissolved silicon. Open ocean surface dAl concentrations range from 10 to 27 nM, while coastal and slope surface waters display lower dAl values of 2 to 8 nM. On the western side of the transect, subsurface (~100 m) dAl concentrations are relatively low, at around 1 nM. Below this depth, dAl gradually increases towards the seafloor, to around 10 to 15 nM. On the eastern side of the transect, and over the continental slope, deep water dAl concentrations are slightly higher (up to 18 nM). Close to the coast, dAl concentrations tend to be relatively low (ranging from 3 to 8 nM).

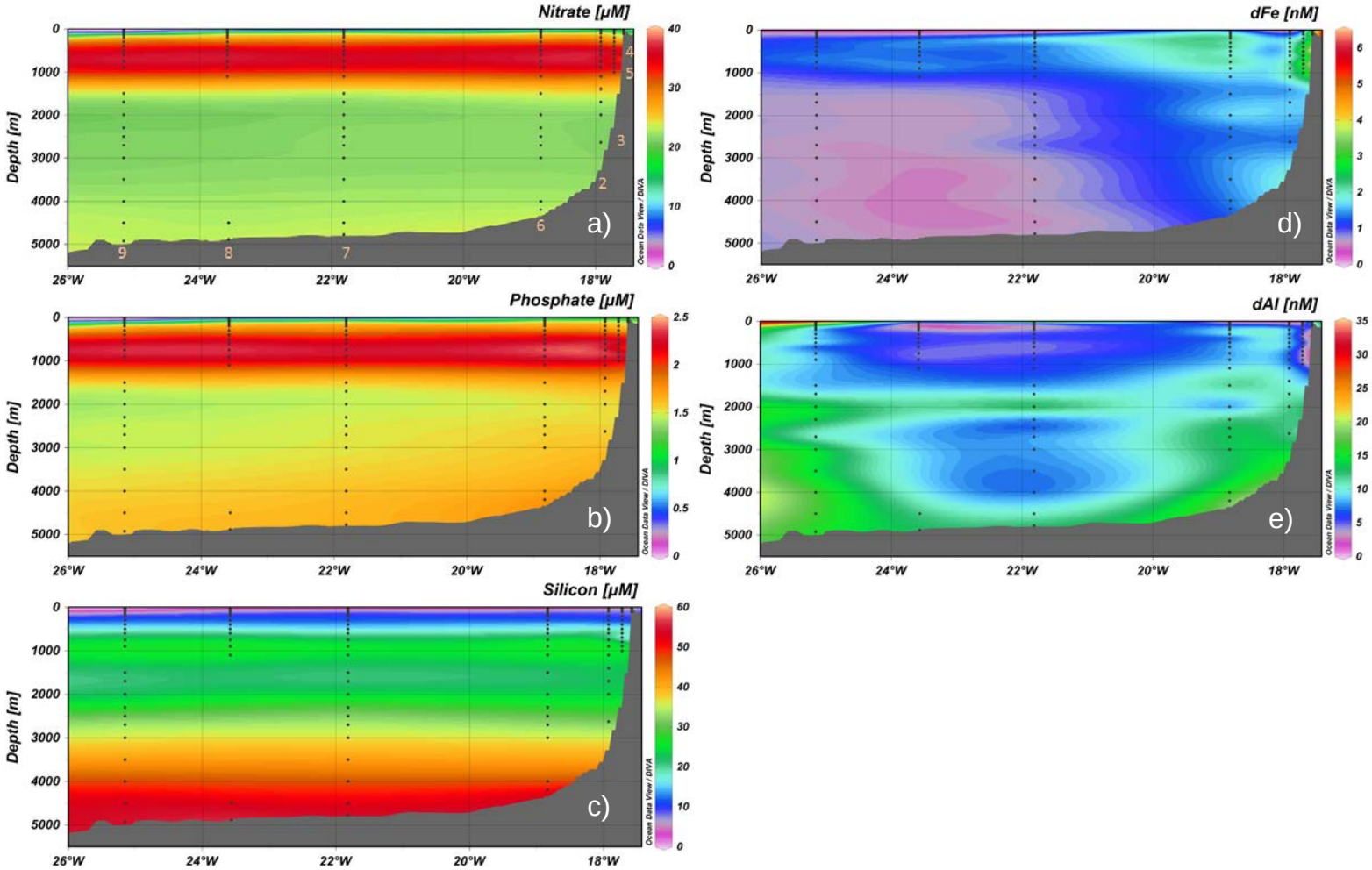

Figure 3-6: Cross sections of a) nitrate, b) phosphate, c) silicon d) dFe and e) dAl along ~12° N. Data are integrated between the discrete measurements shown by the black dots. Station numbers are shown on section a).

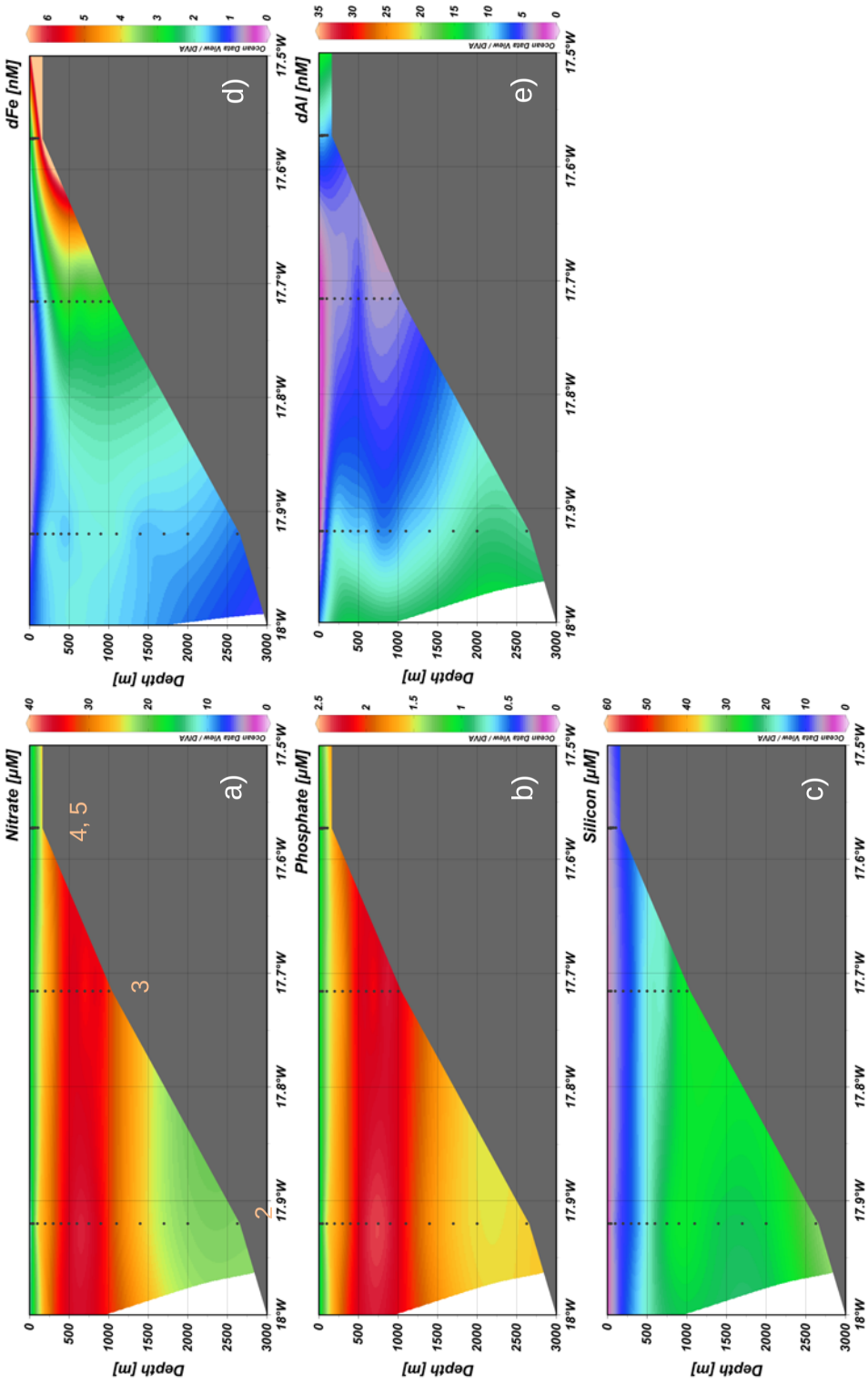

Figure 3-7: Cross section of a) nitrate, b) phosphate c) silicon d) dFe and e) dAl for stations close to the coast along ~12° N.

3.4.3 Profiles of dFe, iron isotopes and oxygen

Results of iron isotope analysis, as well as data for all other parameters measured on the same samples, are given in Table 3-1 and vertical profiles are shown in Figure 3-8 (coastal stations) and Figure 3-9 (open ocean stations). Dissolved Fe concentrations obtained from two different methods, FIA, done by Dr. Christian Schlosser (GEOMAR), and isotope dilution using the double isotope spike, are also displayed. At the shallower stations, Station 4 (51 m depth) and Station 5 (164 m depth), δ^{56}Fe values are relatively low (~ -0.3 ‰) close to the seafloor, and increase towards the crustal value closer to the sea surface (~ +0.0 ‰). Concentrations of dFe are highest close to the seafloor (up to 6.35 nM) and decrease towards the sea surface (~ 3 nM). Oxygen concentrations range from ~ 65 µmol/kg close to the seafloor to > 200 µmol/kg in surface waters. The deeper coastal station, Station 3 (1041 m depth) displays crustal δ^{56}Fe values in subsurface waters (+0.06 ‰ at 200 m depth). Below this depth, δ^{56}Fe values decrease, reaching -0.32 ‰ at 500 m depth. Below 500 m depth, δ^{56}Fe increases slightly, to ~ -0.25 ‰ close to the seafloor. Dissolved Fe concentrations are low in surface waters (~ 1 nM), and increase to ~ 3 nM at 400 m depth. Between 400 m and the seafloor, dFe concentrations vary between 2 and 4 nM. Oxygen concentrations are lowest (as low as 45 µmol/kg) between 300 and 700 m depth. At the seafloor, oxygen concentrations are ~130 µmol/kg, whereas surface waters have concentrations of > 240 µmol/kg.

Located in deeper waters (2656 m), δ^{56}Fe values at Station 2 increase from -0.06 ‰ at 200 m depth to +0.39 ‰ at 500 m depth. Between 600 m and the seafloor, there is little variation in δ^{56}Fe, with values around +0.1 ‰. Dissolved Fe concentrations range from 0.4 nM in surface waters to 0.9 nM at 300 m depth. Between 400 and 1700 m depth, dFe concentrations range from 1.4 nM to 2 nM. Below 1700 m, dFe tends to decrease, to values as low as 1.3 nM above the seafloor. Surface and bottom waters are well oxygenated at station 2 (O_2 > 240 µmol/kg), and the OMZ is defined by low O_2 concentrations (as low as 45 µmol/kg) between 100 and 700 m depth.

Table 3-1: Results of dAl, dFe and $\delta^{56}Fe_{dFe}$ analyses of seawater profiles from the subtropical North Atlantic along ~12º N. The reproducibility of the dAl analyses is reported as the standard deviation of two replicate measurements; the reproducibility of the FIA dFe analyses is reported as the standard deviation of three replicate measurements; the reproducibility of the ID dFe analyses is the standard deviation of a single measurement (in the same order as replicate measurements); the reproducibility of $\delta^{56}Fe$ values is two times the standard deviation of replicate analyses of an external standard measured during the same MC-ICPMS session. The mixed layer depth (MLD) is defined as the surface layer that has less than 0.8 °C change in temperature (Kara *et al.*, 2000).

Sample ID	Depth (m)	dAl (nM)	SD (nM)	dFe FIA (nM)	SD (nM)	**dFe ID (nM)**	SD (nM)	**$\delta^{56}Fe$ (‰)**	2 SD (‰)	Oxygen (µmol/kg)	Nitrate (µM)	Phosphate (µM)	Silicon (µM)
Station 4 (12º 36.50' N; 17º 34.34' W; 51 m water depth)													
11_12	25	8.8	0.4	2.52	0.24	**2.43**	0.07	**0.03**	0.04	133	13.51	0.97	5.68
11_11	38	7.8	0.7	3.36	0.08	**3.10**	0.09	**-0.20**	0.04	103	15.76	1.08	5.75
11_10	40	7.5	0.4	3.49	0.16	**3.30**	0.10	**-0.32**	0.04	101	16.14	1.12	6.54
11_09	49	7.6	0.4	3.82	0.06	**3.84**	0.11	**-0.25**	0.04	88	6.68	1.13	6.33
Station 5 (12º 35.23' N; 17º 34.31' W; 164 m water depth)													
12_23	26	8.2	0.5	3.01	0.10	**3.07**	0.09	**-0.11**	0.05	121	15.48	1.10	5.94
12_21	36	10.2	0.4	2.99	0.13	**3.26**	0.09	**-0.23**	0.05	98	17.26	1.21	6.55
12_19	51	8.2	0.5	3.48	0.20	**3.42**	0.10	**-0.16**	0.05	81	18.03	1.25	6.80
12_17	66	11.4	1.1	3.75	0.06	**3.70**	0.11	**-0.25**	0.05	81	18.08	1.25	6.84
12_15	80	7.5	0.5	3.68	0.09	**4.24**	0.12	**-0.31**	0.05	75	18.89	1.29	7.08
12_13	107	7.7	0.4	6.35	0.47	**6.38**	0.18	**-0.33**	0.05	66	21.51	1.43	8.05

Table 3-1 (cont.)

Sample ID	Depth (m)	dAl (nM)	SD (nM)	dFe FIA (nM)	SD (nM)	**dFe ID (nM)**	SD (nM)	**δ^{56}Fe (‰)**	2 SD (‰)	Oxygen (µmol/kg)	Nitrate (µM)	Phosphate (µM)	Silicon (µM)
Station 3 (12º 36.56' N; 17º 43.02' W; 1041 m water depth)													
08_24	24	1.5	0.4	0.83	0.05					100	16.23	1.07	5.01
08_23	49	2.1	0.4	0.77	0.07					91	19.35	1.20	5.64
08_22	100	3.0	0.4	1.20	0.04					76	22.55	1.42	7.00
08_21	199	4.2	0.4	1.81	0.02	**1.83**	0.02	**0.06**	0.04	74	25.63	1.59	8.83
08_20	300	3.9	0.4	2.58	0.02	**2.65**	0.08	**-0.15**	0.04	58	28.62	1.73	10.70
08_19	400	3.9	0.5	2.86	0.08	**2.59**	0.08	**-0.19**	0.04	46	32.82	1.98	14.01
08_18	500	6.3	0.4	3.77	0.19	**3.38**	0.10	**-0.32**	0.04	51	34.79	2.17	17.49
08_17	599	4.0	0.4	2.14	0.09	**1.87**	0.06	**-0.08**	0.04	61	36.72	2.33	20.19
08_16	699	3.5	0.4	2.66	0.05	**2.81**	0.08	**-0.30**	0.04	75	30.81	1.91	13.62
08_15	799	4.1	0.6	3.59	0.03					83	35.73	2.34	23.25
08_14	899	3.7	0.4	2.69	0.06	**2.69**	0.08	**-0.26**	0.04	103	34.88	2.32	25.03
08_13	1002	4.1	0.6	2.90	0.18	**2.90**	0.09	**-0.27**	0.04	133	31.77	2.16	25.20
						2.94	0.09	**-0.21**	0.05				

Table 3-1 (cont.)

Sample ID	Depth (m)	dAl (nM)	SD (nM)	dFe FIA (nM)	SD (nM)	**dFe ID (nM)**	SD (nM)	**δ^{56}Fe (‰)**	2 SD (‰)	Oxygen (µmol/kg)	Nitrate (µM)	Phosphate (µM)	Silicon (µM)
Station 2 (12º 35.42' N; 17º 54.99' W; 2656 m water depth)													
6_24	25	2.1	0.9	0.44	0.02					180	9.79	0.76	2.77
6_23	50	4.3	0.4	1.31	0.03					65	22.35	1.43	6.67
6_22	100	5.9	0.4	1.18	0.05					68	24.45	1.53	7.73
6_21	200	10.6	0.5	1.85	0.10	**2.09**	0.02	**-0.06**	0.08	69	26.69	1.62	9.46
6_20	300	8.8	0.4	1.89	0.05	**2.49**	0.02	**0.02**	0.08	52	30.37	1.81	11.33
6_19	400	8.8	0.5	1.51	0.08	**2.03**	0.05	**0.19**	0.10	44	33.18	1.98	13.72
6_18	500	8.4	0.5	1.40	0.04	**2.04**	0.05	**0.39**	0.10	51	35.37	2.19	17.24
6_17	600	9.5	0.5	1.96	0.06	**2.15**	0.02	**0.10**	0.08	61	36.89	2.32	20.39
6_16	750	7.1	0.4	1.82	0.05	**2.17**	0.02	**0.12**	0.08	85	36.55	2.37	23.77
						1.99	0.02	**0.10**	0.10				
6_15	900	7.4	0.5	1.74	0.05	**2.00**	0.02	**0.09**	0.08	114	34.61	2.32	25.96
6_14	1100	8.9	0.5	2.01	0.06					146	30.38	2.08	24.85
6_13	1400	9.4	0.6	1.40	0.04					189	25.65	1.78	22.90
6_12	1700	10.7	0.6	1.66	0.03	**2.15**	0.02	**0.12**	0.08	218	22.76	1.60	22.83
6_11	2000	12.0	0.5	1.58	0.02					231	21.51	1.53	23.59
6_10	2625	11.6	0.6	1.33	0.03	**2.10**	0.06	**0.04**	0.10	237	21.18	1.56	31.47

Table 3-1 (cont.)

Sample ID	Depth (m)	dAl (nM)	SD (nM)	dFe FIA (nM)	SD (nM)	**dFe ID (nM)**	SD (nM)	**δ^{56}Fe (‰)**	2 SD (‰)	Oxygen (µmol/kg)	Nitrate (µM)	Phosphate (µM)	Silicon (µM)
Station 9 (12º 18.08' N; 25º 08.44' W; 4980 m water depth)													
22_24	24	27.0	0.8	0.36	0.03					212	0.01	0.02	1.28
22_23	49	21.0	1.3	0.48	0.04	**0.63**	0.01	**0.48**	0.10	212	0.01	0.02	1.07
22_22	78	22.4	0.7	0.40	0.02	**0.66**	0.01	**0.45**	0.10	205	0.42	0.08	1.23
22_21	110	6.5	0.4	0.75	0.10					89	18.70	1.11	4.85
22_20	149	10.1	0.7	0.92	0.02					79	23.63	1.39	7.51
22_19	199	8.9	0.5	1.04	0.02	**1.70**	0.05	**0.26**	0.10	82	25.74	1.56	9.48
22_18	299	10.0	0.5	1.26	0.04					67	29.06	1.75	11.58
22_17	399	7.5	0.4	1.14	0.05	**1.63**	0.04	**0.48**	0.10	53	32.84	1.95	14.12
22_16	500	11.4	0.6	1.27	0.07					58	34.23	2.08	16.64
22_15	599	5.1	0.6	1.30	0.12	**1.81**	0.05	**0.19**	0.10	58	36.30	2.26	19.76
22_14	750	8.9	0.5	1.39	0.06					81	36.48	2.33	23.86
22_13	899	8.7	0.5	1.09	0.02					108	34.92	2.28	26.25
22_11	1499	8.5	0.8	0.74	0.03	**1.29**	0.03	**0.61**	0.10	213	23.43	1.57	21.31
22_10	1699	9.1	0.5	0.65	0.05					231	21.67	1.46	20.93
22_09	1999	14.6	0.6	0.69	0.02	**1.35**	0.04	**0.55**	0.10	241	20.77	1.41	22.49
22_08	2298	13.7	0.5	0.68	0.03					241	20.88	1.43	26.33
22_06	2698	9.7	0.9	0.58	0.04					241	21.39	1.47	33.53
22_05	2998	15.0	0.5	0.63	0.07					244	21.30	1.45	36.00
22_04	3499	14.1	0.9	0.65	0.04					243	21.66	1.51	41.36
22_03	3999	16.9	0.6	0.58	0.04					239	22.37	1.55	47.54
22_02	4499	16.7	0.6	0.63	0.04					236	23.11	1.60	52.98
22_01	4923	15.6	1.2	0.67	0.08	**1.00**	0.01	**0.56**	0.10	237	23.27	1.60	54.23

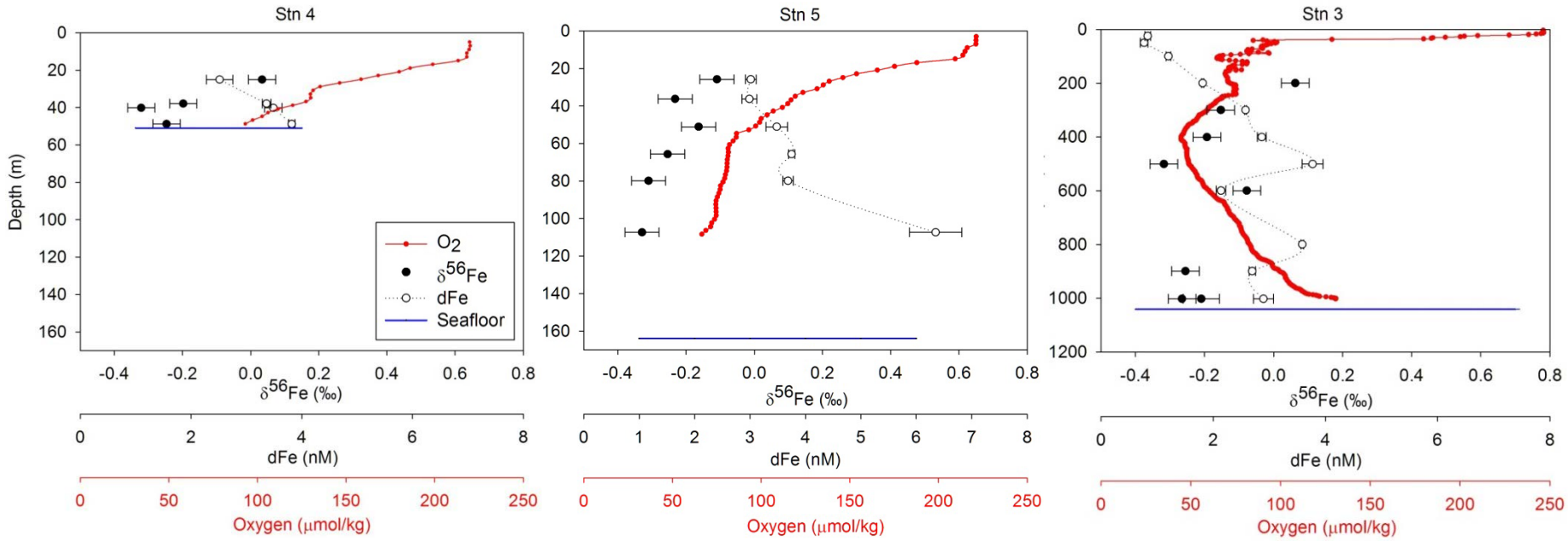

Figure 3-8: Profiles of $\delta^{56}Fe_{dFe}$, dFe and dissolv oxygen for the stations closest to the coast.

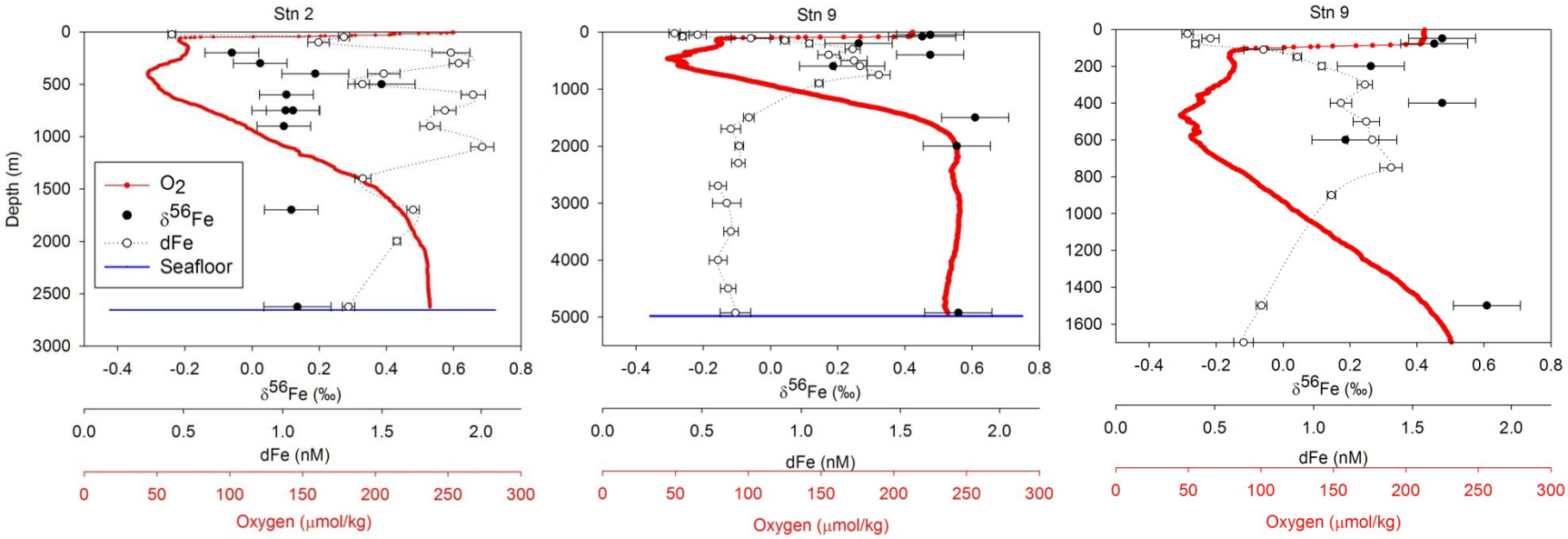

Figure 3-9: Profiles δ^{56}Fe, dFe and dissolved oxygen for the stations over the continental slope (Station 2) and over the abyssal plain (Station 9). The upper 1700 m of Station 9 are shown in an additional graph.

Station 9 (Figure 3-9) is located at 4980 m depth above the Gambia abyssal plain, ~950 km away from the African coast and ~300 km away from the Cape Verde Islands. The δ^{56}Fe profile is slightly different from that recorded at Station 2. δ^{56}Fe decreases from +0.5 ‰ in surface waters to +0.19 ‰ at 600 m depth. Between 1550 m and the seafloor δ^{56}Fe values are more or less constant at around +0.6 ‰. Dissolved Fe concentrations gradually increase from surface waters (0.4 nM) towards 750 m depth (1.4 nM), below which concentrations decrease to ~ 0.6 nM at 1700 m, remaining more or less constant (0.6 to 0.7 nM) below this depth. Oxygen concentrations have a similar distribution to station 2, with well oxygenated waters at the surface and at depth (> 240 µmol/kg), and the OMZ ranging from ~100 to ~900 m depth, with the lowest oxygen concentrations at 450 m (42 µmol/kg).

3.5 Discussion

3.5.1 Iron isotope compositions of coastal waters

The process of dissimilatory iron reduction (DIR) within anoxic sediments produces a light Fe isotope signature (Severmann *et al.*, 2006; Homoky *et al.*, 2009; Severmann *et al.*, 2010). Under anoxic conditions, Fe-reducing bacteria within the sediments convert Fe(III) to Fe(II) (Crosby *et al.*, 2007). The isotopic fractionation signature associated with the Fe reduction is around -3 ‰ (Welch *et al.*, 2003). Fe(II) released into sediment pore waters diffuses towards the sediment-seawater interface, hence DIR can be an important source of dFe to the overlying water column and potentially to the surface ocean, especially if upwelling or advection facilitate the movement of water. When highly soluble Fe(II) is released into the overlying water column it is rapidly oxidized to Fe(III) as oxygen concentrations increase, leaving the Fe(III) pool heavier and the Fe(II) pool lighter (Welch *et al*., 2003). In seawater, Fe(III) does not remain in solution due to its low solubility (Liu and Millero, 2002; Ussher *et al*., 2004), forming inorganic complexes with insoluble (oxy)hydroxides, unless it is stabilised by the formation of soluble Fe-ligand complexes. Fe-L formation is

observed to favour the binding to heavy (Dideriksen *et al*., 2008; Morgan *et al*., 2010) or light (Brantley *et al*., 2004) Fe isotopes. Fe(II) released from sediments can only be transported away from its source when the overlying water column is oxygen depleted (O_2 < 1 µmol/kg), preventing the oxidation of Fe(II) (Millero *et al*., 1987).

Coastal stations 3, 4 and 5 are characterised by low δ^{56}Fe values (down to -0.3 ‰) in the low oxygen waters (~50 – 100 µmol/kg) close to the seafloor (Figure 3-8). Note that no samples were collected within 50 m of the seafloor at Station 5, so even lower δ^{56}Fe and O_2 values may have been found closer to the seafloor. In agreement with previous studies (e.g. Conway and John, 2014), these low δ^{56}Fe values suggest that DIR is a source of dFe to the overlying water column on the eastern tropical Atlantic shelf. Any Fe(II) carrying the negative isotopic signal released into the water column is rapidly oxidised to Fe(III) as O_2 concentrations observed in bottom waters are not low enough for Fe(II) to remain stable. Using the equations from Millero *et al*. (1987) (see equations 1-2 – 1-4), the half-life of Fe(II) ($t_{1/2}$) is calculated to be ~ 40 min in bottom waters at Stations 4 and 5 ([O_2] = 65 µmol/kg, T = 288 °K, pH = 8 and using ionic strength (I) for seawater given in Millero *et al*., 1987). Therefore the presence of organic ligands in seawater to stabilise Fe(III) in solution before it precipitates as (oxy)hydroxide aggregates must play an important role in regulating the supply of Fe from the African shelf sediments. Partial oxidation of Fe(II) to Fe(III) leaves the Fe(III) fraction heavier (Welch *et al*., 2003) and organic ligands that may bind to this Fe(III) also preferentially bind to heavy isotopes (Dideriksen *et al*., 2008; Morgan *et al*., 2010). The overall process, from oxidation of Fe(II) to Fe(III), and then the formation of Fe(III)-L complexes favours the heavy Fe isotopes, which may explain the higher δ^{56}Fe values observed in bottom waters compared values observed in pore waters (as low as ~ -3 ‰; Severmann *et al*., 2006). The hypothesis of a benthic source is also supported by relatively high Fe concentrations (up to 6.35 nM) close to the seafloor.

At Station 3 (1041 m water depth) profiles of Fe isotopes, dFe concentrations and O_2 concentrations change considerably compared to the shallower coastal stations. Slightly negative $\delta^{56}Fe$ values (as low as -0.32 ‰) and relatively high dFe concentrations (up to 3.8 nM) are found close to the OMZ at 300 to 500 m depth. This suggests either that low oxygen waters may be carrying benthic sourced dFe from the shelf, or that remineralisation of particulate material within the OMZ releases Fe with low $\delta^{56}Fe$. In contrast to the shallow coastal stations, bottom waters at station 3 are more oxygenated (up to 140 µmol/kg), and have slightly higher $\delta^{56}Fe$ values (~ -0.2 ‰ compared to ~ -0.3 to -0.4 ‰). Dissolved Fe concentrations in seawater above the seafloor at Station 3 are also lower compared to Stations 4 and 5. The more rapid oxidation of Fe(II) to Fe(III) in the more oxygenated waters (Fe(II) half-life of ~ 30 min, $[O_2]$ = 130 µmol/kg, T = 279 °K) leads to higher amounts of Fe loss due to the formation of (oxy)hydroxides before Fe-L formation can take place, compared to bottom waters at Stations 4 and 5. In addition, the bottom water signature may also be the result of mixing between ligand stabilised sediment sourced dFe with dFe transported within AAIW. AAIW is observed between 800 m depth and the seafloor at Station 3. $\delta^{56}Fe$ values of +0.06 and +0.22 ‰ have been observed in this water mass in the western equatorial Pacific ocean (Radic *et al*., 2011). This may explain why $\delta^{56}Fe$ values are ~ 0.1 to 0.2 ‰ heavier in bottom waters at Station 3 compared to bottom waters at Stations 4 and 5.

Negative seawater $\delta^{56}Fe$ values attributed to the release of Fe(II) from anoxic sediments into the overlying water column have also been observed in an anoxic basin off the coast of southern California (John *et al.*, 2012). $\delta^{56}Fe_{dFe}$ values in bottom waters were as low as -3.45 ‰, and bottom water oxygen concentrations were < 5 µM. At oxygen concentrations similar to those found within the OMZ in this study (~ 50 to 75 µM), $\delta^{56}Fe_{dFe}$ ranged from -1.13 to -0.8 ‰, which may indicate that benthic fluxes of dFe are far greater in the southern California basin because oxygen concentrations close to the seafloor are much lower. In support of this, $\delta^{56}Fe_{dFe}$ values for seawater from close to the seafloor to the north of Cape Verde Islands are ~ -0.5 ‰ (Conway and John, 2014),

which is attributed to Fe released from reducing sediments into a relatively oxygenated water column. In addition, bottom waters in the Peru upwelling area have $\delta^{56}Fe_{dFe}$ values as low as -1.25 ‰, associated with O_2 concentrations of < 35 µM (Chever *et al.*, submitted). These results are comparable to our findings, considering that the OMZ in the equatorial Pacific ocean is far more oxygen depleted than the OMZ in the tropical Atlantic (Stramma *et al.*, 2008). In addition, as a result of analysing Fe isotopic compositions for several size fractions, Chever *et al*. (submitted) have demonstrated that the dFe pool reflects the isotopic composition of the ferrous Fe, which is presumably released from the sediments.

The results of this study are an important complement to the findings in Conway and John (2014). In their study, the shallowest station close to the African shelf is ~ 3000 m deep, hence, missing $\delta^{56}Fe_{dFe}$ values on the continental slope and shelf that may have provided better evidence for tracing benthic Fe released into the water column. Our stations, located ~ 6º to the south of the stations shown in Conway and John (2014), at water depths down to 50 m, fill in this coastal gap of $\delta^{56}Fe_{dFe}$ values and enable to trace the benthic Fe closer to its source.

Although benthic sources of Fe are thought to be insignificant on a global scale, it has recently been suggested that 20 to 30 % of the dFe found in the water column on the continental margins originates from reductive sediments, and that advection of shelf sourced Fe may extend a few thousand kilometres away from the shelf (Conway and John, 2014). Model results also suggest that 10 – 50 % of shelf sediment derived Fe flux is exported offshore (Siedlecki *et al.*, 2012), indicating that DIR may play a substantial role in delivering dFe to ocean waters.

$\delta^{56}Fe_{dFe}$ values increase away from the seafloor at Stations 3, 4 and 5, as the Fe sourced from the sediments mixes with the Fe present in the surrounding waters, which have higher $\delta^{56}Fe$. At the time of sampling, the rate of upwelling was high, so bottom waters rich in sediment-sourced Fe may be transported to

the surface mixed layer. Supporting this, Fe concentrations also decrease towards the surface waters. At the ambient O_2 concentrations in the water column, Fe will be dominantly in the Fe(III) form, hence redox reactions are likely to be insignificant, and are unlikely to explain the variation in $\delta^{56}Fe$ throughout the water column.

By contrast, uptake of dFe as a result of biological activity in surface waters is believed to favour the uptake of light Fe, leaving the surrounding waters with a heavy $\delta^{56}Fe$ signature (Radic *et al.*, 2011). However, by contrast Conway and John (2014) record relatively light $\delta^{56}Fe_{dFe}$ values associated with the fluorescence maximum (indicative of biological activity) in the North Atlantic Ocean. Although no diazotrophs were detected in the coastal water during this study (L. Sargent, personal communication), concentrations of Chlorophyll-a and fluorescence recorded by the CTD sensors indicate that levels of biological activity in the surface waters are high, with Chl-a concentrations of up to ~6 µg/L (Figure 3-10). There are no Chl-a data for Station 5, but we can infer that they are likely to be similar to Station 4 from the fluorescence profiles. Transmittance data also suggest the presence of high amounts of particles, which are likely of biogenic origin, in the surface waters at the coastal stations (Figure 3-11). Maximum Chl-a, fluorescence and transmittance is observed close to the surface layer of the water column at Stations 3, 4 and 5, indicating that highest levels of biological activity are immediately below the ocean surface. Thus, relatively high $\delta^{56}Fe$ values in surface waters (+0.03 and -0.11 ‰ at ~ 25 m depth, below the mixed layer depth) are consistent with uptake of isotopically light dFe by biological activity (Radic *et al*., 2011). No $\delta^{56}Fe$ values were determined in the uppermost ~ 25 m of the water column in this study, so we are unable to determine the Fe signature associated with the Chlorophyll maximum; and the “surface” $\delta^{56}Fe$ value of coastal waters is based on two observations, one from Station 4 and another from Station 5, both at ~ 25 m. The surface mixed layer in the coastal waters is only ~ 15 to 25 m deep, and therefore significant variation in the $\delta^{56}Fe$ values in the upper 100 m is expected. For instance, Chever *et al*. (submitted) observed a significant change

in $\delta^{56}Fe_{dFe}$ values between 10 and 50 m depth, however there is no fluorescence or Chlorophyll data to support whether this is associated with levels of biological activity. There may be alternative explanations, which are explored below.

The mixed surface layer in the North Atlantic is characterised by relatively high $\delta^{56}Fe$ values of +0.3 to +0.7 ‰ (Conway and John, 2014), which has been attributed to isotope fractionation during dissolution of atmospheric dust (with $\delta^{56}Fe$ ~0‰; Waeles *et al*., 2007; Mead *et al*., 2013), perhaps as a result of the formation of strong Fe-binding ligands, which preferentially incorporate the heavier Fe isotopes (Dideriksen *et al.*, 2008; Morgan *et al.*, 2010). The $\delta^{56}Fe$ values of surface waters from the coastal stations sampled in this study are somewhat lower, at -0.11 to +0.03 ‰. The slightly lower $\delta^{56}Fe$ values observed in our study may suggest either that atmospheric inputs are low, and/or that the surface waters receive significant quantities of benthic-sourced dFe as a result of upwelling. In support of the former, we note that even though the study area is located in close proximity to the Sahara and Sahel deserts, which deliver large amounts of dust to the North Atlantic Ocean (Kramer *et al.*, 2004; Jickells *et al.*, 2005), dAl concentrations are relatively low at the coastal stations, with surface mixed layer averages of 0.9 nM at stations 4 and 5 and 1.8 nM at station 3. MADCOW calculations (Table 3-2) indicate that the supply of dust to the surface layer at Station 3, 4 and 5 is relatively low (0.022 to 0.250 g m^{-2} y^{-2}). However, Al is very particle reactive and the high amounts of particles in the mixed layer (Figure 3-11) may have led to the removal of large amounts of Al from the dissolved fraction and therefore the calculated dust fluxes may be underestimated.

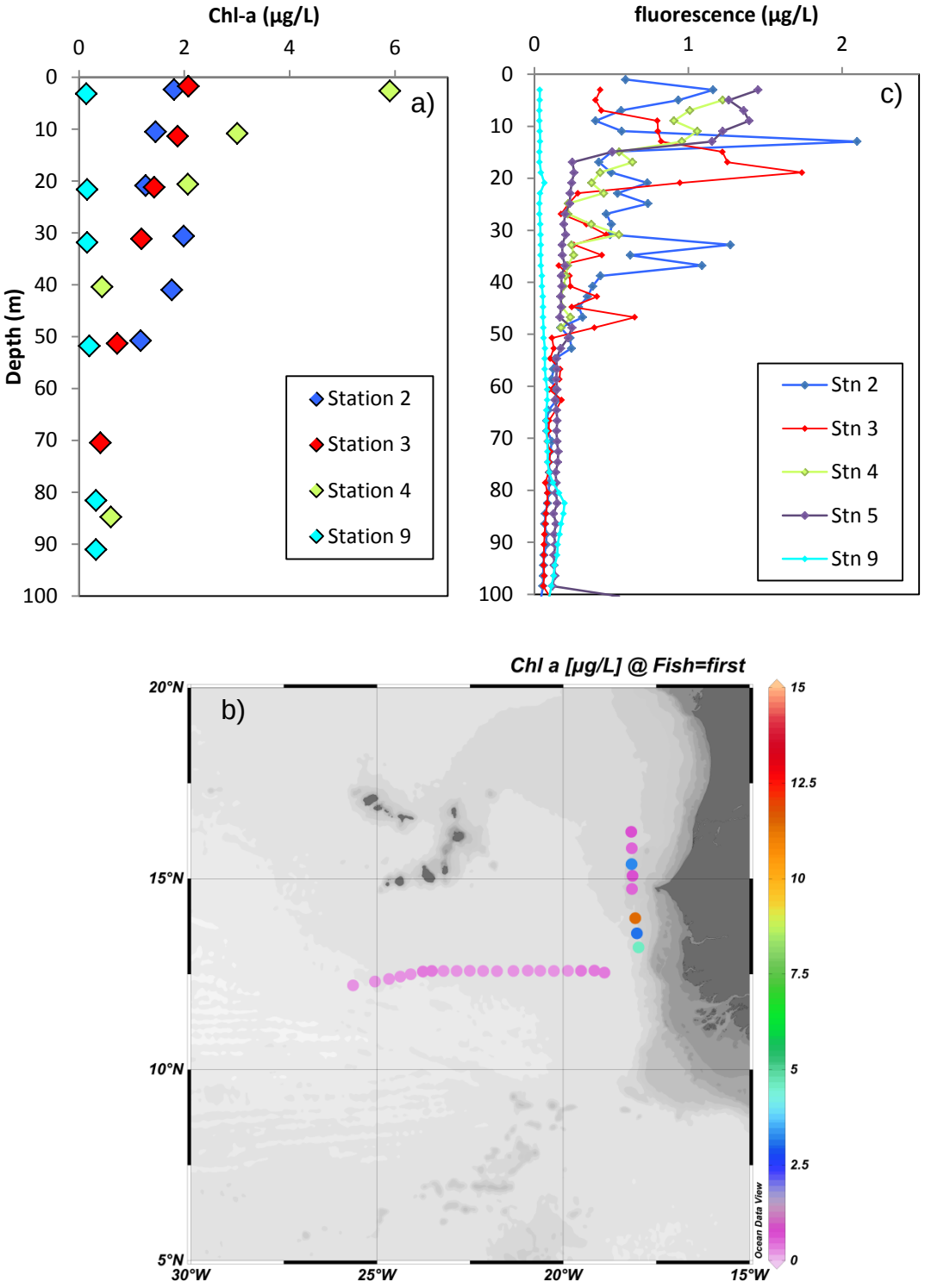

Figure 3-10: Variation in Chlorophyll a concentrations (a) as a function of depth, and (b) for surface waters, (c) variation of fluorescence with depth. All measurements were made using sensors deployed during RRS *Discovery* cruise D361.

Table 3-2: Estimates of dust and dust derived Fe deposition from MADCOW, assuming that the residence time of dAl in surface waters is ~ 4 years (Tria *et al.*, 2007); dust composition is similar to the average continental crust (Taylor, 1964) and the distribution of dAl in the surface mixed layer (SML) is homogeneous.

		1.5 % dust diss.		**5 % dust diss.**		**3.3 % dust diss.**	
Station	**SML depth (m)**	**g dust m^{-2} y^{-1}**	**g Fe m^{-2} y^{-1}**	**g dust m^{-2} y^{-1}**	**g Fe m^{-2} y^{-1}**	**g dust m^{-2} y^{-1}**	**g Fe m^{-2} y^{-1}**
2	15	0.0935	0.00524	0.0281	0.00157	0.0425	0.00238
3	25	0.250	0.0140	0.0751	0.00420	0.114	0.00637
4	15	0.0724	0.00405	0.0217	0.00122	0.0329	0.00184
5	17	0.0820	0.00459	0.0246	0.00138	0.0373	0.00209
6	25	0.380	0.0213	0.114	0.00639	0.173	0.0097
7	55	4.13	0.231	1.24	0.0694	1.88	0.105
8	55	2.19	0.123	0.657	0.0368	0.996	0.0558
9	81	10.5	0.588	3.15	0.177	4.78	0.267

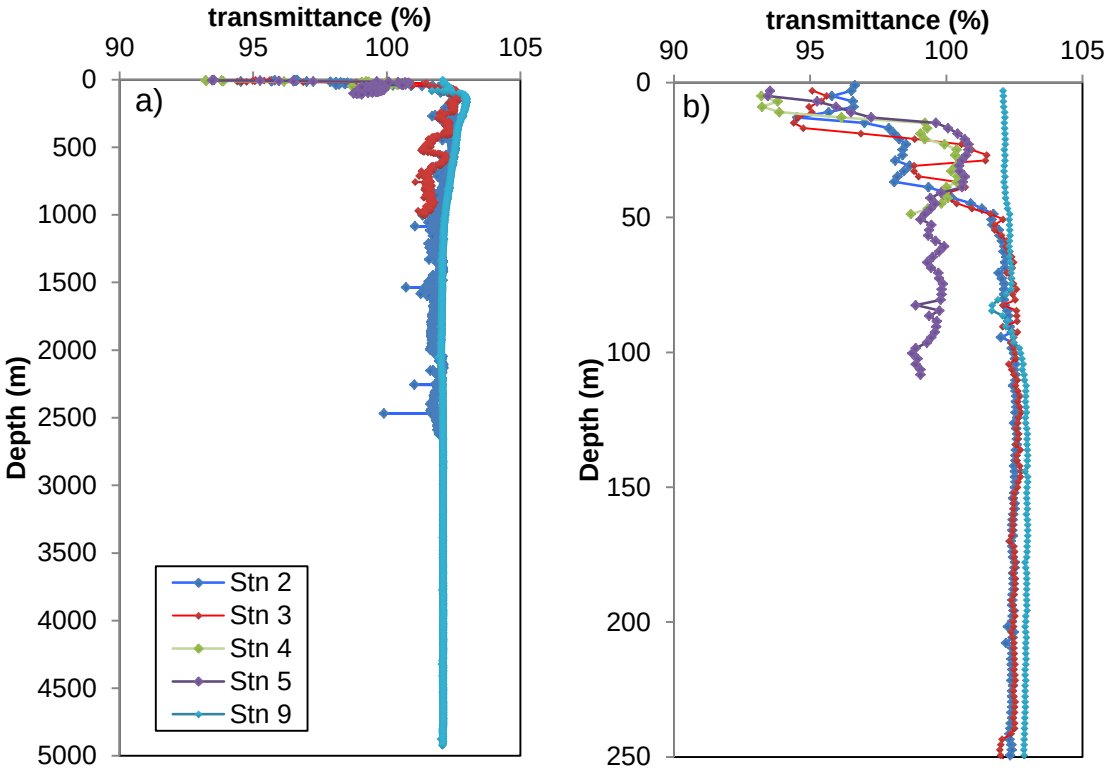

Figure 3-11: Profiles of transmittance for a) full ocean depth and b) the upper 250 m of the water column.

Finally, in addition to input of Fe from aeolian sources and upwelled water, surface waters may be affected by Fe input from lateral mixing with surface water masses, carrying δ^{56}Fe signals from different regions. These include the African Coast Current, which may be carrying dFe sourced north of the study area.

3.5.2 Iron isotopic composition of continental slope and open ocean waters

At Station 9, surface waters between 50 and 80 m depth, both within the surface mixed layer, exhibit positive δ^{56}Fe values of +0.4 to +0.5 ‰ (no surface water samples were analysed for Station 2). No data are available for the top 50 m of the water column, where significant changes in the δ^{56}Fe values are likely. Corresponding dAl concentrations in the surface mixed layer are relatively high at 23.7 nM, which point to relatively high dust deposition in this area, ranging from 3.1 to 10.5 g m^{-2} y^{-1} (Table 3-2). These values are within the range for dust fluxes in the North Atlantic (Jickells *et al*., 2005). However, the δ^{56}Fe values are significantly higher than the average value of the continental crust, or the δ^{56}Fe value of soluble Fe released from aerosols determined in experimental studies (~ +0.13 ‰; Waeles *et al.*, 2007). Nevertheless, as discussed in Section 3.5.1, our results are similar to those reported for surface waters from the North Atlantic Ocean, where δ^{56}Fe values are as high as +0.6 and +0.8 ‰ and have been attributed to the ligand-mediated dissolution of aerosol-derived crustal material (Conway and John 2014). Levels of biological activity at Station 9 are significantly lower than they are at the coastal stations (Figure 3-10 and Figure 3-11), but uptake of lighter Fe isotopes for primary production may also contribute to relatively high δ^{56}Fe in the remaining dFe pool, in support of the findings in Radic *et al*. (2011).

Our data provide some evidence for transport of benthic-sourced dFe from the continental shelf. Iron concentrations within the OMZ are relatively high (up to ~ 2 nM at Station 2 and up to ~ 1.5 nM at Station 9) compared to surface and deep waters, but far lower than measured within the OMZ at the coastal stations (up to ~ 6 nM). This indicates that the strength of the benthic source at these

stations is relatively weak, such that internal processes may overprint the Fe isotope distributions. In addition, the δ^{56}Fe signal of the benthic source will be diluted by mixing with water masses carrying distinct δ^{56}Fe signals, and especially by mixing with surface waters with high δ^{56}Fe. The δ^{56}Fe values from close to the top of the OMZ at both stations are slightly lower (-0.06 to +0.19 ‰) than they are in the adjacent water masses (δ^{56}Fe = +0.2 to +0.6 ‰), but higher than values within the OMZ recorded at the coastal stations (~ -0.3‰; Section 3.5.1). This would suggest that advection of shelf waters is contributing to the supply of dFe to the open ocean, at distances of up to ~ 950 km. This is consistent with other studies that suggest that a shelf signal may be observed up to 1000 km outside the OMZ in the open ocean (with O_2 > 160 µmol/kg) (Conway and John, 2014). The transport of coastal waters carrying the light dFe signal may be facilitated through the westward flowing NECC and the nNECC.

At 200 m depth at both stations, δ^{56}Fe values are relatively low (-0.06 ‰ at Station 2 and +0.26 ‰ at station 9) compared to the surface value (+0.48 ‰). As discussed above, this may be a result of lateral advection of shelf waters within the OMZ, but it is also consistent with remineralisation of sinking biogenic particles at this depth. Biological Fe consumption preferentially takes up the lighter isotopes (Radic *et al.*, 2011), so when sinking phytoplankton cells decompose seawater becomes enriched in Fe with a relatively low δ^{56}Fe signal. However, there is still discrepancy in the fractionation of Fe during biological uptake, as Conway and John (2014) suggest the opposite. In support of remineralisation of organic particles, there is an increase in dFe concentrations at the same or similar depth. However, analysis of Th to U ratios in the water column (K. Pabortsava, personal communication) provides no evidence for remineralisation at this depth at either station.

From 200 to 500 m water depth (the core of the OMZ) a gradual increase in δ^{56}Fe is observed at both stations (from -0.06 ‰ to +0.38 ‰ at Station 2 and from +0.26 ‰ to +0.48 ‰ at Station 9), associated with a decrease in dFe concentrations. Removal of dFe may be the result of scavenging or particle settling and aggregation processes. However, Radic *et al.* (2011) report that

both scavenging and particle settling result in minimal fractionation of Fe isotopes, with differences in δ^{56}Fe values of scavenged Fe relative to seawater of < -0.3 ‰, and differences in δ^{56}Fe values of particle-associated Fe relative to seawater of < -0.1 ‰. To properly assess the controls of dFe and δ^{56}Fe in the part of the water column, additional analyses of the Fe isotopic compositions in the particulate and/or the total dissolvable fractions are required.

In waters below the depth of the OMZ, δ^{56}Fe values gradually increase. Between 700 and 1100 m water depth, AAIW is present at both stations, Station 2 and Station 9. The δ^{56}Fe signature of this water mass is ~ +0.1 ‰ at Station 2 (no data are available for Station 9). As discussed in Section 3.5.1, this value is comparable to that measured in AAIW in the Equatorial Pacific (+0.06 and +0.22 ‰; Radic *et al*., 2011). Between 1100 to 3000 m depth NADW is present at stations 2 and 9. δ^{56}Fe values for this water mass are however distinctly different, ~ +0.1 ‰ at Station 2 and +0.55 to +0.61 ‰ at Station 9. The values for Station 9 are similar to those for upper NADW reported in John and Adkins (2012) (~ +0.4 to +0.7 ‰). Moreover, values for both stations are similar to those measured at similar depths in the North Atlantic Ocean by Conway and John (2014). They report δ^{56}Fe values of ~ +0.21 ‰ at ~ 2000 m depth in the for their eastern-most profile over the continental slope at ~ 18° W (vs. +0.12 ‰ at 1700 m depth at Station 2 in this study), and δ^{56}Fe values of ~ +0.7 ‰ at 2000 m depth at 30° W in the open ocean (vs. +0.55 ‰ at 2000 m depth at Station 9 in this study). Considered together, these data may indicate that high dFe (and low δ^{56}Fe) inputs from sedimentary Fe from the shelf and the slope are mixing with NADW at Station 2. Bottom waters at Station 9 feature AABW, which has a similar Fe isotope composition to the overlying NADW (+0.56 ‰). δ^{56}Fe values measured in AABW from the North Atlantic at ~ 31° N are slightly lower (~ +0.35 ‰; John and Adkins, 2012). AABW measured in the Southern Ocean at ~ 36° S appear to be lower still (~ +0.2 ‰; (Lacan *et al.*, 2008). Increases in δ^{56}Fe values with depth and with water mass age may be partly explained by scavenging and aggregation processes, which leave the residual dFe pool heavier (Radic *et al*., 2011). The relatively heavy Fe isotope

compositions observed in old water masses such as NADW may thus be the result of on-going Fe scavenging and aggregation. A complementary explanation for the Fe isotope composition of NADW (~ +0.5 ‰) is that NADW is dominated by Fe delivered from atmospheric sources (Conway and John, 2014) and high biological activity (Radic *et al*., 2011) as it forms at the surface in the high-latitude North Atlantic.

3.5.3 Comparison of dFe concentrations using isotope dilution vs. FIA

Iron concentrations determined by isotope dilution are more accurate and precise (RSD = 1 to 6 %) than Fe concentrations determined by FIA (RSD = 4 to 11 %). See Chapter 2 for details.

Dissolved Fe concentrations determined using FIA are in good agreement (< 15 % discrepancy) with dFe concentrations using Isotope dilution for concentrations > 2 nM (Table 3-1). However, the discrepancy between the dFe values becomes higher for lower concentration samples (60 to 96 % at 0.4 to 0.7 nM Fe, Figure 3-12). For the FIA analysis, samples were collected in separate 125 ml LDPE bottles and sometimes even from other OTE bottles on the same CTD frame, closed at the same water depths (± 3 m). It is likely that the difference in concentration values may be due to the sample bottles for Fe isotopes having a higher blank than those for FIA. If the disagreement in concentrations was due to the ‘bottle blank’, this would explain the higher discrepancy for lower concentration samples, as the blank would make a greater contribution to the total measured dFe. For dFe concentration < 2 nM > 1 litre of sample was needed, hence doubling or triplicating the blank coming from the sample bottle (because samples are stored in individual 1 L bottles). However, the ‘bottle blank’ has not been determined, as all bottles were used for collecting samples. However, the contribution from the bottle blank should be determined in the future, replicating the sample bottle conditions (i.e., cleaning some new HDPE bottles with the same procedure and storing acidified MQ water in them for a similar amount of time).

In addition, samples for FIA were acidified to pH ~ 2.0, whereas samples for the Fe isotope analysis were acidified to pH < 1.8. Therefore, the discrepancy between dFe concentration measurements may be due to the better dissolution of colloidal phases (including Fe bound to organic ligands) at lower pH, resulting in a higher Fe fraction released during the isotope analysis procedure. In any case, this possibility needs to be further investigated. One way to tackle this problem would be to analyse dFe in the same seawater sample at increasing pH values using NTA resin.

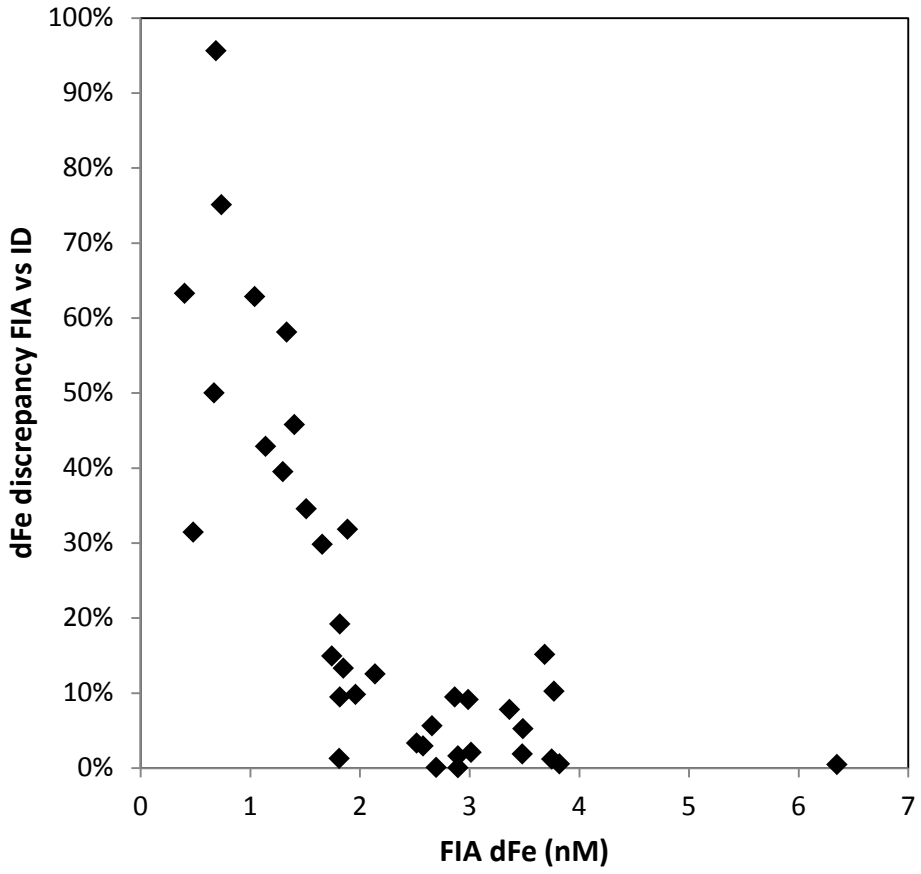

Figure 3-12: Relative discrepancy between dFe concentrations measured with FIA and isotope dilution. % discrepancy = $|dFe_{FIA} - dFe_{ID}| / dFe_{FIA}$

3.6 Conclusions

This study presents isotopic compositions of Fe in the dissolved phase in seawater samples along an E-W transect along ~ 12º N in the Atlantic Ocean. Our data indicate that bottom waters within the OMZ have elevated dFe concentrations and low δ^{56}Fe signatures, as low as ~ -0.3 ‰, which suggests that dFe is principally derived from sediment pore waters that have undergone dissimilatory iron reduction. However, these δ^{56}Fe values are rather higher than those recorded in bottom waters from other regions that have much lower dissolved oxygen concentrations. This is likely due to fractionation during partial oxidation of Fe(II) and Fe(III)-L formation close to the sediment seafloor interface. Moving offshore, concentrations of dFe within the OMZ decrease (from up to 6 nM to about 2 nM), and values of δ^{56}Fe become slightly higher, between ~ -0.1 and +0.2 ‰. Nevertheless, these dFe concentrations and δ^{56}Fe values are respectively, measurably higher and lower than those of adjacent water masses, suggesting that shelf-derived benthic sources of dFe may be transported some considerable distance (approx. 950 km) off the shelf and into the open ocean within the OMZ.

The Fe isotope signal carried within different water masses changes considerably with distance from the shelf, suggesting that Fe fluxes from the shelf are significant. AAIW displays Fe isotope compositions ranging from -0.27 to +0.09 ‰. Fe isotope compositions within NADW shift from +0.04 to +0.61 ‰ between the continental slope and the open ocean. AABW was only observed at one station; it has an Fe isotopic signature of +0.56 ‰ which is indistinguishable from adjacent NADW.

In addition to the identification of different sources of Fe, our Fe isotope data also provide insight into the internal cycling of Fe. Surface waters at the open ocean station have high levels of dAl, which suggests that input of atmospheric dust is significant. However, the Fe isotopic composition of the surface waters (+0.45 to +0.48 ‰) is significantly heavier than the Fe isotopic composition of the continental crust (~ 0 ‰), which suggests that fractionation of Fe isotopes

occurs during dissolution. This fractionation is likely the result of Fe-L complexation of dust-derived Fe and/or biological uptake of Fe in the surface mixed layer. Relatively light Fe isotopic compositions (+0.26 and -0.06 ‰) at 200 m depth on the continental slope and in the open ocean point to remineralisation of sinking organic matter. A shift towards heavier Fe isotopic compositions in deeper waters is likely due to scavenging and particle aggregation processes in continental slope and open ocean profiles.

Chapter 4: Iron isotopes in the dissolved fraction of hydrothermal plumes in the East Scotia Sea

4.1 Introduction

The concentration of iron in high temperature hydrothermal vent fluids is 6-7 orders of magnitude higher than it is in seawater (e.g.; Douville *et al.*, 2002; Gallant and Von Damm, 2006; Klunder *et al.*, 2011; Rijkenberg *et al.*, 2014), and the flux of hydrothermal iron to the oceans (2.3 – 19 $\times 10^{10}$ mol yr^{-1}; Elderfield & Schultz, 1996) is at least as large as the river Fe flux (2.3 $\times 10^{10}$ mol yr^{-1}; Elderfield & Schultz, 1996). However, as the high-temperature, reducing vent fluids mix with cold, oxic seawater after eruption at the seafloor, hydrothermal Fe is thought to be quantitatively removed from solution by precipitation of Fe sulphides and oxides in close proximity to the vents (Field and Sherrell, 2000; Statham *et al.*, 2005). Hence, it is widely assumed that hydrothermal activity is not a major source of Fe. Nevertheless, a number of recent studies, exploring the speciation and size fraction of hydrothermal Fe, have revealed that as much as 46 % of hydrothermal Fe may remain in the dissolved (< 0.2 µm) phase, either in the form of colloids, or as organic complexes (e.g., Bennett, 2008; Hawkes *et al.*, 2013; Hawkes *et al.*, 2014). Some studies indicate that hydrothermal Fe could represent 12 to 22 % of the global deep-ocean Fe budget (Bennett *et al.*, 2008). Furthermore, modelling studies show that observations of dFe distributions in the oceans can only be replicated by models when the Fe flux from hydrothermal sources is included (Tagliabue *et al.*, 2010; Saito *et al.*, 2013).

Hydrothermal vents are found throughout the global oceans (Figure 4-1). They mainly occur along divergent plate boundaries and are associated with plate tectonics and seafloor spreading (German and Von Damm, 2003). Beneath an oceanic spreading axis, asthenospheric mantle is drawn upwards so as to prevent a gap opening between the diverging plates, and seawater (driven by convection) percolates into the newly-formed ocean crust, heating it to > 450 °C

(German and Von Damm, 2003). The heated fluids are then expelled at the seafloor, usually through chimney structures. The chemical composition of hydrothermal fluids is considerably different from seawater (German and Von Damm, 2003). The fluids are depleted in Mg and sulphate (SO_4^{2-}), and enriched in hydrogen sulphide (H_2S). They have low pH (3 – 4), and may be variably enriched or depleted in chloride (Cl^-) if phase separation occurs (e.g., Seyfried *et al.*, 2003). The fluids are enriched in transition metals, especially Fe and Mn, leached from the host rock. Concentrations of Fe in hydrothermal fluids range from < 2 µM to > 10 mM Fe (Douville *et al.*, 2002; Gallant and Von Damm, 2006).

As the hot, buoyant vent fluids are expelled at the seafloor, they mix with ambient seawater and cool, resulting in the precipitation of various mineral phases (sulphides, oxides and carbonates) (Yücel *et al.*, 2011; Gartman *et al.*, 2014). The hydrothermal plume will continue to rise until its density reaches that of background seawater, at which point it spreads laterally, forming the neutrally-buoyant plume (German and Von Damm, 2003), typically at ~ 200 to 300 m height from the seafloor (Bennett *et al.*, 2008; Sands *et al.*, 2012).

Approximately half of the Fe dissolved in the vent fluids is precipitated as Fe-sulphide (FeS) in the early stages of mixing (Rudnicki and Elderfield, 1993). Precipitation of Fe-sulphide preferentially incorporates light Fe isotopes, leaving the fluid isotopically heavy (Bennett *et al.*, 2008; Rouxel *et al.*, 2008; Roy *et al.*, 2012). Some portion of the FeS particles may be in the form of colloidal nanoparticles, and these can be transported long distances from their source within the water column (Yücel *et al.*, 2011).

Figure 4-1. Map showing the global distribution of hydrothermal vent fields. The red markers are confirmed actives sites and the yellow markers are unconfirmed. Circles indicate venting along the Mid-Ocean Ridge, triangles indicate venting on arc volcano sites, squares indicate vents along back-arc spreading centres and the diamonds show the location of venting on intra-plate volcanos and any other geological settings not mentioned. The solid black lines represent the ridges and the dotted black lines represent subduction. The light blue areas of the ocean show the boundaries of EEZ's (Exclusive Economic Zone's). This image is from the InterRidge Vents Database.

As the plume continues to mix with oxygen rich seawater, oxidation of Fe(II) to Fe(III) and the formation of Fe(III)-oxyhydroxides occurs. These Fe(III)-oxyhydroxides mainly coagulate and sink out of the rising plume (Field and Sherrell, 2000; Statham *et al.*, 2005), but Fe(III)-oxyhydroxides in the colloidal size fraction (0.02 to 0.2 µm) may be stable in solution and can be transported away from the hydrothermal source (Hawkes *et al.*, 2013). Oxidation of Fe(II) to Fe(III) results in enrichment of the heavy Fe isotopes in Fe(III) (Welch *et al.*, 2003; Anbar, 2004; Balci *et al.*, 2006). The formation of ferrihydrite (HFO) from Fe(II) also favours the heavy Fe isotopes, leaving the ferrihydrite phase up to 3.2 ‰ heavier than the remaining Fe(II) (Wu *et al.*, 2011). However, the ferrihydrite phase is unstable and rapidly transforms into more stable mineral phases.

Part of the Fe sourced from hydrothermal vents may be stabilised in solution through complexation with organic ligands (Bennett *et al.*, 2008; Sander and Koschinsky, 2011; Hawkes *et al.*, 2013). Fractionation of Fe associated with Fe-L formation is poorly understood. Enrichment of heavy isotopes in the Fe-L fraction has been observed during laboratory experiments (Dideriksen *et al.*, 2008; Morgan *et al.*, 2010; Ilina *et al.*, 2013), whereas enrichment of light Fe isotopes in solution has been observed in experiments investigating mineral dissolution in the presence of organic ligands (Brantley *et al.*, 2004).

Iron concentrations in the deep ocean range from 0.2 to 1.2 nM, and slightly higher concentrations (ranging from 1.2 to 1.9 nM) have been reported in waters adjacent to mid-ocean ridges (Klunder *et al.*, 2011; Saito *et al.*, 2013; Conway and John, 2014). A recent study in the North Atlantic Ocean suggests that hydrothermal Fe is associated with relatively low δ^{56}Fe values, possibly as low as -1.3 ‰ (Conway and John, 2014). This δ^{56}Fe value is lower than the range reported for high temperature hydrothermal fluids (-0.64 to +0.28 ‰; (Sharma *et al.*, 2001; Beard *et al.*, 2003; Severmann *et al.*, 2004; Rouxel *et al.*, 2008; Bennett *et al.*, 2009), and it is also lower than the range of δ^{56}Fe values reported for particles within hydrothermal plumes (-0.7 to +1.3 ‰; Severmann *et al.*, 2004; Bennett *et al.*, 2009).

To date, there are no measurements of the iron isotopic composition of the dissolved phase in hydrothermal plumes. This information is clearly critical for identifying hydrothermal sources of Fe in the deep ocean, and for improving understanding about the processes that deliver stabilised dFe from hydrothermal systems to the ocean. This Chapter presents the first iron isotope data set for dissolved Fe in hydrothermal plumes in the Southern Ocean. Crucially, model calculations predict that uptake of hydrothermal Fe increases productivity in this part of the ocean, fuelling up to 20-30% more carbon export (Tagliabue *et al.*, 2010). The hydrothermal plume samples examined here cover a range of geological settings, including a back-arc spreading centre and a submarine island-arc volcano, and the vent fluids have variable chemistry. These data therefore also provide insight as to the controls on the iron isotopic composition of stabilised dissolved Fe.

4.2 Study area

Hydrothermal plumes were sampled at three separate hydrothermal sites. Two of these sites (E2 and E9) are located on the East Scotia Ridge back-arc spreading centre, and the third (Kemp Caldera) is a submarine volcano located on the South Sandwich Island Arc.

4.2.1 East Scotia Ridge

The East Scotia Ridge (ESR) is located in the East Scotia Sea, in the Atlantic sector of the Southern Ocean. The ESR is an actively forming back-arc spreading centre, extending at an intermediate spreading rate of 62 – 70 mm/yr (Livermore *et al.*, 1997; Larter *et al.*, 2003), and it is situated 250 to 300 km west of the South Sandwich Trench, which has been created by the westward subduction of the South American plate beneath the Sandwich Plate (Barker, 1970; German *et al.*, 2000). The ESR is approximately 500 km long and consists of ten second-order ridge segments, from E1 in the north to E10 in the south, separated by non-transform faults. The morphology and composition of central segments of the ESR are very similar to the Mid-Atlantic Ridge, with a rift-like ridge and mid-ocean ridge basalts (Leat *et al.*, 2000; Fretzdorff *et al.*,

2002). These segments show no sign of hydrothermal activity (Livermore *et al.*, 1997). On the other hand, segments E2 and E9 both have axial volcanic ridges (AVRs), likely due to the inflow of mantle melt into the back-arc around the north and the south edges of the slab (Livermore *et al.*, 1997; Leat *et al.*, 2000; Bruguier and Livermore, 2001) and their dominant crustal lithology is basalt to basaltic andesite which may contain a mantle component and a limited subduction component (Leat *et al.*, 2000; Fretzdorff *et al.*, 2002; Leat *et al.*, 2004). Evidence for hydrothermal activity at these segments was discovered in 1999 (German *et al.*, 2000).

The E2 hydrothermal field is located between 56º 5.2' and 56º 5.4' S and between 30º 19.0' and 30º 19.35' W at ~2600 m water depth (Figure 4-2). Several hydrothermal sites are observed at E2: high-temperature venting at Dog's Head and Sepia and diffuse venting at Crab City (James *et al.*, 2014). Dog's Head chimneys are up to ~12 m high and the chimneys vent fluid at temperatures of up to 351 ºC. The Sepia vent site lies 75 m to the southeast of Dog's Head with chimneys up to ~11 m high and vent fluid temperatures up to 353 ºC. Diffuse fluids emanated from the seafloor at Crab City at temperatures varying from 3.5 to 19.9°C.

The chemical composition of key constituents in the hydrothermal fluids is given in Table 4-1. The recorded pH of E2 fluids is as low as 3.02 (James *et al.*, 2014). Endmember (zero Mg) high temperature hydrothermal fluids have chloride concentrations ($[Cl^-]$) of between 532 and 536 mM, similar to local bottom seawater (540 mM). This suggests that the hydrothermal fluids are not affected by phase separation. Concentrations of dFe range from 794 to 1280 µM in the endmember fluids, and concentrations of dissolved Mn range from 2050 to 2220 µM. Concentrations of H_2S (6.7 – 7.1 mM) and fluoride (~ 39 µM) in the endmember fluids are similar to values for basalt-hosted mid-ocean ridge hydrothermal systems (Von Damm, 1990; Kelley *et al.*, 2002), which indicates that input of magmatic volatiles is negligible (James *et al.*, 2014).

Table 4-1: Chemical composition of hydrothermal fluids from the E2 and E9 vent fields on the East Scotia Ridge, and the Kemp Caldera (KC) submarine volcano on the South Sandwich island arc. Temperature is the maximum in situ measured temperature; pH of E2 and E9 fluids is the lowest measured value (total scale, at 25 °C). All other data are zero-Mg endmember concentrations, calculated by extrapolating from the composition of bottom seawater collected at each vent field, through the Mg concentrations measured in the samples from a given vent. E2 and E9 data are from James *et al*. (2014); KC data are from Cole *et al*. (2014).

	Max T (ºC)*	Min pH*	Cl^- (mM)	H_2S (mM)	F (µM)	Fe (µM)	Mn (µM)	Fe:Mn
E2								
Dog's Head	351	3.0	536	6.7	39.1	1280	2050	0.62
Sepia	353	3.1	532	7.1	38.4	1010	2060	0.49
Sepia Flange	313	2.9	517	7.1	39.8	794	2220	0.36
E9								
Black & White	383	3.4	98.2	9.5	34.6	800	199	4.02
KC (Great Wall, Winter Palace, Disney's Toxic Castle)	212	1 ± 1	90 ± 37	200 ± 15	1000 ± 110	nd	660 ± 140	nd

The E9 hydrothermal field is located between 60º 02.5’ and 60º 03.0’ S and between 29º 59.0’ and 29º 58.6’ W at ~2400 m water depth (Figure 4-2). Two high-temperature vent sites have been found to date. These lie along a fissure that runs from north to south (James *et al.*, 2014). The northernmost site, Black & White, consists of chimney structures that are ~10 m high issuing fluids at temperatures of up to 383 ºC. The Carwash site is located < 5 m south of Black & White, and is emitting low temperature fluids. The southernmost site consists of three chimneys emitting fluids with temperatures between 348 and 351 °C. Ivory Towers is located to the north of the site, with a beehive-like venting structure. Approximately 50 m to the south of Ivory Towers, Pagoda and Launch Pad chimneys are found. Several diffuse venting locations (5-19.9°C) have also been observed. The pH of the high temperature vent fluids is similar to E2 (3.08 – 3.42), but concentrations of Cl^- are much lower, ranging from 98.2 mM at Black & White, to 179 mM at Launch Pad and 220 mM at Ivory Towers and

Pagoda. These low Cl^- concentrations are attributed to phase separation of the fluids (James *et al.*, 2014). In support of this, H_2S concentrations are higher at E9 than they are at E2, ranging from 9.5 to 14 mM. Concentrations of dFe in the endmember fluids (800 - 1210 µM) are similar to those measured at E2, whereas concentrations of dissolved Mn (~200 µM) are lower. Fluoride concentrations in endmember fluids are similar to E2, ranging from 34.6 to 54.4 µM. This suggests that input of magmatic volatiles is also negligible at E9 (James *et al.*, 2014).

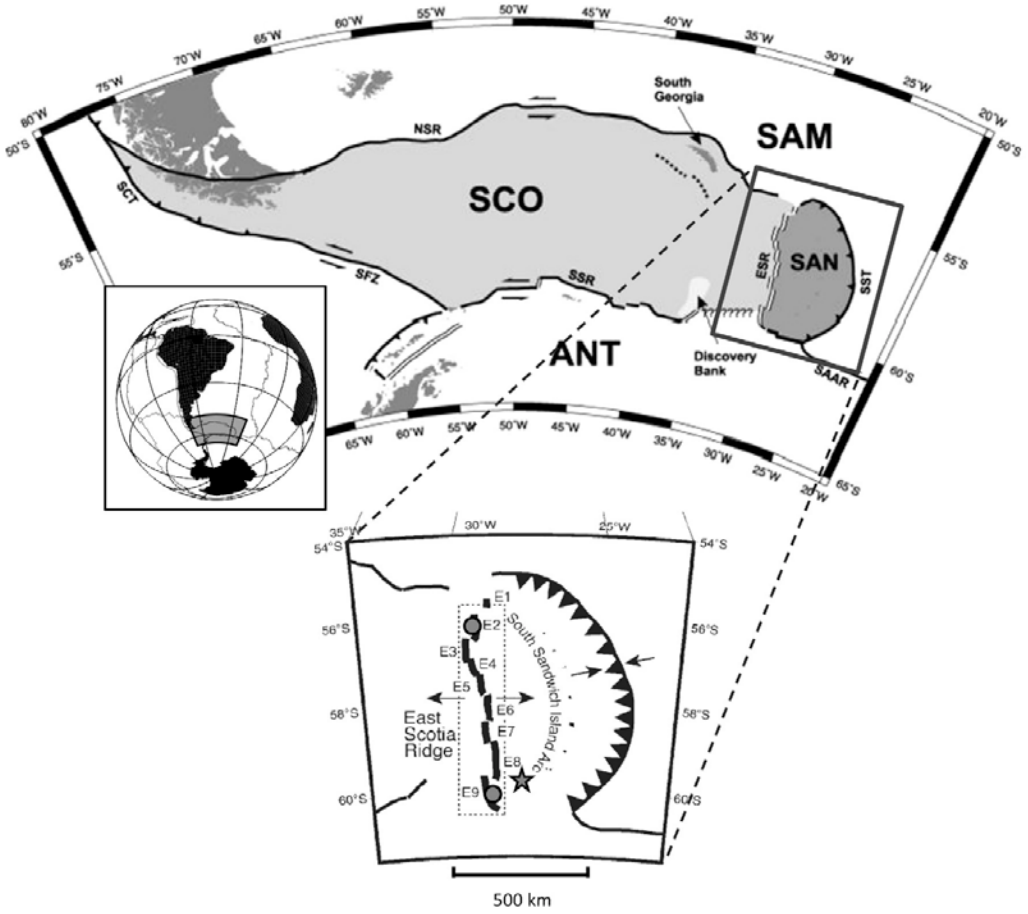

Figure 4-2: Location of the study area, showing the East Scotia Ridge (ESR) and the South Sandwich Island Arc. ESR segments E1 to E9 are labelled and vent fields at E2 and E9 are indicated by the grey circles. Kemp Caldera is indicated by the grey star at the southern end of the South Sandwich Island Arc. SAM: South American plate; ANT: Antarctic plate; SCO: Scotia plate; SAN: Sandwich plate; SFZ: Shackleton Fracture Zone; NSR: North Scotia Ridge; SSR: South Scotia Ridge; SCT: Southern Chile Trench; SST: South Sandwich Trench and SAAR: South American-Antarctic Ridge. Adapted from Cole *et al*. (2014).

4.2.2 South Sandwich Island Arc

The South Sandwich Island Arc is created by the subduction of the South American plate beneath the Sandwich plate (Larter *et al.*, 2003). The volcanic island arc is located in young oceanic crust (8 – 10 Ma), generated by back-arc spreading at the ESR (Leat *et al.*, 2004). The composition of the seven main islands (which extend up to 3 km from the seafloor to the summit) and several smaller islands and seamounts varies from basaltic to rhyolitic (Leat *et al.*, 2004). Kemp seamount is located in the southern end of the South Sandwich Island Arc, ~50 km west-southwest of Thule Island and ~70 km north of the southern subducting edge. Kemp seamount mainly consists of tholeiitic basalt and basaltic andesite with a strong subduction component and minimal sediment-melt influence (Leat *et al.*, 2004). Kemp Caldera is a submarine volcanic crater to the west of Kemp Seamount (Figure 4-2), at 59º 42' S and 28º 18.59' W, at a water depth of ~ 1420 m (Hawkes *et al.*, 2014). Kemp Caldera has a maximum depth of 1600 m, with the sill rising 750 – 850 m above the base and a resurgent cone rising ~ 250 m from the base of the caldera, which hosts sulphide rich hydrothermal fluids (Hawkes *et al,* 2014). Two sites of hydrothermal activity have been identified in this vent field. Winter Palace is located to the west of the centre of the caldera and consists of friable chimneys, expelling white smoker type fluids at temperatures of up to 212 °C. Great Wall is located ~100 m to the northwest of Winter Palace and consists of diffuse venting along a fissure, along which sulphur rich minerals precipitate to form a ~50 cm high 'wall'. The maximum measured temperature of these fluids is 212 ºC, but < 28 ºC during fluid sampling. It is likely that there has been a recent volcanic blow out at Kemp Caldera, as there are large amounts of sulphur and ash deposits covering the floor of the caldera, similar to observations in other calderas (de Ronde *et al.*, 2011; Leybourne *et al.*, 2012).

Although no vent fluids with very low Mg concentrations were collected from Kemp (because of the friable nature of the chimneys), the endmember fluids at Kemp are likely to have low [Cl^-] (~ 90 mM), meaning they are affected by phase separation (Cole *et al.*, 2014). Further, Kemp fluids have very high H_2S (up to ~ 200 mM) and fluoride (~ 1000 µM) concentrations, and low pH (~ 1),

relative to E2 and E9 vent fluids. This is strong evidence that Kemp fluids are affected by input of magmatic volatiles (H_2O, CO_2, SO_2, HCl, HF) (Powell *et al.*, 2011), due to the proximity of the site to the subducting arc (e.g., de Ronde *et al*., 2011). Endmember dFe concentrations cannot be calculated because Fe does not behave conservatively during mixing with seawater, but measured dFe concentrations of up to 2.36 µM were observed in vent fluids. Endmember dMn concentrations are estimated to be ~ 650 µM, but the correlation with Mg is poor.

4.3 Materials and methods

4.3.1 Sample collection

High temperature and diffuse vent fluids, and water samples from the hydrothermal plume, were collected at sea during two cruises, in 2010 (JC042, sampling of E2) and 2011 (JC055, sampling of E9 and Kemp Caldera). Hydrothermal plumes were detected and sampled using a SeaBird +911 CTD on a titanium (Ti) frame, equipped with up to 24 OTE (Ocean Testing Equipment) water sampling bottles, modified for trace metal sampling (fitted with external springs and Teflon taps; and metallic components replaced with Ti). A light scattering sensor (LSS) and a bespoke Eh detector were also mounted onto the frame. The buoyant part of the plume was identified by positive temperature and particle anomalies and a negative Eh anomaly, while the neutrally buoyant plume was identified by a positive particle anomaly and negative temperature and Eh anomalies at 350 - 400 m above the seafloor. The hydrothermal plumes at E2 and E9 are rapidly dispersed by the deep ocean currents. As a result, the plumes sampled at E2 could be sourced from Dog's Head or Sepia, which lie ~ 70 m from each other.

At KC the geographical confinement of the caldera inhibits the dispersion of the hydrothermal plume, but as the vent sites Winter Palace, Great Wall and Disney's Toxic Castle all lay within an area of ~ 200 m, the hydrothermal plume samples in the water column could be sourced from any of the vents. A non-hydrothermal particle plume present at 1000 m depth was also detected and

sampled (called “KC 1000”). A background station (cast 437) was also taken within the Kemp Caldera (called “KC background”), located ~ 2 km to the west from the hydrothermal field, and a control seawater station (cast 434), located approximately 30 km to the west of the vent site, over the Adventure Caldera, was also sampled (called “AC control”).

Upon recovery of the CTD, the OTE bottles were transferred to the clean lab container on board and seawater samples were filtered through a polycarbonate membrane filter (0.2 µm, Whatman) under gentle pressure using filtered oxygen free nitrogen gas and collected in 500 ml acid cleaned LDPE bottles. After filtration of ~ 10 L of seawater through each polycarbonate filter, these were kept for particulate metals analysis (Fe isotope measurements were not determined on these samples). All seawater samples were then acidified to approximately pH 1.9 with thermally distilled nitric acid (Optima, Fisher Scientific). Sample bottles were bagged and shipped back to the NOC for concentration measurements and isotopic analysis.

Vent fluid samples were collected using titanium samplers mounted on the Remotely Operated Vehicle (ROV) *Isis*. Focused vent fluids were collected using Ti syringe samplers, equipped with an inductively coupled link (ICL) temperature sensor at the nozzle tip. Diffuse fluids were collected using a Ti diffuse sampler. This consisted of a pseudo venture tube with a weighted skirt at the base to form a seal at the seafloor. Diffuse fluid sampling was carried out with a Ti syringe introduced at the top of the tube orifice once the temperature reading of the fluids was constant. Once the ROV was recovered on board, the fluids were transferred into 1 L acid cleaned HDPE bottles. The samples were acidified to pH 2 using thermally distilled (TD) nitric acid and shipped back to the NOC, where they were filtered (0.2 µm). Iron isotopes were determined in the filtered fraction.

4.3.2 Iron isotope analysis

All acids used for chemical processing of the samples were thermally distilled and regularly monitored for metal content. MQ water was used for diluting acids and for cleaning. LDPE sample bottles were cleaned for trace metal purposes

using a three step cleaning procedure (2 – 3 days in 2.5 % Decon, 1 week in 50 % HCl and 1 week in 50 % HNO_3). The Teflon filtration unit (Savillex) used during the analytical procedure was cleaned in a similar manner, but the time in the acid bath was increased by a factor of 2. The unit was soaked in a 20 % HCl bath for at least a few hours between uses.

Fe isotopes in the dissolved fraction of hydrothermal plume and vent samples (0.2 µm filtered) were analysed at the NOC following the procedure detailed in Chapter 2. Briefly, a sub-sample was taken into an acid cleaned LDPE bottle, and Fe was preconcentrated from the seawater using the NTA resin batch method. The Fe fraction was then purified by anion exchange chromatography (AG1-X8 resin). The procedure blank, specific for these samples, was 2.5 ± 0.5 ng Fe (n = 6). Sample volumes ranged from 100 to 500 ml for plume samples and ~ 3.5 ml for vent samples.

Isotopic measurements were carried out on a multi-collector inductively coupled plasma mass spectrometer (MC-ICP-MS) (Thermo Fisher Neptune) at the NOC. Instrumental mass bias was corrected using a ^{57}Fe-^{58}Fe double spike and $^{56}Fe/^{54}Fe$ ratios are expressed as $\delta^{56}Fe$ relative to the average $^{56}Fe/^{54}Fe$ value for the iron isotope reference material IRMM-014 determined during the analytical session. The external precision and accuracy were assessed by multiple analyses of two iron isotope standards. The average external precision of the technique is ± 0.07 ‰ (2 SD).

4.3.3 Additional analyses

The salinity (conductivity), temperature and depth (pressure) were measured for each water column profile using a Seabird CTD sensor mounted on the rosette frame. Discrete samples of seawater for salinity analysis were taken from selected OTE bottles on cruise JC055 to cross-calibrate the sensors and to identify miss-fired bottles. This was not done on JC042. The CTD was also equipped with calibrated light scattering (LSS), Eh and oxygen sensors.

The concentration of dissolved and total dissolvable metals (Fe and Mn) was determined by preconcentrating 100 ml of sample by mixed ligand extraction

(Bruland *et al.*, 1979), and analysis by inductively coupled plasma mass spectrometry (ICPMS, Thermo Scientific). These analyses were done by Dr. Jeffrey Hawkes (University of Oldenburg) and are reported in Hawkes (2013). Fe concentrations were used to inform optimum isotope spiking.

4.4 Results

4.4.1 Hydrography

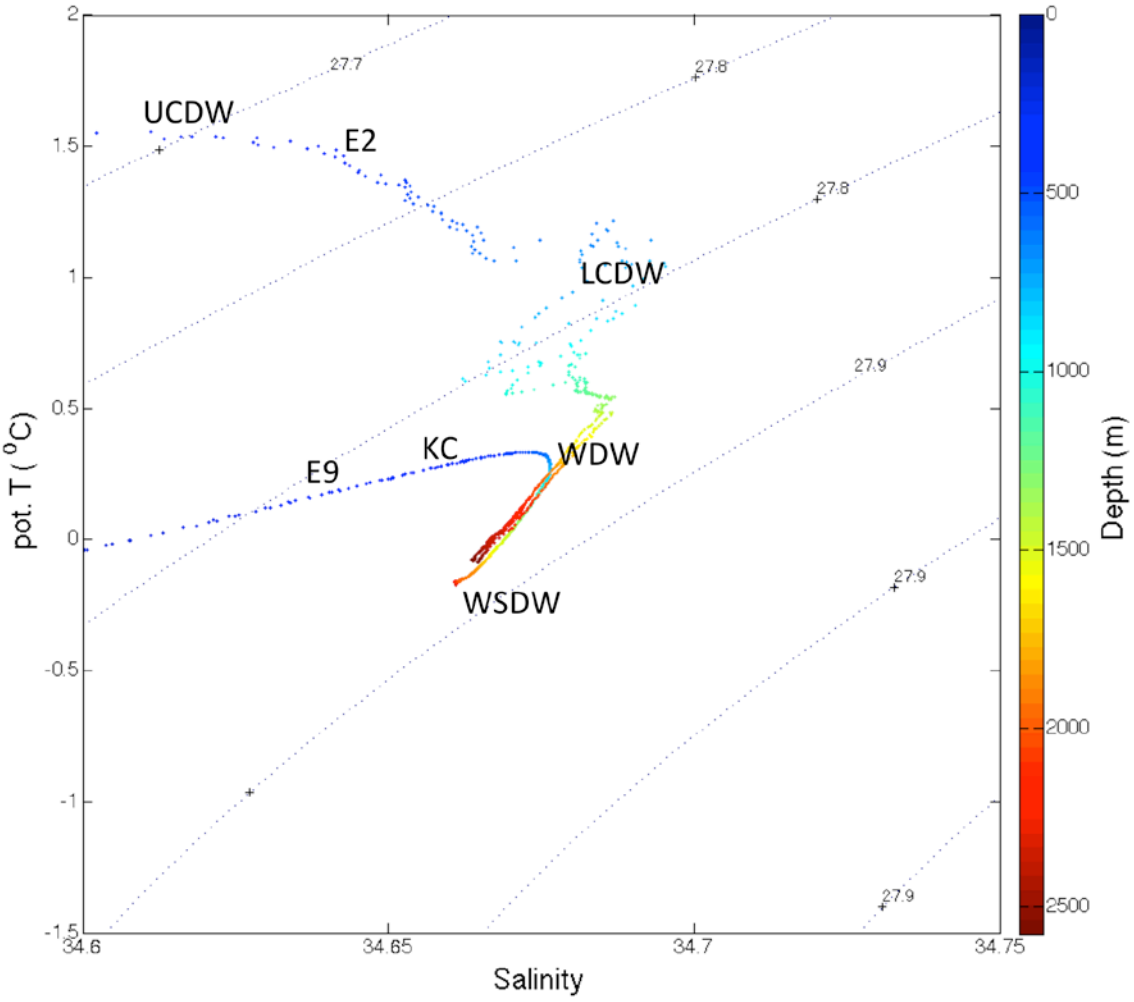

Figure 4-3: Temperature-salinity plot of water column CTD profiles over E2, E9 and Kemp Caldera (KC) vent sites, showing density contours. Water depth is given by the colour scale. Water masses are (Naveira-Garabato *et al*., 2002): Upper Circumpolar Deep Water (UCDW), Lower Circumpolar Deep Water (LCDW), Warm Deep Water (WDW) and Weddell Sea Deep Water (WSDW).

The regional circulation is dominated by the eastward flow of the Antarctic Circumpolar Current (ACC), which enters the Scotia Sea through the Drake Passage (Nowlin *et al.*, 1977). Major strong currents within the ACC associated with the four continuous circum-Antarctic oceanographic fronts are the Subantarctic Front (SAF), the Polar Front (PF), the Southern Antarctic Circumpolar Current Front (SACCF) and the Southern Boundary of the Antarctic Circumpolar Current (SBACC). The SACCF and the SBACC do not have fixed locations away from major topographical constraints, such as the Drake Passage, and are free to move and interact with each other. The locations of the fronts are regionally important as they may influence transportation within the area. In addition to the ACC there is a strong northward component caused by topographic steering and northward outflow waters from the Weddell Sea (Locarnini *et al.*, 1993).

Deep waters formed in the Southern Ocean are transported to lower latitudes, contributing to the cooling and ventilation of the global deep ocean. The upwelling of these waters in other parts of the globe may supply surface waters with nutrients sourced from the Southern Ocean (Rintoul, 1991; Gordon *et al.*, 1992). The Scotia Sea has a large influence on the composition of the deep western boundary currents in the southern hemisphere, mainly in the Atlantic Ocean (Naveira-Garabato *et al*., 2002). Water masses found in the study area are displayed in a potential temperature – salinity plot in Figure 4-3. Weddell Sea Deep Water (WSDW), found below 2000 m water depth at E2 and below 1500 m water depth at E9, is the densest water mass found in the Scotia Sea, with a potential temperature (θ) of -0.7 to 0.2 °C and salinities below 34.70 (Naveira Garabato *et al.*, 2002). WSDW is sourced in the southwestern and western Weddell Sea and then flows northward and eastward following the cyclonic Weddell gyre (Orsi *et al.*, 1993; Fahrbach *et al.*, 1994). Lower Circumpolar Deep Water (LCDW), only observed between 800 and 1200 m water depth at E2, is derived from the North Atlantic Deep Water (NADW) and is characterised by potential temperatures ranging from 0.2 to 1.9 °C and a maximum salinity of > 34.70 (Reid, 1997; Naveira Garabato *et al.*, 2002). The relatively warm and saline composition of the LCDW salinity maximum is attributed to the entrainment of NADW (Naveira-Garabato *et al*., 2002). Only

observed at E2 at water depths > 900 m, Upper CDW (UCDW) is sourced in the Indian and Pacific Oceans and is warmer (1.6 °C < θ < 3.2 °C) and fresher (34.00 < S < 34.71) than LCDW (Callahan, 1972; Naveira Garabato *et al.*, 2002). Warm Deep Water (WDW) is LCDW that enters the Weddell gyre through a gap at 23 to 32 °E in the Southwest Indian Ridge (Orsi *et al.*, 1993). WDW is characterised by relatively lower potential temperature (0.2 °C < θ < 0.6 °C) and salinity (< 34.69) (Naveira-Garabato *et al*., 2002) and is the deepest water mass found at Kemp Caldera. WDW is found between 1500 and 2000 m water depth at E2 and between 500 and 1000 m water depth at E9.

4.4.2 Chemical and isotopic composition of hydrothermal plumes at the ESR

Fe isotope data for the ESR (E2 and E9) hydrothermal plume samples are displayed in Table 4-2 and Figure 4-4. Dissolved Fe concentrations are shown in Table 4-2 and Figure 4-5. The dilution factor of the hydrothermal vent fluid, as a result of mixing with seawater, is calculated as follows:

$$Dilution = \frac{[Mn]_{endmember\ vent\ fluid}}{([Mn]_{plume\ sample} - [Mn]_{seawater})} \qquad \text{Equation 4-1}$$

where [Mn] is the concentration of dissolved Mn. This calculation assumes that Mn behaves conservatively during mixing of the vent fluid with seawater, due to its low reactivity and long oxidation rate in hydrothermal plumes (Rudnicki and Elderfield, 1993). Endmember Mn concentrations are given in Table 4-1; $[Mn]_{seawater}$ is 0.63 nM (average Mn concentration at > 2000 m water depth, ~ 150 km to the west from E9; Hawkes, 2013). It should be noted that this value is significantly higher than previously reported WDW and WSDW Mn concentrations (0.1 to 0.15 nM; Middag *et al.*, 2011).

At E2, nine plume samples covering a wide range of dilutions (3900-37000) were analysed. Only four plume samples were analysed at E9, and the range of dilutions was slightly narrower (5800-35000). δ^{56}Fe values at E2 and E9 show a similar pattern during mixing; δ^{56}Fe values are lowest (-1.19 to -0.76 ‰) during early stages of mixing, sharply increasing and then converging towards higher δ^{56}Fe values of -0.56 to -0.29 ‰ as mixing increases (Figure 4-4). Dissolved Fe concentrations follow a similar pattern. Values are highest (up to 83 nM) in the

least dilute plume samples, and converge towards lower values (as low as 7.3 nM) at higher dilutions (Figure 4-5).

At E2 δ^{56}Fe values range from ~ -1.2 to -0.9 ‰ during the early stages of mixing, and from -0.56 to -0.29 ‰ in the more distal parts of the plume (Figure 4-4). Dissolved Fe concentrations are extremely high (up to 83 nM) relative to background seawater (~ 1.0 to 2.5 nM; Hawkes, 2013) during the early stages of mixing, and converge towards lower values (down to 12 nM) as the plume becomes increasingly diluted by mixing with ambient seawater (Figure 4-5).

The Fe isotopic composition of dissolved Fe in the hydrothermal plume at E9 ranges from -0.76 to -0.23 ‰ at the early stage of mixing, to -0.29 ‰ in the distal parts of the plume (Figure 4-4). At the same time, dFe concentrations decrease from up to 23 nM towards lower values (down to 7 nM) (Figure 4-5).

4.4.3 Kemp caldera vent and plume compositions

δ^{56}Fe values for dissolved Fe in hydrothermal fluid and plume samples from Kemp Caldera are displayed in Table 4-2 and Figure 4-4. Dissolved Fe concentrations for the same samples are displayed in Table 4-2 and Figure 4-5. The dilution of the samples ranges from ~ 12 to > 17000. The two samples with lowest dilutions were taken from hydrothermal chimneys at Winter Palace and Great Wall.

Table 4-2: Results of $\delta^{56}Fe$ analysis of plume samples from the ESR and vent and plume samples from the KC. The reproducibility of $\delta^{56}Fe$ values is two times the standard deviation of replicate analyses of an external standard measured during the same MC-ICPMS session. The total iron concentration (tFe) is the sum of dFe and particulate Fe. Dissolved Fe, dMn and tFe concentrations are from Hawkes (2013). The dilution of the hydrothermal plume is calculated according to Equation 4-1. KC = Kemp Caldera; VF = vent fluid; Pl = Plume; AC = Adventure Caldera; SW = seawater.

Site	Cruise	Sample ID	Lat (°N)	Lon (°E)	Depth (m)	dMn (nM)	Plume dilution	dFe (nM)	tFe (nM)	**$\delta^{56}Fe_{dFe}$ (‰)**	**2 SD (‰)**
E2, Pl	JC-42	3_01	-56.088	-30.319	2586	348	5910	36.1	144	**-0.88**	**0.11**
		3_06			2574	525	3910	83.5	229	**-1.19**	**0.07**
		3_07			2372	112	18300	20.2	173	**-0.75**	**0.07**
		3_11			2277	147	14000	30.9	50	**-0.69**	**0.07**
		5_01	-56.089	-30.319	2567	354	5800	31.6	168	**-1.10**	**0.06**
		7_02	-56.089	-30.318	2272	56	36700	12.1	18	**-0.43**	**0.10**
		7_11			2272	98	21100	14.3	20	**-0.66**	**0.07**
		7_13			2272	58	35500	18.0	24	**-0.56**	**0.10**
		7_17			2272	73	28200	13.1	20	**-0.29**	**0.07**
E9, Pl	JC-55	424_04	-60.043	-29.982	2382	27	7400	14.0	18	**-0.23**	**0.09**
		424_07			2385	35	5800	23.0	27	**-0.76**	**0.06**
		424_10			2144	6	34700	7.31	9	**-0.29**	**0.05**
		424_14			2146	11	19800	10.9	17	**-0.21**	**0.18**

Table 4-1 (cont.)

Site	Cruise	Sample ID	Lat (°N)	Lon (°E)	Depth (m)	dMn (nM)	Plume dilution	dFe (nM)	tFe (nM)	$\delta^{56}Fe_{dFe}$ (‰)	2 SD (‰)
KC, VF	JC-42	147-Y2-01, Great Wall	-59.695	-28.352	1424	22500	29	1.32×10^3		**0.34**	**0.18**
		152-Y1-07, Winter Palace	-59.695	-28.349	1436	55200	12	1.03×10^3		**-0.19**	**0.23**
KC, Pl	JC-55	430_01	-59.695	-28.351	1391	60	11000	17.5	22	**-0.37**	**0.05**
		432_09	-59.695	-28.352	1401	41	16000	11.8	23	**-0.34**	**0.05**
		432_12			1396	58	11400	17.5	18	**-0.24**	**0.08**
		432_19			1391	122	5370	14.5	26	**-0.25**	**0.09**
		432_22			1365	61	10800	12.6	29	**0.01**	**0.05**
		433_01	-59.695	-28.352	986	74	8880	17.9	24	**-0.20**	**0.05**
		437_01	-59.700	-28.317	1395	39	17200	16.5	22	**-0.33**	**0.08**
		437_05			1291	41	16100	14.3	25	**0.11**	**0.07**
		437_21			1172	61	10900	14.9	22	**-0.17**	**0.07**
		438_02	-59.695	-28.351	1066			21.82*		**-0.27**	**0.05**
								21.19*		**-0.18**	**0.10**
		439_11	-59.695	-28.351	1005	73	8980	17.3		**-0.29**	**0.07**
		439_14			912	70	9370	18.7		**-0.19**	**0.07**
AC, SW	JC-55	434_08	-59.709	-27.841	558	7	103000	3.81		**-0.19**	**0.07**

*dFe concentration measured by isotope dilution during isotopic analysis

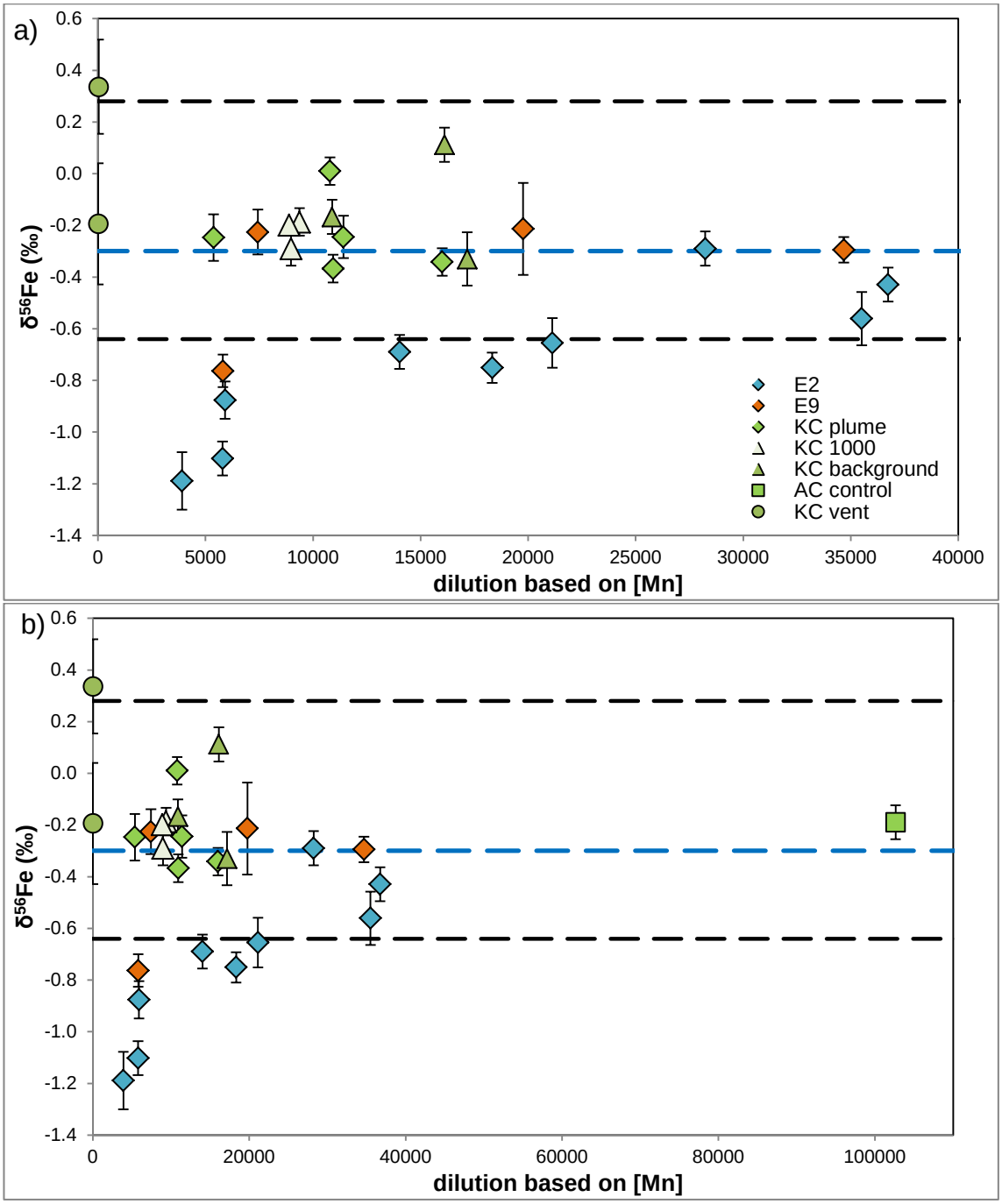

Figure 4-4: $\delta^{56}Fe$ composition of dissolved Fe versus the dilution factor of hydrothermal fluid and plume samples from the ESR and KC. Plot b) is a blow up of a), showing the patterns at low dilution. KC 1000 = non-hydrothermal particle plume sampled at 1000 m water depth over Kemp Caldera. The range of previously reported hydrothermal fluid $\delta^{56}Fe$ values is represented by the dotted black lines (see text for references). The dotted blue line represents the background $\delta^{56}Fe_{dFe}$ composition of WDW (57 °S, 0 °W); (Abadie *et al.*, 2013).

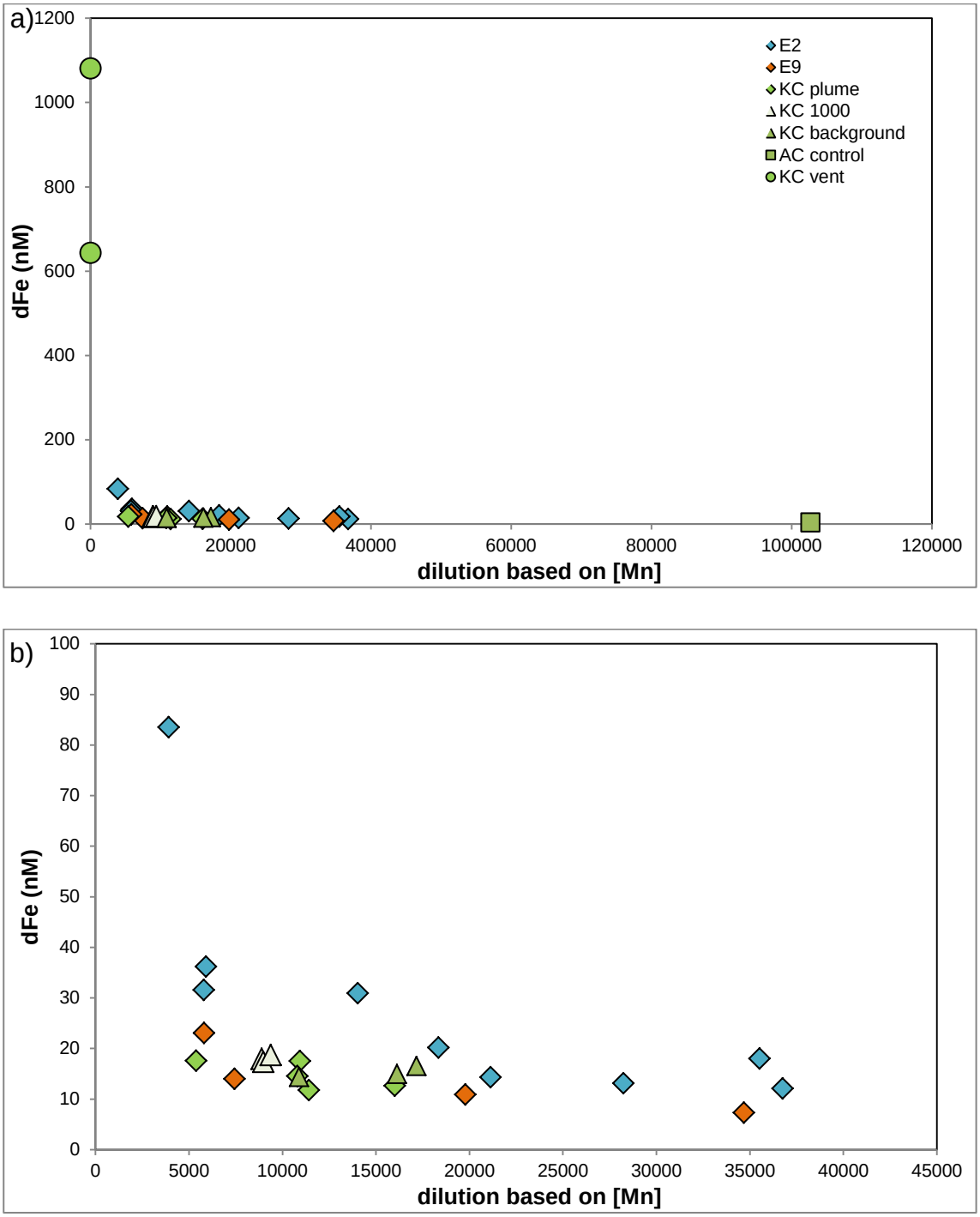

Figure 4-5: dFe concentrations versus the dilution factor of hydrothermal fluid and plume samples from the ESR and KC. Plot b) is a blow up of a) showing the patterns at low dilution.

δ^{56}Fe values for the two vent fluid samples are -0.19 and +0.34 ‰ and corresponding Fe concentrations are 1.03 and 1.32 µM. The plume samples have δ^{56}Fe values from -0.37 to +0.11‰ (Figure 4-4). Dissolved Fe concentrations within the plume at Kemp Caldera are similar to those at the

ESR (between 12 and 18.7 nM, Figure 4-5). There is no obvious relationship between $\delta^{56}Fe$ values and the extent of plume mixing at Kemp Caldera possibly because only one sample was taken at relatively low dilution (< 10000), but the $\delta^{56}Fe$ values are similar to those found in the distal parts of the hydrothermal plume at the ESR. Similar to $\delta^{56}Fe$ values, there is also no pattern between dFe concentrations and the extent of vent fluid dilution. Dissolved Fe concentrations are however similar to those measured in the distal parts of the hydrothermal plume at the ESR.

Samples taken from a particle plume at 1000 m depth were not thought to be associated with hydrothermal venting. However, the $\delta^{56}Fe_{dFe}$ values (-0.29 to -0.19 ‰) are within the range of $\delta^{56}Fe_{dFe}$ values from hydrothermal plumes. The samples taken at the background station (cast 437), which is located ~2 km away from the vent field, have $\delta^{56}Fe$ values ranging from -0.33 to +0.11 ‰ and dFe concentrations between 14.3 and 16.5 nM. A control seawater sample (434_08), taken ~ 30 km to the west of the Kemp Caldera site, has a $\delta^{56}Fe$ value of -0.19 ‰ and a dFe concentration of 3.8 nM.

4.5 Discussion

4.5.1 Behaviour of iron and iron isotopes in the hydrothermal plume at the ESR

Our data indicate that the Fe isotopic composition of dissolved iron in the hydrothermal plume is lightest (down to -1.19 ‰ at E2 and down to -0.76 ‰ at E9) in the early stages of mixing between hydrothermal vent fluids and seawater and becomes heavier as the plume becomes more dilute. Although the Fe isotopic composition of high-temperature hydrothermal fluids from the ESR has not yet been determined, the reported Fe isotope composition in high temperature vent fluids from various mid-ocean ridge sites ranges from -0.64 to +0.28 ‰ (Sharma *et al.*, 2001; Beard *et al.*, 2003; Severmann *et al.*, 2004; Rouxel *et al.*, 2008; Bennett *et al.*, 2009), with an average value of -0.3 ± 0.3 ‰ (1 SD, n=71), which is ~0.46 to 0.89 ‰ higher than the $\delta^{56}Fe$ value measured in these plume samples.

When the hot, acidic and reducing vent fluids come into contact with cold and oxidising seawater, the Fe(II) in the vent fluids precipitates as Fe-sulphide within the first few seconds of venting. Fe-sulphides preferentially incorporate the light Fe isotopes, leaving the dissolved phase enriched in the heavy Fe isotopes (Rouxel *et al.*, 2008; Bennett *et al.*, 2009). Bennett *et al*., (2009) have observed that FeS is 0.60 ± 0.12 ‰ lighter than Fe(II) in the original vent fluid. This process therefore cannot explain the very low δ^{56}Fe values we measure in the early stages of mixing. However, oxidation of Fe(II) to Fe(III) and the formation of ferrihydrite (Fe_2O_3) results in preferential incorporation of heavy Fe isotopes (by up to ~ 3.2 ‰), leaving the remaining dFe pool isotopically light (Wu *et al.*, 2011). This process is therefore likely to be the principal control on the iron isotopic composition of dFe during the early stages of plume mixing. Possible alternative explanations however include: (1) Formation of Fe-L complexes has, in some studies, been shown to favour light Fe isotopes (Brantley *et al.*, 2004). However, other studies suggest that heavy Fe isotopes are preferentially stabilised in ligand complexes (Dideriksen *et al.*, 2008; Morgan *et al.*, 2010) and this is also inferred from measurements of natural samples (Bergquist and Boyle, 2006; Escoube *et al.*, 2009). If light iron isotopes were indeed preferentially incorporated in Fe-L in the proximal part of the hydrothermal plume, then the distal parts of the plume should also have low δ^{56}Fe values, as ligand complexation stabilises the Fe fraction in the dissolved phase. This is not the case. (2) Partial oxidation of Fe(II) may also result in an isotopically heavy Fe(III) phase, leaving the remaining Fe(II) relatively light (Welch *et al.*, 2003; Anbar, 2004; Balci *et al.*, 2006). At the early stages of mixing large amounts of Fe-oxyhydroxides may be precipitating, leaving behind a relatively light dissolved fraction. Welch *et al.* (2003) show that the δ^{56}Fe value of Fe(III) may be up to 2.8 ‰ heavier than Fe(II) during partial oxidation. However, in this case, most of the Fe initially present as Fe(II) is likely to have oxidised to Fe(III) by the time the plume samples were retrieved from the OTE bottles on board the ship; the time interval between sampling and sample processing was > 5 hours (Dr. Jeffrey Hawkes, University of Oldenburg, personal communication), or > 2 Fe(II) oxidation half-lives (Statham *et al.*, 2005). Thus, most of the Fe(II)

will have formed Fe(III)-oxyhydroxides and aggregated into colloids that form part of the 'dissolved' (<0.2 μm) fraction.

As the hydrothermal plume becomes more and more dilute, the Fe isotopic composition of dFe becomes heavier, converging towards $\delta^{56}Fe$ values of between -0.56 and -0.29 ‰. This is consistent with continued Fe oxidation as the plume travels away from its source, forming isotopically heavy Fe(III) colloids that remain in the 'dissolved' fraction (Field and Sherrell, 2000; Bennett *et al.*, 2008; Bennett *et al.*, 2009). Hawkes *et al*. (2013) have shown that ~ 50 % of the dissolved Fe in the plume at the ESR is in the colloidal size fraction (0.02 – 0.2 μm), although these authors note that this may consist of nanoparticulate FeS and Fe-L, as well as Fe(III)-oxyhydroxides.

The transition towards higher $\delta^{56}Fe_{dFe}$ values as the plume becomes more dilute may also be regulated by the formation of organic Fe-L, a process that favours the stabilisation of heavier Fe isotopes (Dideriksen *et al.*, 2008). Organic ligands are produced during microbial dissolution of minerals in hydrothermal systems (Edwards *et al.*, 2004; Homann *et al.*, 2009). The presence of organic ligands and relatively high concentrations of organic carbon have been recorded in diffuse flow areas at a number of hydrothermal sites (Lang *et al.*, 2006; Sander *et al.*, 2007). Hydrothermal Fe may also bind to organic dissolved matter supplied by the cold deep ocean, although the concentration of dissolved organic matter in the deep ocean is relatively low compared to levels of hydrothermal dFe (Hawkes *et al.*, 2013).

A number of other processes occurring in the hydrothermal plume have the potential to affect the Fe isotopic composition of dissolved Fe. For instance, the adsorption and desorption of Fe(II) onto Fe-oxyhydroxides or FeS particles has been shown to favour the heavy Fe isotopes (Icopini *et al.*, 2004; Teutsch *et al.*, 2005; Mikutta *et al.*, 2009). However, it is likely that the adsorbed Fe(II) will be oxidised on the particle surfaces and will not contribute further to the dissolved Fe fraction (Bennett *et al*., 2009).

There are significant differences in the chemical composition of the endmember hydrothermal fluids from E2 and E9. Chloride data suggests that the E9

hydrothermal vent system is affected by subsurface phase separation, and concentrations of Mn are considerably lower in vent fluids from E9. However, the Fe isotopic composition of dFe in the distal hydrothermal plume is similar, suggesting that differences in the chemical composition of the vent fluids are not an overarching control on the δ^{56}Fe value of dFe that may be transported into the open ocean. At lower dilutions (<20000), the δ^{56}Fe value of the plume samples from E9 tends to be higher than the δ^{56}Fe value of the plume samples from E2, which may suggest that a greater proportion of hydrothermal Fe is removed as Fe-sulphides in the early stages of mixing, consistent with higher concentrations of H_2S in the E9 vent fluids (~9.5 mM at E9 vs. 6.7 - 7.1 mM at E2; Table 4-1). However, differences in the availability of organic ligands, water mass compositions and seawater O_2 concentrations, also play an important role.

To date, two previous studies have investigated the behaviour of Fe isotopes in hydrothermal plumes, but these focus on the iron isotopic composition of the particulate, rather than the dissolved, phase (Severmann *et al.*, 2004; Bennett *et al.*, 2009). Figure 4.6 compares the results of our study, with a study conducted at the Red Lion vent field at 5˚S on the Mid-Atlantic Ridge (Bennett *et al*., 2009). Figure 4-6 shows that our data for the dissolved phase, and the Bennett *et al*. (2009) data for the particulate phase, are complementary. As the extent of mixing between the hydrothermal fluid and seawater increases, the δ^{56}Fe value of the particulate fraction decreases and the δ^{56}Fe value of the dissolved fraction increases. This indicates that Fe removed from the dissolved fraction by precipitation is isotopically light, leaving the dissolved fraction enriched in the heavier Fe isotopes. In their study, Bennett *et al*. (2009) argue that isotopically light particulate Fe (which is mainly FeS), incorporates isotopically heavy Fe from the dissolved fraction as mixing progresses, and Fe-oxyhydroxides start to coagulate and precipitate. Thus, these authors suggest that the isotope composition of stabilised dissolved Fe transported to the surrounding ocean is isotopically heavier than the original vent fluid. Our data confirm that dFe becomes heavier during mixing, but not heavier than the original vent fluid.

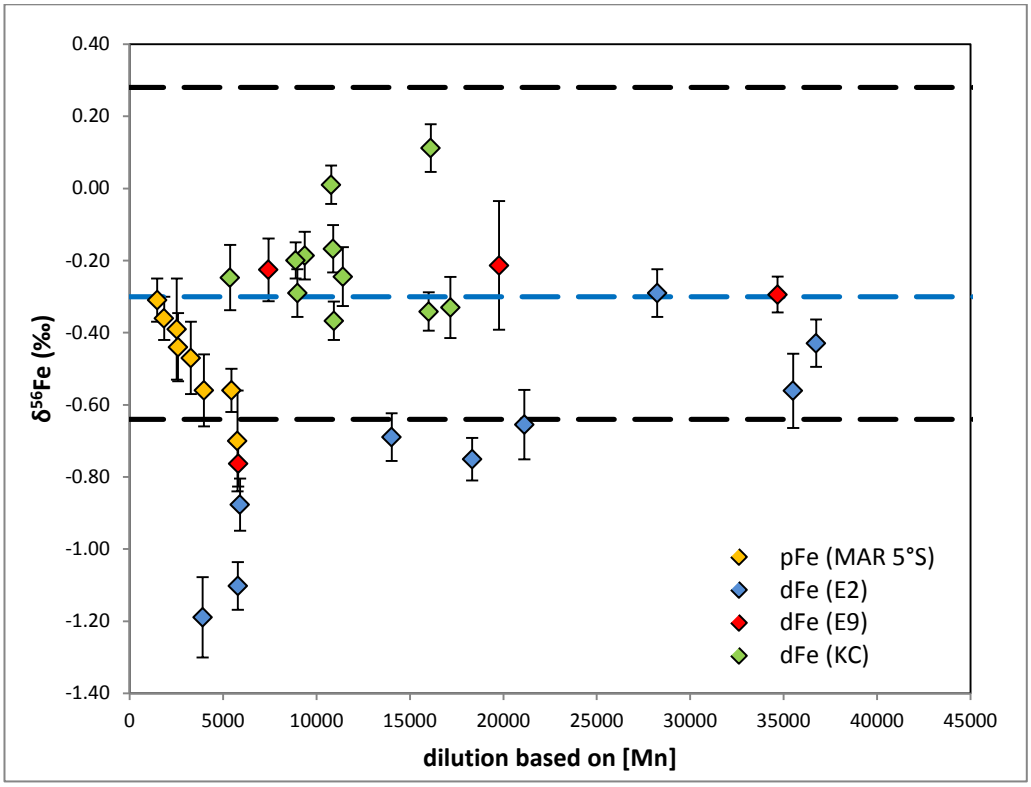

Figure 4-6: Iron isotopic composition of dFe in hydrothermal plumes at the ESR and KC compared to iron isotopic composition of particulate Fe (pFe) in hydrothermal plumes from the Red Lion hydrothermal site, at 5˚S on the MAR (Bennett *et al.*, 2009). The range of previously reported hydrothermal fluid $\delta^{56}Fe$ values is represented by the dotted black lines (see text for references). The dotted blue line represents the background $\delta^{56}Fe_{dFe}$ composition of WDW (57 °S, 0 °W); (Abadie *et al.*, 2013).

Our data indicate that the dissolved Fe fraction in the ESR hydrothermal plumes is most likely stabilised by Fe-L and Fe(III)-oxyhydroxides, and carries a $\delta^{56}Fe$ value ranging between -0.56 to -0.29 ‰. This is within the range of $\delta^{56}Fe$ values measured in high temperature hydrothermal fluids (-0.3 ± 0.3 ‰, 1 SD, n=71; Sharma *et al.*, 2001; Beard *et al.*, 2003; Severmann *et al.*, 2004; Rouxel *et al.*, 2008; Bennett *et al.*, 2009), but it is higher than the $\delta^{56}Fe$ value of hydrothermal Fe inferred from analyses of dFe close to the TAG hydrothermal site on the MAR (-1.35 ‰; Conway and John, 2014). In a separate study, John and Adkins (2012) speculate that high $\delta^{56}Fe_{dFe}$ values (+0.60 to +0.74 ‰) may be the result of input of hydrothermal Fe. While our results are the only direct measurements of $\delta^{56}Fe_{dFe}$ in the hydrothermal plume, it is possible that the $\delta^{56}Fe_{dFe}$ signature of stabilised hydrothermal Fe may vary, depending on the venting system and the surrounding water properties.

4.5.2 Behaviour of iron isotopes in the Kemp Caldera hydrothermal system

The Fe isotopic composition of the Kemp Caldera vent fluids (-0.19 ± 0.23 ‰ and +0.34 ± 0.18 ‰, Table 4-2) is within the range of δ^{56}Fe values reported for high temperature vent fluids (-0.64 to +0.28 ‰; Sharma *et al.*, 2001; Beard *et al.*, 2003; Severmann *et al.*, 2004; Rouxel *et al.*, 2008; Bennett *et al.*, 2009). However, it is important to note that the Kemp Caldera vent fluids contain a significant seawater component (>90 %), and their Mg concentration (48.9 and 49.9 mM), is close to that of ambient seawater (53.51 mM). As previously discussed, this may have resulted in significant fractionation of Fe isotopes relative to the endmember hydrothermal fluid, which is expected to contain zero Mg.

The Kemp Caldera hydrothermal fluids are much more sulphur rich than the ESR fluids (endmember H_2S values are ~ 200 mM for Kemp Caldera and ~ 7 mM for the ESR, Table 4-1). This may mean that large amounts of hydrothermal Fe precipitate as FeS at the seafloor, either as a result of cooling in the subsurface or in the first moments of vent fluid/seawater mixing. The concentration of dissolved Fe in the endmember vent fluid cannot be calculated, but it is likely to be relatively high, as the vent fluids are very acidic, which enables them to carry exceptionally high concentrations of the chalcophile elements, including Fe (Resing *et al.*, 2007; de Ronde *et al.*, 2011; Mottl *et al.*, 2011).

The δ^{56}Fe values of dFe in the hydrothermal plume (-0.37 to 0.01 ‰) are similar to those measured in the hydrothermal plumes at the ESR, although, on average, they are slightly higher at equivalent dilution (Figure 4-4). As discussed above, this may be due to extensive precipitation of FeS during the earliest stages of mixing, which preferentially incorporates the lighter Fe isotopes, leaving the remaining dFe isotopically heavy (e.g. Rouxel *et al*., 2008). In addition, dFe concentrations in the plume are in a similar range to those measured at the ESR at equivalent plume dilutions (Figure 4-5; Hawkes, 2013). This may be because concentrations of dFe are much higher in the endmember hydrothermal fluids at Kemp, maintaining relatively high dFe concentrations in the plume despite extensive precipitation of FeS, or it may be that Fe loss from

the system is minimised at Kemp, because the plume is confined by the caldera.

There is no evidence for any significant change in $\delta^{56}Fe_{dFe}$ values as the plume continues to disperse. As discussed previously, Fe isotope fractionation is likely to be greatest in the earliest stages of mixing, due to formation of Fe(III)-oxyhydroxides and Fe-L. Unfortunately, no samples from this part of the plume were acquired in this study, and as the oxidation half-life of Fe(II) is ~ 0.9 h in the Caldera (Hawkes *et el*., 2014), it is likely that most of the Fe(II) had already been oxidised at the time of sampling.

The hydrothermal plumes at Kemp Caldera are at between ~1260 and ~1400 m water depth, and can be identified by increased light scattering, positive temperature anomalies, an increase in reductive potential (lower Eh) and increased Mn concentrations, but not significantly higher dFe concentrations (Hawkes *et al.*, 2014). Samples (433_01, 438_02, 439_11 and 439_14; Table 4-2) were also taken at ~1000 m water depth, where light scattering increases, but there was no associated change in temperature, Eh, Mn or dFe. This 'particle plume' is thought to be due to resuspension of sediments from the sill of the caldera, rather than hydrothermal processes (Leybourne *et al.*, 2012; Hawkes *et al.*, 2014). However, the $\delta^{56}Fe$ values of dFe in these in these sediment plume samples (-0.29 to -0.18 ‰, average -0.22 ± 0.05, 1 SD, n = 5) are indistinguishable to those collected from the hydrothermal plumes (-0.37 to 0.11, average -0.20 ± 0.17 ‰, 1 SD, n = 8), indicating a similar dFe source. Again, this may indicate that the caldera acts to confine the hydrothermal plume, recirculating, and homogenising the waters within.

As series of water samples were also collected ~ 2 km from the vent field, but still within the caldera (cast 437; Table 4-2), dFe concentrations and $\delta^{56}Fe$ values are indistinguishable from the samples collected over the vent field. However, the concentration of dissolved Mn in these samples is relatively high (39 – 61 nM) compared to background seawater in this part of the ocean (0.63 nM, Hawkes, 2013; or < 0.15 nM in WDW, Middag *et al.,* 2011), suggesting that these samples are strongly affected by hydrothermal inputs. This also supports the idea that dFe supplied to the caldera from hydrothermal fluids is stabilised

and distributed throughout the caldera, due to its topographic confinement, homogenising the Fe isotope signal (Hawkes *et al*., 2014). In contrast, the hydrothermal plumes at the ESR are likely to be rapidly dispersed, due to the relatively flat topography.

Finally, a single seawater sample (434_08) was taken ~30 km to the west of Kemp Caldera, at 558 m water depth (WDW). The $\delta^{56}Fe_{dFe}$ value (-0.19 ‰) of this seawater sample is within the range of the Kemp Caldera plume samples. The concentration of dissolved Mn in this sample is 7 nM is much higher than previously recorded in WDW (Middag *et al.*, 2011), which suggests that the sample is likely to contain a hydrothermal component. Mn concentrations in the Southern Ocean were elevated up to > 550 km south of the Bouvet triple junction suggesting hydrothermal influence (Middag *et al*., 2011). Thus the similar $\delta^{56}Fe$ value may be attributed to transportation of hydrothermally derived dFe with WDW outside the caldera. The seawater $\delta^{56}Fe_{dFe}$ value is in agreement to WDW measured around 57° S and 0° E in the Southern Ocean ($\delta^{56}Fe_{dFe}$ ~ -0.3 ‰; (Abadie *et al.*, 2013), reassuring that hydrothermal dFe may be distributed over large distances in the deep ocean.

The dFe fraction that is stabilised as Fe-L and Fe(III)-oxyhydroxides, provided by the Kemp Caldera hydrothermal fluids thus appears to carry an isotopic signal ($\delta^{56}Fe_{dFe}$ = -0.37 to +0.11 ‰) similar to the ESR hydrothermal plumes. Within the caldera, ~ 46 % of the dFe is in the colloidal fraction, and 10 to 80 % of the Fe is in the labile fraction (Hawkes *et al*., 2014). The labile fraction is the Fe fraction that is bound to weak organic ligands or weakly crystalline mineral phases (Hawkes *et al*., 2013), and it is most likely stabilised in solution. The colloidal and labile Fe fractions may be transported by mixing and diffusion into the overlying water masses, carrying the hydrothermal $\delta^{56}Fe_{dFe}$ signal. The confinement of the caldera possibly results in an accumulation of stabilised dFe, but periodic flushing and horizontal transport due to breaches in the caldera rim may transport dFe into the adjacent ocean (Hawkes *et al*., 2014). The supply of dFe from island arc systems may be an important source of dFe to the ocean (Hawkes *et al*., 2014). Kemp Caldera is probably too deep to have a direct impact on dFe concentrations in the surface ocean layer dFe. However, most of

submarine volcanoes are located at much shallower depths (< 150 m; Hawkes *et al*., 2014) and are likely to make an important contribution of dFe to the photic layer, especially at high latitudes where the mixed layer depth is deeper.

4.6 Conclusions

This is the first study of Fe isotopes in hydrothermal systems at high latitudes, where venting (especially from submarine island arc volcanoes) is thought to play a major role in supplying Fe to the ocean. Island arc volcanoes are more acidic and sulphur rich than conventional black smokers, but the $\delta^{56}Fe$ values of vent fluids from Kemp Caldera, -0.19 and +0.34 ‰, fall within the range of previously reported values for mid ocean ridges (Figure 4-7).

Our analyses of the Fe isotopic composition of dFe in hydrothermal plumes in the East Scotia Sea show that in the early stages of mixing between hydrothermal vent fluids and seawater, $\delta^{56}Fe_{dFe}$ values are very low, down to -1.19 ‰, which can be attributed to precipitation of ferrihydrite, which enriches the dFe pool in the lighter Fe isotopes.

As mixing progresses, $\delta^{56}Fe_{dFe}$ values increase, reaching a plateau of between -0.56 and -0.29 ‰. Enrichment of heavy Fe isotopes in the dissolved phase may be due to the formation of Fe-L that preferentially incorporate the heavy Fe isotopes, or the formation of colloidal Fe(III)-oxyhydroxides from Fe(II), or a combination of both. As the $\delta^{56}Fe$ values are relatively stable in the distal part of the hydrothermal plume, this strongly suggests that the dFe is stable, such that the $\delta^{56}Fe$ signature of dFe delivered to the open ocean will also be in the range -0.56 and -0.29 ‰. To fully understand the fractionation processes occurring within the hydrothermal mixing, $\delta^{56}Fe$ measurements for several size fractions in the same plume samples are needed and over a wider range of plume dilutions.

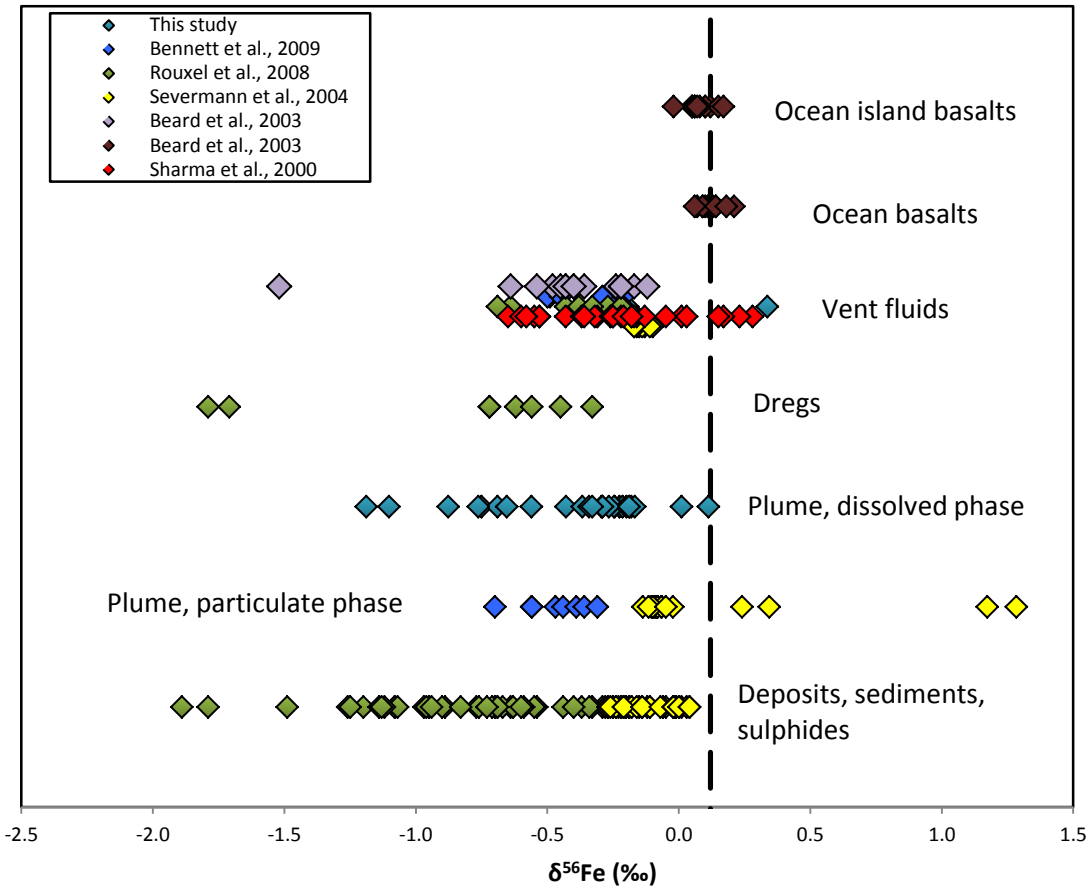

Figure 4-7: Compilation of $\delta^{56}Fe$ values reported for different components of hydrothermal vent systems. The black dotted vertical line shows the $\delta^{56}Fe$ average of Ocean Basalts (the source of Fe at most hydrothermal vent systems).

At the submarine arc volcano, Kemp Caldera, $\delta^{56}Fe$ values for dFe are similar to the $\delta^{56}Fe_{dFe}$ values in the distal parts of the ESR plumes. In addition, $\delta^{56}Fe_{dFe}$ is also similar both within and outside of the hydrothermal plume at Kemp Caldera, suggesting that the caldera acts to confine the dispersion of the plume, homogenising the dFe delivered through hydrothermal venting. Transport through breaches in the caldera rim and sporadic flushes of the caldera may distribute this dFe into the adjacent deep ocean.

More work is required to fully understand the processes that regulate Fe isotope fractionation processes in hydrothermal plumes. These include analyses of the iron isotopic composition of the high-temperature hydrothermal fluids in the East Scotia Sea, and analyses of different size fractions in the hydrothermal plume, especially during the initial stages of mixing between the hydrothermal vent

fluids and seawater. High resolution $\delta^{56}Fe$ profiles in the water column over the ESR and Kemp caldera vent sites, and in the adjacent waters, will provide better insight as to the extent of transport of hydrothermally derived dFe into the open ocean.

Chapter 5: Conclusions and Recommendations for Further Work

The biogeochemical cycle of Fe in the ocean is closely linked to the global carbon cycle, due to its involvement in marine photosynthesis. For this reason, the study of Fe distributions and behaviour in seawater is a key research priority. This is not straightforward, because the behaviour of iron in seawater is complex and Fe is involved in numerous simultaneous chemical reactions, and the information obtained from Fe concentration measurements in seawater is insufficient to disentangle them. To improve global climate model simulations of past and future climate change it is crucial to constrain the fluxes of supply and removal of Fe to the oceans more precisely. As the different sources of Fe, and the processes that affect Fe distributions, are characterised by unique Fe isotope signatures, measurement of the Fe isotopic composition in seawater can be expected to provide an improved understanding of the marine Fe cycle. Moreover, quantifying the distribution of Fe and its isotopes in the ocean is a key goal of the international GEOTRACES project.

Analytical and technological advances in recent years have made it possible to make Fe isotope measurements in seawater at the required precision and accuracy. However, the necessity for a contamination free and high recovery Fe separation technique from seawater, and for correction of induced isotope fractionation, make this a challenging task. The main aims of this thesis were to set up and validate a low blank technique for analysis of Fe isotopes in seawater samples with low Fe concentrations, and to apply this technique to explore the sources and internal cycling of Fe isotopes in (i) the oxygen minimum zone, and (ii) hydrothermal systems, in the Atlantic Ocean.

5.1 Key goals and findings

5.1.1 Methodology for the analysis of Fe isotopes in seawater

To date, only a few laboratories worldwide have been able to measure Fe isotopes in low-concentration seawater samples (Lacan *et al.*, 2008; John and

Adkins, 2010; Lacan *et al.*, 2010; Rouxel and Auro, 2010; Conway *et al.*, 2013). The clean laboratory and instrument facilities available at NOC have enabled the set-up of a low-blank, double-spike technique for the precise and accurate determination of the Fe isotopic composition in low concentration seawater samples, which is presented in Chapter 2 of this thesis. This technique has been fully validated by the analysis of clean seawater doped with isotope standards; replicate analyses of natural seawater samples; and intercalibration exercises with François Lacan's laboratory (LEGOS, Toulouse), all of which confirm accuracy and precision of my δ^{56}Fe measurements for low Fe concentration samples.

Briefly, the protocol for analysis of Fe isotopes in seawater is as follows: (i) Fe is preconcentrated from seawater using NTA resin in a batch or a column method. (ii) Fe is purified by anion exchange chromatography, using AG1-x8 resin. (iii) Fe isotope ratios are determined by high-resolution multi-collector inductively coupled plasma mass spectrometry (Thermo Fisher Neptune).

This technique effectively separates Fe from the seawater matrix, including isobaric elements (Cr and Ni), with a high Fe recovery (> 90 %). The blank associated with the Fe separation and purification steps (1.7 to 2.3 ng Fe) is similar to that reported by other groups (Lacan *et al*., 2010; John and Adkins, 2010; Conway *et al*., 2013), enabling the accurate and precise measurement of Fe isotopes in 1 L of seawater that has an Fe concentration of > 0.8 nM, or even lower for larger sample volumes.

The measurement of Fe isotopes is carried out on an MC-ICP-MS, using a double spike technique to correct for mass fractionation effects. The optimal isotope spike composition was determined by model simulations, and consists of 47 % of ^{57}Fe, 53 % of ^{58}Fe and < 0.5 % of ^{54}Fe). The addition of a small amount of ^{54}Fe is an improvement to existing double spike techniques. Measurements are carried out at high mass resolution ($m/\Delta m \sim 9000$) to effectively separate argon oxide and nitride interferences from Fe (and Cr) signals. The reproducibility of δ^{56}Fe values is 0.06 to 0.07 ‰, 2 SD, as indicated by replicate analyses of two different Fe isotope standards.

5.1.2 Behaviour of Fe isotopes in the Atlantic Ocean

The techniques developed for the analysis of Fe isotopes in seawater are applied in Chapters 3 and 4. Chapter 3 presents $\delta^{56}Fe_{dFe}$ data for seawater samples collected during a UK GEOTRACES cruise to the (sub)tropical North Atlantic Ocean. The aim of this study was to investigate the source of the elevated dFe concentrations in the oxygen minimum zone (OMZ) in the subsurface waters by measuring the Fe isotopic composition in the dissolved phase along an ocean transect at ~ 12 °N, from the African coast to the open ocean. The cycling of redox sensitive elements, such as Fe, is distinct within oxygen low waters, and as OMZs are found in large parts of the ocean, it is essential to understand the processes regulating Fe within OMZs. The $\delta^{56}Fe$ results suggest that elevated dFe in shelf waters within the OMZ is due to the supply from the sediments that have undergone dissimilatory iron reduction (DIR), as $\delta^{56}Fe_{dFe}$ values are lower in the OMZ (down to -0.3 ‰) then they are in adjacent water masses. DIR produces dFe with a light isotopic composition (Severmann *et al.*, 2006; Homoky *et al.*, 2009; Severmann *et al.*, 2010). Our data indicate that the Fe(II) delivered from sediments is either partially oxidised to Fe(III), and/or forms Fe-L, as it is advected upwards into the water column, shifting $\delta^{56}Fe_{dFe}$ towards higher values. Low $\delta^{56}Fe_{dFe}$ values persist in the OMZ up to ~1000 km from the continental shelf, into the open ocean. Benthic sourced dFe may have a significant impact on primary production in the surface ocean if it is made accessible through deep winter mixing, upwelling, diffusion or advection.

The North Atlantic Ocean receives large amounts of aerosol deposition, which supplies Fe to surface waters (Jickells *et al.*, 2005). In support of this, concentrations of dAl are high in surface waters, especially in those further from the continental shelf (up to 27 nM). The corresponding $\delta^{56}Fe$ values for surface waters (up to +0.48 ‰) are, however, significantly higher than bulk silicate Earth (+0.10 ± 0.11 ‰), indicating that dust derived Fe is fractionated during dissolution, either due to Fe-L formation and/or biological uptake. The remineralisation of sinking biogenic particles is associated with relatively low $\delta^{56}Fe_{dFe}$ values at ~ 200 m depth in the open ocean sites.

The Fe isotopic composition of intermediate and deep waters in this region has also been established. There are gradual changes in $\delta^{56}Fe_{dFe}$ in the same water mass between the shelf towards the open ocean, suggesting that benthic sources of Fe may be significant not only within OMZ waters. AAIW displays lower $\delta^{56}Fe_{dFe}$ values (~ +0.1 ‰) than NADW and AABW (~ +0.6 ‰). The iron isotopic composition of NADW and AABW may be affected by scavenging processes.

In addition to atmospheric dust deposition and sediment dissolution, hydrothermal vents are also thought to play a key role in the biogeochemical cycle of Fe in the ocean (Bennett *et al.*, 2008; Tagliabue *et al.*, 2010; Saito *et al.*, 2013). Although most of the Fe supplied by hydrothermal fluids is lost by precipitation of sulphide and oxide mineral phases in the early stages of mixing with seawater, a significant amount of Fe may be stabilised in the dissolved phase and transported into the deep ocean. The Fe isotopic signal of hydrothermal vent fluids is distinct from other sources and may therefore be a useful tool to trace hydrothermally sourced dFe in seawater and to improve flux estimates. To date, however, the Fe isotopic signature of dFe in hydrothermal plumes, which is potentially transported to the open ocean, is unknown. Chapter 4 presents the first study of $\delta^{56}Fe_{dFe}$ in hydrothermal plumes in the East Scotia Sea (Southern Ocean), which hosts hydrothermal activity in unusual back-arc and island arc settings, which display remarkably diverse fluid chemistries (Cole *et al*., 2014; James *et al.*, 2014).

$\delta^{56}Fe_{dFe}$ values measured in the in ESR hydrothermal plumes are as low as -1.2 ‰ in the early stages of mixing between hydrothermal vent fluids and seawater, and increase as mixing increases, converging to values of between -0.56 and -0.29 ‰. This is the signal that is delivered to the open ocean, and it is thought to be stabilised in the form of Fe-L and colloidal Fe(III)-(oxy)hydroxides. The low $\delta^{56}Fe_{dFe}$ values in the early stages of plume formation are attributed to the formation of ferrihydrite. $\delta^{56}Fe_{dFe}$ values found within and outside of the hydrothermal plume in the vicinity of the submarine arc volcano, Kemp Caldera, are within the same range as this measured in the ESR plumes. The homogeneity of the Fe isotopic composition within and outside of the

hydrothermal plume indicates that dFe supplied by hydrothermal activity is distributed and confined by the topography of the caldera.

Hydrothermalism may be an important source of dFe in the Southern Ocean because: (i) Fe delivery from atmospheric dust deposition is scarce, leading to Fe limitation and HNLC conditions, as indicated by excess macronutrients in surface waters; (ii) compared to lower latitudes, dFe supplied to the deep ocean by hydrothermal vents may be more effectively accessed due to the relatively deep winter mixing; (iii) dFe supplied from hydrothermal vents may be transported to the surface Southern Ocean though upwelling, which is extensive in this region; (iv) transport and upwelling of deep water masses formed in the Southern Ocean at lower latitudes may deliver hydrothermally sourced dFe. Our new Fe isotope data indicate that hydrothermal Fe has a unique isotope signature that should enable us to track its movement in future studies of the distribution of iron isotopes in the Southern Ocean.

5.2 Recommendations for further work

There are a number of ways in which methodologies for the analysis of Fe isotopes in seawater could be further enhanced. Firstly, the NTA resin used to preconcentrate Fe from seawater requires considerable cleaning to reduce the Fe blank. Improvements in the manufacture of this resin, and further experimentation with regards to cleaning procedures, may help to improve this situation. Secondly, some studies (Conway *et al*., 2013) have shown that it is possible to achieve a blank as low as 0.3 ng Fe for separation of Fe from the seawater matrix, enabling the analysis of the Fe isotopic signature of seawater samples with very low Fe concentrations (i.e., ~ 0.1 nM Fe) and also reduced volume of sample. Surface waters in the Southern Ocean can have < 0.05 nM Fe (Dr. Christian Schlosser, GEOMAR, personal communication). It may be possible to further reduce procedural blanks by monitoring particle counts in the clean lab, and monitoring Milli-Q water quality more closely. Although most of the components used in the techniques presented in this thesis were constructed from Teflon (PTFE, FEP or PFA), there are some non-Teflon components that could be replaced.

If more time were available, the iron isotopic composition of the high temperature hydrothermal vent fluids from the ESR would have been determined. Although Fe isotope measurements are not limited by the amount of Fe in the sample (vent fluids have high concentrations of Fe, in the mM range), it is critical to ensure that all Fe(II) in the vent fluids is oxidised to Fe(III) for effective equilibration with the iron isotope spike. Furthermore, the Fe isotopic composition of any particles that may have formed during recovery of the samples needs to be quantified, in order to reconstruct the isotope composition of the original vent fluid.

In order to improve understanding of the internal processes that affect dFe distributions in the oceans, future studies should investigate iron isotopes in other size fractions. These should include soluble (sFe), colloidal (cFe) and particulate (pFe). This would provide critical information as to how Fe isotopes are distributed between the different size fractions and which factors control this distribution.

In the future, this work will be extended to the analysis of further samples from both study areas, the (sub)tropical North Atlantic Ocean (GA06, cruise D361) and the East Scotia Sea. From the UK GEOTRACES section GA06, replicate samples are available, which could be used for intercalibration with other labs. We also have an additional full depth water profile along the ~ 12 °N transect, that is located further offshore, as well as samples from a ‘control’ profile outside of the OMZ, at ~ 3 °S, within the southern (sub)tropical gyre (Figure 5-1). The dFe concentrations in these samples range from 0.2 to 1.7 nM and ~ 3 L of water is available. The procedural blank needs to be lowered to measure the samples with lowest dFe concentrations.

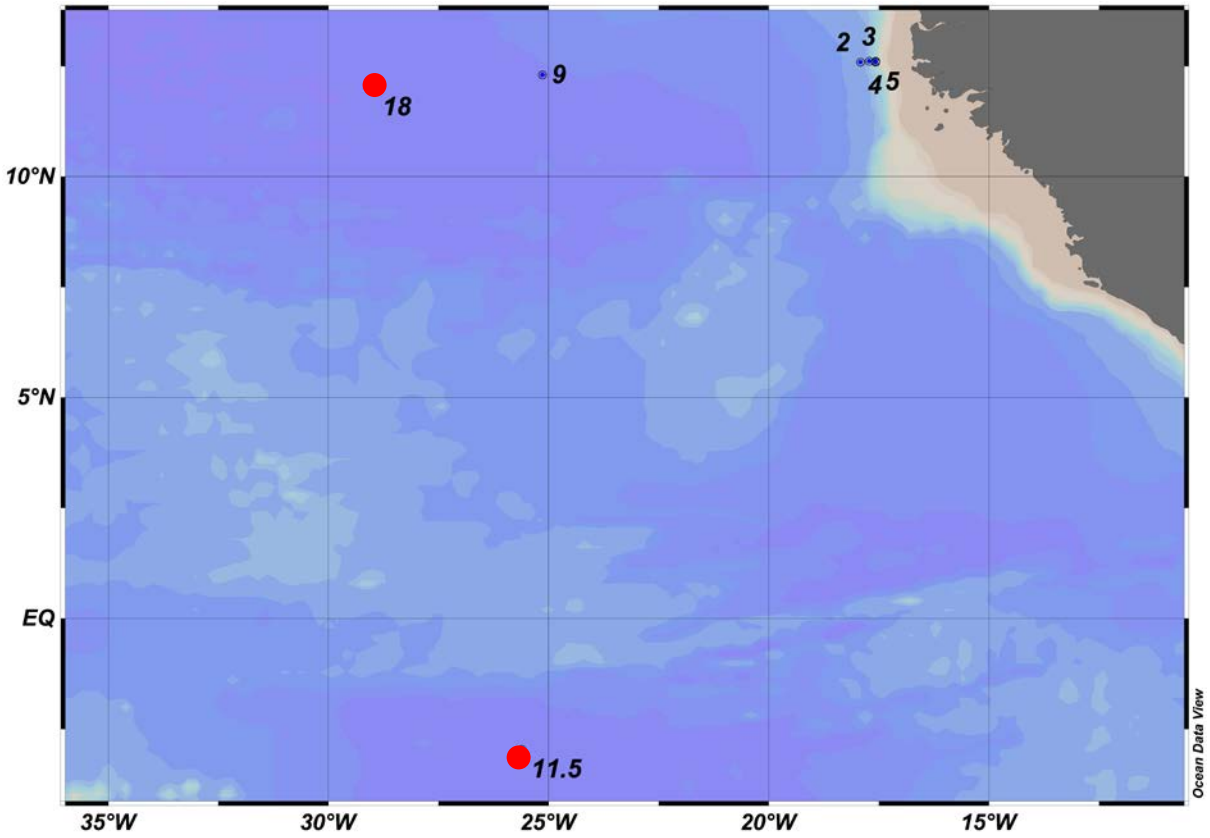

Figure 5-1: Map showing analysed and additional samples (red dots) available for Fe isotopic analysis in the (sub)tropical Atlantic Ocean.

A whole variety of additional samples are also available for the ESS hydrothermal systems. These include a large number of plume samples in the dissolved and in the particulate phases, at a wide range of vent fluid dilutions. In addition there are several high- and low-temperature vent fluid samples, together with any material that precipitated within the titanium sampler due to cooling during the ROV ascent to the ship, from all vent sites. Chimney material and sediments are also available. The analysis of the Fe isotopic composition of all of these samples would enable us to better constrain the chemical modifications of Fe between the different phases. Moreover, we are in the possession of Southern Ocean seawater samples taken both close to and distal from the hydrothermal vent sites (Figure 5-2). The determination of the Fe isotopic composition of these samples may provide us with insight into the extent of hydrothermal influence to the adjacent deep and surface waters in the Southern Ocean.

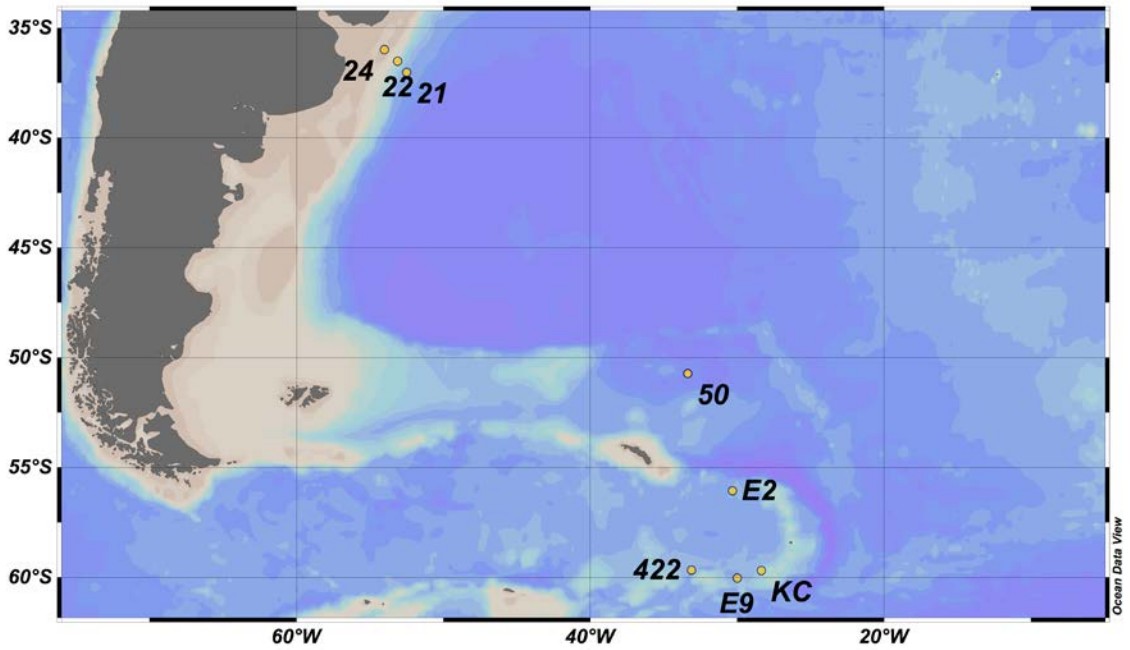

Figure 5-2: Map showing the location of hydrothermal vent sites E2, E9 and Kemp Caldera (KC) and of additional seawater samples in the Southern Ocean.

In addition to the samples mentioned above, a further set of samples is available from UK GEOTRACES section GA 10 (cruise JC 68). Thirty samples of surface seawater were collected along ~ 40 °S in the Atlantic Ocean, for both dissolved (< 0.2 µm) and particulate (> 0.2 µm) Fe. The dissolved Fe concentrations in these samples range from 0.05 to 1.3 nM. In this case the procedural blank also needs to be lowered for the determination of their Fe isotopic composition.

Further international intercalibration exercises are also in the pipeline. These include analysis of 12 seawater samples (0.1 to 430 nM dFe) collected in the North Atlantic Ocean and in the Black Sea, during a GEOTRACES intercalibration cruise and a series of samples from Station 21 in the South Atlantic (shown in Figure 5-2), which were collected in collaboration with Seth John's laboratory (University of South Carolina).

Appendices

Appendix A Isotope spike optimization

The isotope spike optimisation was calculated by Dr. Ian Parkinson (University of Bristol). Optimization of the isotope spiking technique is based on the minimization of the precision of the deconvolved isotope composition via optimizing the isotopic composition of the spike and optimizing the sample to spike ratio. To assess the benefits of various Fe isotope combinations for the optimal spike a series of mathematical model simulations similar to Rudge *et al.* (2009) have been undertaken. The models look at the likely precision that can be produced for each spike for a given set of ion beam size, collection time and electronic background. How the effects of varying background on the likely precision of a given spike is looked at separately. Additionally, a model has been produced to estimate how sensitive spikes are to isobaric interferences (Cr and Ni).

The precision for any Fe isotope ratio (*s*) is calculated by using an ion model and assuming that the uncertainty on each isotope has a Gaussian distribution about the mean voltage. The uncertainty for each Fe isotope (in volts) is defined by using an equation such as the one described by (Ludwig, 1986).

$$\sigma^2_{^{5i}Fe} = \alpha^2\left(\frac{1}{t_p}+\frac{1}{t_b}\right)+\beta^2\left(\frac{1}{t_p}\right)^{5i}Fe \qquad \text{(A1)}$$

where t_p is the integration time on the peak, t_b is the integration time on the background, α is the 'dark' noise (e.g. 0.00005 Vs^{-1}), ^{5i}Fe is the signal size of a given Fe isotope in Vs^{-1} and β is a counting statistics term that converts counts to volts, which for a 10^{11} Ω resistor is:

$$\beta = \sqrt{1.6022\times10^{-19}\bullet10^{11}} \qquad \text{(A2)}$$

Equation (1) therefore has two terms, an electronic background that is related to 'Johnson noise' produced by the amplifiers and a counting statistics term or 'shot-noise', which is related to the size of the ion beam.

For each theoretical measurement, 100 sets of 8 second integrations are produced and it is assumed that the total signal is 10 Vs^{-1} of Fe (spike plus

sample). The measurement simulation uses a Monte Carlo method whereby 1000 sets of voltages are produced for each measurement and the voltages are divided to produce the appropriate isotope ratios (in this case $^{56}Fe/^{54}Fe$, $^{57}Fe/^{54}Fe$ and $^{58}Fe/^{54}Fe$). This method has the advantage that it takes into account any co-variation that occurs because of using the same denominator isotope. Therefore, denominator specific solution effects are eradicated (see Rudge *et al.*, 2009; cf. Galer, 1999) and it allows a straightforward comparison of precision. To facilitate comparison of the various models the internal 2s.e. precision for the deconvolved $\delta^{56}Fe$ in ‰ is plotted as a function of the proportion of spike in the measured mixture. Note that the precision in $\delta^{57}Fe$ and $\delta^{58}Fe$ is scaled by mass difference to that on $\delta^{56}Fe$. The simulations are repeated for the full range of sample-spike mixtures, in order to assess the optimal spike compositions. One way of presenting the model outcome is by plotting results against the proportion of the denominator isotope in the mixture via the following mass balance equation

$$R^i_{mix} = X^{ref}_{sp} R^i_{sp} + \left(1 - X^{ref}_{sp}\right) R^i_{nat} \tag{A3}$$

where R^i_{sp}, R^i_{nat} and R^i_{mix} are the true isotope ratios of *i* in the spike, sample and mixture respectively and X^{ref}_{sp} is the proportion of the reference isotope in the mixture. While equation (3) is still used in the double-spike calculations, it is easier to directly compare data for different spikes by plotting the proportion of spike in the measured mixture and a rearranged version of equation (9) from Rudge *et al.* (2009) is used.

$$p = \left(1 + \left(\frac{1}{X^{ref}_{sp}} - 1\right)\left(\frac{1 + \sum_i R^i_{nat}}{1 + \sum_i R^i_{sp}}\right)\right)^{-1} \tag{A4}$$

where *p* is the proportion of spike in the mixture and Σ_i represents the sum over all isotope ratios for the element, not just the three ratios used in the inversion.

Appendix B Double spike data deconvolution

An excel macro spread-sheet, designed by Dr. Ian Parkinson (University of Bristol), was used to deconvolved the sample/spike mixture data obtained from the analyses on the MC-ICPMS. Double spike data is deconvolved using equations similar to those in Albarède and Beard (2004 a,b). The proportion of the reference isotope, X_{sp}^{ref}, contributed to the mixture by the spike when ^{54}Fe is the denominator isotope is defined by

$$X_{sp}^{ref} = \frac{^{54}Fe_{sp}}{^{54}Fe_{mix}} \quad \text{(B1)}$$

For each of the three Fe isotope ratios, ^{56}Fe/^{54}Fe, ^{57}Fe/^{54}Fe and ^{58}Fe/^{54}Fe, mass balance dictates that

$$R_{mix}^{i} = X_{sp}^{ref} R_{sp}^{i} + \left(1 - X_{sp}^{ref}\right) R_{nat}^{i} \quad \text{(B2)}$$

where R_{sp}^{i}, R_{nat}^{i} and R_{mix}^{i} are the true isotope ratios of the isotope *i* in the spike, sample and mixture respectively. Using the general form of the exponential mass fractionation law

$$R^{i} = r^{i}\left(\frac{M^{i}}{M^{ref}}\right)^{f} \quad \text{(B3)}$$

where r^{i} is the measured isotope ratio, M^{i} and M^{ref} are the true masses of the isotope *i* and reference isotope respectively and *f* is the mass fractionation factor, equation B2 can be expanded to form the equality

$$F^{i}\left(X_{sp}^{ref}, f_{nat}, f_{mix}\right) = X_{sp}^{ref} R_{sp}^{i} + \left(1 - X_{sp}^{ref}\right) r_{nat}^{i}\left(\frac{M^{i}}{M^{ref}}\right)^{f_{nat}} - r_{mix}^{i}\left(\frac{M^{i}}{M^{ref}}\right)^{f_{mix}} = 0 \quad \text{(B4)}$$

where F^{i} is a closure function for the spike-sample mixtures that must equal zero. Equation B4 has three unknowns (X_{sp}^{ref}, f_{nat}, f_{mix}) that need to be solved for each of the three isotope ratios. This is done by taking derivatives of F^{i} for each of the unknowns such that

$$\frac{\partial F^i}{\partial X_{sp}^{ref}} = R_{sp}^i - r_{nat}^i \left(\frac{M^i}{M^{ref}} \right)^{f_{nat}} \quad \text{(B5)}$$

$$\frac{\partial F^i}{\partial f_{nat}} = \ln\left(\frac{M^i}{M^{ref}} \right) \left(1 - X_{sp}^i\right) r_{nat}^i \left(\frac{M^i}{M^{ref}} \right)^{f_{nat}} \quad \text{(B6)}$$

$$\frac{\partial F^i}{\partial f_{mix}} = -\ln\left(\frac{M^i}{M^{ref}} \right) r_{mix}^i \left(\frac{M^i}{M^{ref}} \right)^{fmix} \quad \text{(B7)}$$

which for the three Fe isotopes ratios produces nine derivative equations (Albarède and Beard, 2004b). Equation B4 is solved for the three variables X_{sp}^{ref}, f_{nat}, f_{mix} by an iterative Newton-Raphson technique that is quadratically converging and that is solved using the following vector calculation.

$$x_1 = x_0 - J_0^{-1} y_0 \quad \text{(B8)}$$

An initial estimate (*est*) for the three variables make up the 3 x 1 vector x_0,

$$x_0 = \begin{pmatrix} X_{sp}^{ref} \\ f_{nat} \\ f_{mix} \end{pmatrix}^{est} \quad \text{(B9)}$$

from which values from equation B4 for the three isotope ratios produce a 3 x 1 vector y_0.

$$y_0 = \begin{pmatrix} F^{^{56}Fe} \\ F^{^{57}Fe} \\ F^{^{58}Fe} \end{pmatrix} \quad \text{(B10)}$$

The product of $J_0^{-1} y_0$, where J_0 is a 3 x 3 matrix that contains the nine derivatives (B5, B6 and B7) for each of the three isotopes produces a new estimate for the three variables, x_1 (B11).

$$J_0 = \begin{pmatrix} \frac{\partial F^{56}Fe}{\partial X_{sp}^{ref}} & \frac{\partial F^{56}Fe}{\partial f_{nat}} & \frac{\partial F^{56}Fe}{\partial f_{mix}} \\ \frac{\partial F^{57}Fe}{\partial X_{sp}^{ref}} & \frac{\partial F^{57}Fe}{\partial f_{nat}} & \frac{\partial F^{57}Fe}{\partial f_{mix}} \\ \frac{\partial F^{58}Fe}{\partial X_{sp}^{ref}} & \frac{\partial F^{58}Fe}{\partial f_{nat}} & \frac{\partial F^{58}Fe}{\partial f_{mix}} \end{pmatrix} \quad \text{(B11)}$$

These new estimates are fed back into equation B8 until the values for B4 converge to zero. Convergence is usually met within about four to five iterations.

Appendix C Protocol for the chemical separation of Fe from seawater samples

C.1 Preconcentration using bulk extraction

1. This method can be used for samples of up to 1 litre.
2. Clean of a batch of NTA resin:
   2.1. Transfer the NTA resin to a SPE cartridge and rinse several times with MQ, shaking occasionally, to rinse off the Ethanol it is stored in.
   2.2. Leach the NTA resin in clean 1.5 M HCl for one week: suspend the resin in 1.5 M HCl and leave on a shaker table; renew the acid each day using SPE cartridge
   2.3. Transfer the NTA resin to the SPE cartridge and rinse several times with clean 1.5 M HCl.
   2.4. Rinse the NTA resin with MQ until pH > 4
   2.5. Store NTA resin in MQ in a Teflon bottle and in fridge between uses.
3. Make sure you have enough sample volume for the required ng Fe per analysis and considering the yield of the procedure is 80 to 90 %.
4. Make sure your blanks (acids, NTA resin and NTA procedure) have been checked and that the procedure blank does not exceed 5 % of ng Fe in the recovered sample.
5. 24 h before preconcentration adjust sample pH between 1.7 and 1.8. Fe(III) recovery with NTA is maximum for pH > 1.7 and Fe is Fe is dissociated from organic ligands at pH < 1.8 (Lohan *et al*., 2005).
6. At least 12 h before preconcentration add the relative amount of isotope spike to the sample (Lacan *et al*., 2010). This should be weighed in a clean Teflon vial on a scale beforehand.
7. Add 10 µM H_2O_2 to the sample (Lohan *et al*., 2005). For 1 L of seawater you need to add 50 µL of the 0.2 M H_2O_2 solution.
8. Add 650 µL NTA resin to the seawater sample using a wide mouth pipette. Close sample lid tightly and triple bag it.
9. Shake the sample on a shaker table for at least 2 h (located outside the clean lab).

10. Filter the resin out of the sample using a PFA filter apparatus from Savillex (47 mm diameter and 1.0 µm polycarbonate membrane, Whatman). After filtering all the seawater, rinse the original sample bottle with the filtered seawater 3 times to recover any NTA resin remaining in the bottle.
11. Rinse the NTA resin with 3 x 20 mL MQ on the filter holder. With 4 x 3 mL MQ rinses transfer the NTA resin from the filter holder to the home-made column (made from a Pasteur pipette cut open at the top and bottom and with a Teflon frit) using a Teflon funnel.
12. Elute Fe from the NTA resin with 3 x 2 mL clean 1.5 M HCl and collect in a Teflon vial for evaporation. This elution volume might need to be increased for high amounts of Fe recovered.
13. Evaporate the sample on a hotplate.
14. Reconstitute in 500 µL 6 M HCl (+0.001 % H2O2) and allow 24 h for redissolution.
15. The used NTA resin should be stored in a separate bottle for future cleaning.

C.2 Preconcentration using NTA columns

1. Assemble NTA columns
   1.1. Materials: two pieces of tube 3/8” OD, 1/4” ID (~ 4 cm, Cole Parmer) and one piece 1/2” OD, 3/8” ID (~ 6.5 cm, Cole Parmer); two PE frits (114 µm pore size SPC Technologies Ltd, PE10015); clean NTA resin
   1.2. Assemble one tube 3/8” OD, 1/4“ ID to ½” OD, 3/8” ID with one frit
   1.3. Re-suspend the NTA slightly and pipette 1 mL into column (height of resin in the column should be ~ 1 cm).
   1.4. Place the other frit and the other tubing from the other side to enclose the resin
2. Clean NTA columns with 150 mL clean 1.5 M HCl and rinse with 80 mL MQ. Use a syringe barrel (without the plunger) attached to the top of the column, with a 1.5 cm piece of FEP tubing (5/32” ID, 1/4” OD).
3. Store columns at neutral pH, sealed on both ends with parafilm and bagged in fridge.
4. Make sure column blanks are low before using them.

5. Adjust the sample pH to 1.7 to 1.8 at least 24 h before preconcentration. If the sample had been standing at pH 2 or above allow one week after adjusting the pH to allow iron being desorbed from bottle walls.
6. Add the relative amount of isotope spike to the sample at least 12 h before preconcentration. For this the concentration need to be known beforehand as the optimum sample:spike proportion is 1:1.
7. Add 10 µM H_2O_2 to the sample 30 min before preconcentration. For hydrothermal samples add 100 µL of concentrated and ultraclean H_2O_2 and leave standing for a week (Rouxel, personal communication).
8. Pre-clean the column with 75 mL clean 1.5 M HCl and rinse with 80 mL MQ. Use a syringe barrel (without the plunger) attached to the top of the column.
9. Place the sample on a high surface (make sure the surfaces are cleaned before starting as it will be outside the laminar flow hood, in the clean lab). Place a Teflon tube (1/4" OD, 5/32' ID, Savillex) into the sample bottle, touching the bottom of the sample bottle and attach the clean NTA column to the other end and place it around 1 m below the sample. Place the outlet of the column into a waste bottle. The tube should reach the bottom of the sample to make sure all of the sample will be taken up and should be fixed in place with parafilm. Make sure the sample bottle is sealed to avoid contamination.
10. With the help of a syringe (sucking from the outlet of the column) start the flow of sample over the column. It will continue flowing by gravity until the sample is empty.
11. The flow rate over the column is 10 mL/min.
12. Take the column into the laminar flow hood once the entire sample has flown over the column.
13. For small sample volumes (lower than 25 mL) instead of steps 9 to 12, leave the syringe barrel attached to the top of the column. Let the sample flow over the column after the MQ rinse by pouring it into the syringe barrel and use the same syringe barrel for the following steps.
14. Attach a clean syringe barrel to the top of the column and rinse with 80 mL MQ to wash off the salts.

15. Elute Fe with 10 mL clean 1.5 M HCl and collect in a savillex vial for evaporation.
16. Rinse the column with 70 mL MQ.
17. Give the column a good shake occasionally between the different steps to loosen the resin as it might get clotted up and micro-flow tunnels within the resin might be created, minimising the contact area to the resin. Also inverting the flow direction from time to time prevents the resin from clotting up.
18. Seal the column with parafilm on both sides with some MQ inside to prevent the resin from drying. Store the column at neutral pH in the fridge for next use. Columns can be re-used.

C.3 Purification

1. Clean a batch of AG1-x8 resin:
   1.1. Add some resin to a clean bottle and rinse several times with MQ by decantation
   1.2. Cover the resin with clean 6 M HCl and shake on a shaker table over night; leave to settle and decant solution. Repeat this with new 6 M HCl twice more.
   1.3. Repeat the same procedure with 1 M HCl.
   1.4. Store resin in 0.01 M HCl.
2. Assemble columns:
   2.1. Take 1 mL polyethylene Pasteur pipettes and cut the top and bottom off to the following dimensions of the column: height ~ 40 mm, ID ~ 4 mm. Leave a reservoir on top of the column (~ 5 mL). Subsequently clean them in Decon, 50 % HCl and 50 % HNO_3.
   2.2. Cut out some PE frits (114 µm pore size SPC Technologies Ltd, PE10015) and subsequently clean them in Decon, 50 % HCl and 50 % HNO_3.
   2.3. Place one frit at the bottom of the column and fill with ~ 500 µL AG1-x8 resin. Make sure no bubbles are trapped over the frit and inside the resin reservoir. To avoid bubbles, first fill the column with MQ (make

sure no bubbles are present) and then slowly fill with resin, keeping the MQ topped up.

3. Pre-cleaning: subsequently fill the reservoir (5 mL) with 0.1 M HF, 6 M HCl and 7 M HNO3 (all have 0.001 % H_2O_2). Repeat the procedure 5 times. The HF step is only carried out every 5^{th} time.
4. Columns are stored in 0.1 M HCl (0.001 % H_2O_2). Make sure the resin is fully submerged at all times to avoid it drying out.
5. Immediately before using the column clean it with 3 x 500 µL 1 M HCl.
6. Conditioning: 2 x 500 µL 6 M HCl (0.001 % H_2O_2).
7. Load sample in 500 µL 6 M HCl (0.001 % H_2O_2).
8. Elution of most elements with 3.5 mL 6 M HCl (0.001 % H_2O_2): 2 x 1 mL + 1.5 mL. Rinse the sample vial each time to recover the entire of sample.
9. Elute Fe with 4 mL of 1 M HCl (0.001 % H_2O_2): 2 x 1 mL + 2 mL. Collect all fractions in a clean Teflon vial.
10. Clean columns with one pre-cleaning cycle before storage in 0.1 M HCl. Clean the columns with ideally 5 cleaning cycles between uses.
11. Evaporate sample and reconstitute in 0.3 M HNO_3 for isotopic analysis. Do the redissolution a couple of days before analysis using the same big batch of 0.3 M HNO_3 to redissolved all samples and standards of that analysis session. Reconstitution volume should be according to amount of ng of Fe in sample and aiming for a concentration common to all other samples and standards also analysed in the same isotope analysis session. At first reconstitute the samples in less volume. On the day of isotopic analysis and before starting all samples are screened for signal intensity by carrying out a ”dip test”, according to which the final dilution is made.
12. The purification step should be carried out twice for particulate samples to assure complete matrix removal (Lacan, personal communication).

Appendix D Neptune manual – Fe isotopes

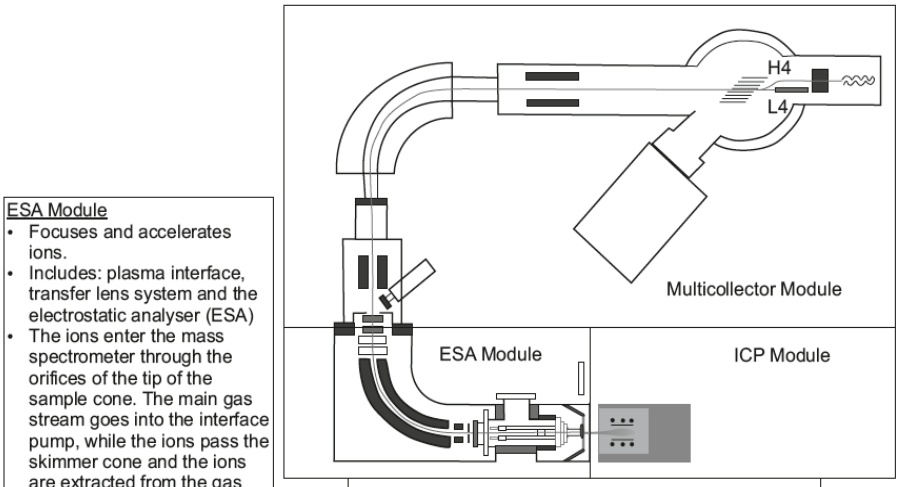

Scheme of the Finnigan Neptune - Main Modules

ESA Module
- Focuses and accelerates ions.
- Includes: plasma interface, transfer lens system and the electrostatic analyser (ESA)
- The ions enter the mass spectrometer through the orifices of the tip of the sample cone. The main gas stream goes into the interface pump, while the ions pass the skimmer cone and the ions are extracted from the gas stream by the extraction lens and led into the following transfer lens system.

Multicollector Module
- Includes: the magnet, zoom optics, multicollector and current amplifier system
- Mass separation and detection of ions takes place here

ICP Module
- Covers the hardware related to plasma generation
- Includes: mass flow controllers for argon supply, RF generator (powers the plasma), ICP matchbox, X-Y-Z- stage to position the torch and supply the chamber and torch itself.
- The nebuliser generates an aerosol, which is guided into the Aridus, and then directed into the injector of the plasma torch, where it is instantaneously desolvated and ionized.

D.1 Preparations before a run

1. Make up 1 litre of TD 0.3 M HNO_3. Take the acid from Matt's clean lab (directly from acid stills) or make more if there is none. Use this acid to make up samples, standards and blanks so it is all from the same batch of acid.
2. Clean cones (Ni); boron cones are usually ok to use after they used them.
   2.1. Find Al powder in rock crushing room (on a shelf near the fly press) and use a cotton wool bud to gently go over the cones with a little added water and remove any impurities. Then rinse before putting them into the ultrasonic bath.
   2.2. Take to instrument lab and rinse with MQ water. Then leave 10 minutes in an ultrasonic bath (in a beaker filled with MQ water).
   2.3. Rinse with MQ again and leave to dry in an oven (or dry with the gas gun at the back of the Neptune)
3. Clean the Apex-Q or the Aridus II (described below)

D.2 Apex cleaning

1. Well before starting, put 500 mL 10 % nitric acid in a Teflon bottle and on a hot plate.
2. Take the Apex-Q to the MQ sink. Get the cleaning kit.
3. Invert the Apex.
4. Connect the squeeze bottle (inlet) to the sample inlet of the Apex-Q (where the nebuliser is connected). You need to remove the screw beforehand.
5. Connect an outlet tube to the sample outlet of the Apex (where the tube towards the torch is connected).
6. Fill the squeeze bottle with the hot 10 % nitric acid and rinse the solution through until most of it has been consumed.
7. Leave the Apex sitting in this solution over night
8. The next morning rinse the rest of the solution through the Apex.
9. Squeeze some air through it.
10. Rinse and fill the squeeze bottle with MQ water. Repeat several times including some inversions and tipping of the Apex.
11. Repeat steps 1 to 10 using heated 10 % HCl if necessary.
12. Disconnect the cleaning kit tubes and carefully invert and tip the Apex to drain any liquid remaining inside. Place the screw back on the sample inlet.
13. Take the Apex back to the Neptune. First of all the Apex needs to be dried.
14. Connect the nebuliser to the Apex and to the sample gas supply of the Neptune.
15. Connect the drain tube to the Apex outlet and lead it into a waste bottle.
16. Connect the Apex to the power supply and put the switches to the desired setting, so that the internal chambers can equilibrate to the temperatures during the drying process.
17. Connect the nebuliser (*home* position) to the inlet and connect a tube on the outlet leading into a waste bucket.

18. Turn on the pump to high speed and put outlet to waste bucket.
19. Turn on the sample gas: *Neptune software*; open *Diagnostic*; click on *Instrument – Connect MS*; in the *ICP Source* tab, click on *Main Gas* supply until green tick, then drag the *sample gas* up to 1 L/min.
20. Leave to dry for 2 hours.

D.3 Aridus cleaning

21. Well before starting place 500 mL of 10 % Nitric Acid on a hot plate (Teflon bottle).
22. Undo the screws on the outer housing and keep the screws in a safe place
23. Remove outer housing
24. Disconnect two data connections (one thin red and black and one broad bunch of multicolour cables)
25. Disconnect two parallel plastic gas lines (one for Ar and one for N_2)
26. Undo all the screws that hold the plate on which the membrane is attached to
27. Remove the plate that is holding the membrane. Take care and handle slowly; carefully slide the membrane input out of round tube; watch nothing is connecting the two plates anymore.
28. The base plate should look like displayed in the following picture:

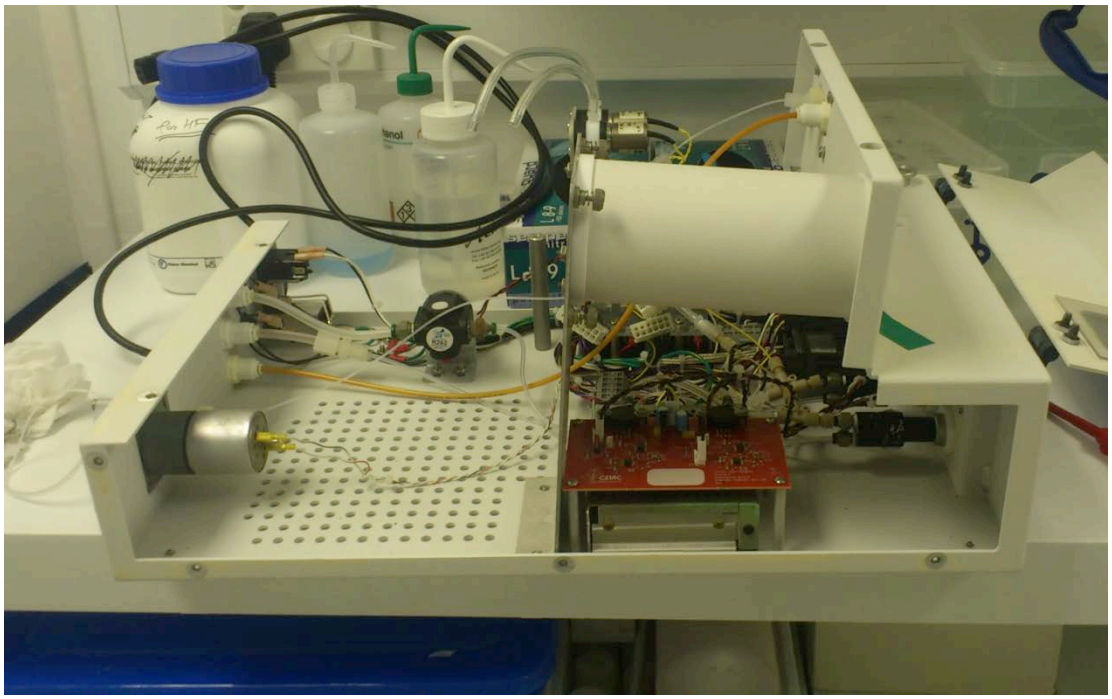

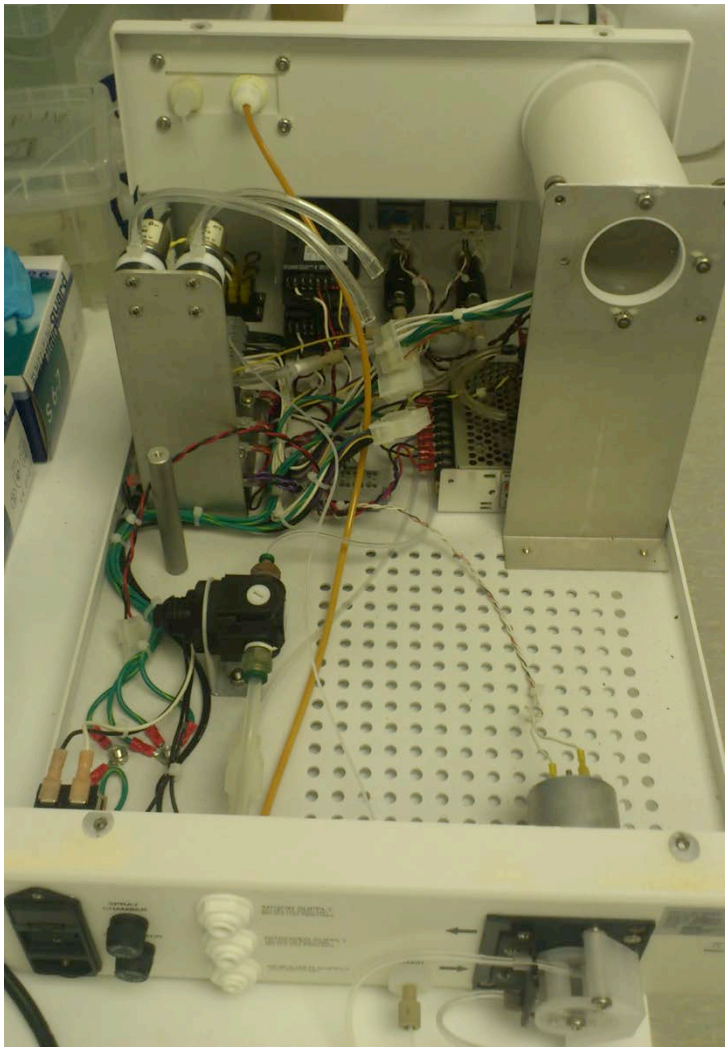

29. Place the membrane next to the sink and connect the cleaning kit tubing.
    29.1. The inlet has a t-connection, one tube should be connected to the inlet of the membrane and the other tubing should be connected to the Sweep gas out.
    29.2. Place a plastic tube between the two gas connections, creating a loop.
    29.3. The outlet tube is also a t-connection; one tube is connected to Rinse and the other to Sample Out.
30. The membrane plate and the tubing connections should look like displayed in the following picture

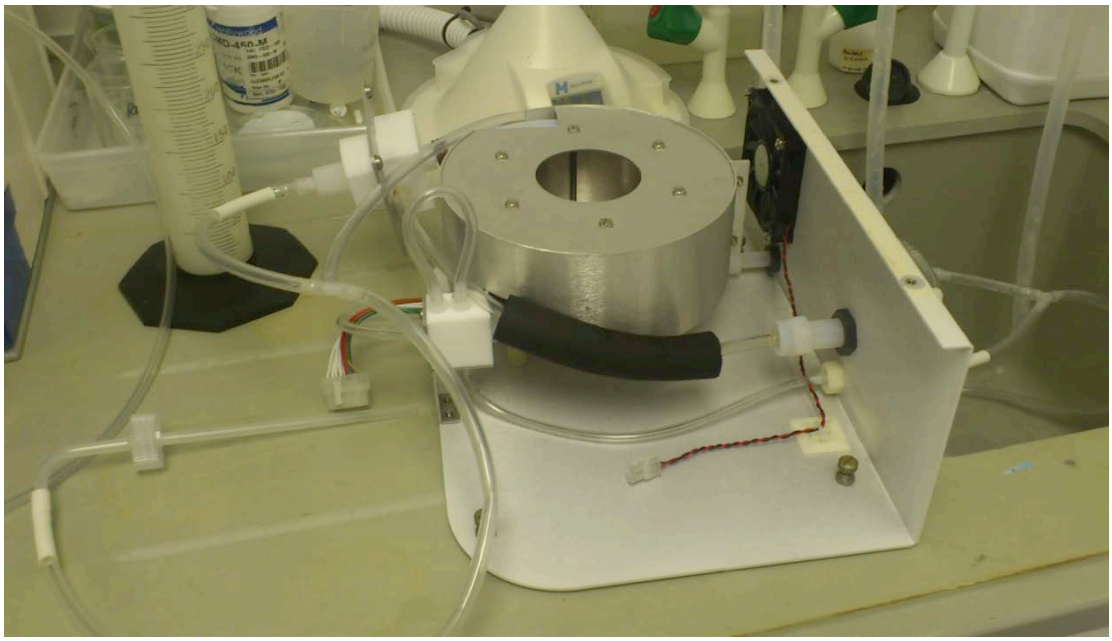

31. To make sure there are no leaks along the circuit, start off by passing MQ water through (use the squeeze bottle attached to the inlet).
32. Once you are sure there are no leaks, fill the squeeze bottle with the hot 10 % Nitric Acid and squeeze it through the circuit. Try to get bubbles out of the circuit.
33. Leave sitting over night
34. The next day, rinse through the rest of 10 % nitric acid left in the squeeze bottle. The rinse the squeeze bottle with MQ water. Fill the bottle with MQ water and rinse it through the circuit. Do this three times. At the end make sure air is flushed through and all the MQ is drained from the system.

35. Disconnect the Cleaning kit tubing, but leave the three tubes on the back of the plate for draining later (see photo); drain the system again by tipping it.

36. Remount the membrane plate onto the base plate, leaving it the same as before dismantling. Take care when connecting membrane inlet to round tube and push into the Teflon housing by pushing from the nebuliser inlet. Make sure all screws are properly fixed, the plastic gas lines (Ar and N_2) are re-connected and the data cables are re-connected.

37. Place the outer housing and fit outer screws (first fit all screws loosely so that there is space for movement and then tighten them at the end).

38. Place the Aridus back into its place on the Neptune, leaving the 3 draining tubes leading to a waste bucket. See photo

39. Connect the Aridus to the gas supply on the instrument (Ar and N_2 lines at back, push in, then slightly wiggle in and out). Connect nebuliser to sample gas supply and to Aridus. Open the gas supplies.

    39.1. For the sample gas: *Neptune software*: open *Diagnostic*; click on *Instrument – Connect MS*; in the *ICP Source* tab, click on *Main Gas* until green tick, then drag the *sample gas* up to 1 L/min.

40. Leave drying over night

D.4 Instrument control panel lights

Parameter	Description	Colour when off
Ar Pressure	If red, Ar gas supply has run out	Green
Torch in Pos.	Indicates the torch is connected.	Green
Cool Gas Flow	Indicates the operating flow of the cool gas	Red
Coil Cooling	Status of the water flow sensor	Red
Interface Cooling	Indicates that the front end of the instrument is being cooled	Red

Interface Pump	Vacuum pump that maintains the vacuum with the cones	Red
Skimmer Valve	Closes when the machine is off	Red
Interlock Hood	Indicates the position of the skimmer valve	Green
HV Electronics	Indicates that there is power to the electronics	Green
Board Check	If red, it indicates power failure at one of the boards	Green
Fore Pump	Turbo pumps that maintain vacuum	Green/Red
FV < 10^{-1}	Indicates if the fore vacuum pressure falls below 10^{-1} mbar	Green
HV > 10^{-4}	Indicates is the main vacuum pressure falls below 10^{-4} mbar	Green
TP > 50%	Indicates higher than 50% nominal rotational speed	Green
Ion Pumps	Indicates the status of ion getter pumps	Green
Analyser Gate	Indicates the position of the analyser gate valve	Green
Amplifier Valve	Not used	Green
Analyser Ok	Indicates the position of the analyser gate valve is ok	Green
Baking	Red if it is running. Gets rid of moisture inside chambers if the vacuums fail. Very bad if this has to be done.	Green

Once the machine is fully switched on, all of these lights should be green, if they aren't, it may indicate that there is a problem.

D.5 Installation of cones

41. Plasma should be off. If it isn't already off, select *Off* in *Stop and Start Plasma*.
42. Turn the black knob clockwise at the front of the machine. This slides the front of the Neptune open to gain access to the cone positions.
43. Use the round metal lock to unlock the sampler cone from its position (maybe use the black magnet to help with this).
44. Take out the graphite ring.
45. Use the screwdriver-like tool to loosen the 3 screws around the skimmer cone (DO NOT TAKE THESE OUT COMPETELY). Turn the cone clockwise, and use the magnet to remove the cone.

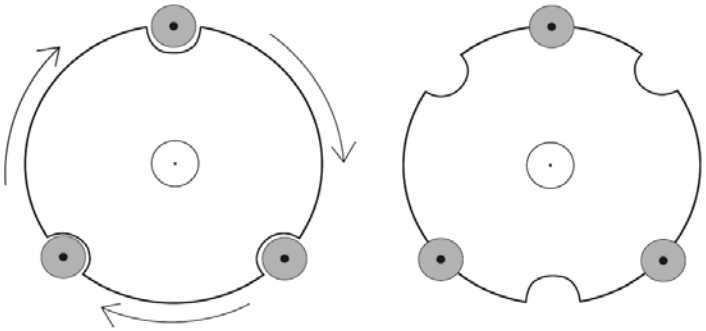

46. Put a clean skimmer cone in, and make sure it is flat and not loose after the screws have been tightened.
47. Place in the graphite ring (replace if it is starting to look worn).
48. Place in a clean sampler cone and lock tightly.
49. Twist black knob anticlockwise at the front of the machine, to close the Neptune.
50. Should hear a click and the *Torch in Pos.* light should go green.

D.6 Install a clean injector into the Torch system

Make a diagram of the torch injector set-up

51. Plasma should be off. If it isn't already off, select 'Off' in 'Stop and Start Plasma'.

52. Undo the screw under the torch on the metal carriage and slide out the torch with care.
53. Place in an injector that is suitable for the Aridus. Need a Standard Injector, which has a rounded end.
54. Choose one out of the acid bath that is clean and has a rounded and not melted end.
55. Rinse in Milli-Q and shake. Use the air compressor at the back of the Neptune to dry it and blow all of the droplets of moisture out of it.
56. Take the dry injector and fit new O-rings onto it. Roll them on until they fit into the grooves. Also place a third O-ring onto the back of the injector for the Aridus tube to fit onto.
57. Place the glass torch onto the injector tightly, so that it goes over both O-rings.
58. Place the torch carriage back into place (the 2 long prongs should line up to help it go in).
59. Place the screw and screw up tightly (there is a bit of a spring on the torch so push slightly while tightening up).

D.7 Setting up with the Apex-Q

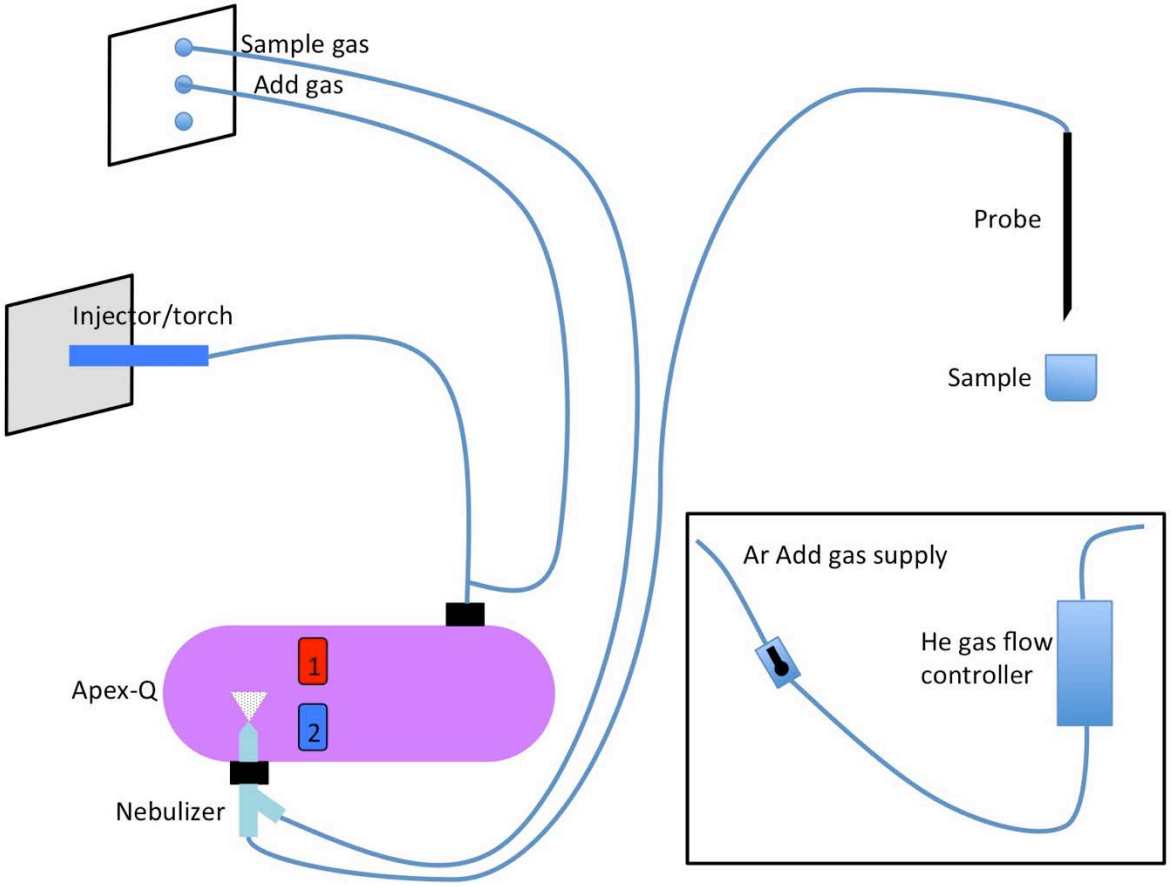

60. Make sure the Apex is connected to the power supply and that the correct settings are active on the red and blue buttons.

    60.1. We want red button set to 1 (100 °C, 100 µL/min flow); blue button to 2 (2°C, aqueous samples). Allow time to equilibrate the temperatures.

61. Connect the nebuliser tip to the Apex inlet and connect the gas line to the sample gas supply on the Neptune (first supply from top). Place the probe in the autosampler with use of the metallic weight (also place a sheet of parafilm between the autosampler arm and the probe weight to avoid contamination).

62. Connect the Apex outlet tubing to the torch with the use of a clamp.

63. The add gas is mixed with the sample immediately at the sample output of the Apex. Connect this gas line to the Nitrogen gas supply of the Neptune (second supply from top; this is labelled nitrogen, but it is used with Argon in this case).

64. For the Add gas, check gas lines are open and connected to the correct gas flow controller (bottom right of instrument, use the helium gas flow controller). If the helium gas flow controller is not connected, look for the tube lines that go into the back of instrument. Disconnect them from the gas flow controller they are on (use spanner with blue tape) and reconnect to the helium controller. Also switch the data cable from one to the other. Then open the valve on the plastic tube coming out of the controller.
65. Set the waste pump speed to the highest speed (this reduces the noise on the signal). Outlet into a waste bucket.

D.8 Setting up with the Aridus II

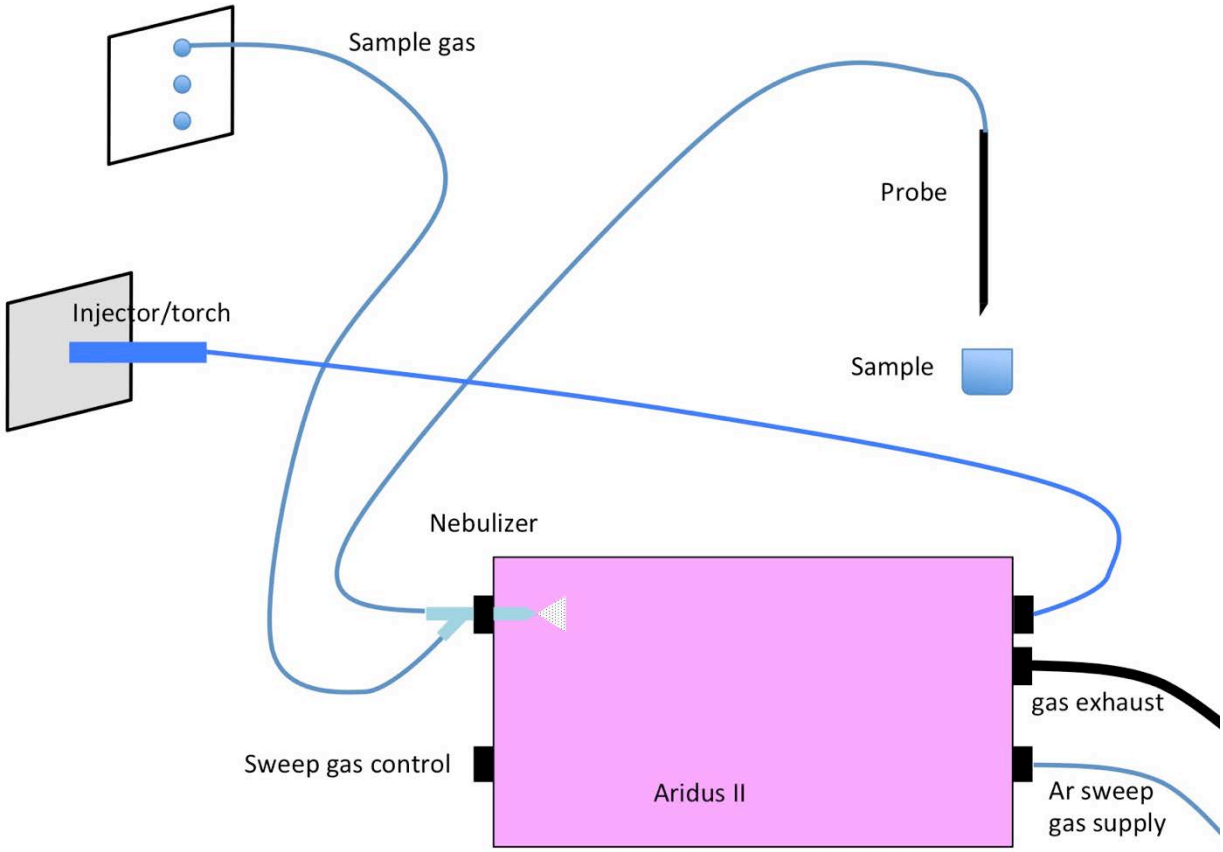

66. Connect the Aridus to the torch/injector with the use of a clamp. The tube comes out of the back of the Aridus.

67. Make sure Ar gas line (top) and N_2 gas line (bottom) are connected at the back of the Aridus. Ar gas line valve should be open and N_2 gas line valve should be closed.
68. Make sure the gas exhaust line is set-up correctly. From the Aridus the exhaust tube (covered in black rubber pipe and with a smooth downward slope) should lead into a container. From this container there should be another tube connected up into the exhaust pipe, also with a smooth slope.
69. Turn sweep gas up to start purging gas through Aridus.
70. Install the nebuliser and connect to gas supply (first gas supply from top over torch)

D.9 Check main Neptune gas supply is a plastic line

71. The instrument should be turned off to make this change
72. Take gas store keys and spanner from room next to instrument lab.
73. Go to gas store and select one of the middle Ar gas cylinders (out of four). Choose the one that has highest levels of Ar.
74. Close the green valve on the gas cylinder
75. Close the valve on the end of the tubing coming out of the cylinder and going to the wall (valve is on the wall).
76. Unscrew the smaller bolt on the regulator on the cylinder (output from green valve). Do not unscrew the bigger screw which is closer to the green tap)
77. Take the regulator attached to the plastic line and screw it onto the cylinder (in place of the other tube that has just been taken off)
78. Tighten the screw with the spanner
79. Make sure all the valves on the new regulator are closed
80. Slowly open the green valve on the cylinder and make sure there are no leaks from the regulator and fittings.
81. Slowly open the valve on the regulator for the plastic line and make sure there is a reading

82. Then go to the Neptune. On the wall behind the Neptune, change the inlet from steel to plastic. First close stainless steel line. Then open the plastic line and make sure there is a reading. For this step it is important the instrument is turned off.

D.10 Checklist before turning on the instrument

83. Plastic line for gas supply
84. New wash 3 % nitric acid
85. Cones fitted, torch, injector in place
86. Sample introduction system in place (Aridus or Apex) and set-up
87. Turn system on with Aridus gas on (in case of using it)
88. Fe cup configuration is loaded. Click on *set collection*.
89. Introduce the mass of the centre cup into the *scan control* panel and click *set*, leave for a few seconds and click *break*.

D.11 Turning on the plasma

90. Send the probe to the *Home* position.
91. Open up the *Neptune software* (if not open already)
    - 91.1. In the *Neptune Software* folder, open *Acquisition*. This should establish communication between computer and instrument. A box should appear saying *System* ok.
    - 91.2. Open *Tune* from the *Neptune System* folder
    - 91.3. Check the watch parameters

Parameter	Colour when off
HV on	Green
Torchbox / Exhaust	Green
Skimmer Valve	Red
Analyser Gate Open	Green

Coil Cooling Ok	Red

Analogue parameters are only really relevant when the instrument is running

92. On *Stop and Start Plasma*, all of the components should be red when the plasma is off.

93. Select *On*. When it asks if you want to start the peristaltic pump, select *Yes* for Aridus or *No* for Apex.

    93.1. It will then begin to check everything:

    93.2. Torch on?

    93.3. Cooling system on?

    93.4. Should hear gas starting to flow through the machine

    93.5. If you haven't already started to turn up the Aridus sweep gas flow, do it now.

    93.6. When the sample gas drops to zero, turn the Aridus sweep gas flow down to zero as well fairly quickly, after ~30 seconds the plasma should ignite.

    93.7. The sample gas should now increase back up to ~1 L/min.

94. The skimmer valve opens and a message comes up: 'Plasma is on'. All of

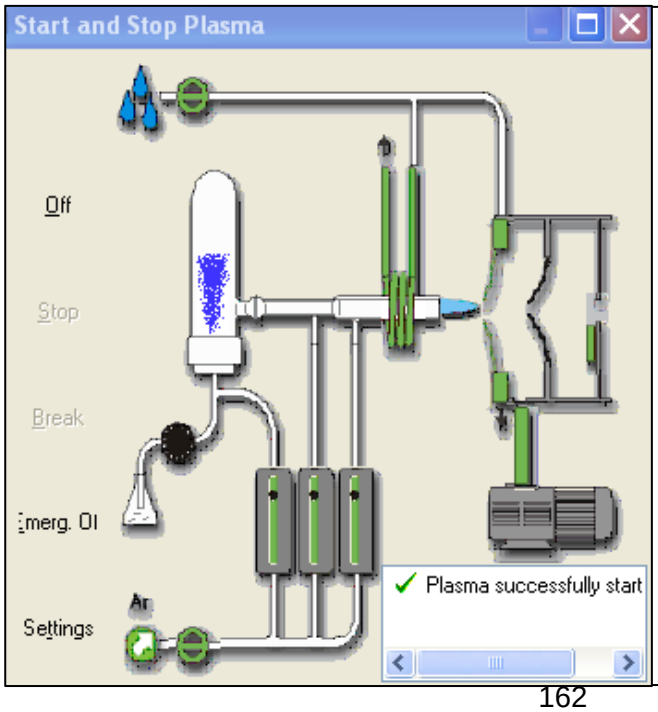

Allows to control the plasma generation of the instrument.

- Break = Active only when a start-up process or stop sequence is being processed. Click on continue to resume the sequence.
- Emergency off = Active only during the plasma ignition step or when the plasma is on.
- Settings = Used to customise the parameters for the plasma start and stop sequences.

the components on *Stop and Start Plasma* should now go green.

95. Under *Inlet System*, open up either the most recent file for Fe isotopes, or another recent file that has used similar set-up to the current set-up (Aridus or Apex, HR, x cones). Once a file is selected, you will hear sounds from the machine as the torch changes position and the gas flows change. Even if a tuning file is open at the time of turning the instrument on, it needs to be re-opened in order to work.

96. Increase the flow into the Aridus, do slowly so as not to disturb the torch. If flicker starts, slow down

97. Send the Autosampler into the wash and check that solution is being taken up. If there are air bubbles in the tube and no solution is being taken up:

    97.1. Send the Autosampler to the *Home* position.

    97.2. Use a syringe containing 3 % HNO_3 to pump into the tube to remove air bubbles and to un-block it.

    97.3. Send it back to the wash solution and watch to see if solution is now being taken up.

98. If the Autosampler doesn't move when given a command, then switch it off and on at the front of the machine. Give it about 1 minute to settle, and then try giving it another command.

D.12 Changing a nebuliser while instrument is on

You might want to change nebulisers while the system is running.

99. Close *analyser gate*

100. Slowly turn down the sample gas until cero

101. Slowly turn down sweep gas (or add gas)

102. Disconnect the tube connecting the Aridus (or Apex) to the torch.

103. Disconnect nebuliser from Aridus (or Apex) and from gas supply.

104. Place new nebuliser and connect to Aridus (Apex) and gas supply.

105. Take sample gas up to 1 L/min and sweep gas (add gas) up to normal working flow (take them up fast) to purge air out of the tubes.

106. After a few moments, take gases down to cero again.

107. Connect Aridus outlet tube to the torch and clamp it on.

108. Slowly take up the sample gas (critical between 0.2 and 0.5 l/min). If the change in gas is too sudden it would turn the plasma off. While taking the gases up, watch the panel on the left hand side of the Neptune and watch the reflected power, this would increase if a change in gas is made too suddenly. A drastic change in gas would also produce flicker in the plasma, so keep an eye on this as well.

109. Slowly take up the sweep gas with the same care.

D.13 Changing Amplifiers in the Faraday Cups

110. We want to use 10^{12} Ω Amplifiers for the low signals of ^{53}Cr (L3) and ^{60}Ni (H3) and 10^{11} Ω Amplifiers for the rest of the cups. Amplifiers 1 and 2 are 10^{12} Ω and the rest are 10^{11} Ω.

Cup	Isotope	Amplifier
L3 (motorized)	^{53}Cr	10^{12} Ω
L2		
L1 (motorized)	^{54}Fe	10^{11} Ω
C	^{56}Fe	10^{11} Ω
H1 (motorized)	^{57}Fe	10^{11} Ω
H2	^{58}Fe	10^{11} Ω
H3 (motorized)	^{60}Ni	10^{12} Ω

111. Go to *Executive* in the *Neptune software* folder, and then click on *SYS* and then *Mounted Detectors* tab.

112. Expand all the Cups.

113. To change Amplifiers from one cup to another: first drag the existing Amplifier from the Cup and drop it into its *home position* at the bottom so that the cup becomes free for the new Amplifier. The target Faraday for that Cup should be dragged from the home position to the cup (drop it on top of the Earth symbol).

114. Close all other open software windows (Excel, Scan control, chart recorder, sequence editor etc.) and press OK to save the changes made to the Faraday cups. It will ask *Do you want to update?*, click *Yes*.

115. Open up *Tune* from the *Neptune software* folder. *Stop and Start Plasma* then checks if there is a connection and parameters should go green.

116. Re-open the *Cup configuration* and click on *Set Collection*.

117. Upload the tune file again.

D.14 Carry out a Gain calibration at the beginning of the session

118. This matches up the sent and detected signal intensities and applies a correction factor, normalising the entire array of detectors. During the gain calibration the analyser gate closes (the light goes red) and a fixed voltage of 3.3 V are set to each collector. If the detector measures a signal other than 3.3 V a correction factor is applied.

119. This only has to be done once per session (if the session is one week, then only once at the beginning), or if the instrument has been turned off and on, or if Amplifiers have been changed.

120. In the *Tune* window, in the *Detector calibration* tab press Gain. This takes approx. 20 minutes.

121. The *Gain calibration* automatically runs a baseline calibration as well.

122. After approx. 15 min run another *baseline calibration*. This is because the 10^{12} Ω Amplifiers are receiving a relatively high signal (compared to what they will receive during analysis) during the detector calibration and the baseline is not representative for a real measurement signal.

123. Upload the tune file again

D.15 Fixing the mass calibration

124. If the mass calibration is wrong, i.e., the wrong isotopes measured in the different cups, perform a peak centre on mass ^{88}Sr and another one on mass ^{55}Mn. For this you need a Mn solution and a Sr solution.

D.16 Tuning for signal and stability

125. Make sure the instrument is running in High Resolution.

126. Make sure the instrument has been switched on for at least an hour before starting the tuning (for it to be stable).

127. Open a tune file of a previous day using a similar setting (introduction system, cones and resolution)

128. Tune the instrument using a Tuning Solution containing 200 ppb natural iron. Some tuning should be done with a solution also containing small amounts of Cr and Ni (0.1 ppb) to align the cups.

129. During the tuning, the signal and stability should be maximised. Aim for 2 % stability on the ^{56}Fe signal on the chart recorder.

130. In first place do a mass scan to find out in which mass range the peaks are and to select the correct mass for the chart recorder (in the middle of the flat part of the peak).

Inlet system

131. Adjust the gases using the chart recorder. They should be changed slowly. If a flicker in the plasma is observed, stop changing the gases and wait for the plasma to become stable again. An abrupt change in gases might turn the plasma off.

131.1. Aridus: adjust the *Sweep gas* with the wheel on the Aridus to achieve maximum signal

131.2. Apex: set the *Add gas 2* between 0.10 and 0.12 L/min. Set to one position and then use sample gas to optimize signal hereafter.

131.3. Adjust the *sample gas* simultaneously (around 1 L/min, up to 1.2 L/min). Bear in mind that oxide formation is promoted with higher sample gas, so lower sample gas flow is preferred. With higher sample gas, the sample flow rate is reduced.

132. Adjust the *Torch position*, x y and z. It is useful to make a mental note of x y and z positions before loading the tune file, as the last positions will be closer to the target. Be careful with z position, if too close towards the cones (i.e. lower z value), the torch will melt! The closer the torch towards the plasma, the lower the mass bias. The further away the torch is from the cones, the lower the oxide production. After adjusting the torch position, re-adjust sweep gas (or Add gas 2) and sample gas.

133. Do not adjust: *Cool gas* (prevents gas from melting), *Aux gas* (alters the position of the plasma hot spot, this is the supply of Ar feeding the ignition, never below 0.7), *RF power*, *Peri-pump*, *Add-gas 1* and *Add-gas 2* (only if working with Apex).

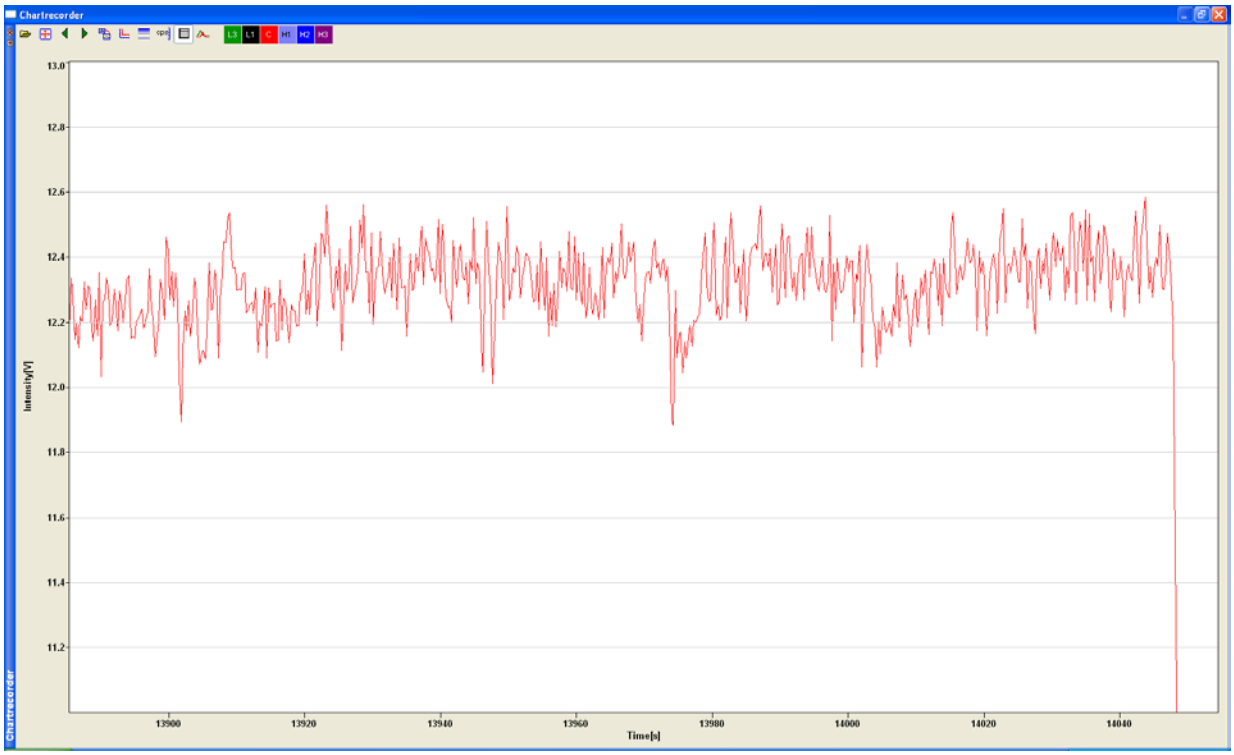

Figure: chart recorder signal with approx. 2 % error

Source lenses

134. Adjust after finding the most stable signal for inlet system. Adjust while looking at the mass scan. Most parameters have an optimum range.

135. *Extraction*: has a typical consistent value of -2000 V. The extraction voltage is switched off while the instrument is not measuring, but is switched on while measuring. Do not adjust.

136. *Source offset*: Typically set by the engineer and does not require tuning. It should have very little effect on the sensitivity if tuned properly.

137. *Focus*: affects signal stability and intensity.

138. *X-Deflection*: influence on signal stability and intensity

139. *Y-Deflection*: influence on signal stability and intensity

140. *Shape*: influence on signal stability and intensity. Influence on peak shape as well. Tune for mass resolution.

141. *Rot Quad*: Should be cero in HR. Do not adjust. (Lacan: influence on stability and peak shape).

142. *Source Offset*: do not adjust. Influence on peak shape

143. *Focus Quad*: influence on peak shape

144. *Focus Offset*: influence on peak shape

145. *Matsuda plate*: influence on peak shape

Zoom optics:

146. *Focus Quad*: to increase **steepness of slope**, squareness of peak.

147. *Dispersion Quad*: moves the **relative position of peaks** (and adjusts the **flatness of plateau**). Always leave set to cero. If the relative positions of the peaks needs to be changed, do this by moving the cup positions (cup configuration tab).

Finally…

148. Save tuning parameters (mention cones, resolution, inlet system and date).

149. Read Zoom Optics to the Cup Configuration file in the cup configuration tab.

150. Make sure the cups are perfectly aligned, looking at the mass scan in an iron solution (always do IRMM) and the mass scan in a blank solution. If needed move the cup positions in the cup configuration. Cups L3, L1, H1 and H3 are motorized. When a low cup (L4, L3, L2, L1) needs to be moved to the left relative to the centre cup, it is necessary to decrease the *Target position*, however to move it towards the left, it is necessary to increase the *Target position*. It is the opposite for the high cups 9H1, H2, H3, H4). To move a high cup to the right relative to the centre cup, it is necessary to increase the *Target position*, while to move it to the left, the *Target position* needs to be decreased. *'A displacement of 0.0045 g on the scan control corresponds to a modification of 0.08 mm of the cup position' (Radic)*

151. Select centre mass from the mass scan in IRMM (showing ^{53}Cr interference) and mas scan in blank (interferences are observed further into the flat part of the peak). Choose the centre of plateau, (Rachael) or 2/5th of plateau from the right (Lacan), to avoid measuring on the interferences.

152. Save the cup configuration and calculate mass resolution before measuring. Mass resolution should be above 8000 and plateau above 200 ppm. Print screen Alt Gr + Print Screen.

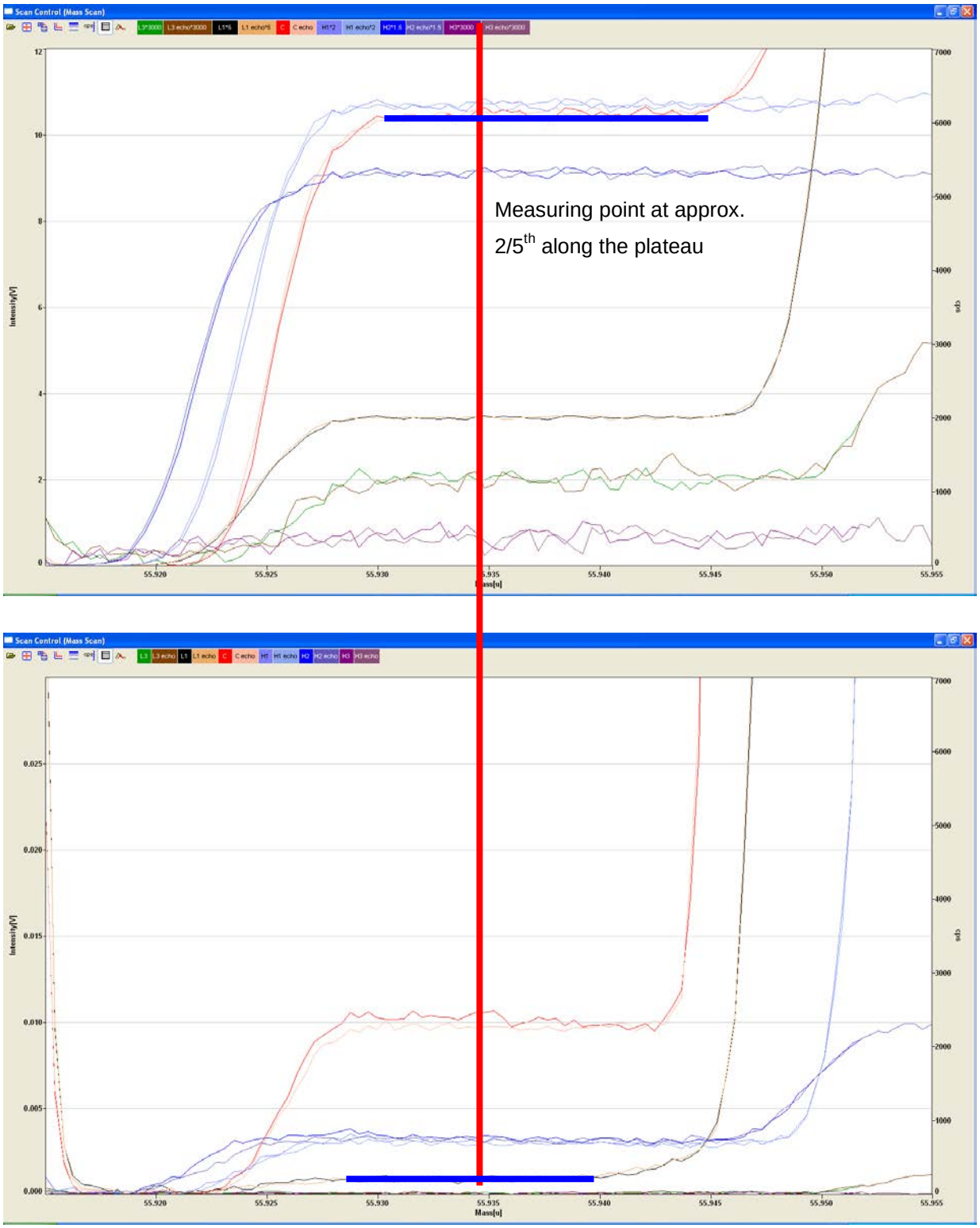

Figure: first image is mass scan for IRMM 14 and second image is for mass scan in blank. Note that the plateau appears to be shorter in the blank, and therefore it is crucial for selecting the measuring point.

D.17 Method editor

153. From the *Neptune software* folder open up *Method editor*.

154. Open up the previously used method files (Fe sample and Fe blank). Make sure these files are linked to the cup configuration in use.

155. When a new cup configuration is selected, all fields in the method file are re-set, so the parameters will have to be set-up again.

156. We measure all isotopes and the following raw ratios: 56/54, 57/54, 58/54. Make sure all isotopes and ratios are ticked (View – Display data evaluation – report parameter – measured data).

157. Perform 2-sigma rejection performed on ratios. 30 seconds baseline is measured at start.

158. Sample method: 4 s idle time, 50 times 4.2 s integration, 1 block

159. Blank method: 4 s idle time, 20 times 4.2 integration, 1 block

160. It is possible to run a test sequence on MQ to find out exactly how much volume is needed per analysis (weigh the MQ before and after this test run).

161. A test run can also be performed on a standard to make sure everything is working correctly before running a sequence.

162. Before running a sequence open the method files, then save the cup configuration and then save the method files and close them.

D.18 Sequence editor

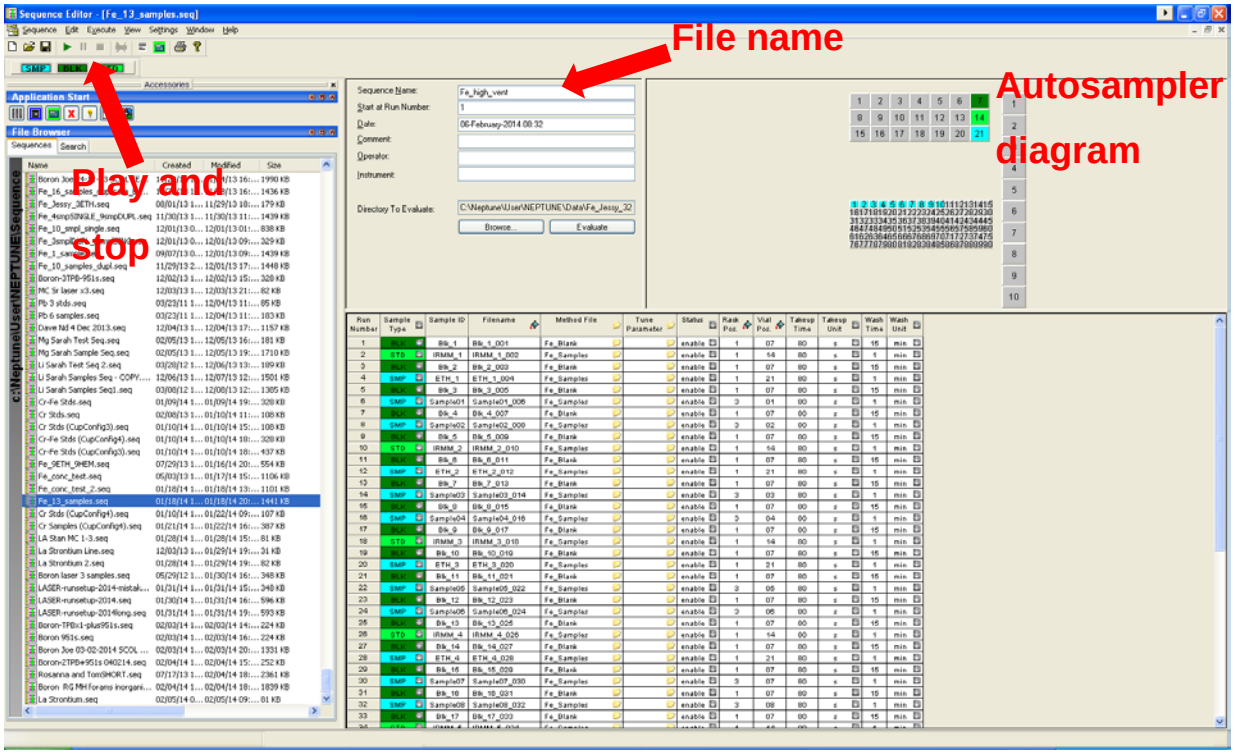

163. Every sample / standard is bracketed by blank measurements.

164. Standard test run after tuning and before analysing samples to make sure the instrument is working fine: IRMM – ETH – HEM – IRMM three times

165. Sample run: IRMM – ETH or HEM – Sample 1 – Sample 2 – IRMM… etc.

Run Number	Sample Type	Sample ID	Filename	Method File	Tune Parameter	Status	Rack Pos.	Vial Pos.	Takeup Time	Takeup Unit	Wash Time	Wash Unit
1	BLK	Blk_1	Blk_1_001	Fe_Blank		enable	1	07	80	s	15	min
2	STD	IRMM_1	IRMM_1_002	Fe_Samples		enable	1	14	80	s	1	min
3	BLK	Blk_2	Blk_2_003	Fe_Blank		enable	1	07	80	s	15	min
4	SMP	ETH_1	ETH_1_004	Fe_Samples		enable	1	21	80	s	1	min
5	BLK	Blk_3	Blk_3_005	Fe_Blank		enable	1	07	80	s	15	min
6	SMP	Sample01	Sample01_006	Fe_Samples		enable	3	01	80	s	1	min
7	BLK	Blk_4	Blk_4_007	Fe_Blank		enable	1	07	80	s	15	min
8	SMP	Sample02	Sample02_008	Fe_Samples		enable	3	02	80	s	1	min
9	BLK	Blk_5	Blk_5_009	Fe_Blank		enable	1	07	80	s	15	min
10	STD	IRMM_2	IRMM_2_010	Fe_Samples		enable	1	14	80	s	1	min
11	BLK	Blk_6	Blk_6_011	Fe_Blank		enable	1	07	80	s	15	min

166. During the process of building the sequence, regularly save the file. The sequence software crashes easily especially if sample labels (individual lines) are repeated within the sequence.

167. Uptake time should be measured using a stop-watch and looking at the chart recorder. Same uptake time for samples, standards and blanks (approx. 80 s).

168. Wash time: Before a blank, using the Aridus, set to 15 min and using the Apex, set to 8 min; before a sample/standard, set to 1 min (as it follows a blank).

169. Give the sequence a name (next to Autosampler diagram), under which the data folder will be saved.

170. Check if 'switch plasma off at end' is ticked or unticked as required; under Executive drop down menu. This can be amended during the run.

171. Make sure all the lines of the sequence (or the ones to be analysed) are 'enabled'.

172. Start the sequence by clicking on the play button at the top left of the sequence editor window. Tick the box 'Online Ascii Export'. Click ok.

173. During the run keep an eye on the signals produced while measuring. If the signal has dropped considerably the nebuliser might be blocked or the tuning conditions might not be optimal anymore. Stop the run if necessary by clicking the 'Stop' button.

174. If the sequence has been stopped in the middle of a run, wait for the Autosampler to reconnect to the instrument. Close and re-open the sequence editor. The same sequence can be run again, and the first lines already analysed can be disabled.

175. Sample files get saved in the following directory: my computer-C/-Neptune-User-Neptune_Data, first folder by date; 3 files for each sample (.dat, .exp, .log)

176. How to produce a data summary: "flag button" next to *PC Start* – double click on file - select current directory – name the file; when opening in Excel, select us-ASCII.

D.19 Before running a sequence

177. Make sure all samples and standards have the same concentration. Carry out a dip-test if necessary. While recording on the chart recorder (54, 56, 57, 58), manually put the probe 10 seconds into each pot, washing the probe for 50 seconds between samples/standards. Dilute samples/standards where necessary.

178. Check wash is full and waste is empty.

179. Check if sample volume is ok for uptake rate and measurement time.

180. Check the probe depth of the different vial racks.

181. Check mass resolution > 8000 and plateau > 200 ppm. If mass resolution is > 13,000 and working with low concentration samples, switch to MR and re-tune if necessary.

182. Check mass scan during blank to be sure of measurement point.

183. Check if 'switch plasma off at end' is ticked or unticked.

184. Save Cup Configuration to Method files before starting a sequence:

184.1. Open method file(s)

184.2. Tuning window: save cup configuration with "save as"; overwrite the cup configuration file

184.3. Save the method files (leave open or closed)

184.4. Start sequence

D.20 Data processing

185. Results are expressed in delta notation. $\delta^{56}Fe$ is expressed relative to ^{54}Fe and relative to IRMM

186. All samples and standards are double spiked

187. In first place the raw ratio needs to be calculated by using the deconvolution spreadsheet. Here a macro normalises any isobaric interferences caused by Cr and Ni, and calculates the original sample or standard isotope ratios.

188. Then δ^{56}Fe can be calculated, relative to bracketing IRMM and average IRMM of that session

189. At first a sequence of standards is analysed to make sure the instrument is analysing accurately and the external error is low.

190. During the analysis of samples it is important to keep an eye on the standard values as the tuning might deteriorate throughout the run. If the standards look bad, stop the run and re-tune, followed by re-running a standard test run.

D.21 Turn the Neptune off

191. Leave the probe in the wash for 5 minutes at least before turning off.

192. Send the probe to the *home* position

193. On *Stop and start plasma*, select *Off*.

194. Turn the Aridus sweep gas to cero and switch it off at the back. Or if using the Apex, switch it off, disconnect it and store it.

195. Disconnect the inlet system (Aridus or Apex) from the torch.

Appendix E Element manual

E.1 Set-up the instrument

1. Check Argon gas availability on the white board. According to needs gas lines can be changed from one instrument to another in the gas room situated on corridor 181.
2. Fit H-skimmer and sampler cones (cleaned with Al_2O_3 powder).
3. Fit the injector (replace O-rings if necessary) to the torch and the spray chamber to the injector. Place the waste line from the spray chamber on the pump.
4. Connect the Add gas line to the spray chamber and connect the sample gas line to the. Connect the nebulizer to the spray chamber. Fit the sample line on the pump. Connect add-gas to spray chamber.
5. Prepare clean 3 % HNO_3 wash.

E.2 Turning the system on.

1. Instrument screen: turn on the high voltage (HV) so that it appears green.
2. Make sure sample gas and add gas are connected and on. Add gas might need to be turned up manually
3. Turn on the spray chamber cooler and switch to “droplets” (wet plasma). This needs 30 min to cool down.
4. Send the probe to the “home” position.
5. Instrument screen: ON button to turn the system on. Set up the right direction of peristaltic pump flow.
6. Initialize the auto-sampler. Start the sample pump: ESI screen, FAST, peripump, RUN. Check that pump rotates in the right direction.
7. When the ignition starts, the sample and add gas will be automatically stopped. If the add gas is controlled manually, turn it down when the sample gas is turned off (watch this on the screen).
8. When the ignition is successful, the light in the torch is bright white. If the colour of this light is different turn the system off immediately.
9. Sample gas will ramp up slowly up to 1 L/min. It is critical while sample gas is between 0.1 and 0.4 L/min, the plasma could turn itself off.

10. If add gas is controlled manually, increase the flow gently after the sample gas reached 1 L/min.
11. Check the waste is draining (i.e., pump is turning in the right direction) and the sample is being taken up in the tubing.

E.3 Auto-sampler

1. The auto-sampler ESI software communicates with the Element software. The sample disposition in the ESI software needs to coincide with the sample disposition in the Element software. The sample racks are numbered from 1 to 5, where the number of samples per rack (i.e., the rack type) needs to coincide in both softwares.
2. Element screen, executive, customize auto-sampler, drag the desired rack type into place
3. ESI screen: select number of racks and click on the rack to determine the number of samples per rack and the probe depth for that rack.
4. Element screen: WASH button sends the probe to the wash; HOME button sends the probe to the Home position (in the air above the wash); select a sample position and press GO TO sends the probe to that position.

E.4 Tuning

1. Open the last tuning file, which has similar settings. “Standard tune OC3 Pumped”. PC3 is the make of the spray chamber.
2. Tuning in tuning solution (contains U 0.1 ppb):
3. Aim for a signal intensity of about 180,000 V for U
4. Aim for 5 % UO (less than 8 %), this is an indicator of oxide production
5. Tune torch position and gases (only change Add gas 1)
6. Tune lenses (all except extraction). This has no impact on the UO
7. Use MR for Fe
8. Tune high-resolution lenses. Look at Fe peak height and resolution from ArO interference.
9. Leave the probe in Eden drinking water for a few hours, until the Fe, Ni, Cr blanks are low. This is especially important for clean cones, as they need to be galvanised.

E.5 Method editor

1. Select the elements to be analysed and the ratios to be created
2. Different elements need different magnet positions. The further apart the masses are the more magnet movement is involved and the larger the offset will be.
3. The editor will suggest the appropriate resolution (HR, MR or LR) for each element.
4. Mass window is the percentage of the peak analysed.
5. 2 min analysis time per sample
6. Run the method in a solution containing these elements
7. Look if the measuring window is looking at the peaks
8. If necessary set offsets to the measuring window. Move the mass calibration to the peak. Add to move the peak to the right and subtract to move the peak to the left.

E.6 Sequence editor

1. Set up sequence
2. Analyse a drift monitor followed by a blank every 10th sample or so
3. Select method (on right hand side)
4. Set wash time between samples to 6 min
5. Set uptake time to 60 s
6. Download data after a run:
   1.1. Select all (reset item button)
   1.2. Untick Acquire
   1.3. Tick evaluate
   1.4. Tick ascii sample report
   1.5. Tick ascii report sequence browse
   1.6. Select the required output style (normally Andy intensity and Ratio Average, SD, Relative SD it isotope ratios are measured)

References

Abadie, C., Lacan, F., Radic, A. and Poitrasson, F. (**2013**). Dissolved and particulate iron concentrations and isotopic compositions in the South Atlantic and Southern Ocean. *Goldschmidt.* Florence, Italy.

Achterberg, E. P., Moore, C. M., Henson, S. A., Steigenberger, S., Stohl, A., Eckhardt, S., Avendano, L. C., Cassidy, M., Hembury, D., Klar, J. K., Lucas, M. I., Macey, A. I., Marsay, C. M. and Ryan-Keogh, T. J. (**2013**) Natural iron fertilization by the Eyjafjallajökull volcanic eruption. *Geophysical Research Letters,* 40**,** 921-926.

Albarède, F. and Beard, B. L. (**2004b**) Correction to Reviews in Mineralogy and Geochemistry Vol. 55, Geochemistry of Non-Traditional Stable Isotopes Chapter 4 "Analytical Methods for Non-Traditional Isotopes" Pages 113-152.

Albarède, F. and Beard, B., (**2004a**) Analytical methods for non-traditional isotopes. *In:* Johnson, C. M., Beard, B. L. & Albarède, F. (eds.) *Geochemistry of Non-Traditional Stable Isotopes.*

Aller, R. C., (**2001**) Transport and reaction in the bioirrigated zone. *In:* Boudreau, B. P. & Jørgensen, B. B. (eds.) *The Benthic Boundary Layer. Transport Processes and Biogeochemistry.* Oxford: Oxford University Press.

Anbar, A. D. (**2004**) Iron stable isotopes: beyond biosignatures. *Earth and Planetary Science Letters,* 217**,** 223-236.

Anbar, A. D., Jarzecki, A. A. and Spiro, T. G. (**2005**) Theoretical investigation of iron isotope fractionation between Fe(H2O)(3+)(6) and Fe(H2O)(2+)(6) : Implications for iron stable isotope geochemistry. *Geochimica et Cosmochimica Acta,* 69**,** 825-837.

Anbar, A. D., Roe, J. E., Barling, J. and Nealson, K. H. (**2000**) Nonbiological fractionation of iron isotopes. *Science,* 288**,** 126-128.

Baker, A. R. and Croot, P. L. (**2010**) Atmospheric and marine controls on aerosol iron solubility in seawater. *Marine Chemistry,* 120**,** 4-13.

Baker, A. R., Kelly, S. D., Biswas, K. F., Witt, M. and Jickells, T. D. (**2003**) Atmospheric deposition of nutrients to the Atlantic Ocean. *Geophysical Research Letters,* 30.

Baker, A. R., Lesworth, T., Adams, C., Jickells, T. D. and Ganzeveld, L. (**2010**) Estimation of atmospheric nutrient inputs to the Atlantic Ocean from 50 degrees N to 50 degrees S based on large-scale field sampling: Fixed nitrogen and dry deposition of phosphorus. *Global Biogeochemical Cycles,* 24.

Balci, N., Bullen, T. D., Witte-Lien, K., Shanks, W. C., Motelica, M. and Mandernack, K. W. (**2006**) Iron isotope fractionation during microbially stimulated Fe(II) oxidation and Fe(III) precipitation. *Geochimica Et Cosmochimica Acta,* 70**,** 622-639.

Barker, P. F. (**1970**) Plate Tectonics of Scotia-Sea region. *Nature,* 228**,** 1293-&.

Beard, B. L., Johnson, C. M., Cox, L., Sun, H., Nealson, K. H. and Aguilar, C. (**1999**) Iron isotope biosignatures. *Science,* 285**,** 1889-1892.

Beard, B. L., Johnson, C. M., Skulan, J. L., Nealson, K. H., Cox, L. and Sun, H. (**2003a**) Application of Fe isotopes to tracing the geochemical and biological cycling of Fe. *Chemical Geology,* 195**,** 87-117.

Beard, B. L., Johnson, C. M., Von Damm, K. L. and Poulson, R. L. (**2003b**) Iron isotope constraints on Fe cycling and mass balance in oxygenated Earth oceans. *Geology,* 31**,** 629-632.

Bennett, S. A., Achterberg, E. P., Connelly, D. P., Statham, P. J., Fones, G. R. and German, C. R. (**2008**) The distribution and stabilisation of dissolved Fe in deep-sea hydrothermal plumes. *Earth and Planetary Science Letters,* 270**,** 157-167.

Bennett, S. A., Rouxel, O., Schmidt, K., Garbe-Schönberg, D., Statham, P. J. and German, C. R. (**2009**) Iron isotope fractionation in a buoyant hydrothermal plume, 5 degrees S Mid-Atlantic Ridge. *Geochimica Et Cosmochimica Acta,* 73**,** 5619-5634.

Bergquist, B. A. and Boyle, E. A. (**2006**) Iron isotopes in the Amazon River system: Weathering and transport signatures. *Earth and Planetary Science Letters,* 248**,** 54-68.

Bourles, B., Molinari, R. L., Johns, E., Wilson, W. D. and Leaman, K. D. (**1999**) Upper layer currents in the western tropical North Atlantic (1989-1991). *Journal of Geophysical Research-Oceans,* 104**,** 1361-1375.

Boyd, P. W. and Ellwood, M. J. (**2010**) The biogeochemical cycle of iron in the ocean. *Nature Geoscience,* 3.

Boyle, E. and Jenkins, W. (**2008**) Hydrothermal iron in the deep western South Pacific. *Geochimica Et Cosmochimica Acta,* 72**,** A107-A107.

Brandt, P., Hormann, V., Kortzinger, A., Visbeck, M., Krahmann, G., Stramma, L., Lumpkin, R. and Schmid, C. (**2010**) Changes in the Ventilation of the Oxygen Minimum Zone of the Tropical North Atlantic. *Journal of Physical Oceanography,* 40**,** 1784-1801.

Brantley, S. L., Liermann, L. J., Guynn, R. L., Anbar, A., Icopini, G. A. and Barling, J. (**2004**) Fe isotopic fractionation during mineral dissolution with and without bacteria. *Geochimica Et Cosmochimica Acta,* 68**,** 3189-3204.

Brown, M. T. and Bruland, K. W. (**2008**) An improved flow-injection analysis method for the determination of dissolved aluminum in seawater. *Limnology and Oceanography-Methods,* 6**,** 87-95.

Bruguier, N. J. and Livermore, R. A. (**2001**) Enhanced magma supply at the southern East Scotia Ridge: evidence for mantle flow around the subducting slab? *Earth and Planetary Science Letters,* 191**,** 129-144.

Bruland, K. W., Franks, R. P., Knauer, G. A. and Martin, J. H. (**1979**) Sampling and analytical methods for the determination of copper, cadmium, zinc, and nickel at the nanogram per liter level in sea-water. *Analytica Chimica Acta,* 105**,** 233-245.

Bullen, T. D., White, A. F., Childs, C. W., Vivit, D. V. and Schulz, M. S. (**2001**) Demonstration of significant abiotic iron isotope fractionation in nature. *Geology,* 29**,** 699-702.

Callahan, J. E. (**1972**) The structure and circulation of deep water in the Antarctic. *Deep-Sea Research,* 19**,** 536-75.

Chan, F., Barth, J. A., Lubchenco, J., Kirincich, A., Weeks, H., Peterson, W. T. and Menge, B. A. (**2008**) Emergence of anoxia in the California current large marine ecosystem. *Science,* 319**,** 920-920.

Cheah, S. F., Kraemer, S. M., Cervini-Silva, J. and Sposito, G. (**2003**) Steady-state dissolution kinetics of goethite in the presence of desferrioxamine B and oxalate ligands: implications for the microbial acquisition of iron. *Chemical Geology,* 198**,** 63-75.

Chester, R. (**2000**) *Marine Geochemistry,* London, Wiley-Blackwell.

Chester, R., Murphy, K. J. T., Lin, F. J., Berry, A. S., Bradshaw, G. A. and Corcoran, P. A. (**1993**) Factors controlling the solubilities of trace-metals from nonremote aerosols deposited to the sea-surface by the dry deposition mode. *Marine Chemistry,* 42**,** 107-126.

Chever, F., Rouxel, O., Croot, P., Ponzevera, E., Wuttig, K. and Auro, M. (**submitted**) Total dissolvable and dissolved iron isotopes in the water column of the Peru upwelling regime. *Geochimica et Cosmochimica Acta*.

Chiang, J. C. H., Kushnir, Y. and Giannini, A. (**2002**) Deconstructing Atlantic Intertropical Convergence Zone variability: Influence of the local cross-equatorial sea surface temperature gradient and remote forcing from the eastern equatorial Pacific. *Journal of Geophysical Research: Atmospheres,* 107**,** ACL 3-1-ACL 3-19.

Cole, C. S., James, R. H., Connelly, D. P. and Hathorne, E. C. (**2014**) Rare earth elements as indicators of hydrothermal processes within the East Scotia subduction zone system. *Geochimica et Cosmochimica Acta,* 140**,** 20-38.

Conway, T. M. and John, S. G. (**2014**) Quantification of dissolved iron sources to the North Atlantic Ocean. *Nature,* advance online publication.

Conway, T. M., Rosenberg, A. D., Adkins, J. F. and John, S. G. (**2013**) A new method for precise determination of iron, zinc and cadmium stable isotope ratios in seawater by double-spike mass spectrometry. *Analytica Chimica Acta,* 793**,** 44-52.

Corami, F., Capodaglio, G., Turetta, C., Soggia, F., Magi, E. and Grotti, M. (**2005**) Summer distribution of trace metals in the western sector of the Ross Sea, Antarctica. *Journal of Environmental Monitoring,* 7**,** 1256-1264.

Croal, L. R., Johnson, C. M., Beard, B. L. and Newman, D. K. (**2004**) Iron isotope fractionation by Fe(II)-oxidizing photoautotrophic bacteria. *Geochimica et Cosmochimica Acta,* 68**,** 1227-1242.

Crosby, H. A., Roden, E. E., Johnson, C. M. and Beard, B. L. (**2007**) The mechanisms of iron isotope fractionation produced during dissimilatory Fe(III) reduction by Shewanella putrefaciens and Geobacter sulfurreducens. *Geobiology,* 5**,** 169-189.

Dauphas, N., Pourmand, A. and Teng, F. Z. (**2009**) Routine isotopic analysis of iron by HR-MC-ICPMS: How precise and how accurate? *Chemical Geology,* 267**,** 175-184.

de Jong, J., Schoemann, V., Tison, J. L., Becquevort, S., Masson, F., Lannuzel, D., Petit, J., Chou, L., Weis, D. and Mattielli, N. (**2007**) Precise measurement of Fe isotopes in marine samples by multi-collector inductively coupled plasma mass spectrometry (MC-ICP-MS). *Analytica Chimica Acta,* 589**,** 105-119.

de Ronde, C. E. J., Massoth, G. J., Butterfield, D. A., Christenson, B. W., Ishibashi, J., Ditchburn, R. G., Hannington, M. D., Brathwaite, R. L., Lupton, J. E., Kamenetsky, V. S., Graham, I. J., Zellmer, G. F., Dziak, R. P., Embley, R. W., Dekov, V. M., Munnik, F., Lahr, J., Evans, L. J. and Takai, K. (**2011**) Submarine hydrothermal activity and gold-rich mineralization at Brothers Volcano, Kermadec Arc, New Zealand. *Mineralium Deposita,* 46**,** 541-584.

Dideriksen, K., Baker, J. A. and Stipp, S. L. S. (**2006**) Iron isotopes in natural carbonate minerals determined by MC-ICP-MS with a Fe-58-Fe-54 double spike. *Geochimica et Cosmochimica Acta,* 70**,** 118-132.

Dideriksen, K., Baker, J. A. and Stipp, S. L. S. (**2008**) Equilibrium Fe isotope fractionation between inorganic aqueous Fe(III) and the siderophore complex, Fe(III)-desferrioxamine B. *Earth and Planetary Science Letters,* 269**,** 280-290.

Douville, E., Charlou, J. L., Oelkers, E. H., Bienvenu, P., Colon, C. F. J., Donval, J. P., Fouquet, Y., Prieur, D. and Appriou, P. (**2002**) The rainbow vent fluids (36 degrees 14 ' N, MAR): the influence of ultramafic rocks and phase separation on trace metal content in Mid-Atlantic Ridge hydrothermal fluids. *Chemical Geology,* 184**,** 37-48.

Duggen, S., Olgun, N., Croot, P., Hoffmann, L., Dietze, H., Delmelle, P. and Teschner, C. (**2010**) The role of airborne volcanic ash for the surface ocean biogeochemical iron-cycle: a review. *Biogeosciences,* 7**,** 827-844.

Edwards, K. J., Bach, W., McCollom, T. M. and Rogers, D. R. (**2004**) Neutrophilic iron-oxidizing bacteria in the ocean: Their habitats, diversity, and roles in mineral deposition, rock alteration, and biomass production in the deep-sea. *Geomicrobiology Journal,* 21**,** 393-404.

Elderfield, H. and Schultz, A. (**1996**) Mid-ocean ridge hydrothermal fluxes and the chemical composition of the ocean. *Annual Review of Earth and Planetary Sciences,* 24**,** 191-224.

Elrod, V. A., Berelson, W. M., Coale, K. H. and Johnson, K. S. (**2004**) The flux of iron from continental shelf sediments: A missing source for global budgets. *Geophysical Research Letters,* 31.

Elrod, V. A., Johnson, K. S., Fitzwater, S. E. and Plant, J. N. (**2008**) A long-term, high-resolution record of surface water iron concentrations in the upwelling-driven central California region. *Journal of Geophysical Research-Oceans,* 113.

Escoube, R., Rouxel, O. J., Sholkovitz, E. and Donard, O. F. X. (**2009**) Iron isotope systematics in estuaries: The case of North River, Massachusetts (USA). *Geochimica Et Cosmochimica Acta,* 73**,** 4045-4059.

Fahrbach, E., Rohardt, G., Schroder, M. and Strass, V. (**1994**) Transport and structure of the Weddell gyre. *Annales Geophysicae-Atmospheres Hydrospheres and Space Sciences,* 12**,** 840-855.

Falkowski, P. G. (**1997**) Evolution of the nitrogen cycle and its influence on the biological sequestration of CO2 in the ocean. *Nature,* 387**,** 272-275.

Falkowski, P. G., Barber, R. T. and Smetacek, V. (**1998**) Biogeochemical controls and feedbacks on ocean primary production. *Science,* 281**,** 200-206.

Fantle, M. S. and Depaolo, D. J. (**2004**) Iron isotopic fractionation during continental weathering. *Earth and Planetary Science Letters,* 228**,** 547-562.

Field, M. P. and Sherrell, R. M. (**2000**) Dissolved and particulate Fe in a hydrothermal plume at 9 degrees 45 ' N, East Pacific Rise: Slow Fe (II) oxidation kinetics in Pacific plumes. *Geochimica et Cosmochimica Acta,* 64**,** 619-628.

Fitzsimmons, J. N., Zhang, R. and Boyle, E. A. (**2013**) Dissolved iron in the tropical North Atlantic Ocean. *Marine Chemistry,* 154**,** 87-99.

Fretzdorff, S., Livermore, R. A., Devey, C. W., Leat, P. T. and Stoffers, P. (**2002**) Petrogenesis of the back-arc east Scotia Ridge, South Atlantic Ocean. *Journal of Petrology,* 43**,** 1435-1467.

Galer, S. J. G. (**1999**) Optimal double and triple spiking for high precision lead isotopic measurement. *Chemical Geology,* 157**,** 255-274.

Gallant, R. M. and Von Damm, K. L. (**2006**) Geochemical controls on hydrothermal fluids from the Kairei and Edmond Vent Fields, 23 degrees-25 degrees S, Central Indian Ridge. *Geochemistry Geophysics Geosystems,* 7.

Gartman, A., Findlay, A. J. and Luther, G. W., Iii (**2014**) Nanoparticulate pyrite and other nanoparticles are a widespread component of hydrothermal vent black smoker emissions. *Chemical Geology,* 366**,** 32-41.

Gehlen, M., Beck, L., Calas, G., Flank, A. M., Van Bennekom, A. J. and Van Beusekom, J. E. E. (**2002**) Unraveling the atomic structure of biogenic silica: Evidence of the structural association of Al and Si in diatom frustules. *Geochimica et Cosmochimica Acta,* 66**,** 1601-1609.

Geider, R. J. and LaRoche, J. (**1994**) The role of Iron in phytoplankton photosynthesis, and the potential for Iron-limitation of primary productivity in the Sea. *Photosynthesis Research,* 39**,** 275-301.

German, C. R. and Von Damm, K. L., (**2003**) Hydrothermal circulation. *In:* Holland, H. D. & Turekian, K. K. (eds.) *Treatise on Geochemistry.* Amsterdam: Elsevier.

German, C. R., Livermore, R. A., Baker, E. T., Bruguier, N. I., Connelly, D. P., Cunningham, A. P., Morris, P., Rouse, I. P., Statham, P. J. and Tyler, P. A. (**2000**) Hydrothermal plumes above the East Scotia Ridge: an isolated high-latitude back-arc spreading centre. *Earth and Planetary Science Letters,* 184**,** 241-250.

Gledhill, M. and Buck, K. N. (**2012**) The organic complexation of iron in the marine environment: a review. *Frontiers in Microbiology,* 3.

Gledhill, M. and van den Berg, C. M. G. (**1994**) Determination of complexation of iron(III) with natural organic complexing ligands in seawater using cathodic stripping voltametry. *Marine Chemistry,* 47**,** 41-54.

Gordon, L. A., Weiss, R. F., Smethie, W. M., Jr. and Warner, M. J. (**1992**) Thermocline and intermediate water communication between the South Atlantic and Indian Oceans. *Journal of Geophysical Research,* 97**,** 7223-40.

Hawkes, J. A. (**2013**) *Iron Speciation in Hydrothermal Plumes.* Doctor of Philosophy, University of Southampton.

Hawkes, J. A., Connelly, D. P., Gledhill, M. and Achterberg, E. P. (**2013**) The stabilisation and transportation of dissolved iron from high temperature hydrothermal vent systems. *Earth and Planetary Science Letters,* 375**,** 280-290.

Hawkes, J. A., Connelly, D. P., Rijkenberg, M. J. A. and Achterberg, E. P. (**2014**) The importance of shallow hydrothermal island arc systems in ocean biogeochemistry. *Geophysical Research Letters***,** 2013GL058817.

Homann, V. V., Sandy, M., Tincu, J. A., Templeton, A. S., Tebo, B. M. and Butler, A. (**2009**) Loihichelins A-F, a Suite of Amphiphilic Siderophores Produced by the Marine Bacterium Halomonas LOB-5. *Journal of Natural Products,* 72**,** 884-888.

Homoky, W. B., John, S. G., Conway, T. M. and Mills, R. A. (**2013**) Distinct iron isotopic signatures and supply from marine sediment dissolution. *Nat Commun,* 4.

Homoky, W. B., Severmann, S., Mills, R. A., Statham, P. J. and Fones, G. R. (**2009**) Pore-fluid Fe isotopes reflect the extent of benthic Fe redox recycling: Evidence from continental shelf and deep-sea sediments. *Geology,* 37**,** 751-754.

Icopini, G. A., Anbar, A. D., Ruebush, S. S., Tien, M. and Brantley, S. L. (**2004**) Iron isotope fractionation during microbial reduction of iron: The importance of adsorption. *Geology,* 32**,** 205-208.

Ilina, S. M., Poitrasson, F., Lapitskiy, S. A., Alekhin, Y. V., Viers, J. and Pokrovsky, O. S. (**2013**) Extreme iron isotope fractionation between colloids and particles of boreal and temperate organic-rich waters. *Geochimica et Cosmochimica Acta,* 101**,** 96-111.

Ingri, J., Malinovsky, D., Rodushkin, I., Baxter, D. C., Widerlund, A., Andersson, P., Gustafsson, O., Forsling, W. and Ohlander, B. (**2006**) Iron isotope fractionation in river colloidal matter. *Earth and Planetary Science Letters,* 245**,** 792-798.

James, R. H., Green, D. R. H., Stock, M. J., Alker, B. J., Banerjee, N. R., Cole, C., German, C. R., Huvenne, V. a. I., Powell, A. M. and Connelly, D. P. (**2014**) Composition of hydrothermal fluids and mineralogy of associated chimney material on the East Scotia Ridge back-arc spreading centre. *Geochimica et Cosmochimica Acta,* 139**,** 47-71.

Jickells, T. D. and Spokes, L. J., (**2001**) Atmospheric Iron Inputs to the Oceans. *In:* Turner, D. R. & Hunter, K. A. (eds.) *The Biogeochemistry of Iron in Seawater.* Chichester: John Wiley & Sons Ltd.

Jickells, T. D., An, Z. S., Andersen, K. K., Baker, A. R., Bergametti, G., Brooks, N., Cao, J. J., Boyd, P. W., Duce, R. A., Hunter, K. A., Kawahata, H., Kubilay, N., Laroche, J., Liss, P. S., Mahowald, N., Prospero, J. M., Ridgwell, A. J., Tegen, I. and Torres, R. (**2005**) Global iron connections between desert dust, ocean biogeochemistry, and climate. *Science,* 308**,** 67-71.

John, S. G. and Adkins, J. (**2012**) The vertical distribution of iron stable isotopes in the North Atlantic near Bermuda. *Global Biogeochemical Cycles,* 26.

John, S. G. and Adkins, J. F. (**2010**) Analysis of dissolved iron isotopes in seawater. *Marine Chemistry,* 119**,** 65-79.

John, S. G., Mendez, J., Moffett, J. and Adkins, J. (**2012**) The flux of iron and iron isotopes from San Pedro Basin sediments. *Geochimica et Cosmochimica Acta,* 93**,** 14-29.

Johnson, C. M., Skulan, J. L., Beard, B. L., Sun, H., Nealson, K. H. and Braterman, P. S. (**2002**) Isotopic fractionation between Fe(III) and Fe(II) in aqueous solutions. *Earth and Planetary Science Letters,* 195**,** 141-153.

Johnson, K. S., Gordon, R. M. and Coale, K. H. (**1997**) What controls dissolved iron concentrations in the world ocean? *Marine Chemistry,* 57**,** 137-161.

Kara, A. B., Rochford, P. A. and Hurlburt, H. E. (**2000**) An optimal definition for ocean mixed layer depth. *Journal of Geophysical Research: Oceans,* 105**,** 16803-16821.

Keeling, R. F., Koertzinger, A. and Gruber, N. (**2010**) Ocean Deoxygenation in a Warming World. *Annual Review of Marine Science,* 2**,** 199-229.

Kelley, D. S., Baross, J. A. and Delaney, J. R. (**2002**) Volcanoes, fluids, and life at mid-ocean ridge spreading centers. *Annual Review of Earth and Planetary Sciences,* 30**,** 385-491.

Klunder, M. B., Laan, P., Middag, R., De Baar, H. J. W. and Van Ooijen, J. C. (**2011**) Dissolved iron in the Southern Ocean (Atlantic sector). *Deep Sea Research Part II: Topical Studies in Oceanography,* 58**,** 2678-2694.

Kramer, J., Laan, P., Sarthou, G., Timmermans, K. R. and de Baar, H. J. W. (**2004**) Distribution of dissolved aluminium in the high atmospheric input region of the subtropical waters of the North Atlantic Ocean. *Marine Chemistry,* 88**,** 85-101.

Lacan, F., Radic, A., Jeandel, C., Poitrasson, F., Sarthou, G., Pradoux, C. and Freydier, R. (**2008**) Measurement of the isotopic composition of dissolved iron in the open ocean. *Geophysical Research Letters,* 35.

Lacan, F., Radic, A., Labatut, M., Jeandel, C., Poitrasson, F., Sarthou, G., Pradoux, C., Chmeleff, J. and Freydier, R. (**2010**) High-Precision Determination of the Isotopic Composition of Dissolved Iron in Iron Depleted Seawater by Double Spike Multicollector-ICPMS. *Analytical Chemistry,* 82**,** 7103-7111.

Laës, A., Blain, S., Achterberg, E. P., Sarthou, G. and de Baar, H. J. W. (**2003**) Deep dissolved iron profiles in the eastern North Atlantic in relation to water masses. *Geophysical Research Letters,* 30**,** OCE8-1-4.

Lang, S. Q., Butterfield, D. A., Lilley, M. D., Johnson, H. P. and Hedges, J. I. (**2006**) Dissolved organic carbon in ridge-axis and ridge-flank hydrothermal systems. *Geochimica Et Cosmochimica Acta,* 70**,** 3830-3842.

Larter, R. D., Vanneste, L. E., Morris, P. and Smyth, D. K., (**2003**) Tectonic evolution and structure of the South Sandwich arc. *In:* Larter, R. D. & Leat, P. T. (eds.) *Intra-Oceanic Subduction Systems: Tectonic and Magmatic Processes.* London: Geol. Soc. London Spec. Publ.

Leat, P. T., Livermore, R. A., Millar, I. L. and Pearce, J. A. (**2000**) Magma supply in back-arc spreading centre segment E2, East Scotia Ridge. *Journal of Petrology,* 41**,** 845-866.

Leat, P. T., Pearce, J. A., Barker, R. F., Millar, I. L., Barry, T. L. and Larter, R. D. (**2004**) Magma genesis and mantle flow at a subducting slab edge: the South Sandwich arc-basin system. *Earth and Planetary Science Letters,* 227**,** 17-35.

Lee, J. M., Boyle, E. A., Echegoyen-Sanz, Y., Fitzsimmons, J. N., Zhang, R. F. and Kayser, R. A. (**2011**) Analysis of trace metals (Cu, Cd, Pb, and Fe) in seawater using single batch nitrilotriacetate resin extraction and isotope dilution inductively coupled plasma mass spectrometry. *Analytica Chimica Acta,* 686**,** 93-101.

Leybourne, M. I., Schwarz-Schampera, U., de Ronde, C. E. J., Baker, E. T., Faure, K., Walker, S. L., Butterfield, D. A., Resing, J. A., Lupton, J. E., Hannington, M. D., Gibson, H. L., Massoth, G. J., Embley, R. W., Chadwick, W. W., Jr., Clark, M. R., Timm, C., Graham, I. J. and Wright, I. C. (**2012**) Submarine Magmatic-Hydrothermal Systems at the Monowai Volcanic Center, Kermadec Arc. *Economic Geology,* 107**,** 1669-1694.

Lim, B. and Jickells, T. D. (**1990**) Dissolved particulate and acid-leachable trace metal concentrations in North Atlantic precipitation collected on the global change expedition. *Global Biogeochemical Cycles,* 4**,** 445-458.

Liu, X. and Millero, F. J. (**2002**) The solubility of iron in seawater. *Marine Chemistry,* 77**,** 43-54.

Liu, X. W. and Millero, F. J. (**1999**) The solubility of iron hydroxide in sodium chloride solutions. *Geochimica Et Cosmochimica Acta,* 63**,** 3487-3497.

Livermore, R., Cunningham, A., Vanneste, L. and Larter, R. (**1997**) Subduction influence on magma supply at the East Scotia Ridge. *Earth and Planetary Science Letters,* 150**,** 261-275.

Locarnini, R. A., Whitworth, T. and Nowlin, W. D. (**1993**) The importance of the Scotia Sea on the outflow of Weddell Sea deep-water *Journal of Marine Research,* 51**,** 445-445.

Lohan, M. C., Aguilar-Islas, A. M., Franks, R. P. and Bruland, K. W. (**2005**) Determination of iron and copper in seawater at pH 1.7 with a new commercially available chelating resin, NTA Superflow. *Analytica Chimica Acta,* 530**,** 121-129.

Ludwig, K. R. (**1986**). Contraints on time-efficient data-taking strategies for single-collector, isotope-ratio mass spectrometers. *Shorter contributions to isotope research.* U.S. Geological Survey Bulletin.

Mahowald, N. M., Baker, A. R., Bergametti, G., Brooks, N., Duce, R. A., Jickells, T. D., Kubilay, N., Prospero, J. M. and Tegen, I. (**2005**) Atmospheric global dust cycle and iron inputs to the ocean. *Global Biogeochemical Cycles,* 19.

Mandernack, K. W., Bazylinski, D. A., Shanks, W. C. and Bullen, T. D. (**1999**) Oxygen and iron isotope studies of magnetite produced by magnetotactic bacteria. *Science,* 285**,** 1892-1896.

Maring, H. B. and Duce, R. A. (**1987**) The impact of atmospheric aerosols on trace metal chemistry in open ocean surface seawater. 1. Aluminum. *Earth and Planetary Science Letters,* 84**,** 381-392.

Martin, J. H. and Fitzwater, S. E. (**1988**) Iron-deficiency limits phytoplankton growth in the northeast Pacific Subarctic. *Nature,* 331**,** 341-343.

Martin, J. H., Coale, K. H., Johnson, K. S., Fitzwater, S. E., Gordon, R. M., Tanner, S. J., Hunter, C. N., Elrod, V. A., Nowicki, J. L., Coley, T. L., Barber, R. T., Lindley, S., Watson, A. J., Vanscoy, K., Law, C. S., Liddicoat, M. I., Ling, R., Stanton, T., Stockel, J., Collins, C., Anderson, A., Bidigare, R., Ondrusek, M., Latasa, M., Millero, F. J., Lee, K., Yao, W., Zhang, J. Z., Friederich, G., Sakamoto, C., Chavez, F., Buck, K., Kolber, Z., Greene, R., Falkowski, P., Chisholm, S. W., Hoge, F., Swift, R., Yungel, J., Turner, S., Nightingale, P.,

Hatton, A., Liss, P. and Tindale, N. W. (**1994**) Testing the iron hypothesis in ecosystems of the Equatorial Pacific-Ocean. *Nature,* 371**,** 123-129.

Martin, J. H., Fitzwater, S. E. and Gordon, R. M. (**1990**) Iron deficiency limits phytoplankton growth in Antarctic waters. *Global Biogeochemical Cycles,* 4**,** 5-12.

Mead, C., Herckes, P., Majestic, B. J. and Anbar, A. D. (**2013**) Source apportionment of aerosol iron in the marine environment using iron isotope analysis. *Geophysical Research Letters,* 40**,** 5722-5727.

Measures, C. I. and Brown, E. T., (**1996**) Estimating dust input to the Atlantic Ocean using surface water Al concentrations. *In:* Guerzoni, S. & Chester, R. (eds.) *The Impact of Desert Dust Across the Mediterranean.* Dortrecht: Kluwer Academic Publishers.

Measures, C. I. and Vink, S. (**2000**) On the use of dissolved aluminum in surface waters to estimate dust deposition to the ocean. *Global Biogeochemical Cycles,* 14**,** 317-327.

Measures, C. I., Landing, W. M., Brown, M. T. and Buck, C. S. (**2008**) High-resolution Al and Fe data from the Atlantic Ocean CLIVAR-CO2 repeat hydrography A16N transect: Extensive linkages between atmospheric dust and upper ocean geochemistry. *Global Biogeochemical Cycles,* 22.

Middag, R., de Baar, H. J. W., Laan, P., Cai, P. H. and Van Ooijen, J. C. (**2011**) Dissolved manganese in the Atlantic sector of the Southern Ocean. *Deep Sea Research Part II: Topical Studies in Oceanography,* 58**,** 2661-2677.

Mikutta, C., Wiederhold, J. G., Cirpka, O. A., Hofstetter, T. B., Bourdon, B. and Von Gunten, U. (**2009**) Iron isotope fractionation and atom exchange during sorption of ferrous iron to mineral surfaces. *Geochimica Et Cosmochimica Acta,* 73**,** 1795-1812.

Millero, F. J., Sotolongo, S. and Izaguirre, M. (**1987**) The oxidation-kinetics of Fe(II) in seawater. *Geochimica et Cosmochimica Acta,* 51**,** 793-801.

Mittelstaedt, E. (**1983**) The upwelling area off northwest Africa - a description of phenomena related to coastal upwelling. *Progress in Oceanography,* 12**,** 307-331.

Molinari, R. L., Garzoli, S. L., Katz, E. J., Harrison, D. E., Richardson, P. L. and Reverdin, G. (**1986**) Asynthesis of the 1st GARP global experiment (FGGE) in the equatorial Atlantic-Ocean. *Progress in Oceanography,* 16**,** 91-112.

Moore, C. M., Mills, M. M., Achterberg, E. P., Geider, R. J., Laroche, J., Lucas, M. I., Mcdonagh, E. L., Pan, X., Poulton, A. J., Rijkenberg, M. J. A., Suggett, D. J., Ussher, S. J. and Woodward, E. M. S. (**2009**) Large-scale distribution of Atlantic nitrogen fixation controlled by iron availability. *Nature Geoscience,* 2**,** 867-871.

Moran, S. B. and Moore, R. M. (**1992**) Kinetics of the removal of dissolved aluminum by diatoms in seawater: A comparison with thorium. *Geochimica et Cosmochimica Acta,* 56**,** 3365-3374.

Morel, F. M. M. and Price, N. M. (**2003**) The biogeochemical cycles of trace metals in the oceans. *Science,* 300**,** 944-947.

Morgan, J. L. L., Wasylenki, L. E., Nuester, J. and Anbar, A. D. (**2010**) Fe Isotope Fractionation during Equilibration of Fe-Organic Complexes. *Environmental Science & Technology,* 44**,** 6095-6101.

Mottl, M. J., Seewald, J. S., Wheat, C. G., Tivey, M. K., Michael, P. J., Proskurowski, G., McCollom, T. M., Reeves, E., Sharkey, J., You, C. F., Chan, L. H. and Pichler, T. (**2011**) Chemistry of hot springs along the Eastern Lau Spreading Center. *Geochimica et Cosmochimica Acta,* 75**,** 1013-1038.

Naveira Garabato, A. C., Heywood, K. J. and Stevens, D. P. (**2002**) Modification and pathways of Southern Ocean Deep Waters in the Scotia Sea. *Deep Sea Research Part I: Oceanographic Research Papers,* 49**,** 681-705.

Nielsdottir, M. C., Moore, C. M., Sanders, R., Hinz, D. J. and Achterberg, E. P. (**2009**) Iron limitation of the postbloom phytoplankton communities in the Iceland Basin. *Global Biogeochemical Cycles,* 23.

Nowlin, W. D., Jr., Whitworth, T., Iii and Pillsbury, R. D. (**1977**) Structure and transport of the Antarctic Circumpolar Current at Drake Passage from short-term measurements. *Journal of Physical Oceanography,* 7**,** 779-87.

Obata, H., Karatani, H. and Nakayama, E. (**1993**) Automated-determination of iron in seawater by chelating resin concentration and chemiluminescence detection. *Analytical Chemistry,* 65**,** 1524-1528.

Orians, K. J. and Bruland, K. W. (**1986**) The biogeochemistry of aluminum in the Pacific Ocean. *Earth and Planetary Science Letters,* 78**,** 397-410.

Orsi, A. H., Nowlin, W. D. and Whitworth, T. (**1993**) On the circulation and stratification of the Weddell gyre. *Deep-Sea Research Part I-Oceanographic Research Papers,* 40**,** 169-203.

Parekh, P., Follows, M. J. and Boyle, E. A. (**2005**) Decoupling of iron and phosphate in the global ocean. *Global Biogeochemical Cycles,* 19.

Poitrasson, F. (**2006**) On the iron isotope homogeneity level of the continental crust. *Chemical Geology,* 235**,** 195-200.

Poitrasson, F. and Freydier, R. (**2005**) Heavy iron isotope composition of granites determined by high resolution MC-ICP-MS. *Chemical Geology,* 222**,** 132-147.

Poitrasson, F., Halliday, A. N., Lee, D. C., Levasseur, S. and Teutsch, N. (**2004**) Iron isotope differences between Earth, Moon, Mars and Vesta as possible records of contrasted accretion mechanisms. *Earth and Planetary Science Letters,* 223**,** 253-266.

Poulton, S. W. and Raiswell, R. (**2002**) The low-temperature geochemical cycle of iron: From continental fluxes to marine sediment deposition. *American Journal of Science,* 302**,** 774-805.

Powell, A. M., Banerjee, N. R., Munro, L. E., Hisao, G. and James, R. H. (**2011**). Investigations of deep-sea hydrothermal samples for isotopic composition and interfering compounds using CRDS. *International Symposium on Stable*

Isotopes in Hydrology,Marine Ecosystems and Climate change Studies. Oceanographic Museum of Monaco.

Prospero, J. M., Glaccum, R. A. and Nees, R. T. (**1981**) Atmospheric transport of soil dust from Africa to South-America. *Nature,* 289**,** 570-572.

Radic, A., Lacan, F. and Murray, J. W. (**2011**) Iron isotopes in the seawater of the equatorial Pacific Ocean: New constraints for the oceanic iron cycle. *Earth and Planetary Science Letters,* 306**,** 1-10.

Raiswell, R., Benning, L. G., Tranter, M. and Tulaczyk, S. (**2008**) Bioavailable iron in the Southern Ocean: the significance of the iceberg conveyor belt. *Geochemical Transactions,* 9.

Raiswell, R., Tranter, M., Benning, L. G., Siegert, M., De'ath, R., Huybrechts, P. and Payne, T. (**2006**) Contributions from glacially derived sediment to the global iron (oxyhydr)oxide cycle: Implications for iron delivery to the oceans. *Geochimica Et Cosmochimica Acta,* 70**,** 2765-2780.

Reid, J. L. (**1997**) On the total geostrophic circulation of the Pacific Ocean: flow patterns, tracers, and transports. *Progress in Oceanography,* 39**,** 263-352.

Resing, J. A. and Measures, C. I. (**1994**) Fluorometric determination of Al in seawater by Flow-Injection-Analysis with in-line preconcentration. *Analytical Chemistry,* 66**,** 4105-4111.

Resing, J. A., Lebon, G., Baker, E. T., Lupton, J. E., Embley, R. W., Massoth, G. J., Chadwick, W. W., Jr. and De Ronde, C. E. J. (**2007**) Venting of acid-sulfate fluids in a high-sulfidation setting at NW rota-1 submarine volcano on the mariana arc. *Economic Geology,* 102**,** 1047-1061.

Richier, S., Macey, A. I., Pratt, N. J., Honey, D. J., Moore, C. M. and Bibby, T. S. (**2012**) Abundances of Iron-Binding Photosynthetic and Nitrogen-Fixing Proteins of Trichodesmium Both in Culture and In Situ from the North Atlantic. *Plos One,* 7.

Rijkenberg, M. J. A., Middag, R., Laan, P., Gerringa, L. J. A., Van Aken, H. M., Schoemann, V., de Jong, J. T. M. and de Baar, H. J. W. (**2014**) The distribution of dissolved iron in the west atlantic ocean. *PloS one,* 9**,** e101323-e101323.

Rijkenberg, M. J. A., Steigenberger, S., Powell, C. F., Van Haren, H., Patey, M. D., Baker, A. R. and Achterberg, E. P. (**2012**) Fluxes and distribution of dissolved iron in the eastern (sub-) tropical North Atlantic Ocean. *Global Biogeochemical Cycles,* 26.

Rintoul, S. R. (**1991**) South-Atlantic interbasin exchange. *Journal of Geophysical Research-Oceans,* 96**,** 2675-2692.

Rouxel, O. J. and Auro, M. (**2010**) Iron Isotope Variations in Coastal Seawater Determined by Multicollector ICP-MS. *Geostandards and Geoanalytical Research,* 34**,** 135-144.

Rouxel, O., Shanks, W. C., Bach, W. and Edwards, K. J. (**2008a**) Integrated Fe- and S-isotope study of seafloor hydrothermal vents at East Pacific rise 9-10 degrees N. *Chemical Geology,* 252**,** 214-227.

Rouxel, O., Sholkovitz, E., Charette, M. and Edwards, K. J. (**2008b**) Iron isotope fractionation in subterranean estuaries. *Geochimica Et Cosmochimica Acta,* 72**,** 3413-3430.

Roy, M., Rouxel, O., Martin, J. B. and Cable, J. E. (**2012**) Iron isotope fractionation in a sulfide-bearing subterranean estuary and its potential influence on oceanic Fe isotope flux. *Chemical Geology,* 300**,** 133-142.

Rudge, J. F., Reynolds, B. C. and Bourdon, B. (**2009**) The double spike toolbox. *Chemical Geology,* 265**,** 420-431.

Rudnicki, M. D. and Elderfield, H. (**1993**) A chemical model of the buoyant and neutrally buoyant plume above the TAG vent field, 26 degrees N, Mid-Atlantic Ridge. *Geochimica et Cosmochimica Acta,* 57**,** 2939-2957.

Rue, E. L. and Bruland, K. W. (**1995**) Complexation of iron(III) by natural organic-ligands in the central North Pacific as determined by a new competitive

ligand equilibration adsorptive cathodic stripping voltammetric method. *Marine Chemistry,* 50**,** 117-138.

Saito, M. A., Noble, A. E., Tagliabue, A., Goepfert, T. J., Lamborg, C. H. and Jenkins, W. J. (**2013**) Slow-spreading submarine ridges in the South Atlantic as a significant oceanic iron source. *Nature Geoscience,* 6**,** 775-779.

Sander, S. G. and Koschinsky, A. (**2011**) Metal flux from hydrothermal vents increased by organic complexation. *Nature Geoscience,* 4**,** 145-150.

Sander, S. G., Koschinsky, A., Massoth, G., Stott, M. and Hunter, K. A. (**2007**) Organic complexation of copper in deep-sea hydrothermal vent systems. *Environmental Chemistry,* 4**,** 81-89.

Sands, C. M., Connelly, D. P., Statham, P. J. and German, C. R. (**2012**) Size fractionation of trace metals in the Edmond hydrothermal plume, Central Indian Ocean. *Earth and Planetary Science Letters,* 319**,** 15-22.

Schauble, E. A., Rossman, G. R. and Taylor, H. P. (**2001**) Theoretical estimates of equilibrium Fe-isotope fractionations from vibrational spectroscopy. *Geochimica et Cosmochimica Acta,* 65**,** 2487-2497.

Schlosser, C. and Croot, P. L. (**2008**) Application of cross-flow filtration for determining the solubility of iron species in open ocean seawater. *Limnology and Oceanography-Methods,* 6**,** 630-642.

Schlosser, C., Klar, J. K., Wake, B. D., Snow, J. T., Honey, D. J., Woodward, E. M. S., Lohan, M. C., Achterberg, E. P. and Moore, C. M. (**2013**) Seasonal ITCZ migration dynamically controls the location of the (sub)tropical Atlantic biogeochemical divide. *Proceedings of the National Academy of Sciences*.

Schoenberg, R. and Von Blanckenburg, F. (**2005**) An assessment of the accuracy of stable Fe isotope ratio measurements on samples with organic and inorganic matrices by high-resolution multicollector ICP-MS. *International Journal of Mass Spectrometry,* 242**,** 257-272.

Severmann, S., Johnson, C. M., Beard, B. L. and Mcmanus, J. (**2006**) The effect of early diagenesis on the Fe isotope compositions of porewaters and authigenic minerals in continental margin sediments. *Geochimica Et Cosmochimica Acta,* 70**,** 2006-2022.

Severmann, S., Johnson, C. M., Beard, B. L., German, C. R., Edmonds, H. N., Chiba, H. and Green, D. R. H. (**2004**) The effect of plume processes on the Fe isotope composition of hydrothermally derived Fe in the deep ocean as inferred from the Rainbow vent site, Mid-Atlantic Ridge, 36 degrees 14' N. *Earth and Planetary Science Letters,* 225**,** 63-76.

Severmann, S., Mcmanus, J., Berelson, W. M. and Hammond, D. E. (**2010**) The continental shelf benthic iron flux and its isotope composition. *Geochimica Et Cosmochimica Acta,* 74**,** 3984-4004.

Seyfried, W. E., Seewald, J. S., Berndt, M. E., Ding, K. and Foustoukos, D. I. (**2003**) Chemistry of hydrothermal vent fluids from the Main Endeavour Field, northern Juan de Fuca Ridge: Geochemical controls in the aftermath of June 1999 seismic events. *Journal of Geophysical Research-Solid Earth,* 108.

Sharma, M., Polizzotto, M. and Anbar, A. D. (**2001**) Iron isotopes in hot springs along the Juan de Fuca Ridge. *Earth and Planetary Science Letters,* 194**,** 39-51.

Siedlecki, S. A., Mahadevan, A. and Archer, D. E. (**2012**) Mechanism for export of sediment-derived iron in an upwelling regime. *Geophysical Research Letters,* 39.

Siedler, G., Zangenberg, N. and Onken, R. (**1992**) SEASONAL-CHANGES IN THE TROPICAL ATLANTIC CIRCULATION - OBSERVATION AND SIMULATION OF THE GUINEA DOME. *Journal of Geophysical Research-Oceans,* 97**,** 703-715.

Statham, P. J., German, C. R. and Connelly, D. P. (**2005**) Iron(II) distribution and oxidation kinetics in hydrothermal plumes at the Kairei and Edmond vent sites, Indian Ocean. *Earth and Planetary Science Letters,* 236**,** 588-596.

Stramma, L. and Schott, F. (**1999**) The mean flow field of the tropical Atlantic Ocean. *Deep-Sea Research Part Ii-Topical Studies in Oceanography,* 46**,** 279-303.

Stramma, L., Huttl, S. and Schafstall, J. (**2005**) Water masses and currents in the upper tropical northeast Atlantic off northwest Africa. *Journal of Geophysical Research-Oceans,* 110.

Stramma, L., Johnson, G. C., Sprintall, J. and Mohrholz, V. (**2008**) Expanding oxygen-minimum zones in the tropical oceans. *Science,* 320**,** 655-658.

Strelow, F. W. E. (**1980**) Improved separation of iron from copper and other elements by anion-exchange cgromatography on a 4% cross-linked resin with high concentrations of hydrochloric acid. *Talanta,* 27**,** 727-732.

Tagliabue, A., Bopp, L., Dutay, J. C., Bowie, A. R., Chever, F., Jean-Baptiste, P., Bucciarelli, E., Lannuzel, D., Remenyi, T., Sarthou, G., Aumont, O., Gehlen, M. and Jeandel, C. (**2010**) Hydrothermal contribution to the oceanic dissolved iron inventory. *Nature Geoscience,* 3**,** 252-256.

Taylor, P. D. P., Maeck, R. and De Bièvre, P. (**1992**) Determination of the absolute isotopic composition and atomic weight of a reference sample of natural iron. *International Journal of Mass Spectrometry and Ion Processes,* 121**,** 111-125.

Taylor, S. R. (**1964**) Abundance of chemical elements in the continental crust: a new table. *Geochimica et Cosmochimica Acta,* 28**,** 1273-1285.

Teutsch, N., Von Gunten, U., Porcelli, D., Cirpka, O. A. and Halliday, A. N. (**2005**) Adsorption as a cause for iron isotope fractionation in reduced groundwater. *Geochimica Et Cosmochimica Acta,* 69**,** 4175-4185.

Tria, J., Butler, E. C. V., Haddad, P. R. and Bowie, A. R. (**2007**) Determination of aluminium in natural water samples. *Analytica Chimica Acta,* 588**,** 153-165.

Turner, D. R., Hunter, K. A. and De Baar, H. J. W., (**2001**) Introduction. *In:* Turner, D. R. & Hunter, K. A. (eds.) *The Biogeochemistry of Iron in Seawater.* Chichester: John Wiley & Sons Ltd.

Ussher, S. J., Achterberg, E. P. and Worsfold, P. J. (**2004**) Marine Biogeochemistry of Iron. *Environmental Chemistry,* 1**,** 67-80.

van den Berg, C. M. G. (**1995**) Evidence for organic complexation of iron in seawater. *Marine Chemistry,* 50**,** 139-157.

Von Damm, K. L. (**1990**) Seafloor hydrothermal activity - black smoker chemistry and chimneys. *Annual Review of Earth and Planetary Sciences,* 18**,** 173-204.

Waeles, M., Baker, A. R., Jickells, T. and Hoogewerff, J. (**2007**) Global dust teleconnections: aerosol iron solubility and stable isotope composition. *Environmental Chemistry,* 4**,** 233-237.

Walczyk, T. and Von Blanckenburg, F. (**2002**) Natural iron isotope variations in human blood. *Science,* 295**,** 2065-2066.

Watson, A. J., (**2001**) Iron Limitation in the Oceans. *In:* Turner, D. R. & Hunter, K. A. (eds.) *The Biogeochemistry of Iron in Seawater.* Chichester: John Wiley & Sons Ltd.

Welch, S. A., Beard, B. L., Johnson, C. M. and Braterman, P. S. (**2003**) Kinetic and equilibrium Fe isotope fractionation between aqueous Fe(II) and Fe(III). *Geochimica Et Cosmochimica Acta,* 67**,** 4231-4250.

Weyer, S. and Schwieters, J. (**2003**) High precision Fe isotope measurements with high mass resolution MC-ICPMS. *International Journal of Mass Spectrometry,* 226**,** 355-368.

Witter, A. E., Hutchins, D. A., Butler, A. and Luther, G. W. (**2000**) Determination of conditional stability constants and kinetic constants for strong model Fe-binding ligands in seawater. *Marine Chemistry,* 69**,** 1-17.

Woodward, E. M. S. and Rees, A. P. (**2001**) Nutrient distributions in an anticyclonic eddy in the northeast Atlantic Ocean, with reference to nanomolar ammonium concentrations. *Deep-Sea Research Part Ii-Topical Studies in Oceanography,* 48**,** 775-793.

Wu, L., Beard, B. L., Roden, E. E. and Johnson, C. M. (**2011**) Stable Iron Isotope Fractionation Between Aqueous Fe(II) and Hydrous Ferric Oxide. *Environmental Science & Technology,* 45**,** 1847-1852.

Yücel, M., Gartman, A., Chan, C. S. and Luther, G. (**2011**) Hydrothermal vents as a kinetically stable source of iron-sulphide-bearing nanoparticles to the ocean. *Nature Geoscience,* 4**,** 367-371.

Zhou, M., Paduan, J. D. and Niiler, P. P. (**2000**) Surface currents in the Canary Basin from drifter observations. *Journal of Geophysical Research-Oceans,* 105**,** 21893-21911.

Zhu, X. K., Guo, Y., Williams, R. J. P., O'nions, R. K., Matthews, A., Belshaw, N. S., Canters, G. W., De Waal, E. C., Weser, U., Burgess, B. K. and Salvato, B. (**2002**) Mass fractionation processes of transition metal isotopes. *Earth and Planetary Science Letters,* 200**,** 47-62.

Zhu, X. K., O'nions, R. K., Guo, Y. L. and Reynolds, B. C. (**2000**) Secular variation of iron isotopes in North Atlantic Deep Water. *Science,* 287**,** 2000-2002.